

# Theoretical Studies of Epitaxial Bain Paths of Metals

Dissertation

zur Erlangung des akademischen Grades

Doctor rerum naturalium  
(Dr. rer. nat.)

vorgelegt

der Fakultät Mathematik und Naturwissenschaften  
der Technischen Universität Dresden

von

Dipl.-Phys. Stephan Schönecker

geboren am 25.04.1979 in Großröhrsdorf

Eingereicht am 29.03.2011, verteidigt am 23.08.2011

Diese Dissertation wurde in der Zeit von September 2007 bis März 2011 im Leibniz-Institut für Festkörper- und Werkstoffforschung Dresden angefertigt.

1. Gutachter: Prof. Dr. Jeroen van den Brink
2. Gutachter: Prof. Dr. Niels Egede Christensen

# Contents

<b>List of figures</b>	<b>vii</b>
<b>List of tables</b>	<b>ix</b>
<b>List of abbreviations</b>	<b>xii</b>
<b>1 Introduction and motivation</b>	<b>1</b>
<b>2 Non-relativistic density functional theory</b>	<b>3</b>
<b>3 The Bain path</b>	<b>9</b>
3.1 Introduction . . . . .	9
3.2 Conceptual details . . . . .	10
3.3 Symmetry argument . . . . .	16
3.4 Symmetry argument: magnetic order . . . . .	20
3.5 Applications of Bain paths (examples) . . . . .	22
<b>4 Transition metals, selected alkaline earth metals and lanthanides</b>	<b>25</b>
4.1 Introduction and motivation . . . . .	25
4.2 Trends in transition metal series: insights from empirical models	26
4.3 Literature survey . . . . .	30
4.4 Computational aspects . . . . .	32
4.4.1 Band structure code and settings . . . . .	32
4.4.2 Convergence of basis set . . . . .	35
4.4.3 Brief remark on ground states . . . . .	37
4.4.4 Epitaxial Bain path calculational procedure . . . . .	38
4.5 Epitaxial Bain path of transition metals, selected alkaline earth metals and lanthanides . . . . .	39
4.5.1 General overview and remarks on tables . . . . .	39
4.5.2 General remarks on figure overviews . . . . .	42
4.5.3 Group 2 elements: Ca, Sr, and Ba . . . . .	44
4.5.4 Group 3 elements: Sc, Y, La, and Lu . . . . .	50
4.5.5 Group 4 elements: Ti, Zr, and Hf . . . . .	56
4.5.6 Group 5 elements: V, Nb, and Ta . . . . .	61
4.5.7 Group 6 elements: Cr, Mo, and W . . . . .	66
4.5.8 Group 7 elements: Mn, Tc, and Re . . . . .	71

## CONTENTS

---

4.5.9	Group 8 elements: Fe, Ru, and Os . . . . .	75
4.5.10	Group 9 elements: Co, Rh, and Ir . . . . .	85
4.5.11	Group 10 elements: Ni, Pd, and Pt . . . . .	92
4.5.12	Group 11 elements: Cu, Ag, and Au . . . . .	96
4.5.13	Group 12 elements: Zn, Cd, and Hg . . . . .	97
4.6	Trends and regularities in epitaxial Bain paths . . . . .	102
4.6.1	Structural energy differences . . . . .	103
4.6.2	Classification of epitaxial Bain paths . . . . .	108
4.7	Stability of extremal points: prediction of metastable phases . . .	109
4.7.1	Connection between structural stability and curvature of $E(a)$ . . . . .	109
4.7.2	Elastic properties of cubic structures . . . . .	110
4.7.3	Elastic stability of minima of $E(a)$ . . . . .	113
4.8	Summary of main results . . . . .	116
<b>5</b>	<b>Uranium</b> . . . . .	<b>119</b>
5.1	Introduction . . . . .	119
5.2	Computational details . . . . .	121
5.3	Results and discussion . . . . .	122
5.3.1	The epitaxial Bain path of uranium . . . . .	122
5.3.2	Bulk-like uranium overlayer with HCP structure . . . . .	130
5.4	Summary of main results . . . . .	133
<b>6</b>	<b>Summary and outlook</b> . . . . .	<b>135</b>
<b>A</b>	<b>Elastic constants</b> . . . . .	<b>137</b>
A.1	Theoretical considerations . . . . .	137
A.2	Technical considerations . . . . .	138
A.3	Tables . . . . .	140
A.3.1	BCC structures . . . . .	140
A.3.2	FCC structures . . . . .	142
A.3.3	BCT structures . . . . .	143
	<b>Bibliography</b> . . . . .	<b>145</b>

# List of figures

3.1	Delineation of the BCT lattice in the FCC and the BCC lattice . . . . .	9
3.2	Phase space of the BCT lattice . . . . .	11
3.3	Bain paths for model energy surface $E(a, c)$ . . . . .	15
3.4	Contour plot of $E(a, c)$ and Bain paths for Cr . . . . .	17
3.5	UBP and EBP for model energy surface $E(a, c)$ and differences in the localisation of stationary points between both Bain paths . . . . .	17
3.6	EBP for model energy surface $E(a, c)$ with discontinuous transition between local and global minimum . . . . .	19
3.7	Nearest neighbour distances in BCT lattices . . . . .	20
3.8	AF1 and AF2 orders on FCC and BCC lattices . . . . .	21
4.1	Elements from the periodic table under consideration in Chap. 4 . . . . .	26
4.2	Structural energy difference for canonical $d$ -bands as function of the band filling . . . . .	29
4.3	Convergence of basis set by means of the CVBP using the example of Ti and Zr . . . . .	38
4.4	Sensitivity of the DOS of FCC Sr to the Brillouin zone integration mesh and band structure of Sr . . . . .	45
4.5	EBPs of Ca, Sc, and Ba . . . . .	47
4.6	Type of stationary point of BCC Ca on the CVBP as function of the employed volume . . . . .	49
4.7	Necessity of the enhanced 3D-grid to determine stationary points of the EBP of Ba . . . . .	49
4.8	Illustration of a double well in $E(c)$ and implication for the EBP and for quantities plotted along the EBP . . . . .	51
4.9	EBPs of Sc, Y, La, and Lu . . . . .	53
4.10	$E(c)$ in the vicinity of $a_{\text{BCC}}$ of La (double wells) and discontinuity of the EBP . . . . .	54
4.11	$D(E_{\text{F}})$ as function of $c$ in the vicinity of $a_{\text{BCC}}$ of La . . . . .	55
4.12	EBPs of Ti, Zr, and Hf . . . . .	59
4.13	CVBPs of Ti and Zr at the respective theoretical FCC equilibrium volumes and their alteration in response to a charge variation by means of VCA . . . . .	60
4.14	EBPs of V, Nb, and Ta . . . . .	63
4.15	$E(c)$ in the vicinity of $a_{\text{FCC}}$ of V and of Nb (double wells) causing the discontinuity of the EBP . . . . .	64

## LIST OF FIGURES

---

4.16	Peak in the electronic DOS of V as possible reason for the discontinuity of the EBP . . . . .	66
4.17	$d$ -band dominated DOS of TMs at nearly half band filling: the case of BCC and FCC Cr . . . . .	67
4.18	EBPs of Cr, Mo, and W . . . . .	69
4.19	EBPs of Mn, Tc, and Re . . . . .	73
4.20	Presence of a secondary minimum in $E(c/a)$ at the BCC structure of Mn, FM order on the EBP and respective spin moment . . . . .	74
4.21	EBPs of Fe, Ru, and Os . . . . .	77
4.22	$E_{m_s}(a, c)$ as function of $c$ in the vicinity of $a = 2.575 \text{ \AA}$ of Fe (double well) causing the discontinuity of the EBP . . . . .	79
4.23	Magnetisation $E(m_s)$ in the vicinity of $a = 2.575 \text{ \AA}$ of Fe, and transition from a state with low moment to a state with high moment . . . . .	79
4.24	$E(a)$ of NM Fe and with FM, AF1, and AF2 orders . . . . .	80
4.25	Site resolved spin magnetic moments of Fe along the EBP for FM, AF1, and AF2 orders . . . . .	80
4.26	$E(c)$ in the vicinity of $a_{\text{BCC}}$ of Ru and of Os (double wells) and the local stability of BCC Os with respect to a tetragonal strain $\epsilon_{zz}$ . . . . .	83
4.27	Site resolved spin magnetic moments of Ru along the EBP for FM and AF2 order, and energy difference between NM states and magnetically ordered states . . . . .	84
4.28	Site resolved spin magnetic moments of Os along the EBP for FM order and energy difference between NM and FM states . . . . .	85
4.29	EBPs of Co, Rh, and Ir . . . . .	87
4.30	Spin moment of Co along the EBP and comparison to experiments . . . . .	89
4.31	$E(c)$ in the vicinity of $a_{\text{FCC}}$ of Ir (double wells) causing the discontinuity of the EBP . . . . .	90
4.32	$D(E_{\text{F}})$ as function of $c$ in the vicinity of $a_{\text{BCC}}$ of Ir . . . . .	91
4.33	Spin moment of Ni along the EBP and comparison to experiments . . . . .	93
4.34	EBPs of Ni, Pd, and Pt . . . . .	95
4.35	Enlarged picture detail of the local BCT minimum of Cu . . . . .	97
4.36	EBPs of Cu, Ag, and Au . . . . .	99
4.37	EBPs of Zn, Cd, and Hg . . . . .	101
4.38	Total energy differences between BCC and FCC and between BCT and FCC as function of the $d$ -band filling for elements from the fourth and fifth period . . . . .	104

---

**LIST OF FIGURES**

4.38	<i>Continued.</i> Total energy differences between BCC and FCC and between BCT and FCC as function of the $d$ -band filling for elements from the sixth period . . . . .	105
4.39	Mapping of types of EBP's on the elements in the periodic table .	108
4.40	Bulk moduli and elastic constants of the BCC and the FCC structure for elements of the fourth, fifth, and sixth period, and identification of trends and violation of stability conditions . . . . .	112
4.41	Elastic constants of states whose energy corresponds to the global minimum of $E(a)$ for elements of the fourth, fifth, and sixth period, and identification of trends and violation of stability conditions	114
4.42	Elastic constants of states whose energy corresponds to the local minimum of $E(a)$ for elements of the fourth, fifth, and sixth period, and identification of trends and violation of stability conditions . . . . .	115
5.1	Crystal structure of $\alpha$ -U at 50 K . . . . .	120
5.2	$E - E_\alpha$ and magnetic order along the EBP of U . . . . .	124
5.3	Total, spin, and orbital magnetic moments for FM order along the EBP of U in R1 and energy difference between NM and FM states . . . . .	124
5.4	Total, spin, and orbital magnetic moments for FM order along the EBP of U in R2 and energy difference between NM and FM states . . . . .	125
5.5	EBP of U and relative volume $V/V_\alpha$ along the EBP of U . . . . .	126
5.6	Total DOS at $E_F$ along the EBP and contributions from $5f$ states	126
5.7	Comparison of the total DOS of $\alpha$ -U, BCT-U ( $a = 3.00 \text{ \AA}$ ), and HCP-U . . . . .	128
5.8	Comparison of the EBP with the CVBP at $V_{\alpha, \text{EXP}}$ and the CVBP at $V_{\text{FCC}}$ to study the effect of symmetry and volume on the DOS at $E_F$ . . . . .	129
5.9	Total, spin, and orbital magnetic moments for FM order along the EBP of U in R1 using OPC . . . . .	131
5.10	Total energy and DOS at $E_F$ for an epitaxially strained HCP structure of U modelling a lattice mismatch between film and substrate . . . . .	132





# List of tables

4.1	Literature survey of computed EBPs, UBPs, CSBPs, CVBPs, and investigated magnetic order for EBPs . . . . .	31
4.2	Default and extended basis set for specific elements . . . . .	37
4.3	GS data and properties of SPs of Ca, Sr, and Ba . . . . .	46
4.4	GS data and properties of SPs of Sc, Y, La, and Lu . . . . .	52
4.5	$d$ -band occupation numbers for the FCC and the BCC configurations of Ti, Zr, and Hf . . . . .	57
4.6	$d$ -band occupation numbers for the FCC and the BCC configurations of Zr and a virtual element of reduced atomic charge by means of VCA . . . . .	57
4.7	GS data and properties of SPs of Ti, Zr, and Hf . . . . .	58
4.8	GS data and properties of SPs of V, Nb, and Ta . . . . .	62
4.9	GS data and properties of SPs of Cr, Mo, and W . . . . .	68
4.10	GS data and properties of SPs of Mn, Tc, and Re . . . . .	72
4.11	GS data and properties of SPs of Fe, Ru, and Os . . . . .	76
4.12	GS data and properties of SPs of Co, Rh, and Ir . . . . .	86
4.13	Spin moment of Co in various bulk structures and comparison to theoretical and experimental references . . . . .	88
4.14	Spin moment of Ni in various bulk structures and comparison to theoretical and experimental references . . . . .	93
4.15	GS data and properties of SPs of Ni, Pd, and Pt . . . . .	94
4.16	GS data and properties of SPs of Cu, Ag, and Au . . . . .	98
4.17	GS data and properties of SPs of Zn, Cd, and Hg . . . . .	100
5.1	Positions of extrema of $E$ on the EBP of U and their energy difference to the GS . . . . .	122
A.1	Setups appropriate for the calculation of elastic constants of BCT cells with $I4/mmm$ symmetry. . . . .	139
A.2	Elastic constants, bulk moduli, and stability conditions of elements in the BCC structure . . . . .	141
A.3	Elastic constants, bulk moduli, and stability conditions of elements in the FCC structure . . . . .	142
A.4	Elastic constants, bulk moduli, and stability conditions of elements in the BCT structure . . . . .	144



# List of abbreviations

(m)Ha	.....	(milli) Hartree
AFM	.....	anti-ferromagnetic
ASA	.....	atomic sphere approximation
BCC	.....	body-centred cubic
BCT	.....	body-centred tetragonal
CDW	.....	charge density wave
CSBP	.....	cancelling slope Bain path
CVBP	.....	constant volume Bain path
DFT	.....	density functional theory
DHCP	.....	double HCP
DOS	.....	(electronic) density of states
EBP	.....	epitaxial Bain path
EXP	.....	experiment (used in tables)
FCC	.....	face-centred cubic
FM	.....	ferromagnetic
FP	.....	full potential
FSM	.....	fixed spin moment
GGA	.....	generalised gradient approximation
GS	.....	ground state
HCP	.....	hexagonal closed packed
ISS	.....	initial spin split
L(S)DA	.....	local (spin) density approximation
LAPW	.....	linearised augmented plane wave
LCAO	.....	linear combination of atomic orbitals
LCLO	.....	linear combination of local orbitals
LEED	.....	low energy electron diffraction
LMTO	.....	linear muffin tin orbitals
MAX	.....	maximum (used in tables)
MIN	.....	minimum (used in tables)
ML	.....	mono layer
NM	.....	non-magnetic
OPC	.....	orbital polarisation correction
PAW	.....	projector augmented wave
PBE96	.....	$V_{XC}$ parameterisation after Perdew, Burke, and Ernzerhof [172] (GGA)
PW92	.....	$V_{XC}$ parameterisation after Perdew and Wang [174] (LSDA)
RP	.....	room pressure
RT	.....	room temperature
RTP	.....	room temperature and room pressure

## **LIST OF TABLES**

---

SC .....	stability condition
SDW .....	spin density wave
SP .....	stationary point (used in tables)
TB .....	tight binding
TM .....	transition metal
UBP .....	uniaxial Bain path
VCA .....	virtual crystal approximation
XC .....	exchange-correlation

# 1

## Introduction and motivation

Diamond and graphite are two well known crystalline configurations of carbon. Both allotropes have unique properties. The transparent, electrically insulating diamond is an excellent thermal conductor and an extremely hard material, hence used as abrasive. In contrast, the opaque graphite is an electrical conductor, thermally insulating and used as lubricant. Recently synthesised new allotropes of carbon, e.g., fullerenes, carbon nanotubes, and graphene, have again outstanding chemical and physical properties and potentially lead to new applications [80].

The introductory example of diamond and graphite suggests, that the metastable phase (diamond) is a material essentially different from the thermodynamically stable configuration (graphite) at room temperature and room pressure (RTP). But diamond is a rare case where one experiences a bulk metastable allotrope. The situation is different for, say Co, for which there is only one bulk configuration at RTP, namely hexagonal closed packed (HCP) Co. At temperatures above 696 K, face-centred cubic (FCC) Co is the stable phase [43]. Crystalline forms of Co other than HCP were however stabilised at RTP by means of epitaxial growth, e.g., body-centred cubic (BCC) Co [182]. All three mentioned configurations of Co exhibit ferromagnetic (FM) order, but magnetic properties like the spin moment depend on the crystal structure. Bulk BCC Co does not exist in the known region of the pressure-temperature phase diagram [43, 256].

The example of BCC Co demonstrates, that epitaxial growth can stabilise non-equilibrium structures at RTP. In heteroepitaxy, overlayer and substrate material are not identical [61]. Hence, lattice parameters and possibly the crystal structure of film and substrate material are distinct. In case of coherent or pseudomorphic epitaxy, the overlayer adapts the in-plane lattice parameters of the substrate, i.e., the overlayer is strained to match the lattice parameters parallel to the substrate surface (in-plane directions). Simultaneously, a relaxation of the film dimension perpendicular to the substrate-film interface occurs (out-of-plane direction). Thus, coherent epitaxy provides a method to put phases under strain, and it can stabilise a metastable state of the film material, if the substrate lattice matches this metastable structure. The energy of a metastable or a strained state is higher than in the equilibrium state, which limits the thickness of pseudomorphic films. Strain in epitaxial film growth is a mean to influence material properties in, e.g., semiconductors, multiferroic materials, and ferromagnets. Tunable properties of FM elements, alloys and multilayers are, for example, orbital and spin magnetic moments, the Curie temperature, and the magnetic anisotropy [17, 26, 29].

## CHAPTER 1. INTRODUCTION AND MOTIVATION

---

Films in the body-centred tetragonal (BCT) structure are typically obtained by pseudomorphic epitaxy on a planar quadratic lattice, e.g., on the  $\{001\}$  surfaces of a cubic lattice [4] (the tetragonal axis of the film is oriented perpendicular to the substrate-film interface). The substrate determines in-plane and out-of-plane lattice parameters of films with BCT geometry. A symmetry property of the BCT structure states, that it is identical to the BCC structure or the FCC structure for definite ratios of the tetragonal lattice parameters. The geometric concept of the Bain transformation describes a transformation between the FCC structure and the BCC structure via intermediate BCT structures [9]. The sum of all states along a Bain transformation is then called a Bain path. A particular Bain path is the epitaxial Bain path (EBP). All states of the EBP are modelled by epitaxial constraints: coherency to the substrate and relaxation of the overlayer in the out-of-plane direction [4]. Thus, the EBP singles out all BCT structures (including higher symmetric cubic ones), that (in principle) can be stabilised by pseudomorphic epitaxy on a suitable substrate. The knowledge of the EBP therefore allows to study properties of the overlayer as function of the substrate lattice parameter.

Interest in magnetic materials in BCT structures has been induced by, e.g., an increase of the magnetocrystalline anisotropy energy in response to a symmetry reduction from cubic to tetragonal for the strained FCC and BCC phases of Ni and Fe, respectively [26], or by a stabilisation of cubic non-equilibrium structures of the magnetic elements and a characterisation of their magnetic structure (cf. aforementioned example Co). Alloys in a tetragonal structure, e.g., ordered FePt [27] and FeCo [28], possess a high uniaxial magnetocrystalline anisotropy energy for certain compositions and axial ratios, and are potential new materials for high density recording materials in hard disks.

Density functional theory (DFT) is an established and transferable method to describe the electronic structure of condensed matter in the ground state (GS). It allows for the computation of, e.g., structural and mechanical properties, magnetic order, and phase transitions under pressure. Since we apply total energy calculations based on DFT in this thesis, a brief introduction into the theory is given in the next chapter. In Chapter 3, we elaborately discuss the concept of the Bain path, in particular the EBP and three other commonly studied Bain paths. A symmetry argument for BCT Bravais lattices states, that cubic configurations on the EBP are stationary points in total energy [133]. This argument guarantees the existence of (at least) two minima in energy along the EBP, unless the energy for one of the cubic structures is a horizontal inflection point. The minima may correspond to metastable states of the respective element. Earlier computations of the EBP for various alkali and transition metals (TMs) indicated that usually two minima occur on the EBP, e.g., see Ref. 133. We study the EBP for all TMs, as well as selected alkaline earth metals and selected lanthanides in the fourth chapter of this thesis. We focus on the existence of metastable tetragonal states, magnetic order along the EBP, and analyse trends and regularities of EBPs in TMs. In the fifth Chapter, we investigate the EBP of uranium motivated by recent progress in the epitaxial stabilisation of a non-equilibrium HCP structure of uranium. This work is summarised in Chapter 6.



# 2

## Non-relativistic density functional theory

If not stated otherwise, we use atomic units throughout this Chapter. A calligraphic symbol denotes the abstract Hilbert space operator,  $\hat{\mathcal{H}}$ , an italic symbol denotes the Hamiltonian operator in Schrödinger representation,  $\hat{H}$ , and a letter without hat signifies the functional,  $H$ .

The physical model under consideration is a solid state as a non-relativistic, interacting ion-electron system. The interaction of all charged particles is via mutual Coulomb forces. Due to its complexity, the problem is not exactly solvable apart from simple cases. As a first step, the electronic sub-system, containing kinetic part and pairwise interaction between electrons as well as the Coulomb interaction with the nuclei, can be tackled separately under certain prerequisites elucidated below. In the framework of DFT,<sup>1</sup> the electronic GS of the many particle problem is reduced to effective single particle equations, which have to be solved self-consistently at the end. Primal contributions to the DFT came from Hohenberg, Kohn, and Sham [85, 107]. Important for the mathematical foundation of the DFT were the seminal papers by Lieb and Levy [117, 122]. Perturbations arising from, e.g., a probing external magnetic field, which couples to spin and orbital moments, are not considered here. The spin of electrons is included in the theory, spin-orbit coupling is part the relativistic DFT. In the following, we outline important aspects of DFT which are taken from textbooks [44, 53, 168].

The full ion-electron Hamiltonian may be sketched according to different contributions,

$$\hat{\mathcal{H}} = \hat{\mathcal{H}}_{\text{nuclei}} + \hat{\mathcal{H}}_{\text{electrons}} + \hat{\mathcal{H}}_{\text{nuclei-electrons}}, \quad (2.1)$$

whereat the notation already suggests the splitting of purely nuclear and electronic contributions into  $\hat{\mathcal{H}}_{\text{nuclei}}$  and  $\hat{\mathcal{H}}_{\text{electrons}}$ , respectively. Both operators contain kinetic and interacting parts. The third term on the right hand side of Eq. (2.1) comprises the interaction between the two different particle species. The *adiabatic approximation* allows to separate the ionic motion from  $\hat{\mathcal{H}}$ . The other term is an adiabatic Hamiltonian parametrically dependent on nuclear positions. One part of the adiabatic Hamiltonian is given by the constant inter-nuclear interactions (fixed nuclear positions). The remaining electronic part,

$$\hat{\mathcal{H}}_{\text{el}} = \hat{\mathcal{H}}_{\text{electrons}} + \hat{\mathcal{H}}_{\text{nuclei-electrons}}, \quad (2.2)$$

---

<sup>1</sup>When we speak of DFT we exclude early versions, e.g., Thomas-Fermi theory.

## CHAPTER 2. NON-RELATIVISTIC DENSITY FUNCTIONAL THEORY

can be solved independently (the parametric nuclear positions in  $\hat{\mathcal{H}}_{\text{el}}$  are not explicitly indicated). For solids, the internuclear Coulomb energy must be added to Eq. (2.2) in order to get a finite energy per volume in the thermodynamic limit. We skip this term in the following short presentation. The adiabatic approximation can be done due to the small ratio of electron mass to nucleus mass, typically being  $10^{-3} \dots 10^{-5}$ . In simple words, the coupling strength between non-degenerate (electronic) eigenstates of a molecule or solid depends on the ratio of electron mass to nucleus mass; the coupling would even vanish if this ratio approaches zero. With this small ratio, electrons do not undergo a transition to another state. The electron state follows the nuclear displacement progressively [22]. In particular, the electrons remain in their GS at all times.<sup>2</sup>

Formally, we are looking for solutions of the time-independent Schrödinger equation

$$\hat{\mathcal{H}}_{\text{el}}|\Psi\rangle = |\Psi\rangle E, \quad \langle\Psi|\Psi\rangle = 1, \quad (2.3)$$

$E$  being the eigenvalue (energy) and  $|\Psi\rangle$  the many particle quantum state. Considering the huge number of interacting nuclei, electrons, and similarly a huge number of degrees of freedom in a typical solid state, the exact solution of the previous equation is impossible to obtain. Alternatively, an equivalent variational problem may be applied [168],

$$\delta \left\{ \langle\Psi|\hat{\mathcal{H}}_{\text{el}}|\Psi\rangle - E\langle\Psi|\Psi\rangle \right\} = 0. \quad (2.4)$$

$E$  serves as Lagrange multiplier to ensure normalisation of  $|\Psi\rangle$ . Allowable approximations on  $|\Psi\rangle$ , say  $|\tilde{\Psi}\rangle$ , will give energies  $\tilde{E}$ ,  $\tilde{E} \geq E_{\text{GS}}$ ,  $E_{\text{GS}}$  being the eigenenergy of the true GS,  $|\Psi_{\text{GS}}\rangle$ .

At this point we are left with the following type of Schrödinger Hamiltonian:

$$\begin{aligned} \hat{H}_{\text{el}}[v, M] &= -\frac{1}{2} \sum_{i=1}^M \nabla_i^2 + \sum_{i=1}^M v_{s_i s'_i}(\mathbf{r}_i) + \frac{1}{2} \sum_{i \neq j}^M w(|\mathbf{r}_i - \mathbf{r}_j|) \\ &\equiv \hat{T} + \hat{U} + \hat{W}, \end{aligned} \quad (2.5)$$

with kinetic part,  $\hat{T}$ , external potential part,  $\hat{U}$ , and interaction part,  $\hat{W}$ , for an integer number  $M$  of electrons at positions  $\mathbf{r}_i$ .  $w$  is the Coulomb potential. The external potential,  $v$ , is restricted to cover collinear spin order in this work. Its spin matrix therefore has the following form:

$$v_{ss'}(\mathbf{r}) = v(\mathbf{r})\delta_{ss'}. \quad (2.6)$$

Generally, an admissible potential  $v$  comes from the space of  $p$  integrable functions,  $\mathbf{L}^p$ . Additionally, we demand  $v$  to have a  $N$  particle GS. We define first the set  $\mathcal{V}_N$ ,  $1 \leq p < +\infty$ ,

$$\mathcal{V}_N \stackrel{\text{def}}{=} \left\{ v \mid v \in \oplus \mathbf{L}^p \text{ for some } p\text{'s, and } \hat{H}_{\text{el}}[v] \text{ has a GS} \right\}.$$

<sup>2</sup>There are cases when the adiabatic approximation is unfeasible, like strong electron-phonon coupling, or two molecular energy surfaces, which energetically approach for certain nuclear configuration.



---

For spin-independent  $v \in \mathcal{V}_N$  the Hohenberg-Kohn lemma holds [85]:

$v$  is a unique function of the GS density  $n$ .

We now state the functional spaces of admissible potentials  $v$  and of densities  $n$ . The position space is a Torus  $\mathbf{T}^3$  (a box with periodic boundary conditions and finite volume) instead of the Euclidian space  $\mathbf{R}^3$ , i.e., the domain (of the position space) of  $v$  and  $n$  is  $\mathbf{T}^3$ . This choice ensures the reflexivity property for functional spaces of densities and potentials, and excludes scattering states, where part of the electrons are not bound by  $v$  in  $\mathbf{R}^3$ . Then it can be shown, that  $v \in X^* \stackrel{\text{def}}{=} \mathbf{L}^{3/2}(\mathbf{T}^3) \subseteq \mathcal{V}_N$  and  $n \in X \stackrel{\text{def}}{=} \mathbf{L}^3(\mathbf{T}^3)$ . Variations over  $v$  and  $n$  are always understood as variations over  $v \in X^*$  and  $n \in X$ , respectively. For spin matrices (Eqs. (2.6), and Eq. (2.12) below) each component belongs to the respective space.

Before we state an expression for the GS energy, we need to introduce ensemble states first. Such are combinations of Fock states,  $|\Psi_K^M\rangle$ , given by the density matrix  $\hat{\gamma}$  with

$$\hat{\gamma} = \sum_{K,M} |\Psi_K^M\rangle p_K^M \langle \Psi_K^M|, \quad 0 \leq p_K^M, \quad \sum_{K,M} p_K^M = 1, \quad (2.7)$$

and  $p_K^M$  are probabilities. The  $|\Psi_K^M\rangle$  are eigenstates of the particle number operator,  $\hat{N}$ , with integer particle number,  $M$ ,

$$\hat{N}|\Psi_K^M\rangle = |\Psi_K^M\rangle M. \quad (2.8)$$

Expectation values of, e.g., the Hamilton operator in Eq. (2.5) and the particle number operator,  $\hat{N}$ , of the ensemble are defined via the trace ( $\text{tr}$ ) ( $[\hat{H}_{\text{el}}, \hat{N}] = 0$ ),

$$\begin{aligned} \langle \hat{H}_{\text{el}} \rangle_{\hat{\gamma}} &= \text{tr}(\hat{H}_{\text{el}} \hat{\gamma}) \\ &= \sum_{K,M} p_K^M \langle \Psi_K^M | \hat{H}_{\text{el}}[v, M] | \Psi_K^M \rangle \end{aligned} \quad (2.9)$$

$$\begin{aligned} \langle \hat{N} \rangle_{\hat{\gamma}} &= \text{tr}(\hat{N} \hat{\gamma}) \\ &\stackrel{(2.8)}{=} \sum_{K,M} p_K^M M. \end{aligned} \quad (2.10)$$

The particle number,  $N$ , of an ensemble state (2.7) is a real number. For later use we define the expectation value of the external potential,

$$\text{tr}(\hat{U} \hat{\gamma}) = \sum_{ss'} \int d^3r v_{ss'}(\mathbf{r}) n_{s's}(\mathbf{r}) \stackrel{\text{def}}{=} (v|n), \quad (2.11)$$

with the spin density matrix,  $n_{ss'}$ , which is given by the expectation value of the density operator  $\hat{n}$ ,

$$n_{ss'}(\mathbf{r}) = \text{tr}(\hat{n} \hat{\gamma}). \quad (2.12)$$

## CHAPTER 2. NON-RELATIVISTIC DENSITY FUNCTIONAL THEORY

---

Both matrices,  $v_{ss'}$  and  $n_{ss'}$ , are hermitian. We define the GS energy by

$$\begin{aligned} E[v, N] &= \inf_{\hat{\gamma}} \left\{ \text{tr}(\hat{H}_{\text{el}}\hat{\gamma}) \mid \text{tr}(\hat{N}\hat{\gamma}) = N \right\} \\ &= \inf_{\{p_K^M, \Psi_K^M\}} \left\{ \sum_{K,M} p_K^M \langle \Psi_K^M | \hat{H}_{\text{el}} | \Psi_K^M \rangle \mid \sum_{K,M} p_K^M M = N \right\}. \end{aligned} \quad (2.13)$$

The previous equality was derived with the help of the above defined expectation values of ensemble states. The infimum in (2.13) exists if  $w$  in (2.5) is repulsive for fixed  $v$  ( $w \geq 0$ ). Further, we denote three important properties of  $E[v, N]$  ( $z \in \mathbf{R}$ ,  $0 \leq z \leq 1$ ):

1.  $E[v, N]$  is convex in  $N$  for fixed  $v$ :

$$E[v, zN_1 + (1-z)N_2] \leq zE[v, N_1] + (1-z)E[v, N_2] \quad (2.14)$$

2.  $E[v, N]$  is concave in  $v$  for fixed  $N$ :

$$E[zv_1 + (1-z)v_2, N] \geq zE[v_1, N] + (1-z)E[v_2, N] \quad (2.15)$$

3.  $E[v, N]$  is gauge covariant with respect to a constant  $c$ :

$$E[v + c, N] = E[v, N] + cN. \quad (2.16)$$

The following passage makes use of duality theory. To begin with, we consider the Legendre transform  $\tilde{G}[v, \mu]$  of  $E[v, N]$ ,

$$\tilde{G}[v, \mu] = \sup_N \{ \mu N - E[v, N] \} \quad (2.17)$$

$$\stackrel{(2.16)}{=} \sup_N \{ -E[v - \mu, N] \} \quad (2.18)$$

$$= \tilde{G}[v - \mu, 0] \stackrel{\text{def}}{=} G[v - \mu], \quad (2.19)$$

and obtain,

$$G[v] = \sup_N \{ -E[v, N] \} \quad (2.20)$$

$$= -\inf_N \{ E[v, N] \}. \quad (2.21)$$

$G$  is convex in  $v$  and a functional of one variable due to the gauge property.  $\mu$  is the chemical potential at  $T = 0$  K. From Eqs. (2.17) and (2.19) we identify the Legendre transform of  $G$ ,

$$E[v, N] = \sup_{\mu} \{ N\mu - G[v - \mu] \}. \quad (2.22)$$

$N$  and  $\mu$  are dual variables, and  $E$  and  $G$  are a pair of dual functionals.  $v$  and  $-n$  form another pair of dual variables, and  $G[v]$  and  $\tilde{H}[-n]$  form another pair of dual functionals,

$$H[n] \stackrel{\text{def}}{=} \tilde{H}[-n] = \sup_v \{ (-n)v - G[v] \} \quad (2.23)$$

$$G[v] = -\inf_n \{ H[n] - (n)v \}. \quad (2.24)$$

---

Relating  $H$  to  $E$  with the help of Eqs. (2.21) and (2.22) leads to

$$E[v, N] = \sup_{\mu} \left\{ N\mu + \inf_n \{ H[n] + (v - \mu|n) \} \right\} \quad (2.25)$$

$$= \inf_n \left\{ H[n] + \sup_{\mu} \{ (N - (1|n))\mu \} \right\}. \quad (2.26)$$

The previous equality is obtained from a special investigation since in general only  $\sup \inf \leq \inf \sup$  holds. The next relation is obtained by noting, that an infimum over  $n$  implies that the supremum over  $\mu$  is finite and hence  $(1|n) = N$ . We obtain the Hohenberg-Kohn variational principle:

$$E[v, N] = \inf_n \{ H[n] + (v|n) \mid (1|n) = N \}. \quad (2.27)$$

The Hohenberg-Kohn functional,  $H$ , is convex in  $n$  and often called universal functional, because it is independent of  $N$  and of  $v$ . However, it is not known and must be modelled.

In the following we briefly derive the Kohn-Sham equations [107]. For the spin density matrix, we employ the ansatz,

$$n_{ss'}(\mathbf{r}) = \sum_i \phi_i(\mathbf{r}s) n_i \phi_i^*(\mathbf{r}s'), \quad 0 \leq n_i \leq 1, \quad (2.28)$$

with orthonormal Kohn-Sham orbitals,  $\phi_i$ , occupation numbers,  $n_i$ , and the particle number,  $N = \sum_i n_i = (1|n)$ .  $H[n]$  is decomposed into

$$H[n] = K[n] + E_H[n] + E_{XC}[n]. \quad (2.29)$$

$K[n]$  is defined as the kinetic energy functional for non-interacting reference systems,

$$K[n] = \inf_{\{\phi_i, n_i\}} \left\{ \sum_i n_i \sum_s \int d^3r \phi_i^*(\mathbf{r}s) \left( -\frac{\nabla^2}{2} \right) \phi_i(\mathbf{r}s) \right. \\ \left. (\phi_i | \phi_j) = \delta_{ij}, \quad 0 \leq n_i \leq 1, \quad \sum_i \sum_s n_i |\phi_i(\mathbf{r}, s)|^2 = n(\mathbf{r}) \right\}, \quad (2.30)$$

with pre-defined density. The Hartree energy,  $E_H[n]$ , is the classical interaction of a density with itself,

$$E_H[n] = \frac{1}{2} \iint d^3r d^3r' \frac{n(\mathbf{r})n(\mathbf{r}')}{|\mathbf{r} - \mathbf{r}'|}. \quad (2.31)$$

The exchange-correlation (XC) energy,  $E_{XC}$ , is defined by Eq. (2.29), however unknown, and again subject to modelling. Assuming functional derivatives to exist, we vary  $n$  through  $\phi_i^*$  in Eq. (2.27) with the help of Relations (2.29) and (2.11), including the side conditions of  $K[n]$  and  $E[v, N]$ , and obtain the Kohn-Sham equations for the  $\phi_i$  with an effective potential,  $v_{\text{eff}}$ ,

$$\left( -\frac{\nabla^2}{2} + v_{\text{eff}} \right) \phi_i = \phi_i \epsilon_i, \quad v_{\text{eff}} \stackrel{\text{def}}{=} v + v_H + v_{XC}. \quad (2.32)$$

## CHAPTER 2. NON-RELATIVISTIC DENSITY FUNCTIONAL THEORY

---

The Hartree potential,  $v_H$ , is straightforwardly derived from the Hartree energy,  $E_H$ , in contrast to the exchange-correlation potential,  $v_{XC}$ , which is just defined as

$$v_{XC,ss'} \stackrel{\text{def}}{=} \frac{\delta E_{XC}[n]}{\delta n_{s's}}. \quad (2.33)$$

For the minimising density, the electronic energy (total energy) is given by

$$E[v, N] = \sum_i n_i \epsilon_i - E_H[n] - \sum_{ss'} \int d^3r n_{ss'} v_{XC,s's} + E_{XC}[n], \quad (2.34)$$

where the first term on the right hand side sums over Kohn-Sham energies,  $\epsilon_i$ , whose occupation follows the Aufbau principle.

What is left, is to introduce approximations for the exchange and correlation energy. The local (spin) density approximation (L(S)DA) assumes the exchange and correlation energy per particle to be local in the density,

$$E_{XC}[n] \approx E_{XC}^{\text{LDA}}[n] = \int d^3r n(\mathbf{r}) \epsilon_{XC}(n(\mathbf{r}), \zeta(\mathbf{r})). \quad (2.35)$$

$\epsilon_{XC}$  is the exchange and correlation energy per particle of the homogeneous electron liquid, taken at the system's 'real' total density,  $n$ , and spin polarisation,  $\zeta$ , at each  $\mathbf{r}$ . The degree of spin polarisation gives the normalised difference between both spin components of the density in the collinear situation.  $\epsilon_{XC}$  has to be parameterised and there several parameterisations available. We use the version of Perdew and Wang (PW92) [174] in this work. Generalised gradient approximations (GGA) are non-local functionals of the density, since they include the density gradient. We employ the parameterisation after Perdew, Burke, and Ernzerhof (PBE96) [172]. A less stringent assumption on the functional derivative of  $E_{XC}$  results in the possibility of nonlocal and orbital dependent exchange and correlation potentials like in LSDA+U or in self-interaction corrected (SIC) functionals [54].



# 3

## The Bain path

### 3.1 Introduction

In the general discussion of Bain paths, it is certainly a good starting point to clarify the origin of the term 'Bain' first. The eponym was the north American metallurgist Edgar C. Bain, who pioneered the fundamental principles of alloy steels [10]. In an earlier paper [9], he investigated the martensitic transformation. More precisely, Bain suggested a mechanism of how the high temperature FCC phase of iron can be transformed into the low temperature BCC phase of iron 'with atomic shifts requiring minimum motion'. This transformation can be achieved relying on the BCT structure. In Fig. 3.1 we sketch the FCC and the BCC lattice and delineate the BCT lattice therein. Let us denote the lattice parameters of the BCT unit cell with  $a$  and  $c$ .  $a$  is the lattice parameter of the quadratic basal plane.  $c$  specifies the lattice parameter perpendicular to the basal plane, and parallel to the  $C_4$  axis. The correspondence between FCC and BCT structures is achieved if the axial ratio,  $c/a$ , of the BCT lattice equals  $\sqrt{2}$ . Likewise, the correspondence between BCC and BCT structures is achieved if  $c/a = 1$ . A change of  $c/a$  from 1 to  $\sqrt{2}$  transforms a lattice with BCC structure into a lattice with FCC structure via intermediate BCT structures [9]. Since the three cubic axes are equivalent, there are three possibilities corresponding to three orthogonal directions to transform BCC into FCC (or vice versa). This is Bain's geometrical description of the allotropic transformation of iron via intermediate BCT structures. For convenience, we choose the  $[001]$ -axis as

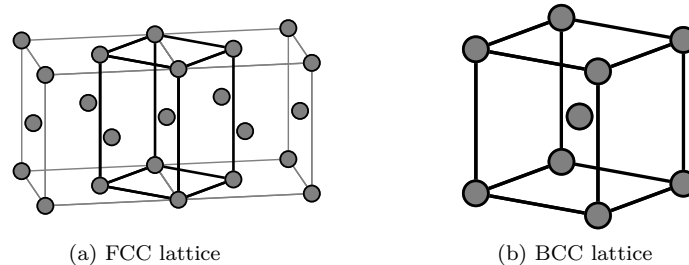


Figure 3.1: Delineation of the BCT lattice (thick lines) in the (a) FCC lattice (thin lines, two unit cells), and in the (b) BCC lattice. BCT and BCC lattice are on top of each other.

tetragonal transformation axis.

At this point we give a few remarks, that intend to sharpen the use of the term Bain transformation in this work. The Bain transformation relies on symmetry matches of the underlying lattices (cf. Sec. 3.2) and a certain transformation instruction via intermediate tetragonal structures, that has to be specified. Moreover, there is no conceptual limitation to confine the axial ratio  $c/a$  along the transformation to the limits 1 and  $\sqrt{2}$ . In spite of its historical origin from the martensitic transformation, we use the term Bain transformation (and later Bain path) for the just described geometrical construction without any assumptions for the boundaries of  $c/a$ .

### 3.2 Conceptual details

The relation between FCC or BCC lattices and BCT lattices, that we described in the preceding section, implies relations between their crystallographic space groups. Those can be analysed by group-subgroup relations. More precisely, the maximal non-isomorphic subgroups can be considered (or vice versa the minimal non-isomorphic supergroups) [74]. The FCC lattice has space group type  $Fm\bar{3}m$ , BCC has  $Im\bar{3}m$ . For the case considered here, both cubic space groups have the common maximal non-isomorphic  $t$ -subgroup  $I4/mmm$  (of index 3), which is the space group type of the BCT lattice. This is the group theoretical argument of why there is a structural relation of the BCT lattices on the one hand and FCC or BCC lattices on the other hand.

There are infinitely many Bain transformations, since there are infinitely many ways to transform an FCC structure into a BCC structure, if, besides  $c/a$ ,  $a$  or  $c$ , and hence the volume, are allowed to vary independently, see Fig. 3.2 for a diagrammatic explanation. The tetragonal phase space (parameter space) of BCT lattices is spanned by its lattice parameters  $a$  and  $c$ . Every line in the phase space, that connects the straight lines of FCC and BCC, represents a Bain transformation. The line (or the path) in the phase space corresponding to this transformation is called Bain path. Per definition, the Bain path includes only tetragonal geometries. Any arbitrary point in the parameter space is denoted by  $(a, c)$ .

Among all possible Bain paths, we discuss four in more detail in the following. These four types are the commonly studied ones in the literature (cf. Section 4.3). They essentially model different underlying physical processes or applications and differ in the actual transformation instruction. The discussion below serves to point out important similarities among the four Bain transformations. These similarities permit the reader in some cases to transfer results from one Bain path to another. It simplifies the separation of relevant literature from less relevant literature for the discussion of the epitaxial Bain path, which is the main topic of this work. Further, it allows to adjudicate on the relevance of approximations to the epitaxial Bain path, which are normally associated with constant volume. Last but not least, the contact to experiments is established.

The discussion of a specific Bain transformation is often accompanied by the definition of a certain state of stress or a certain state of strain, that translates to a definite deformation of the tetragonal unit cell as a result of the applied

### 3.2. CONCEPTUAL DETAILS

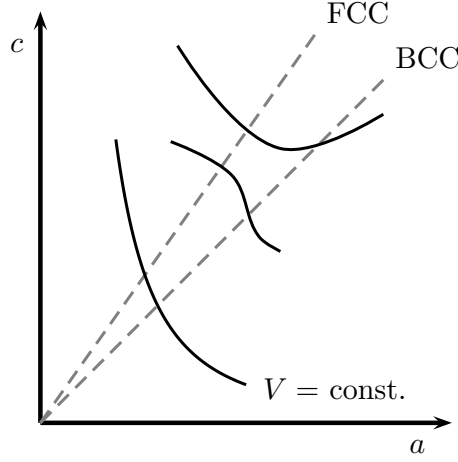


Figure 3.2: The lattice parameters  $a$  and  $c$  span the phase space of BCT lattices. The FCC and the BCC structures are indicated by dashed straight lines in this plane. Every line in that plane, that connects FCC and BCC, represents a Bain transformation (in the wider sense as discussed in the text). The line, that follows a tetragonal deformation with constant unit cell volume,  $V$ , is explicitly indicated and discussed in the text.

stress(es) or strain(s). Any deformation of the lattice is considered a homogeneous one, so that a BCT lattice always remains a BCT lattice. That is, an atom at a centre of symmetry remains one if the lattice is subject to external strains, and no internal strains occur [22]. The coordinate system is naturally oriented such, that the normal components of the stress tensor,  $\sigma_{ii}$ ,  $i = \{x, y, z\}$ , are oriented parallel to the tetragonal axes of the BCT lattice, i.e.,  $\sigma_{xx} \parallel [100]$  and  $\sigma_{yy} \parallel [010]$  acting in-plane,  $\sigma_{zz} \parallel [001]$  acting out-of-plane [113].

If the deformation is assumed to be isothermal, reversible, and at  $T = 0$  K, quantitative information about the state of stress can be gained from derivatives of the total energy  $E$  with respect to components of the strain tensor,  $\epsilon_{ij}$ ,  $i, j = \{x, y, z\}$ , or with respect to the lattice parameters  $a$  and  $c$  [113, 163]. The total energy is described by DFT calculations following Eq. (2.34). The solution of the Kohn-Sham equations for any BCT structure with lattice parameters  $a$  and  $c$  is called a state with total energy  $E(a, c)$ . Accordingly, the total energy per unit volume,  $V$ , is given by

$$\frac{dE}{V} = \sum_{i,j} \sigma_{ij} d\epsilon_{ij}, \quad \sigma_{ij} = \frac{1}{V} \frac{\partial E}{\partial \epsilon_{ij}}, \quad (i, j = \{x, y, z\}). \quad (3.1)$$

With the definition of infinitesimal normal strains,

$$\epsilon_{xx} = \frac{\delta a}{a}, \quad \epsilon_{zz} = \frac{\delta c}{c}, \quad (3.2)$$

we obtain for the stresses  $\sigma_{xx}$  and  $\sigma_{zz}$

$$\sigma_{xx} = \frac{a}{V} \frac{\partial E}{\partial a}, \quad \sigma_{zz} = \frac{c}{V} \frac{\partial E}{\partial c}. \quad (3.3)$$

### CHAPTER 3. THE BAIN PATH

---

In the following we will need the directional derivative of  $E(a, c)$  with reference to the just introduced phase space. The derivative is defined [77] as the derivative of  $E(a, c)$  along a vector,  $\mathbf{v}$ ,

$$\nabla_{\mathbf{v}}E(a, c) \stackrel{\text{def}}{=} \nabla E(a, c) \cdot \mathbf{v} = \frac{\partial E(a, c)}{\partial a}v_a + \frac{\partial E(a, c)}{\partial c}v_c, \quad (3.4)$$

with any unit vector  $\mathbf{v} = (v_a, v_c)^T = v_a\mathbf{e}_a + v_c\mathbf{e}_c$ , whereat  $\mathbf{e}_a$  and  $\mathbf{e}_c$  are the Cartesian unit vectors that span the tetragonal phase space.

In what follows we introduce four Bain paths. We assume  $E(a, c)$  is known (or can be accessed) in a reasonable part of the parameter space. On physically motivated grounds, we assume  $E$  to increase sufficiently far away from some equilibrium configuration (without loss of generality, there might be an area of some metastable configurations close to the equilibrium). That is, there is an increase in  $E$  for decreasing parameters  $a$  or  $c$  due to repulsive forces away from equilibrium, as well as an increase of  $E$  in the limit of large interatomic distances for approaching an unbound state [38].

**The uniaxial Bain path (UBP)** is composed by the set of points in the tetragonal plane  $\{(a_c, c)\} \subset \{(a, c)\}$ , for which we define

$$\text{UBP} \stackrel{\text{def}}{=} \left\{ (a_c, c) \mid E(a_c, c) = \min_a E(a, c) \right\}. \quad (3.5)$$

Since  $c$  is the independent lattice parameter, all quantities *along* the UBP are given as function of  $c$ , e.g., the total energy along the UBP is  $E_{\text{UBP}}(c) \stackrel{\text{def}}{=} E(a_c, c)$ . The following definition of the UBP is usually found in the literature [143, 240]: for arbitrary  $c$ ,

$$\left. \frac{\partial E(a, c)}{\partial a} \right|_{a_c} = \left( \nabla_{\mathbf{v}=(1,0)^T} E(a, c) \Big|_{a_c} \right) = 0. \quad (3.6)$$

The two definitions are only equivalent for ranges of  $c$ , where  $E(a, c)$  has only one minimum  $a_c \neq \{0, \infty\}$  and no saddle point. A vanishing derivative in Eq. (3.6) of course exists for local and global minima and maxima, and saddle points of  $E(a, c)$  determining a set of Bain paths, while Definition (3.5) finds the global minimum. The UBP models the physical situation of uniaxial loading,  $\sigma_{zz} \neq 0$ , which will change the lattice parameter  $c$  away from its equilibrium value. At the same time—since there are no external stresses in the directions perpendicular to the applied load—a relaxation of the lattice parameters will take place along these directions due to the perturbation. For the corresponding stresses, it holds  $\sigma_{xx}(\sigma_{zz}) = \sigma_{yy}(\sigma_{zz}) = 0$ . Hence, non-zero strain components are  $\epsilon_{xx}$ ,  $\epsilon_{yy} = \epsilon_{xx}$ , and  $\epsilon_{zz}$ .

There exists a special case, when additionally to  $\partial E/\partial a$  the other partial derivative in Eq. (3.4),  $\partial E/\partial c$ , vanishes. These special points in the phase space are stationary points in total energy. Due to the request, that for each  $c$ , there is an  $a_c$  so that  $E(a_c, c)$  is the minimum of  $E(a, c)$  over all  $a$ , the type of stationary point of  $\partial E(c)/\partial c|_{c_0} = 0$  at  $c_0$  determines whether the special point is a minimum along the UBP = a minimum of  $E_{\text{UBP}}(c)$  at  $c_0$ , (hence a minimum of  $E(a, c)$  at  $(a_c, c_0)$ ) or a maximum or saddle point along the UBP =



---

### 3.2. CONCEPTUAL DETAILS

a maximum or saddle point of  $E_{\text{UBP}}(c)$  at  $c_0$ , (hence a saddle point in  $E(a, c)$  at  $(a_c, c_0)$ ). For such special points,  $\sigma_{ii} = 0$  (cf. Eq. (3.3)). A minimum in total energy in the tetragonal phase space is referred to as *tetragonal minimum*. The UBP according to the Definition (3.5) cannot go through local maxima in energy in the tetragonal phase space.

**The epitaxial Bain path (EBP)** is composed by the set of points in the tetragonal plane  $\{(a, c_a)\} \subset \{(a, c)\}$ , for which we define

$$\text{EBP} \stackrel{\text{def}}{=} \left\{ (a, c_a) \left| E(a, c_a) = \min_c E(a, c) \right. \right\}. \quad (3.7)$$

The independent variable is  $a$ . Quantities *along* the EBP are therefore only dependent on  $a$ , e.g., the total energy  $E_{\text{EBP}}(a) \stackrel{\text{def}}{=} E(a, c_a)$ . The following definition is usually found in the literature [133]: for arbitrary  $a$ ,

$$\left. \frac{\partial E(a, c)}{\partial c} \right|_{c_a} = \left( \nabla_{\mathbf{v}=(0,1)^T} E(a, c) \Big|_{c_a} \right) = 0. \quad (3.8)$$

The two definitions are again only equivalent for ranges of  $a$ , where  $E(a, c)$  has only one minimum  $c_a \neq \{0, \infty\}$  and no saddle point. Equation (3.8) is fulfilled for all maxima, minima, and horizontal inflection points of  $E(a, c)$  determining a set of Bain paths, while Definition (3.7) finds the global minimum. The difference between the EBP and the UBP are the applied stresses. The EBP models a bidirectionally isotropic state of stress in the basal plane,  $\sigma_{xx} = \sigma_{yy}$ , with uniaxial relaxation in the perpendicular direction,  $\sigma_{zz} = 0$ , while the UBP models an uniaxial state of stress in the out-of-plane direction with relaxation in two perpendicular directions,  $\sigma_{xx} = \sigma_{yy} = 0$ . Non-zero strain components are  $\epsilon_{xx}$ ,  $\epsilon_{yy} = \epsilon_{xx}$ , and  $\epsilon_{zz}$  in both cases.

Similar to the UBP, there are special points,  $a_0$ , on the EBP, where all normal stresses vanish,  $\sigma_{ii} = 0$ . If  $E_{\text{EBP}}(a_0)$  resides at a minimum, then the EBP locates a tetragonal minimum at  $(a_0, c_a)$ . If  $E_{\text{EBP}}(a)$  at  $a_0$  is a maximum or a horizontal inflection point, then the EBP locates a saddle point in  $E(a, c)$  at  $(a_0, c_a)$ . The EBP according to the definition in Eq. (3.7) does not go through local maxima in total energy in the tetragonal phase space.

Chapters 4 and 5 elaborately deal with EBPs in various metals. At this point we only give important references. To the best of our knowledge, the idea of the EBP was formulated by Alippi *et al.* [4] for the first time. A comprehensive discussion of the EBP was given by Marcus *et al.* [133].

**The cancelling slope Bain path (CSBP)** is obtained by fixing the axial ratio in a first step. For this fixed ratio, the unit cell volume ( $V$ ) is varied to minimise the total energy. This procedure is repeated for several  $c/a$  ratios. The tetragonal parameter space may as well be spanned by  $c/a$  and  $V$ , so that an arbitrary point in that space has the coordinates  $(c/a, V)$ . The CSBP is then composed by the set of points  $\{(c/a, V_{c/a})\} \subset \{(c/a, V)\}$ , for which we define

$$\text{CSBP} \stackrel{\text{def}}{=} \left\{ (c/a, V_{c/a}) \left| E(c/a, V_{c/a}) = \min_V E(c/a, V) \right. \right\}. \quad (3.9)$$

### CHAPTER 3. THE BAIN PATH

---

The independent variable is  $c/a$ , so that, e.g., the total energy along the CSBP is  $E_{\text{CSBP}}(c/a) \stackrel{\text{def}}{=} E(c/a, V_{c/a})$ . If a stationary point of  $E_{\text{CSBP}}(c/a)$  is a minimum, then the CSBP locates a tetragonal minimum. If  $E_{\text{CSBP}}(c/a)$  resides at a maximum or saddle point, then the CSBP locates a saddle point in the tetragonal phase space.

We compute  $dE(a, c)/dV$  for a constant  $c/a$  ratio and assume  $a = a(c/a, V)$  and  $c = c(c/a, V)$ . From the volume per atom,  $V = a^2c/2$ , we readily get

$$a = \left(2V \frac{a}{c}\right)^{\frac{1}{3}}, \quad c = \left(2V \left(\frac{c}{a}\right)^2\right)^{\frac{1}{3}}.$$

The derivative at  $V_{c/a}$  has to vanish,

$$\begin{aligned} \left. \frac{dE(a, c)}{dV} \right|_{V_{c/a}} &= \left. \frac{\partial E}{\partial a} \frac{da}{dV} \right|_{V_{c/a}} + \left. \frac{\partial E}{\partial c} \frac{dc}{dV} \right|_{V_{c/a}} \\ &= \frac{1}{3} \left( \frac{2}{V_{c/a}^2} \frac{a}{c} \right)^{\frac{1}{3}} \left( \frac{\partial E}{\partial a} + \frac{\partial E}{\partial c} \frac{c}{a} \right) = 0. \end{aligned} \quad (3.10)$$

Both slopes in the previous equation, if non-zero, must have opposite signs, and the modulus of  $\partial E/\partial c$  must be a factor  $(c/a)^{-1}$  smaller than the modulus of  $\partial E/\partial a$ , so that both summands cancel each other. The term CSBP is derived from the latter equation: both terms ( $\sim$  slopes) in parentheses have to cancel each other to fulfil the equation.

The CSBP is conceptionally different from the former two, because in general it does not model any realistic physical situation to the best knowledge of the author. The knowledge of this Bain path itself is therefore of little importance. A possible advantage remains though, since the CSBP also locates stationary points, whenever both partial derivatives in Eq. (3.10) vanish simultaneously. This is the case for minima, maxima, and saddle points. Equation (3.10) determines a set of Bain paths, while Definition (3.9) finds the global minimum.

**The constant volume Bain path (CVBP)** traverses the Bain transformation at constant unit cell volume. The constant volume is usually taken to be the (theoretical or experimental) equilibrium volume of either the BCC or the FCC structure. In what follows, we choose  $a$  as independent variable. For the predefined structure (subscript 0) with atomic volume,  $V_0 = a_0^2c_0/2$ , the CVBP has the analytic form

$$c(a) = \frac{2V_0}{a^2} \quad \text{or} \quad \epsilon_c(\epsilon_a) = \frac{-\epsilon_a(\epsilon_a + 2)}{(\epsilon_a + 1)^2}, \quad (3.11)$$

when we define a strain,  $\epsilon_x$ ,  $x = \{a, c\}$ ,

$$\epsilon_x = \frac{x - x_0}{x_0}.$$

The function  $c(a)$  is a cubic hyperbola in the phase space in Fig. 3.2 on Page 11. Due to its analytic form, the complexity of actual electronic structure calculation is considerably smaller for the CVBP than for the three other Bain paths, since

### 3.2. CONCEPTIONAL DETAILS

for the CVBP the dependent lattice parameter can be calculated straightforwardly following Eq. (3.11). In the other cases, the dependent lattice parameter is to be searched for with the help of additional conditions on the total energy. Of course, if one compares the CVBP with, e.g., the EBP, the quality of the constant volume approximation to the EBP depends on the volume change along the EBP.

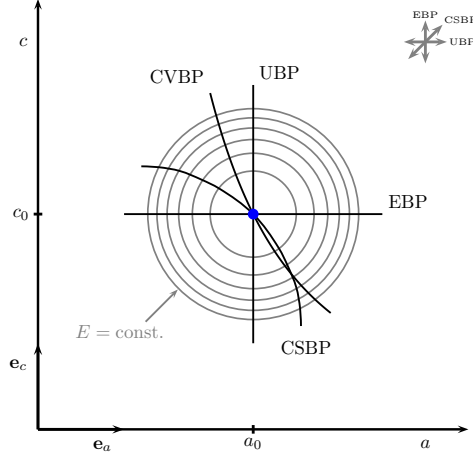


Figure 3.3: Illustrative picture of a contour diagram of the total energy,  $E(a, c)$ , as function of the phase space variables  $a$  and  $c$  after Eq. (3.12). The minimum in total energy is located at  $(a_0, c_0)$  (blue solid dot), grey circles indicate lines of constant energy. The UBP, EBP, CSBP, and CVBP are the four solid black lines which go through  $(a_0, c_0)$ . UBP and EBP are vertical and horizontal lines, respectively, due to the assumed functional dependence of  $E(a, c)$ . The 'rose' in the upper right part is to remind the reader on the cardinal direction along which the minimum search for the respective Bain path was done.

We will summarise the last paragraphs by an illustration given in Fig. 3.3. We model a minimum in the total energy around the point  $(a_0, c_0)$  by

$$E(a, c) - E_0 = (a - a_0)^2 + (c - c_0)^2, \quad E_0 = E(a_0, c_0). \quad (3.12)$$

The UBP, EBP, CSBP, and the CVBP (at  $V_0$ ) were constructed and plotted in Fig. 3.3. Even for this model minimum, the figure clearly distinguishes among the four Bain paths. A realistic plot of  $E(a, c)$  and the Bain paths is shown in Fig. 3.4 for Cr. The three tetragonal structures, for which  $E(a, c)$  is stationary, approximately have the same volume, i.e., they are in a good approximation lined up along a path of constant volume (we plotted the CVBP at the theoretical equilibrium volume in Fig. 3.4). The UBP, the EBP, and the CSBP go through the two minima and the saddle point.

The elaborate discussion of the four different Bain paths leads us to two important conclusions:

1. For the *global* tetragonal minimum in the phase space, UBP, EBP, and CSBP coincide in general, because they scan the complete parameter space. Results of those calculations at that particular point are transferable among each other.

2. For other possible stationary points in the phase space, UBP, EBP, and CSBP may coincide but need not. Although the three Bain paths scan the complete parameter space, they need not to coincide because the minimum search is along different directions (for the UBP over  $a$ , for the EBP over  $c$ , for the CSBP over  $V$ ). See the example in Fig. 3.5, for which the UBP runs through the local and the global minimum as well as the saddle point of  $E(a, c)$ , but the EBP goes only through the global minimum.

### 3.3 Symmetry argument

Milstein *et al.* studied the energetics of Bain transformations along the UBP [143]. The authors argued that this path exhibits the minimum barrier energy between the BCC and the FCC configuration of Na, ‘when the crystal passes through a special unstressed tetragonal state, that lies on a local energy maximum’ on the UBP. It was originally assumed that BCC and FCC structures coincide with minima of  $E(a, c)$  [9]. Several total-energy calculations showed, that cubic structures can reside at the maximum position on the UBP as well as on the EBP, e.g., Refs. 4,38,131 and Fig. 3.4. This finding also proved the existence of minima with tetragonal symmetry. Alippi *et al.* reported, that the UBP and the EBP of V go through the same unstressed state, which coincides with the smallest barrier energy between the two minima of  $E(a, c)$ . Marcus *et al.* then defined a Bain path as the path in the tetragonal plane, that goes through two tetragonal minima, be the corresponding structures cubic or not [133]. This definition was convenient, because more and more total-energy calculations predicted the existence of two tetragonal minima for each element (an overview of references is given in Sec. 4.3). The atomic volumes of both tetragonal minima were regularly found to differ by few percent, which means the minima can approximately be lined up along a path of constant volume in the tetragonal parameter space. We notice, that the definition of Marcus is not strict. For example, assume a pathological case with two unequally deep minima in the phase space, which are located at  $(a_1, c_1)$  and  $(a_2, c_2)$ , and assume  $a_1 = a_2$ . By the definition of the EBP, only the minimum with lower total energy is accounted for, say  $(a_1, c_1)$ , but the UBP runs through both minima. Figure 3.5 illustrates a case with two unequally deep minima of  $E(a, c)$ , but with  $a_1 \neq a_2$ . In that particular energy landscape, the EBP does not run through both minima, but the UBP does. According to Marcus’ definition, the CVBP is not a Bain path, because the minima in the tetragonal plane do not necessarily possess the same volume.

In the following, we deal with the symmetry argument for cubic structures. The question of symmetry related extrema was discussed in Ref. 133 in the framework of the EBP. It was stated, that the EBP must have an extremum in total energy at structures with cubic symmetry. We repeat in short form the original argument given in Ref. 133, which uses the Definition (3.8):

*Part a* Denote the three lattice parameters of an orthorhombic structure with  $a$ ,  $b$ , and  $c$ . This orthorhombic structure has tetragonal symmetry if exactly two lattice parameters are equal, and cubic symmetry if all three lattice parameters are equal. Denote the lattice

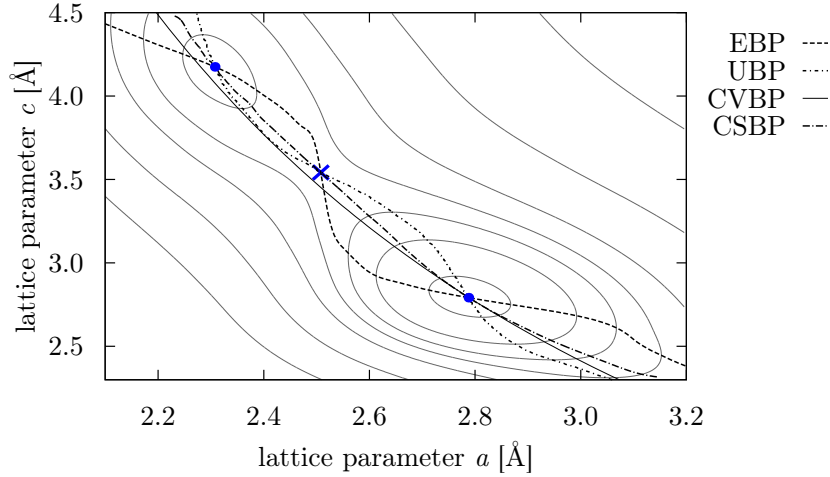


Figure 3.4: Contour plot of the total energy in the tetragonal parameter space,  $E(a, c)$ , for  $\text{Cr}$ , as obtained by DFT within this work (detailed discussion in Sec. 4.5.7).  $E(a, c)$  has two minima (blue solid dots) and one saddle point (blue cross). The contour levels (grey solid lines) are in arbitrary units. The coordinates (in  $\text{\AA}$ ) of the global minimum (BCC) and of the local minimum (BCT) are  $(2.79, 2.79)$  and  $(2.31, 4.18)$ , respectively. There is a saddle point (FCC) at  $(2.51, 3.56)$ . EBP, UBP, and CSBP run through all three stationary points. The volume of the CVBP is fixed to that of the global minimum state.

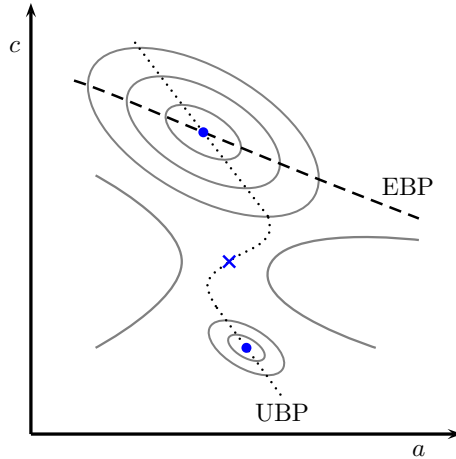


Figure 3.5: Illustrative picture of  $E(a, c)$  with two minima (blue solid dots) and one saddle point (blue cross). The global minimum has the larger  $c$  and the smaller  $a$ . The contour levels (grey solid lines) are in arbitrary units. The EBP only runs through the global minimum, while the UBP goes through both minima and the saddle point.

### CHAPTER 3. THE BAIN PATH

---

parameters for cubic symmetry (FCC or BCC) with  $a_0 = b_0 = c_0$ . Let this cubic structure be a point on the EBP. Since  $\partial E/\partial c|_{c_0} = 0$  by construction for any point of the EBP (Eq. (3.8)), the other derivatives  $\partial E/\partial a|_{a_0} = \partial E/\partial b|_{b_0} = 0$  vanish by symmetry of the cubic axes. Hence, the derivative of  $E$  along the EBP at the cubic structure vanishes.<sup>1</sup>

*Part b* It is further concluded, that there are at least three extrema on the EBP, since the BCT structure includes two structures with cubic symmetry. A third extremum is required to get a minimum - maximum - minimum sequence in the total energy along the EBP, since the energy along the EBP rises for small and large  $c/a$  beyond the position of the minima.

An EBP with three extrema is by far the most frequent case, although there are exceptions with three minima (five extrema), see discussion in Sec. 4.6.2. A special case, not considered in *part b*, would be a single minimum - saddle point sequence.

We argue, that cubic structures need not be on the EBP. In order to be a state of the EBP, the definition in Eq. (3.7) must be complied with. This requirement need not be true for cubic structures. Assume a cubic structure whose energy is minimal in the parameter space of cubic lattices. This structure can be unstable with respect to a certain tetragonal deformation, i.e., the total energy decreases for a variation of the out-of-plane lattice parameter  $c$  away from  $c_0$  ( $a_0 = b_0$  assumed fixed). Hence  $E = E(c_0)$  resides at a maximum position or saddle point. This cubic structure is therefore not a point on the EBP, because it does not fulfil the construction.

That is, *part a* of the above argument is true with the premise: 'Let this cubic structure be a point on the EBP'. It is, however, not relevant for *part b*. The conclusion in *part b* of the above argument is only true if both cubic structures are points on the EBP. We show in Chapter 4, that there are few elements, for which either the BCC structure or the FCC structure is not on the EBP, because the respective structure is unstable with respect to a certain tetragonal deformation. This instability is expressed by the elastic constant  $c_{zzzz}$  ( $c_{zzzz} = c_{xxxx}$  for cubic symmetry), which is proportional to the curvature  $\partial^2 E(c)/\partial c^2$  at  $c_0$  (see discussion in Sec. A.1 on Page 137 et seqq.). We model an energy landscape in the tetragonal parameter space with an unstable cubic point, coordinates  $(a_0, c_0)$ ,  $a_0 = c_0$ , in Fig. 3.6. This point is not on the EBP because  $\partial^2 E(c)/\partial c^2|_{c_0} < 0$ ; as an additional consequence, the EBP is discontinuous. We hearken back to Fig. 3.6 in Sec. 4.5.4, when we discuss the EBP of La, for which  $E(a, c)$  from Fig. 3.6 is applicable. Note that the case of Cr (Fig. 3.4) is different: there, the saddle point (at BCC) belongs to the EBP.

The following discrimination holds: if  $c_{zzzz}(c_0) > 0$  and  $c_0$  is the global minimum of  $E(c)$  at fixed  $a_0$  (if  $c_{zzzz}(c_0) < 0$ ) for any arbitrary cubic structure, then the EBP goes (does not go) through the point  $(a_0, c_0)$ . Our finding is at variance with Ref. 133, which assumed that both cubic structures would be included in the EBP *per se* (*part b* of the symmetry argument).

---

<sup>1</sup>Presuming  $E$  is differentiable, the directional derivative is zero along any vector since all partial derivatives are zero [77].

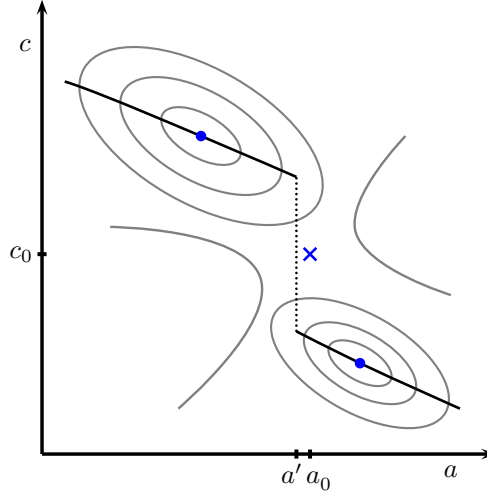


Figure 3.6: Illustrative picture of  $E(a, c)$  with two minima (blue solid dots) and a saddle point at  $(a_0, c_0)$  (blue cross). The EBP is the black solid line, which is discontinuous at  $a'$ . The global minimum has the larger  $c$  and the smaller  $a$ . The contour levels (grey solid lines) are in arbitrary units (the contour lines are however such, that there is one contour line centred around the global minimum which represents the same energy as one contour line centred around the local minimum, and both lines coincide at  $a'$ ). The EBP runs through both minima, but there is a discontinuous transition from the area around the global minimum to the area around the local minimum. The discontinuity at  $a'$  is indicated by a dotted line, and need not be at the coordinate of the saddle point. Since  $\partial^2 E(c)/\partial c^2|_{c_0} < 0$  ( $a_0$  fixed), the saddle point of  $E(a, c)$  in this model cannot be on the EBP.

States with cubic symmetry on the EBP can in principle correspond to a maximum, a minimum, or a saddle point in total energy. A saddle point has not been reported so far, although there exist elements with small energy barrier between a minimum and the adjacent maximum of the EBP, e.g., copper [95].

We finally consider atomic neighbourhood relations of BCT lattices. In Fig. 3.7 we plot the distance among nearest and next nearest neighboring atoms, and atoms further apart of BCT lattices as a function of the axial ratio  $c/a$ . All interatomic distances,  $d$ , were rescaled by the lattice parameter  $a$ , so that the actual distances depend on  $c/a$  only. For example, consider the distance of two atoms, one has the coordinates  $(000)$  and another one is located at  $(111)$ . The coordinates are given in units of the lattice parameters  $(a a c)$  of the BCT lattice (Cartesian unit vectors coincide with tetragonal axes). The distance  $d$  and the reduced distance  $d/a$  are then

$$d = (2a^2 + c^2)^{\frac{1}{2}}$$

and

$$\frac{d}{a} = \left( 2 + \left( \frac{c}{a} \right)^2 \right)^{\frac{1}{2}},$$

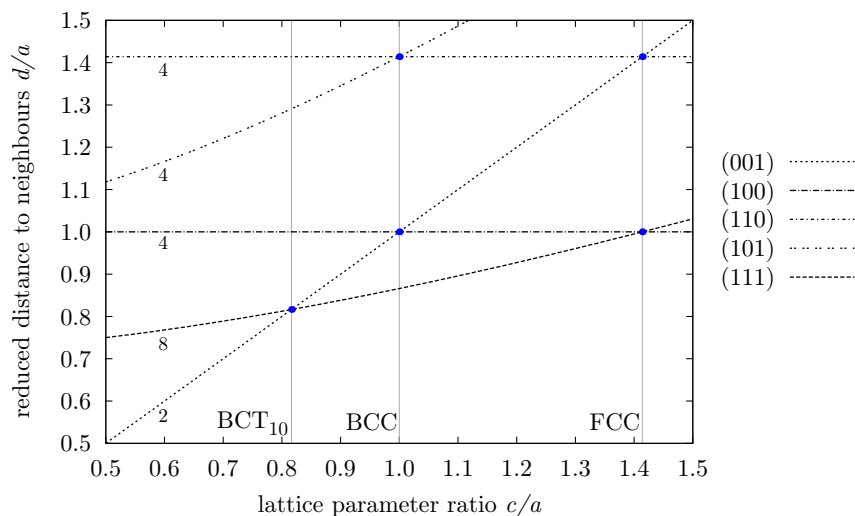


Figure 3.7: Reduced interatomic distance,  $d/a$ , as a function of the axial ratio  $c/a$  for selected pairs of atoms. The origin (position of the first atom) is located at (000). The position of the respective second atom is given by the coordinates as stated in the legend (all coordinates in terms of the lattice parameters). Solid vertical lines indicate structures with a high coordination number. Cross-over points of certain lines leading to such structures are denoted by solid blue dots. The number of atoms whose reduced distance corresponds to a certain line is specified by the number next to it.

respectively. Certain  $c/a$  ratios bring along a high coordination number. The so-called  $BCT_{10}$  structure for  $c/a = \sqrt{2/3} \approx 0.816$  has ten nearest neighbours at exactly the same distance [257]. BCC has eight nearest and six next nearest neighbours, FCC has twelve nearest neighbours. That high number of nearest and next nearest neighbours originates from symmetry and can be reconstructed from crossing points of the lines in Fig. 3.7. Such crossing points also exist for atoms further away.

### 3.4 Symmetry argument: magnetic order

We assume the absence of spin-orbit coupling and confine the discussion to collinear magnetic order. First of all we introduce the types of magnetic order considered in this work. We note that the same types are conventionally studied in the literature due to their computational feasibility, see Table 4.1 on Page 31 for an overview of references, which included magnetic order in the calculation of the EBP.

The considered magnetic order types are FM, and two anti-ferromagnetic (AFM) configurations compatible with the BCT lattice. AFM order types with in-plane enlarged unit cells are not considered, hence our AFM structures are in-plane FM. The symmetry argument from the previous section holds for FM order as well, because the external potential and the spin density preserve the full symmetry of the lattice. The situation is different for an AFM configuration: the



### 3.4. SYMMETRY ARGUMENT: MAGNETIC ORDER

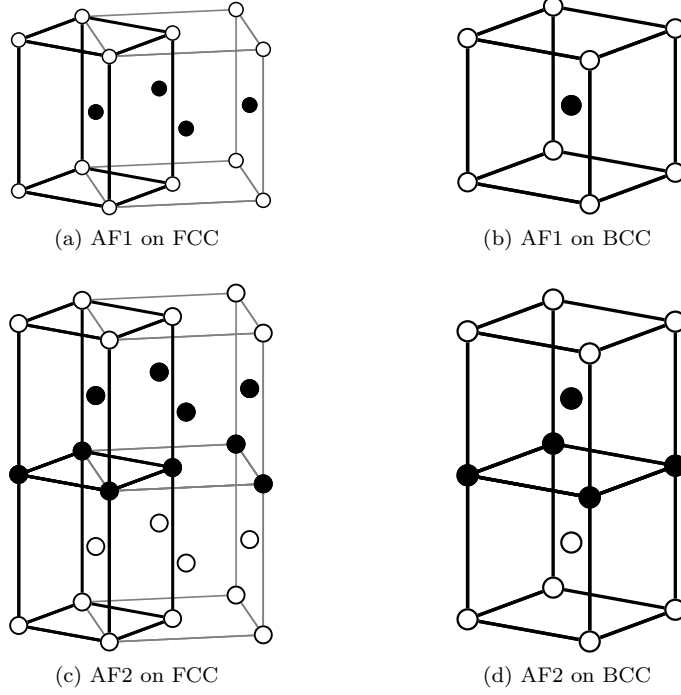


Figure 3.8: Possible types of AFM order on FCC and BCC lattices. The symbols  $\bullet$  and  $\circ$  refer to  $\uparrow$  ('up') and  $\downarrow$  ('down') magnetic moments, respectively. The BCC lattice (thick lines) is delineated in the cubic lattices (thin lines). BCC and BCC lattice are on top of each other.

first considered order is single layer AFM (moment sequence  $\uparrow\downarrow\uparrow\downarrow$  on successive (001) planes;  $\uparrow$  'up' and  $\downarrow$  'down') and referred to as AF1. Since up and down moments per unit cell sum up to a zero net magnetic moment, there is only one degree of freedom, which is the modulus of the magnetic moment per site. The second commonly assumed order has a double layer moment sequence ( $\uparrow\uparrow\downarrow\downarrow$  on successive (001) planes) and is called AF2 [185] or likewise AFMD (AFM double layer) [258] order in the literature. We will stick to the term AF2 in this work. Denote the moment sequence  $m_1 m_2 m_3 m_4$ . Then it holds  $m_1 = m_2 = -m_3 = -m_4$  ( $\sum_i m_i = 0$ ). Again, the modulus of the magnetic moment is the only degree of freedom. We have for AF1 in terms of the reciprocal  $q$ -vector,  $\mathbf{q}_1 = (0, 0, 1)^T (2\pi/c_{\text{cub}})$ , where  $c_{\text{cub}}$  is the lattice parameter of the BCC or the FCC conventional unit cell, respectively. Accordingly, AF2 has a  $q$ -vector  $\mathbf{q}_2 = (0, 0, 1/2)^T (2\pi/c_{\text{cub}})$ .

The following considerations were done with the help of the *International Tables for Crystallography* [74] and FINDSYM [218]. A BCC lattice has  $Im\bar{3}m$  symmetry. AF1 order on a BCC lattice leads to two interpenetrating simple cubic lattices with  $Pm\bar{3}m$  symmetry, see Fig. 3.8b. Hence, the symmetry theorem is valid for AF1 order on a BCC lattice. In response to a tetragonal distortion,  $Im\bar{3}m$  symmetry reduces to  $I4/mmm$  symmetry (BCT),  $Pm\bar{3}m$  symmetry reduces to  $P4/mmm$  symmetry (simple tetragonal), see Fig. 3.8a. AF1 order on an FCC lattice leads to two interpenetrating simple tetragonal lattices with

$c/a = \sqrt{2}$ , but cubic symmetry is not retained. Hence, the symmetry theorem does not apply to AF1 order on an FCC lattice. AF2 order on BCC or FCC lattices has  $P4/nmm$  symmetry and cubic symmetry is never retained, see Figs. 3.8c and 3.8d.

### 3.5 Applications of Bain paths (examples)

Calculations of the UBP were recently discussed in connection with structural transformations in nanowires of late TMs with FCC structure [42, 64, 72]. The length of the wire is much larger than its dimensions in the transversal directions. Tensile stresses on exposed surfaces of the wire lead to an intrinsic uniaxial state of stress with net compression along the wire axis. The intrinsic uniaxial stress can drive a structural transformation, if the surface stresses are strong enough and the wire narrow enough. This transformation was studied by molecular dynamics simulations in gold nanowires [42]. Induced by surface stresses alone, a gold wire with FCC structure transformed to a stable BCT structure. For a  $\{001\}$  oriented wire, the uniaxial intrinsic state of stress along  $[001]$  corresponds to the one of the UBP, when the  $[100]$  and the  $[010]$  axes can relax freely. The transformed BCT structure, and the critical stress to drive the transformation from FCC to BCT was estimated from the UBP. Above the critical stress, the wire relaxes spontaneously to BCT [72].

The mechanical strength of several BCC TMs (V, Fe, Nb, Mo, Ta, and W) in response to uniaxial tensile loading along the  $[001]$  axis was estimated with the help of their UBP [36, 128, 156, 240]. The UBP of those elements has an energy minimum at the BCC structure, and possesses an adjacent maximum at a BCT structure with  $c/a > 1$ . The position of the steepest slope of the total energy along the UBP between the two stationary points coincides with the position of maximum stress (Eq. (3.3)). This point defines the ideal mechanical strength in response to uniaxial loading. This description is a description for ideal single crystals without any defects [88]. The calculations also revealed, that for Nb and V the state of maximum stress cannot be achieved, because the lattice becomes unstable towards an orthorhombic distortion before [128, 156].

The magneto-elastic anisotropy energy density,  $F(\hat{\mathbf{M}}, \boldsymbol{\epsilon})$ , is one constituent in the phenomenological theory of magnetic anisotropy [18, 23].  $F$  accounts for the interaction of magnetic anisotropy (represented by the normalised direction of magnetisation,  $\hat{\mathbf{M}} = (\alpha_x, \alpha_y, \alpha_z)$ ) and the elastic deformation of a lattice (represented by the strain tensor,  $\boldsymbol{\epsilon}$ ). The lowest order, non-vanishing term of  $F$  in terms of  $\hat{\mathbf{M}}$  and  $\boldsymbol{\epsilon}$  is linear in  $\epsilon_{ij}$ ,

$$F(\hat{\mathbf{M}}, \boldsymbol{\epsilon}) = \sum_{ijkl} B_{ijkl} \epsilon_{ij} \alpha_k \alpha_l \quad i, j, k, l = \{x, y, z\}.$$

The coefficients,  $B_{ijkl}$ , are the magneto-elastic constants and depend on the material. For cubic systems in response to a tetragonal deformation,  $F$  is given by [18, 23]

$$\begin{aligned} F(\hat{\mathbf{M}}, \boldsymbol{\epsilon}) = & B_{xxxx} (\epsilon_{xx}(\alpha_x^2 + \alpha_y^2) + \epsilon_{zz}\alpha_z^2) + \\ & + B_{xxyy} [\epsilon_{xx}(1 + \alpha_z^2) + \epsilon_{zz}(\alpha_x^2 + \alpha_y^2)]. \end{aligned}$$

### 3.5. APPLICATIONS OF BAIN PATHS (EXAMPLES)

The EBP relates  $\epsilon_{xx}$  to  $\epsilon_{zz}$  for tetragonal structures.  $\epsilon_{xx}$  is determined by the lattice mismatch of substrate and film. Hence, volume magneto-elastic contributions to the anisotropy energy of strained films can be estimated, if the parameters  $B$  are known [23]. On the basis of the EBP (in a linear elastic approximation for  $\epsilon_{zz}$ , Eq. (3.14)) and the previous relation for  $F$ , Ref. 23 predicted the critical spin-reorientation thickness in strained Fe and Ni films.

The EBP can be helpful to interpret the structure of pseudomorphically grown films. Possible related questions are, whether a BCT film of a certain material is strained from its FCC phase or strained from its BCC phase—if this material has both phases —, and what are the strains in the film. This is typically done with the so-called strain analysis based on a (presumed) linear elastic behaviour of the overlayer material [13,121], i.e., the ratio of out-of-plane strain and in-plane strain is given by

$$\frac{\epsilon_{zz}}{\epsilon_{xx}} = -\frac{2\nu}{1-\nu} \quad (3.13)$$

$$= -\frac{2c_{xxyy}}{c_{xxxx}}. \quad (3.14)$$

The Poisson ratio,  $\nu$ , and the elastic constants,  $c_{ijkl}$ ,  $i, j, k, l = \{x, y, z\}$ , are material specific and different for different phases of the same material. The strain ratio of the bulk structure of the film, i.e., the left hand side of Eq. (3.13), is experimentally determined by means of, e.g., quantitative low energy electron diffraction (LEED) analysis, see Sec. 4.5.1 for details. If the elastic constants of cubic phases are known, the right hand side of Eq. (3.14) with the elastic constants of the 'correct' unstrained phase should match the measured strain ratio, and the film is then a strained form of the 'correct' phase. If the elastic constants are not known, e.g., if the film is a strained form of a metastable cubic phase, the lattice parameter and structure may be deduced from Eq. (3.13) for reasonable assumptions of  $\nu$ , i.e.,  $0 < \nu < 0.5$  for most materials. Unreasonable choices for the equilibrium structure then lie outside this interval [13]. The EBP relates  $a$  to  $c$ , hence  $\epsilon_{xx}$  to  $\epsilon_{zz}$ , *beyond* the limits of linear elasticity, which fails to be valid for lattice mismatches larger than, e.g., few percent for Co and Cu [4]. The structure of the bulk part of a BCT film can be placed on the EBP, i.e., the phase, of which the film is a strained form, can in that way be identified.





# 4

## Transition metals, selected alkaline earth metals and lanthanides

### 4.1 Introduction and motivation

This chapter addresses the EBPs of elements from the periodic table, which belong to the second to twelfth group and to the fourth to sixth period. The place in the third group and the sixth period is disputed between La and Lu [139]. We consider both elements in this thesis, see Fig. 4.1. The majority of the selected elements are from the  $d$ -block, which comprises the groups three to twelve but not La [139]. The atomic  $d$ -shell is successively filled across a  $d$ -block series.<sup>1</sup> Transition elements (transition metals) are  $d$ -block elements apart from Zn, Cd, Hg, and Lu according to the IUPAC definition [139].<sup>2</sup> The former three elements are referred to as post-transition elements and Lu is counted to the lanthanides. Besides (proper and post) TMs and the two lanthanides, we investigate the alkaline earth metals Ca, Sr, and Ba.

The selection of (or limitation to) the aforementioned elements is partly motivated by a general interest in epitaxial growth of TM elements, particularly the FM elements Fe, Co, and Ni [138]. This implies a large experimental database to compare with. The concept of the EBP has been proven to be fruitful, for example, to identify stress-free tetragonal states for a number of elements, see Sec. 4.3. While there is a specific interest in particular elements and particular properties, such as the magnetic structure of Fe, Co, and Ni in non-equilibrium structures, many properties of TMs are determined by the occupation of the  $d$ -band. A striking effect are similarities such as trends in cohesive energies, bulk moduli, and crystal structures as function of the  $d$ -band filling. E.g., the sequence of equilibrium crystal structures, HCP  $\rightarrow$  BCC  $\rightarrow$  HCP  $\rightarrow$  FCC, across the non-magnetic (NM) TM series is striking (Fig. 4.1). There are as well differences in the electronic structure, which for example determine the absence or presence of bulk magnetism. In turn, a finite spin-polarisation can dictate the lattice geometry [212].

---

<sup>1</sup> $s^2d^1$  configuration for third group elements,  $s^2d^{10}$  configuration for twelfth group elements. There are irregularities in the filling, e.g., the eleventh group has  $s^1d^{10}$ .

<sup>2</sup>International Union of Pure and Applied Chemistry (IUPAC): a transition element is an element 'whose atom has an incomplete  $d$ -sub-shell or which can give rise to cations with an incomplete  $d$ -sub-shell'.

## CHAPTER 4. TRANSITION METALS, SELECTED ALKALINE EARTH METALS AND LANTHANIDES

	2	3	4	5	6	7	8	9	10	11	12
4	<sup>20</sup> <b>Ca</b> FCC	<sup>21</sup> <b>Sc</b> HCP	<sup>22</sup> <b>Ti</b> HCP	<sup>23</sup> <b>V</b> BCC	<sup>24</sup> <b>Cr</b> BCC	<sup>25</sup> <b>Mn</b> CUB	<sup>26</sup> <b>Fe</b> BCC	<sup>27</sup> <b>Co</b> HCP	<sup>28</sup> <b>Ni</b> FCC	<sup>29</sup> <b>Cu</b> FCC	<sup>30</sup> <b>Zn</b> HCP
5	<sup>38</sup> <b>Sr</b> FCC	<sup>39</sup> <b>Y</b> HCP	<sup>40</sup> <b>Zr</b> HCP	<sup>41</sup> <b>Nb</b> BCC	<sup>42</sup> <b>Mo</b> BCC	<sup>43</sup> <b>Tc</b> HCP	<sup>44</sup> <b>Ru</b> HCP	<sup>45</sup> <b>Rh</b> FCC	<sup>46</sup> <b>Pd</b> FCC	<sup>47</sup> <b>Ag</b> FCC	<sup>48</sup> <b>Cd</b> HCP
6	<sup>56</sup> <b>Ba</b> BCC	<sup>57,71</sup> <b>La,Lu</b> DHCP,HCP	<sup>72</sup> <b>Hf</b> HCP	<sup>73</sup> <b>Ta</b> BCC	<sup>74</sup> <b>W</b> BCC	<sup>75</sup> <b>Re</b> HCP	<sup>76</sup> <b>Os</b> HCP	<sup>77</sup> <b>Ir</b> FCC	<sup>78</sup> <b>Pt</b> FCC	<sup>79</sup> <b>Au</b> FCC	<sup>80</sup> <b>Hg</b> BCT

Figure 4.1: Part of the periodic table of elements between the second and twelfth group (numbers on top) and between the fourth and sixth period (numbers on the left hand side). These are the elements considered in this chapter. For every element, we state its atomic number, as well as the experimental crystal structure at lowest temperatures. La and Lu are both counted to the third group. Data were taken from Refs. 43, 256. DHCP = double HCP, CUB = cubic.

The current chapter serves two major interests: a particular interest in element-specific EBPs with attention to magnetic order, as well as a general interest in EBPs with focus on similarities and dissimilarities among the TM series.

### 4.2 Trends in transition metal series: insights from empirical models

TMs are characterised by a narrow valence  $d$ -band that hybridises with a broader valence nearly-free-electron  $sp$ -band [63, 178]. The nearly parabolic trend in the cohesive energy across the TM series, peaked at the refractory metals, is a well known feature of all TM series (although there are modifications due to magnetism in the  $3d$  series), and was shown to be a feature of  $d$ -band contributions [5, 63, 66, 178, 204]. The mentioned trend in the crystal structure sequence can be understood in a band picture [179, 221]. Other trends in TMs were discussed in the literature, such as the volume dependence [75, 154], the electronic density of states (DOS) [68], the bulk modulus [152], and elastic constants [211, 251].

Empirical models offer a simple way to understand and interpret trends in TM series. Hereafter we focus on the cohesive energy and the crystal structure of the NM series. In the framework of empirical tight binding (TB) theory, the bond energy,  $E_{\text{bond}}$ , in terms of the band DOS,  $D(\epsilon)$ , is obtained by [178, 179]

$$E_{\text{bond}} = \int^{\epsilon_F} (\epsilon - E_d) D(\epsilon) d\epsilon, \quad (4.1)$$

whereat  $E_d$  is the centre of gravity. The Friedel model of the  $d$ -band assumes a rectangular DOS of width  $W$  and height  $10/W$ , whose bond energy for a

## 4.2. TRENDS IN TRANSITION METAL SERIES: INSIGHTS FROM EMPIRICAL MODELS

---

number of valence  $d$ -electrons,  $N_d$ ,  $0 \leq N_d \leq 10$ , is [178, 221]

$$E_{\text{bond}}^{\text{FR}} = -\frac{W}{20}N_d(10 - N_d) \quad (4.2)$$

$$N_d = \frac{10}{W} \left( E_{\text{F}} - E_d + \frac{W}{2} \right).$$

The lower integration limit is the band bottom,  $E_d - W/2$ , the upper integration limit is the Fermi energy,  $E_{\text{F}}$ , which is related to  $N_d$  by the previous relation.  $E_{\text{bond}}^{\text{FR}}(N_d)$  on the basis of a rectangular DOS resembles a parabolic function of the number of  $d$ -electrons.  $E_{\text{bond}}^{\text{FR}}$  is largest for half band filling ( $N_d = 5$ ). The approximation of a rectangular DOS discards any realistic structure of the DOS.

A minimum model to describe equilibrium volumes and binding energies at equilibrium requires at least a repulsive term,  $E_{\text{rep}}$ , in addition to  $E_{\text{bond}}$ . The binding energy,  $E_{\text{bind}}$ , is then the sum of both terms [178, 179],

$$E_{\text{bind}} = E_{\text{rep}} + E_{\text{bond}}. \quad (4.3)$$

The term  $E_{\text{rep}}$  is assumed to be a sum of central pair potentials. The bond energy may be approximated with the Friedel model.

In what follows, we consider a TB lattice Hamiltonian with one TM atomic species,  $\hat{H}$ . We assume a complete set of atomic  $d$ -orbitals,  $\alpha$ , on each atomic site,  $i$ ,  $|i\alpha\rangle$  [179]. More precisely, the two-centre, orthogonal TB approximation is used, that is, neglect of three-centre integrals, neglect of overlap integrals between different sites, and neglect of (on-site) crystal field integrals of type  $\langle i\alpha|v_j|i\alpha\rangle$ ,  $v_j$  is the atomic potential at  $j \neq i$ . In the Friedel model, the bond energy is proportional to the bandwidth (Eq. (4.2)). Pettifor related the bandwidth of a rectangular DOS to bond integrals via the second moment of the local DOS [179]. This is illustrated in the following. The local DOS is the site and orbital projected DOS,  $D_{i\alpha}(\epsilon)$ . The  $p$ th moment,  $\mu_{i\alpha}^{(p)}$ , of the local DOS is defined as [179, 221]

$$\mu_{i\alpha}^{(p)} = \int (\epsilon - E_d)^p D_{i\alpha}(\epsilon) d\epsilon. \quad (4.4)$$

Cyrot-Lackmann and Ducastelle showed [39, 45], that the moments of the local DOS of an atom at site  $i$  are related to its local environment,

$$\begin{aligned} \mu_{i\alpha}^{(p)} &= \langle i\alpha|\hat{H}^p|i\alpha\rangle \\ &= \sum_{\substack{i\alpha, j_1\beta_1, j_2\beta_2, \\ \dots, j_{p-1}\beta_{p-1} \\ j_1\beta_1 \neq i\alpha \\ j_2\beta_2 \neq j_1\beta_1 \neq i\alpha \\ \dots}} H_{i\alpha, j_1\beta_1} H_{j_1\beta_1, j_2\beta_2} \cdots H_{j_{p-1}\beta_{p-1}, i\alpha}. \end{aligned} \quad (4.5)$$

The Hamilton matrix elements,  $H_{i\alpha, j\beta}$ , are identified with hopping parameters,  $\langle i\alpha|v_i|j\beta\rangle$ , so that the  $p$ th moment of the local DOS is given by the sum of all closed hopping path of length  $p$  starting (and ending) at atom  $i$ . Note that

## CHAPTER 4. TRANSITION METALS, SELECTED ALKALINE EARTH METALS AND LANTHANIDES

---

$E_d = H_{i\alpha, i\alpha}$ . The second moment of a local rectangular DOS (so-called mean square width), evaluated with the help of Eq. (4.4), is ( $D_{i\alpha} = 1/W$ )

$$\mu_i^{(2)} = \sum_{\alpha} \mu_{i\alpha}^{(2)} = \frac{10}{12} W^2.$$

$H_{i\alpha, j\beta}$  is diagonal in the Slater-Koster bond integrals,  $dd\sigma$ ,  $dd\pi$ , and  $dd\delta$ , if the  $z$ -axis is chosen along the position vector from site  $i$  to site  $j$  [205]. Assuming a lattice with  $\kappa$  nearest neighbours, evaluation of Eq. (4.5) yields [179]

$$\mu_i^{(2)} = 10\kappa h^2,$$

where

$$h^2 = \frac{1}{5} (dd\sigma + 2dd\pi + 2dd\delta).$$

Combining both expressions for  $\mu_i^{(2)}$ , we obtain  $W = \sqrt{12\kappa}|h|$ . Hence, the bandwidth  $W$  as well as the bond energy in Eq. (4.2) vary with the square root of the number of nearest neighbours  $\kappa$ .<sup>3</sup> The bandwidth is also proportional to  $|h|$ , and  $|h|$  decreases with increasing interatomic distance [179]. In order to describe the binding energy in Eq. (4.3), reasonable functions for the distance dependence of  $h$  and the aforementioned repulsive pair potentials must be chosen. These functions are not parameter-free. Reference 179 fitted the parameters to an assumed  $d$ -bandwidth of 10 eV for an element in the middle of the series (Mo), and the experimentally observed variation of the Wigner-Seitz radius across the series. In doing so, Pettifor was able to reproduce quantitative trends across the 4d-TM series, e.g., the cohesive energy and the bulk modulus. The description is erroneous for noble metals due to neglect of  $sp - d$  hybridisation [179, 221]. The rectangular  $d$ -band model in the approximation of the second moment features structure independent binding energies, because binding energies are  $\kappa$  independent at equilibrium [178, 221]. Hence, the binding energy differences are identical zero among, say, BCC, FCC, and HCP lattices.

Energy differences between typical crystal structures in TMs for the same number of valence electrons (structural energy differences) were attributed to higher order moments of the band DOS, i.e., in terms of closed paths with more than two steps in the local environment of atom  $i$  [39, 45]. In other words, features of the crystal structure are resembled in the band DOS, which itself determines the relative stability of a crystal structures with respect to another. Accordingly, the structural stability of the BCC structure for approximately half band-filling is determined by the smallness of  $\mu^{(4)}/(\mu^{(2)})^2$  [179, 221]. The bimodal character of the BCC DOS for half band filling brings along an according to amount higher bond energy compared to a unimodal DOS. Structural energy differences between FCC and HCP are primarily determined by differences in  $\mu^{(5)}$  and  $\mu^{(6)}$ . Following Refs. 75, 179, marked minima in the HCP DOS at  $d$ -band fillings of four and eight electrons per atom determine the stability of HCP against FCC at these points. Structural energy differences on the basis of the band DOS are given by an integration [221],

$$\delta E = \int^{E_F} (\epsilon - E_F) \delta D(\epsilon) d\epsilon, \quad (4.6)$$

---

<sup>3</sup>The relation  $W \propto \sqrt{\kappa}$  is as well used to qualitatively interpret the reduction of the bandwidth at surfaces due to the reduced coordination number [220].



## 4.2. TRENDS IN TRANSITION METAL SERIES: INSIGHTS FROM EMPIRICAL MODELS

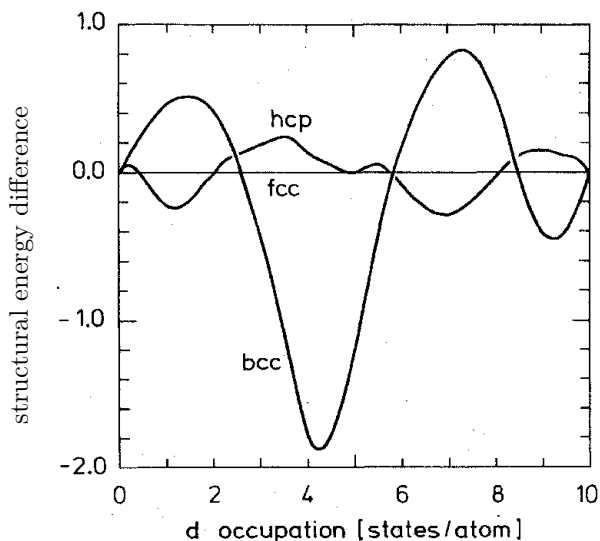


Figure 4.2: Structural energy differences obtained from the first moment of the canonical  $d$  DOS of FCC, BCC, and HCP structures as function of the  $d$ -electron occupation. Structural energy differences are in arbitrary units, and given relative to FCC. A negative difference indicates higher stability than FCC. Figure taken from Ref. 204.

whereat  $\delta\epsilon$  and  $\delta D(\epsilon)$  are the differences in the bond energy and the model band DOS of two distinct structures, respectively (same band filling implicitly assumed). A model DOS can be constructed from the moment theorem (Eq. (4.5)) [45]. Indeed, the observed crystal structure trend across the NM TM series (HCP  $\rightarrow$  BCC  $\rightarrow$  HCP  $\rightarrow$  FCC) was reproduced within the  $d$ -orbital only model and the moment theorem, apart from the noble metals where  $sp-d$  hybridisation is required to yield a stable FCC lattice [177, 179].

Another model approach is canonical band theory within the KKR method (named after Korringa, Kohn, and Rostoker) in the atomic sphere approximation (ASA) [5, 204]. The KKR-ASA formalism includes energy independent structure constants,  $S$ , and energy dependent potential functions. The structure constants depend solely on the crystal structure. The potential functions are defined inside the atomic sphere and contain information on the atomic species and atomic volume. Neglecting the hybridisation with  $s$  and  $p$ -bands, a so-called canonical band structure for  $d$ -bands can be calculated within KKR-ASA [5, 204]. Canonical bands depend only on the crystal structure. From canonical bands, one can obtain the canonical DOS and canonical structural energy differences similar to Eq. (4.6). In Fig. 4.2 we depict structural energy differences from canonical band theory for NM TMs. The energy differences resemble the stability of BCC near the middle of the series, as well as the stability of HCP in the beginning of the series and for a  $d$ -occupation approximately 6 states/atom. The BCC structure is incorrectly found to occur at the end of the series, which is among other things due to the neglect of hybridisation effects [5, 204]. Furthermore, the  $d$ -occupation ranges of stable structures

## CHAPTER 4. TRANSITION METALS, SELECTED ALKALINE EARTH METALS AND LANTHANIDES

---

are wrongly described, for example the HCP stability for a  $d$ -occupation of 8 states/atom.

So far, we mentioned only three different crystal structures in the discussion of the TM series (BCC, FCC, and HCP), which was mainly motivated by their abundance among the crystal structures of TM elements (cf. Fig. 4.1). Clearly, the previous thoughts can be done in regard to other crystal structures. In doing so, canonical theory failed to predict the correct crystal structures in the  $d$ -occupation range from 1.6 to 2.6 states/atom [204].

We finally establish important macro-trends for the three TM series [19]. The number of nodes in the radial part of the wave function and simultaneously the extension of the wave function increases from the  $3d$  to  $4d$  to  $5d$ -orbitals. The hopping matrix element in a TB picture ( $h$ ) increases with the extension of the wave function for constant interatomic distance, hence  $h_{3d} < h_{4d} < h_{5d}$ , and the band width increases with an increasing hopping matrix element,  $W \sim h$ . The DOS in this simple picture scales inversely with the band width,  $D \sim 1/W$ . The important macro-trends for the  $3d$ ,  $4d$ , and  $5d$  TM series are:

$$W_{3d} < W_{4d} < W_{5d},$$

$$D_{3d} > D_{4d} > D_{5d},$$

$$I_{3d} < I_{4d} < I_{5d}.$$

The last line states a global trend for the exchange integral (Stoner parameter),  $I$ , found by Ref. 89. There is also a micro-trend within one  $d$ -series: the  $d$ -wave functions at the beginning of a series are more extended than at the end of a series due to an incomplete screening of the Coulomb potential of the nucleus by the  $d$ -electrons. The band width at the beginning of a series is therefore broader than at the end of a series.

To conclude, simple models can provide insight into trends in TM series such as cohesive energies and structural energy differences. Furthermore, they may be used in the interpretation of results obtained from more accurate one-electron theory, which extended the limits of canonical theory [58, 165, 169, 204].

### 4.3 Literature survey

This section gives an overview of references that addressed the calculation of EBPs, UBPs, CSBPs, and CVBPs for the elements depicted in Fig. 4.1 on Page 26. Only DFT electronic structure calculations are considered, irrespective of the method used to solve the Kohn-Sham-equations and irrespective of the XC potential. Results from empirical potential calculations of any kind are not considered here, although empirically constructed potentials qualitatively reproduce DFT results of the Bain transformation, for instance for Fe [155], Ca [6], and Cu, Ag, and Au [232]. Such empirical potentials are fitted to experimental values (which are constricted to phases accessible in experiments) and DFT results. We compile the references to all 34 elements in Table 4.1. The focus is on the EBP in this thesis. As pointed out in Sec. 3.2, data for tetragonal minima can be transferred among EBP, UBP, and CSBP under certain assumptions. This increases the amount of theoretical data we can compare our results

### 4.3. LITERATURE SURVEY

Table 4.1: Survey of literature that dealt with the computation of EBPs, UBPs, CS-BPs, and CVBPs. Investigated magnetic order for EBPs is explicitly listed.

element	CVBP	CSBP	UBP	EBP	magnetic order (EBP)
20 Ca	[183, 206]	[140]			
21 Sc					
22 Ti	[206]			[131–133]	
23 V	[38] <sup>†</sup> [206]	[140, 160]	[4]	[4, 131, 133, 225]	
24 Cr	[38] <sup>†</sup>	[160]			
25 Mn	[38] <sup>†</sup> [184]	[70]		[133]	NM, FM, AF1, AF2 [70] AFM <sup>‡</sup> [70], AF1 [133]
26 Fe	[38, 109] <sup>†</sup> [62, 170, 171, 227, 240] <sup>¶</sup> [62, 134, 150, 170, 171, 184, 242]		[240] <sup>†</sup>	[133, 185]	NM, FM, AF1 [133, 185] AF2 [185]
27 Co	[124, 150, 258] [60, 258] <sup>¶</sup>		[4]	[4, 133, 258]	NM [133], FM [4, 133, 258] AF1, AF2 [258]
28 Ni	[38] <sup>†</sup> [258] <sup>¶</sup> [150]		[72]	[258]	FM, AF1, AF2 [258]
29 Cu	[236, 243, 244] [92] <sup>¶</sup>	[140]	[4, 72]	[4, 95, 133]	
30 Zn				[133]	
38 Sr	[206]	[140]		[131, 133]	
39 Y					
40 Zr				[93]	
41 Nb	[38] <sup>†</sup> [244]	[140, 160]			
42 Mo	[38] <sup>†</sup> [244]	[140, 160]			
43 Tc					
44 Ru	[38] <sup>†</sup>	[247]			
45 Rh	[38] <sup>†</sup>	[140]			
46 Pd		[140]		[96, 133, 197]	
47 Ag		[140]	[72]		
48 Cd					
56 Ba		[140]			
57 La	[251] <sup>†</sup>				
71 Lu					
72 Hf	[2, 251] <sup>†</sup>				
73 Ta	[38, 251] <sup>†</sup> [244]	[160]			
74 W	[38, 251] <sup>†</sup> [241, 244]	[140, 160]			
75 Re	[38, 251] <sup>†</sup>				
76 Os	[38, 251] <sup>†</sup>				
77 Ir	[38, 251] <sup>†</sup> [241]	[140]			
78 Pt	[251] <sup>†</sup>		[72]		
79 Au	[251] <sup>†</sup>	[140]	[64, 72]		
80 Hg	[149]				

<sup>†</sup> results for  $1 \leq c/a \leq \sqrt{2}$  only

<sup>‡</sup>  $(2 \times 2)$  AFM order in the (001) plane

<sup>¶</sup> total energy contour plot in the tetragonal phase space

## CHAPTER 4. TRANSITION METALS, SELECTED ALKALINE EARTH METALS AND LANTHANIDES

---

to. We also tabulate references to CVBP calculations for the sake of completeness. The CVBP list is not exhaustive. Results from CVBP calculations can in general not be used for a quantitative comparison to the EBP, because the volume per atom changes along the EBP. One often can derive qualitative information on the general structure of the EBP by the calculation of the CVBP. In particular, statements on the number of extrema and their (approximate) location in the tetragonal phase space can be gained. The preference of a possible magnetic order over another can be tested for with the CVBP.

Some references only comprehended the Bain path within the limits  $1 \leq c/a \leq \sqrt{2}$ . In these cases, there is no information on potential stationary points outside this interval. Such references are distinguished in Table 4.1.

The references in Table 4.1 are augmented with informations on the magnetic order, that was incorporated in the calculation of the EBPs. This concerns the elements Mn, Fe, Co, and Ni. The considered order types are FM, AF1, and AF2, which were defined in Sec. 3.4. All other calculations assumed no magnetic order.

The main interest has been in elements from the fourth period, see Table 4.1. Especially the elements V, Ti, and Cu, and the magnetic elements Fe, Co, and Ni were frequently investigated. The EBP has been computed for most elements of the fourth period. In contrast, there are few or no data published for the elements of the fifth and sixth periods.

### 4.4 Computational aspects

This section addresses all computational aspects. We briefly introduce the employed band structure code, explain our settings, and elaborately discuss the convergence of important numerical parameters. We end by describing the procedure of how we obtained the EBPs.

#### 4.4.1 Band structure code and settings

All band structure calculations were performed with the full-potential local orbital program package FPLO, version 7.00 – 28 [104]. This code is an all-electron and full-potential code. The basis functions in FPLO are overlapping atom-centred local orbitals. We use the acronym FP-LCLO (full-potential linear combination of local orbitals). In the scalar-relativistic notation, the local orbitals,  $\psi_{snL}$ , read [55]

$$\psi_{snL}(\mathbf{r} - \mathbf{R} - \mathbf{s}) \stackrel{\text{def}}{=} f_{snl}(|\mathbf{r} - \mathbf{R} - \mathbf{s}|) Y_L(\mathbf{r} - \mathbf{R} - \mathbf{s}), \quad (4.7)$$

with numerical radial part,  $f$ , and analytic angular part,  $Y$ . A local orbital is centred at site  $\mathbf{s}$  in the elementary cell defined by the lattice vector  $\mathbf{R}$ .  $L$  is a multi-index of the usual non-relativistic atom-like quantum numbers,  $L = \{l, m\}$ .  $n$  denotes the principal quantum number. The radial functions ( $f$ ) are derived from full-relativistic local orbitals [55]. The basis set splits into core and valence orbitals. Core orbitals, as well as the non-relativistic and the full-relativistic basis sets are not further discussed here, but can be found in Refs. 55, 103, 104. There can be several sets of valence orbitals. The first set of valence

#### 4.4. COMPUTATIONAL ASPECTS

orbitals are the chemical valence orbitals, which are substantially occupied. The second and further sets of valence orbitals are the lowest unoccupied atomic shells and are used to complete the basis. Examples are given in the next section. FPLO7 uses a predefined and adjusted basis. We investigated the applicability of the default basis for the EBP. Characteristic energy differences of the Bain path, for example the BCC–FCC energy difference,  $E_{\text{BCC}} - E_{\text{FCC}}$ , should not depend on the basis set, once the basis is converged. Our results show, that these characteristic energy differences are not converged for all elements using the default basis. We report more elaborately on the completeness of the basis in the next section.

**Brillouin zone integration mesh** Few other numerical settings have to be converged to ensure stability of quantities of interest with respect to these numerical parameters. The most important one is the Brillouin zone integration mesh ( $k$ -mesh). The quantities of interest are primarily lattice parameters, total energies (and based on the latter, accurate total energy differences), and magnetic moments. The convergence test for the  $k$ -mesh was done in the less symmetric BCT crystal structure (space group  $I4/mmm$ ) compared with cubic symmetry. The lattice parameters of the tetragonal unit cell are again  $a$  and  $c$  as previously defined. The procedure is to a large extent identical to the calculation of the EBP, hence we stick to the same notation. For an arbitrarily chosen  $a$ , we calculated the energy minimum over all  $c$ 's according to Eq. (3.7) on Page 13. The minimum is found at  $c_a$  by a polynomial fit of fourth order to a set of energies  $E(a, c)$ . The set of energies was computed for sampling points in a narrow range of approximately  $0.2 \text{ \AA}$  around  $c_a$ . We monitored the change of  $c_a$  and of  $E(a, c_a)$  with the number of  $k$ -points. The  $k$ -integration mesh was considered converged, if the modulus of the change in total energy at the minimum with respect to a doubling of the  $k$ -points in each Cartesian direction accounted for less than  $10 \mu\text{Hartree/atom}$ . Elements from the second group have the lowest structural energy differences, typically in the order of  $0.1 \dots 1 \text{ mHartree/atom}$ . Our convergence criterion ensures the stability of such small energy differences with respect to the  $k$ -points.

An isotropic  $k$ -mesh requires  $N_x a_x \approx N_y a_y \approx N_z a_z$ , due to the inverse relation of length in position and reciprocal space ( $k$ -space).  $a_i$  and  $N_i$  are the lattice parameter and the number of  $k$ -points in one of the three Cartesian directions,  $x$ ,  $y$ , or  $z$ , respectively. For the conventional unit cell of the BCT lattice we have  $a \equiv a_x = a_y$ ,  $c \equiv a_z$ , so  $N_a a \approx N_c c \approx \text{const}$ . The ratio of the lattice parameters  $c$  and  $a$  changes in some range along the EBP, the largest  $c/a$  ratio being roughly three times the smallest ratio in the region of interest. To ensure an isotropic mesh for all BCT structures along the EBP, the number of  $k$ -points must be adjusted for each geometry. Due to symmetry properties of the centred tetragonal space group ( $I4/mmm$ ), FPLO requires an equal  $k$ -point number in each Cartesian direction,  $N_a \stackrel{!}{=} N_c$ . Hence, an isotropic  $k$ -integration mesh cannot be realised for all tetragonal structures of the Bain path. We overcome this shortcoming by choosing a relatively dense mesh of not less than  $24 \times 24 \times 24$   $k$ -points (24  $k$ -points in each Cartesian direction). In what follows, we abbreviate an  $N \times N \times N$  Brillouin zone integration mesh with  $N^3$ . This number of  $k$ -points is sufficient to stabilise the total energy ( $E(a, c_a)$ ) of most of the con-

## CHAPTER 4. TRANSITION METALS, SELECTED ALKALINE EARTH METALS AND LANTHANIDES

---

sidered systems at a level of smaller than  $10 \mu\text{Hartree/atom}$  against an increase to  $48^3$ . The only exceptions are Ni, Cu, Ru, Ir, and Pt, which require a mesh of  $48^3$   $k$ -points. The lattice parameter for which  $E$  takes the minimum,  $c_a$ , is converged to a value smaller than  $|2 \times 10^{-3} \text{ \AA}|$  for the chosen number of  $k$ -points.

In the singular case of Ba we used a denser point mesh for the two-centre and three-centre integrals. This point grid is referred to as ‘3D-grid’. With the default 3D-grid, we were not able to make a clear statement about an energy difference between two adjacent, virtually degenerate stationary points on the EBP of Ba, see the detailed discussion in Sec. 4.5.3. The enhanced, denser 3D-grid has 200 radial grid points compared to 80 of the default settings. For its angular part, we used a higher order Lebedev grid with more grid points than default. Using the enhanced 3D-grid, we were able to distinguish these two adjacent stationary states into a maximum and a minimum. The associated relative energy shift between the two stationary points, that allowed the distinction in the first place, is  $10 \mu\text{Hartree/atom}$ . This shift is small and not significant for the other elements, because the energy scale of their structural energy differences is larger, typically  $0.1 \dots 10 \text{ mHartree/atom}$ . The default 3D-grid is hence sufficient for all elements but Ba. The electronic DOS is a sensitive quantity to the  $k$ -mesh. A well converged integration mesh prevents erroneous spikes and variations in the DOS due to an insufficient grid. We calculated every DOS preventively with (at least)  $48^3$   $k$ -points.

To summarise the previous paragraphs, a convergence of the  $k$ -mesh and the enhanced 3D-grid for Ba ensures the stability of the total energy, the DOS, and the lattice parameters. All EBPs were calculated with the number of  $k$ -points as stated above.

**Relativity and XC potential** The EBPs for elements of the fourth period (Ca–Zn) and of the fifth period (Sr–Cd) were computed in the scalar-relativistic mode. All other elements (Ba–Hg, Lu) are entirely treated full-relativistically in the four component implementation of FPLO [55]. Earlier works [55,164] studied the differences between scalar-relativistic and full-relativistic calculations for the elements Cu, Ag, and Au using an older version of FPLO. Accordingly, the theoretical FCC equilibrium lattice parameter of the heavy element Au differs by at most 0.5% between the scalar-relativistic mode and the full-relativistic mode (spin-orbit coupling related change in the lattice constant). The effect on structural properties is smaller for elements with smaller spin-orbit coupling (examples Cu and Ag). In contrast, the bulk modulus of FCC Au is 4 to 9% larger with spin-orbit coupling than without (the exact value depends on the choice of the basis set). This effect associated with spin-orbit coupling is again considerable smaller for the lighter elements Cu and Ag [164]. Spin-orbit coupling lifts degeneracies in the band structure and introduces new feature in the DOS, which are again most significant for the heavy element Au, but may alter parts of the Fermi surface, as for example reported for Pd [25]. We used the LSDA for the XC potential in the parameterisation of Perdew and Wang [174]. Note that no GGA functional is implemented in FPLO7.

---

## 4.4. COMPUTATIONAL ASPECTS

**Magnetic order** The possibility of a finite spin polarisation was taken into consideration for the elements Mn, Fe, Co, and Ni throughout this thesis, due to the presence of magnetic order in their GSs. We can in principle not exclude a magnetic instability for some states of the EBP for the other elements, although a new magnetic state may be unexpected. Thus, the possibility of magnetic order on the EBP was checked for each element for special points on the EBP. Special points are points that exhibit a high DOS in the NM state.

We considered FM, AF1, and AF2 orders. Both AFM arrangements were introduced in Sec. 3.4. We employed two methodical approaches: the fixed spin moment (FSM) method and calculations with initial spin split (ISS). The FSM method [41, 198, 250], as implemented in FPLO, constrains the spin moment per primitive unit cell. The total energy,  $E(m_s)$ , can be studied as function of the spin moment,  $m_s$ , in that way. The entire  $E(m_s)$  curve is of interest, for example, for Invar alloys [49, 145], magnetocaloric and metamagnetic materials [129, 198]. The FSM method helps to resolve convergence problems related to several, possibly degenerate, energy minima with different spin moment, or generally, if the total energy versus spin moment landscape is flat. Of course, it requires more self-consistent calculations to map  $E$  as function of  $m_s$  (and to find the minimum of  $E(m_s)$ ) than without the fixed moment constraint. The FSM method is not available in the full-relativistic mode. Calculations with ISS do not fix the spin moment during the self-consistency cycle. A finite spin-split is initially created in the input density prior the first iteration cycle. An ISS is available for scalar-relativistic and full-relativistic calculations, and ISSs can be invoked for each Wyckoff position individually. We performed scalar-relativistic AFM calculations with FSM and ISS simultaneously: we set the spin-moment of the whole unit cell to zero (by FSM), and applied a Wyckoff position specific spin split in the spin-up and spin-down density modelling an AFM arrangement.

Magnetic moments were obtained with the same number of  $k$ -points as the total energy and lattice parameters, if not stated otherwise.

### 4.4.2 Convergence of basis set

Special attention was attributed to the completeness of the basis. FPLO7 and higher versions use a predefined and adjusted basis set for each element. Each basis set was optimised to meet requirements of three physically distinct situations: a homonuclear dimer at equilibrium, a closed packed structure at equilibrium, and a closed packed structure under very high pressure (300 GPa) [103, 189]. The tetragonal structures of the EBP are more open than the closed packed structure the basis was optimised for. The lattice parameter ratio  $c/a$  changes along the EBP in a wide range. Accordingly change the number of nearest and next nearest neighbours, as well as interatomic distances (bond length) and enclosed angles (see Fig. 3.7 on Page 20). We checked the applicability of the default valence basis for the EBP. Lattice parameters for the tetragonal structures of the EBP and for the GS crystal structure in general turned out to be converged using the default basis set. This is in line with the change of the Fe dimer bond length as function of the valence basis [103]. Therefore we focused on the total energy along the EBP. More precisely, we studied total energy differences,  $\Delta E$ , between two stationary points of the energy along

## CHAPTER 4. TRANSITION METALS, SELECTED ALKALINE EARTH METALS AND LANTHANIDES

---

the EBP for different basis set,<sup>4</sup> for example  $\Delta E = E_{\text{BCC}} - E_{\text{FCC}}$ .

We performed the basis check for the CVBP instead of the EBP, because we were interested in the convergence of the total energy only. The procedure was firstly to evaluate the CVBP with the default basis set and consecutively with an extended basis set. The increase of the number of basis states (basis orbitals) followed a rigid procedure, that we outline in the following.

The radial part of the basis orbitals,  $f_{snl}$ , is the numerical solution of the radial Schrödinger equation with the radially symmetric potential  $V(r)$ ,

$$V(r) = V_0 + V[Q_{nl}] + V_{\text{conf}}.$$

$V_0$  is the potential of the free atom,  $V[Q_{nl}]$  is an  $nl$ -dependent ionic potential of ionicity  $Q_{nl}$  to account for charge fluctuations, and  $V_{\text{conf}}$  is a confining potential to compress tails of orbitals at large distance  $r$  [103]. The latter term has an effect on all sets of valence states.  $V[Q_{nl}]$  affects only the second and third set of valence orbitals. The extended basis was constructed by adding another set of valence orbitals to the existing sets of valence orbitals. Note that a maximum number of three sets of valence orbitals with the same  $l$  are destined. More precisely, if we denote the default valence basis orbitals with the highest principal quantum numbers ( $n$ ) for each angular quantum number ( $l$ ) by  $n_1l_1$ ,  $n_2l_2, \dots$ , we added another set of basis orbitals with quantum numbers  $(n_1+1)l_1$ ,  $(n_2+1)l_2, \dots$ . Each new orbital,  $(n_i+1)l_i$ , was assigned the parameter  $Q_{(n_i+1)l_i} = Q_{n_i l_i} + 2$  when the default orbital  $n_i l_i$  had the value  $Q_{n_i l_i}$ . We adjusted the parameter  $Q_{nl}$  for each additional basis state. We illustrate the procedure using the example of Ti. The default valence basis consists of  $4s$  (with  $Q_{4s} = 0$ ) and  $5s$  ( $Q_{5s} = 3.5$ ),  $3d$  ( $Q_{3d} = 0$ ) and  $4d$  ( $Q_{4d} = 4.7$ ), and  $4p$  ( $Q_{4p} = 1$ ) states. The extended basis comprises a third set of  $s$  and  $d$ -valence states,  $6s$  and  $5d$ , and a second set of  $p$ -states,  $5p$ , with  $Q$ -parameters  $Q_{6s} = 5.5$ ,  $Q_{5d} = 6.7$ , and  $Q_{5p} = 3$ . In short hand notation, the default valence basis consists of double  $s$  ( $4s5s$ ) and double  $d$  ( $3d4d$ ) orbital sets, and a single  $4p$  orbital set. The extended basis set is then triple  $s$  ( $4s5s6s$ ), triple  $d$  ( $3d4d5d$ ), and double  $p$  ( $4p5p$ ).

For elements with BCC GS structure, we calculated the CVBP at the theoretical BCC equilibrium volume. We used the theoretical FCC equilibrium volume for all other elements. The numerical settings were identical to those described in the previous subsection. The Brillouin zone integration mesh was converged using the default basis set. The basis set is considered to be complete, if the relative change of the energy difference between any two extrema of the CVBP is less than 0.1, i.e.,

$$\max_j \left| \frac{\Delta E_j^{\text{ext}} - \Delta E_j^{\text{def}}}{\Delta E_j^{\text{def}}} \right| < 0.1, \quad (4.8)$$

whereat  $\Delta E_j^{\text{ext}}$  and  $\Delta E_j^{\text{def}}$  are the total energy differences between a pair  $j$  of two extrema along the CVBP for the extended and default basis, respectively. If the basis set turned out to be incomplete in the spirit of the aforementioned criterion, we increased the number of valence and polarisation basis states accordingly and repeated the test.

---

<sup>4</sup>The procedure was recommended by the author of FPLO, Klaus Koepernik.



## 4.4. COMPUTATIONAL ASPECTS

Table 4.2: Valence basis setup for default and extended settings. The extended basis was used only for elements tabulated here. The notation is written shortened: S = single, D = double, T = triple basis. Explicitly,  $Snl$  means orbital set  $nl$ ,  $Dnl$  means orbital sets  $nl$  and  $(n+1)l$ , and  $Tnl$  stands for three orbital sets with quantum numbers  $nl$ ,  $(n+1)l$  and  $(n+2)l$ .

element	default	extended
Ca	$D4sS4pD3d$	$T4sD4pT3d$
Ti	$D4sS4pD3d$	$T4sD4pT3d$
Mn	$D4sS4pD3d$	$T4sD4pT3d$
Sr	$D5sS5pD4d$	$T5sD5pT4d$
Zr	$D5sS5pD4d$	$T5sD5pT4d$
Pd	$D5sS5pD4d$	$T5sD5pT4d$
Ba	$D6sS6pS5d$	$T6sD6pD5d$
La	$D6sS6pD5dS4f$	$T6sD6pT5dD4f$
Lu	$D6sS6pD5dD4f$	$T6sD6pT5dT4f$
Au	$D6sS6pD5d$	$T6sD6pT5d$

**Results** An extended basis was employed for ten elements. Their default and extended basis are listed in Table 4.2.<sup>5</sup> Zr is the only element, for which the shape of the CVBP is significantly altered by the extended basis (Fig. 4.3b). In contrast, elements like Ti just exhibit a change in the structural energy differences in the order of few 0.1 mHartree/atom (Fig. 4.3a). This is the typical shift in total energy associated with the change from the default basis to the extended basis for each element. The relevant energy scale of structural energy differences is decisive whether the extended basis has a noticeable effect (in terms of Eq. (4.8)). Typical structural energy differences are  $\approx 0.1 \dots 1$  mHartree/atom for elements of the Ca and Zn groups, while  $\approx 5 \dots 50$  mHartree/atom for refractory metals. It is hence not surprising, that the extended basis is needed only for those elements, whose structural energy differences are not significantly larger than the total energy difference associated with the change from the default basis to the extended basis.

### 4.4.3 Brief remark on ground states

In the process of obtaining the EBPs, we also calculated the GSs of all selected elements. We applied the same numerical settings as described in the two preceding subsections. The convergence test of the Brillouin zone integration mesh was repeated because different crystal structures occurred. We used a Brillouin zone integration mesh of  $12^3$   $k$ -points for Mn, due to its large and complex unit cell. The space groups for the various lattices are [74, 237]:

<sup>5</sup>We make use of the spectroscopic notation for the quantum numbers of local orbitals [192], although full-relativistic calculations imply four-component basis orbitals with atomic quantum numbers in relativistic notation.

## CHAPTER 4. TRANSITION METALS, SELECTED ALKALINE EARTH METALS AND LANTHANIDES

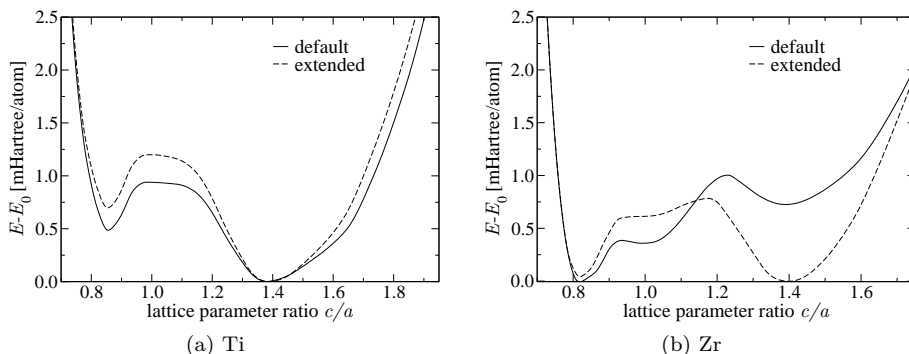


Figure 4.3: Total energy along the CVBP at the theoretical FCC equilibrium volume for Ti (*left hand side*) and Zr (*right hand side*) using the default and the extended basis setup. The minimum energy value for each curve,  $E_0$ , was subtracted from the calculated total energies.

FCC	$Fm\bar{3}m$
BCC	$Im\bar{3}m$
BCT	$I4/mmm$
(D)HCP	$P6_3/mmc$
CUB (Mn)	$I\bar{4}3m$ .

Lattice parameters were optimised in all cases. The indicated space group for Mn describes the paramagnetic cubic structure at ambient conditions [83], see also discussion in Sec. 4.5.8 on Page 71. Three out of four Wyckoff positions for Mn are not fixed by symmetry. We used the experimental data from Villars and Calvert for simplicity [237].

Total energy calculations in the LSDA are known to give the incorrect GSs of Cr and Fe. BCC Cr is found to be NM instead of having an incommensurate AFM GS [37, 71], and an NM HCP phase of Fe is found to be more stable than the experimental FM BCC phase of Fe [150, 231]. The LSDA also gives HCP Mn lower in total energy than both BCC and FCC Mn [169, 204, 259].

### 4.4.4 Epitaxial Bain path calculational procedure

To obtain the EBP of an element, we have to find the set of points  $(a, c_a)$ , which define the EBP according to its definition in Eq. (3.7) on Page 13. The principle procedure therefor was elaborately described by us in Ref. 197, Chapter 3, and is not repeated here to the full extend. The procedure is also similar to what we did in Sec. 4.4.1 to check the convergence of the Brillouin zone integration mesh.

We initially chose an equidistant grid for  $a$  with a step size of  $0.05 \text{ \AA}$  between two neighbouring points. This grid was arbitrarily refined if needed, for example at interesting (unexpected) kinks, steps, shoulders or stationary points associated with the EBP or the total energy along the EBP. The initial grid for  $c$  was kept coarse to narrow down the approximate position of  $c_a$ . Typically, we ended up with a distance of  $0.03 - 0.05 \text{ \AA}$  between two neighbouring points for

## 4.5. EPITAXIAL BAIN PATH OF TRANSITION METALS, SELECTED ALKALINE EARTH METALS AND LANTHANIDES

---

*c*. This distance is comparable with the distance between two sampling points that we employed to check the convergence of the Brillouin zone integration mesh. The position of  $c_a$  was obtained by a polynomial fit of fourth order to the set of energies  $E(c)$ ,  $a$  fixed.

If FSM calculations are applied, the total energy must also be minimised with respect to the spin moment,  $m_s$ . Denote the total energy as function of  $a$ ,  $c$ , and  $m_s$  with  $E = E(a, c, m_s)$ . We firstly minimised  $E$  with respect to  $m_s$  with fixed  $a$  and  $c$ , and afterwards minimised  $E$  with respect to  $c$  for fixed  $a$  in accordance with the definition of the EBP:

$$E_{m_s}(a, c) \stackrel{\text{def}}{=} E(a, c, m_{s,(a,c)}) = \min_{m_s} E(a, c, m_s)$$

$$E_{\text{EBP}, m_s}(a) \stackrel{\text{def}}{=} E_{m_s}(a, c_a) = \min_c E_{m_s}(a, c).$$

The second line is analogous to Definition (3.7). The energy as function of the spin moment was calculated in steps of  $0.1 \mu_B/\text{atom}$ . The total energy as function of the spin moment (by means of FSM) for fixed lattice is denoted by  $E = E(m_s)$ .

Calculations with an ISS were started with two different spin splits to check whether both calculations converge into the same self-consistent magnetic moment, namely a low spin split of  $0.1 \mu_B/\text{atom}$  and a large one with  $2.0 \mu_B/\text{atom}$ .

## 4.5 Epitaxial Bain path of transition metals, selected alkaline earth metals and lanthanides

We present and discuss the results of our calculations in this section. Elements belonging to the same group in the periodic table are dealt with together. The main results for each group are summarised on a double page consisting of tabulated values and four figures. Since the structure of these tables and figures is identical for each group, we give general comments on them in the two subsequent subsections.

### 4.5.1 General overview and remarks on tables

Each table summarises our calculated results, and it comprises published theoretical and experimental data which we compare our data to.

**Ground state (GS)** We give the theoretical, optimised lattice parameter,  $a$ , in the experimental GS crystal structure. For elements, whose crystal structure is (D)HCP or BCT, we also give the optimised lattice parameter ratio,  $c/a$ . The total energy in the GS is referred to as  $E_0$ . The presence of magnetic order in the GS is indicated. We compare our computed values with the experimentally determined lattice parameters and ratios. Experimental data (lattice parameter(s), GS crystal structure, phase diagram) are taken from standard references [43, 237, 256].

## CHAPTER 4. TRANSITION METALS, SELECTED ALKALINE EARTH METALS AND LANTHANIDES

---

We compare our calculated values to other computed values published in the literature, if available. We made a point of choosing references that employed all-electron, FP implementations of the DFT scheme and the L(S)DA XC potential, preferably in the parameterisation of PW92. Full-relativistic calculations for elements of the sixth period (Ba–Hg, Lu) are preferred, otherwise results of scalar-relativistic calculations are tabulated. Scalar-relativistically calculated GSs of elements in the sixth period are labelled with a dagger, ‘†’. A large set of elements was recently published by Ref. 226, using the FP-LAPW (linearised augmented plane wave) code WIEN2K [16] and PW92.

**Characteristics of Bain paths (stationary points)** The tables list important characteristics for each EBP. Such are the type and the coordinates of each stationary point (abbreviated to SP in tables) in total energy along the EBP, as well as its energy difference to the GS,  $E - E_0$ . The lattice parameter and the axial ratio of BCT lattices are also denoted by  $a$  and  $c/a$ , respectively. According to our considerations in Sec. 3.2, stationary points of the EBP are stationary points in the energy landscape  $E(a, c)$ : a minimum (MIN) in energy along the EBP corresponds to a minimum in energy in the tetragonal parameter space. A maximum (MAX) in energy along the EBP corresponds to a saddle point in  $E(a, c)$ . EBP, CSBP, and UBP go through the same global energy minimum of  $E(a, c)$ , possibly through other local minima and saddle points. We use this property common to EBP, CSBP, and UBP to increase the number of references which we compare our results to. We extract lattice parameters, energy differences, and possible magnetic states of stationary points from the references. Publications often contain sparse numerical data and favour figures instead. If possible, we also extract data from figures in references. In order to give a transparent picture, we distinguish among different implementations to solve the DFT scheme and different XC functionals. Band structure calculations with GGA XC functionals are taken into consideration. GGA results are typeset in *italics*. Scalar-relativistically calculated stationary points of elements in the sixth period are again labelled with a dagger. The presence of magnetic order for stationary points is explicitly mentioned.

In some references, energies are not stated with respect to the GS, but rather with respect to the global energy minimum of the EBP, especially if the GS structure is neither FCC nor BCC. In order to enter such ‘incomplete’ data into our tables anyway, we assign a constant,  $C$ , to the unpublished (unknown) energy difference between the global energy minimum of the EBP and the GS,  $E_{\text{MIN}} - E_0 \equiv C$ . We give an example for Ti: Refs. 131, 132 did not state the energy difference between the minimum at  $c/a = 1.40$  and the HCP GS (Table 4.7 on Page 58). Hence we assigned it to  $C$ ,  $E_{\text{MIN}} - E_0 \equiv C$ . The energy difference between the maximum at  $c/a = 1.05$  and the GS,  $E_{\text{MAX}} - E_0$ , is then  $E_{\text{MAX}} - E_{\text{MIN}} + C = 1.30 \text{ mHartree/atom} + C$ .

The indicated numerical precision should be commented. Lattice parameters for GS structures are given with three digits, because the structural parameters were accurately optimised in the respective crystal structure. Stationary points of the EBP were determined from spline-fitted curves  $E(a)$  and  $E(c/a)$  (two adjacent sampling points were at most  $0.05 \text{ \AA}$  apart). We did not a priori assume that cubic structures coincide with stationary points in energy along the EBP (cf. symmetry argument in Secs. 3.3 and 3.4). Instead, we determined  $c/a$

#### 4.5. EPITAXIAL BAIN PATH OF TRANSITION METALS, SELECTED ALKALINE EARTH METALS AND LANTHANIDES

---

for each stationary point with two digits precision for every element. A variation from ideal ratios ( $\sqrt{2}$  for FCC, 1 for BCC) could be related to numerical accuracy. Note that our approach is in contrast to some publications which a priori assume that cubic structures always coincide with stationary points. We distinguish data from such references by stating the  $c/a$  ratio as ' $\sqrt{2}$ ' and '1' for FCC and BCC, respectively, i.e., without two digits precision.

Without wishing to anticipate outcomes of further research in this section, there are EBPs, which are discontinuous in  $c(a)$ . A discontinuous EBP is due to the existence of a saddle point or local maximum in  $E(a, c)$ , see Fig. 3.6 for an illustration. We elaborately discuss this case in Sec. 4.5.4 using the example of La. Elements with a discontinuous EBP are La, V, Nb, Fe, Ru, Os, and Ir. For those elements but Ru, there are two lattice parameters  $c$ , that fulfil Eq. (3.7) for the same  $a$ , and  $E_{\text{EBP}}(a)$  is maximum. Hence, we list two  $c$ -parameters in the table. In the case of Ru, the EBP is discontinuous, but the discontinuity does not coincide with a maximum of  $E_{\text{EBP}}(a)$ . Hence, we list one  $c$ -parameter for Ru.

**Data from epitaxial growth** We added references to experiments for each element, if such data were available. Experiments concern the heteroepitaxial growth of overlayers in a BCT structure. The overlayer must be coherent (pseudomorphic) to the substrate. The overlayer is coherent to the substrate, if the overlayer adopts the lattice parameter(s) of the substrate within the crystal plane parallel to the substrate surface [121]. This is equivalent to a  $(1 \times 1)$  ordered overlayer on a  $\{001\}$  crystal plane of any BCC or FCC substrate [84]. We state the substrate material and the substrate interface plane, the in-plane lattice parameter and the axial ratio  $c/a$  of the overlayer, and the film thickness in the tables. If available, the precision is given as well. These data deserve a few remarks.

A frequently used technique to investigate the structure of thin films is LEED [84, 253]. Typical electron energies in LEED are in the range of 20 – 200 eV. Electrons in this energy range probe about four to five atomic layers deep into the material, while the coherence length in LEED is a few hundred Ångströms across the surface [121, 253]. Hence, quantitative statements in LEED are for surface regions of a few hundred Ångströms across. A LEED analysis reveals whether a film grows coherently or incoherently on the substrate. In the relevant case of coherence, the in-plane lattice parameter of the film is simply deduced from the one of the substrate. Information about the out-of-plane lattice parameter of the film are indirectly provided by an analysis of the energy dependence of the intensities of the diffraction spots (so-called  $I(V)$  curves) [84, 253]. Experimental  $I(V)$  curves are compared to theoretical ones in order to derive interatomic distances. The theoretical  $I(V)$  curves are calculated based on a model structure of the surface region, which is refined until good agreement between experimental and theoretical LEED intensity curves is achieved (the so-called  $R$ -factor quantifies the degree of agreement). It is important to note, that the model structure of the surface region takes into account the relaxation of the first few atomic layers beneath the surface with respect to a bulk value,  $d_{\text{bulk}}$  (relaxation perpendicular to the surface). Typically, a full-dynamical LEED calculation for a semi-infinite film accounts for the distance between the surface layer and the first subsurface layer,  $d_{12}$ , as well as for the distance between the

## CHAPTER 4. TRANSITION METALS, SELECTED ALKALINE EARTH METALS AND LANTHANIDES

---

first subsurface layer and the second subsurface layer,  $d_{23}$ , see our experimental Refs. 40, 90, 93, 101, 102, 118, 119, 121, 125, 126, 186, 224, 225. The out-of-plane distance between all other layers is then considered to be identical to  $d_{\text{bulk}}$ , which is another parameter in the LEED calculations. Few references include a fourth interlayer distance [31, 196],  $d_{34}$ , – the distance between the third and the fourth layer beneath the surface of the film. In both above references, the difference between  $d_{34}$  and  $d_{\text{bulk}}$  is smaller than the precision of the experiment. The agreement between theory and experiment in LEED is in general good for metal surfaces, so that atomic positions are given within a tenth of an Ångström or better [84]. We neglected surface reconstruction in the short discussion above. According to Ref. 84, most metal surfaces do not reconstruct.

The geometry of the bulk part of an epitaxially grown film with BCT structure, as determined from the LEED analysis, i.e.,  $d_{\text{bulk}}$ , can be placed on the EBP to identify the (metastable) phase of which the film is a strained form [4].

The lattice parameter ratio of BCT overlayers, as listed in the tables, is in all cases the value  $2 \cdot d_{\text{bulk}}$  divided by the in-plane lattice parameter. The film thickness is also stated and given in monolayers (MLs). If the thickness is reported in units of Ångström, this value is converted to the number of ML with the help of  $d_{\text{bulk}}$ . This conversion is approximative because of interlayer relaxation at the interface and at the surface. We only included those experimental references that reported on a number of pseudomorphically grown ML larger than nine. The number of ML, as taken from the references and stated in the tables, can specify two different things. It is either the maximum number of pseudomorphic ML before the film becomes incoherent. Or it is the maximum number of pseudomorphically grown ML, but the film need not to become incoherent for larger thicknesses. We do not distinguish both cases in the tables. Experiments for superlattices were not accounted for.

### 4.5.2 General remarks on figure overviews

On an individual page, we present four figures for each group of elements from the periodic table. Each figure depicts graphs for three elements. Lu is counted to the third group, these figures thus comprise four elements. The four figures show for each element *along the EBP*:

- (a)  $c(a)/a$ : the EBP in the tetragonal phase space
- (b)  $(E - E_{\text{MIN}})(c/a)$ : the total energy along the EBP with respect to  $E_{\text{MIN}}$ , which is the lowest calculated total energy of all states of the EBP
- (c)  $D(E_{\text{F}})(c/a)$ : the DOS at the Fermi energy,  $E_{\text{F}}$ , along the EBP;  $D(E_{\text{F}})$  is calculated in the non-spinpolarised mode
- (d)  $(V/V_0)(c/a)$ : the volume along the EBP divided by  $V_0$ , which is the theoretical equilibrium volume in the experimental GS structure.

Since the above quantities are always plotted along the EBP, we skip the subscript 'EBP' which we previously introduced in Sec. 3.2 during the discussion of the EBP. Quantities along the EBP are, however, plotted either as function of the (independent) variable  $a$ , e.g.,  $c(a)$  or  $E(a)$ , or as function of the axial ratio  $c/a$ , e.g.,  $E(c/a)$  or  $D(E_{\text{F}})(c/a)$ . Figures (b) to (d) are plotted as function of

#### 4.5. EPITAXIAL BAIN PATH OF TRANSITION METALS, SELECTED ALKALINE EARTH METALS AND LANTHANIDES

$c/a$ , because this eases the study of similarities and dissimilarities among the elements in one group. It also increases the clearness in every figure. The values in figures (b) to (d) can be transformed from a function of  $c/a$  to a function of  $a$  with the help of (a). In all figures, brown hatched lines indicate high symmetry or special neighbourhood structures (BCT<sub>10</sub>, BCC, FCC). These lines are not continuously labelled, however uniquely defined by their  $c/a$  ratio. In general, an EBP is obtained in a spin-polarised mode allowing for magnetic order and lattice relaxation due to the presence of magnetism. We then calculated the quantity  $D(E_F)$  along that EBP in the non-spin-polarised mode.

We use a unified shape and colour code to represent calculated and experimental data in figure overviews. Calculated data of elements of the fourth period are black coloured squares, data of elements of the fifth period are red coloured circles, and elements of the sixth period are blue coloured up triangles. Lu, as the fourth element in the third group, is depicted by green coloured left triangles. NM states are represented by open symbols, FM states by filled symbols in the respective colour and shape. Experiments (with possible error bars) are pictures by crosses in the element specific colour. The generic legend using the example of the third group with four elements would be

		element			
		Sc	Y	La	Lu
quantity	NM	□	○	△	◁
	FM	■	●	▲	◀
	EXP	×	×	×	×

Structural experimental data from epitaxy experiments (previous subsection) are indicated in the phase space diagrams  $c(a)/a$ . LSDA tends to underestimate lattice parameters in metallic systems due to its overbinding effect [105]. We determined the mean relative error (MRE) and the mean absolute relative error (MARE) for lattice constants in PW92. Let  $a_{\text{LSDA}}$  and  $a_{\text{EXP}}$  be the actual value and the target value, respectively. With  $n$  running over a set of elements, the MRE and the MARE for lattice parameters are defined by

$$\text{MRE} = \frac{1}{n} \sum_n \frac{a_{n,\text{LSDA}} - a_{n,\text{EXP}}}{a_{n,\text{EXP}}}$$

$$\text{MARE} = \frac{1}{n} \sum_n \left| \frac{a_{n,\text{LSDA}} - a_{n,\text{EXP}}}{a_{n,\text{EXP}}} \right|.$$

The MARE of the lattice parameter for all elements with BCC and FCC GS is 2.1%. Since all lattice parameters are underestimated, the MRE is  $-2.1\%$ . The MARE of the in-plane lattice parameter for elements with HCP GS is 2.2%; the same quantity for the out-of plane lattice parameter is slightly larger, 2.9%. Again, all lattice parameters are underestimated. The MARE for  $c/a$  of HCP elements is 1.0%, the MRE is  $-0.7\%$ . This means, lattice parameter ratios for HCP elements are more accurately computed than lattice parameters. This is most likely due to the isotropic arrangement of interatomic bonds in HCP lattices, which are approximately equally underestimated. BCT lattices are more open than HCP structures, and interatomic bonds are distributed less isotropic in BCT than in HCP. Hence, we do not expect cancellation of LSDA overbinding

## CHAPTER 4. TRANSITION METALS, SELECTED ALKALINE EARTH METALS AND LANTHANIDES

---

effects in the  $c/a$  ratio to be as good in BCT structure as in HCP structures. If there is, however, (partial) cancellation in  $c/a$ , experimentally determined lattice parameters for BCT structures are best compared to theoretical ones by taking the ratio  $c/a$  instead of comparing the lattice parameters themselves [55].

A comparative study of the LSDA overbinding for 18 elements with FCC and BCC crystal structure was done by Tran *et al.* [226], who reported an MRE of  $-2.2\%$  for PW92 using the FP-LAPW implementation (WIEN2K) of the DFT scheme. This MRE agrees with our value, obtained on a slightly different ensemble of systems.

### 4.5.3 Group 2 elements: Ca, Sr, and Ba

The alkaline earth metals Ca and Sr occur at RTP and lower temperatures in the FCC structure, Ba in the BCC configuration. Ca as well as Sr have BCC allotropes [43, 256]. The phase diagram of Ba exhibits no further cubic or tetragonal phases. Phase transitions in Sr (to BCC) and Ba (to HCP) at low temperatures are induced already at few GPa. The  $d$ -electron occupation number at  $T = 0$  K, as calculated in an earlier work by Skriver, is small, however increases from Ca (0.6/atom) over Sr to Ba (0.8/atom) [203]. We confirm this trend (Fig. 4.38). Reference 203 also reported on the  $s - d$  electron transfer under pressure for all three elements, which was suspected to trigger the FCC to BCC phase transformation for Ca and Sr, likewise the BCC to HCP phase transition in Ba.

**Incorrect ground state of Sr** Instead of FCC, we obtained a BCC GS for Sr. The second lowest state in total energy has tetragonal symmetry with  $c/a = 1.39$  (Fig. 4.5b). The energy difference between the latter state and the BCC GS is 0.051 mHartree/atom. This energy difference is stable with respect to an increase of the valence basis set, and with respect to the number of Brillouin zone integration points: for  $96^3$   $k$ -points, we also obtained 0.051 mHartree/atom. We could further rule out the numerical settings of the default 3D-grid as source of error by running an additional check with the enhanced 3D-grid. The position of the minimum at  $c/a = 1.39$ , which is close to the ratio of the FCC geometry, is affected by neither of the numerical changes.

In order to narrow down the source of error for the incorrectly predicted GS of Sr, we studied Sr as calculated in the literature. Several references [131, 133, 206], employing LDA and volume relaxation, also obtained a BCC GS for Sr. Reference 206 reported a value of 0.025 mHartree/atom for the FCC-BCC energy difference,  $\Delta E = E_{\text{FCC}} - E_{\text{BCC}}$  (FP-LAPW [16] (WIEN95), LDA by Hedin and Lundqvist [76]). This is in contrast to an older work [203], which correctly found an FCC GS for Sr, however using the experimentally determined equilibrium volume of Sr (linear muffin tin orbital (LMTO) method, LDA by Hedin and Lundqvist). Sliwko *et al.* further studied the volume dependence of  $\Delta E$  [206]. According to their results,  $\Delta E < 0$  at the experimentally determined equilibrium volume, i.e., FCC is the GS, and  $\Delta E > 0$  for considerably smaller volumes than the experimental one (in particular at the theoretical LDA equilibrium volume), i.e., BCC is the GS. Note that the theoretical atomic equilibrium volume of FCC Sr in PW92 is underestimated by 13% compared to the experimental



## 4.5. EPITAXIAL BAIN PATH OF TRANSITION METALS, SELECTED ALKALINE EARTH METALS AND LANTHANIDES

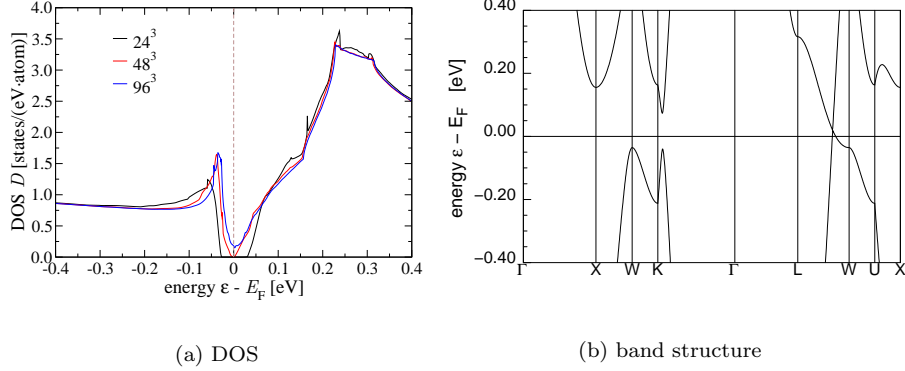


Figure 4.4: (a) Total DOS of FCC Sr close to  $E_F$  for different numbers of  $k$ -points, as indicated in the legend. For  $24^3$   $k$ -points, the DOS exhibits a clear gap of width 0.06 eV, which is significantly smaller with  $48^3$   $k$ -points. For  $96^3$   $k$ -points, a dip with a finite number of states remains at the Fermi energy. The curve for  $24^3$   $k$ -points was shifted by 0.03 eV to have  $E_F$  in the middle of the gap. (b) Band structure of FCC Sr.

value (obtained with numbers from Table 4.3). Other FP band structure calculations including volume relaxation with different parameterisations of the GGA XC potential consistently confirmed the experimentally found FCC structure for Sr [98, 140, 181]. In summary, we argue by the examples given, that PW92 most likely gives the wrong GS of Sr. The mentioned total energy calculations indicate, that  $|\Delta E|$  is in general small, i.e., less than 0.1 mHartree/atom in LDA and few 0.1 mHartree/atom in GGA.

**Sensitivity of the DOS of FCC Sr to the  $k$ -mesh** A second point of interest concerns the DOS of FCC Sr at the theoretical equilibrium volume. The DOS in the region of the Fermi level is strongly  $k$ -point dependent, see Fig. 4.4a. The DOS exhibits a gap at  $E_F$ , when it is calculated with an integration mesh of  $24^3$   $k$ -points. Significantly higher number of  $k$ -points must be used to converge the DOS of FCC Sr. Eventually the gap reduces to a dip in the single particle DOS at the Fermi energy. Because of this sensitivity, we generally computed the DOS of Sr with  $96^3$   $k$ -points. Figure 4.4b depicts the band structure of FCC Sr, which reveals two bands between the high symmetry points **L** and **W** crossing each other close to the Fermi level. This crossing is treated as a gap if the  $k$ -mesh is too sparse. Note that the FCC lattice parameter of Sr remains virtually unchanged for  $k$ -points beyond  $24^3$ . The 'erroneous' gap in the FCC DOS of Sr can also be found in the *Handbook of band structures* [167]. The depicted DOS in this book was obtained with approximately  $12^3$   $k$ -points.

**Discussion of EBPs** The complete results for the EBPs of Ca, Sr and Ba are presented in Table 4.3 and Fig. 4.5.  $c/a = 1$  (BCC) is the position of one symmetry dictated minimum for all three elements. The second minimum of  $E(a)$  coincides with the FCC configuration for Ba. The EBPs of Ca and Sr have their second energy minimum at  $c/a = 1.39$  close to  $\sqrt{2}$  (FCC). The deviation from

Table 4.3: Overview of calculated GS properties and numerical data of stationary points for the elements **Ca**, **Sr**, and **Ba** in comparison to computations and experiments from the literature, if available. General remarks on this Table are given in Sec. 4.5.1.

element	this work					literature							
	structure			$E - E_0$ [mHa]	theory			Ref.	experiment			Ref.	
	type	$a$ [Å]	$c/a$		$a$ [Å]	$c/a$	$E - E_0$ [mHa]		structure				
							system [ML]	$a$ [Å]	$c/a$				
<b>Ca</b>	GS	FCC	5.336	–	0	5.333	–	0	[226] <sup>αα</sup>	bulk	5.588	–	[237]
	SP	MIN	3.79	1.39	–0.004	$\sqrt{2}$	$0$	$0$	[140] <sup>γa</sup>				
		MAX	4.09	1.10	0.281	$1$	$0.824$	$0.824$	[140] <sup>γa</sup>				
		MIN	4.21	1.00	0.233	$0.91$	$0.737$	$0.737$	[140] <sup>γa</sup>				
<b>Sr</b>	GS	FCC	5.790	–	0	5.758	–	0	[226] <sup>αα</sup>	bulk	6.076	–	[237]
	SP	MIN	4.12	1.39	–0.005	$\sqrt{2}$	$C$	$0$	[131] <sup>αc</sup>				
		MAX	4.32	1.20	0.129	$1$	$0.143 + C$	$0.365$	[131] <sup>αc</sup>				
		MIN	4.57	1.00	–0.056	$0.71$	$–0.055 + C$	$0.365$	[131] <sup>αc</sup>				
<b>Ba</b>	GS	BCC	4.780	–	0	4.753	–	0	[226] <sup>αa†</sup>	bulk	5.013	–	[237]
	SP	MIN	4.26	1.41	0.666	$1.41$	$0.530$	$0.530$	[140] <sup>γa†</sup>				
		MAX	4.35	1.33	0.681	$1.31$	$0.530$	$0.530$	[140] <sup>γa†</sup>				
		MIN	4.78	1.00	0	$1$	$0$	$0$	[140] <sup>γa†</sup>				

legend			
<sup>α</sup>	L(S)DA [174] (PW92)	<sup>abc</sup>	FP-LAPW [16] ( <sup>a</sup> WIEN2K, <sup>b</sup> WIEN97, <sup>c</sup> WIEN95)
<sup>β</sup>	L(S)DA [30, 239]	<sup>d</sup>	FP-LMTO [141]
<sup>γ</sup>	GGA [172] (PBE96)	<sup>e</sup>	PAW [110] (VASP)
<sup>†</sup>	scalar-relativistic		

#### 4.5. EPITAXIAL BAIN PATH OF TRANSITION METALS, SELECTED ALKALINE EARTH METALS AND LANTHANIDES

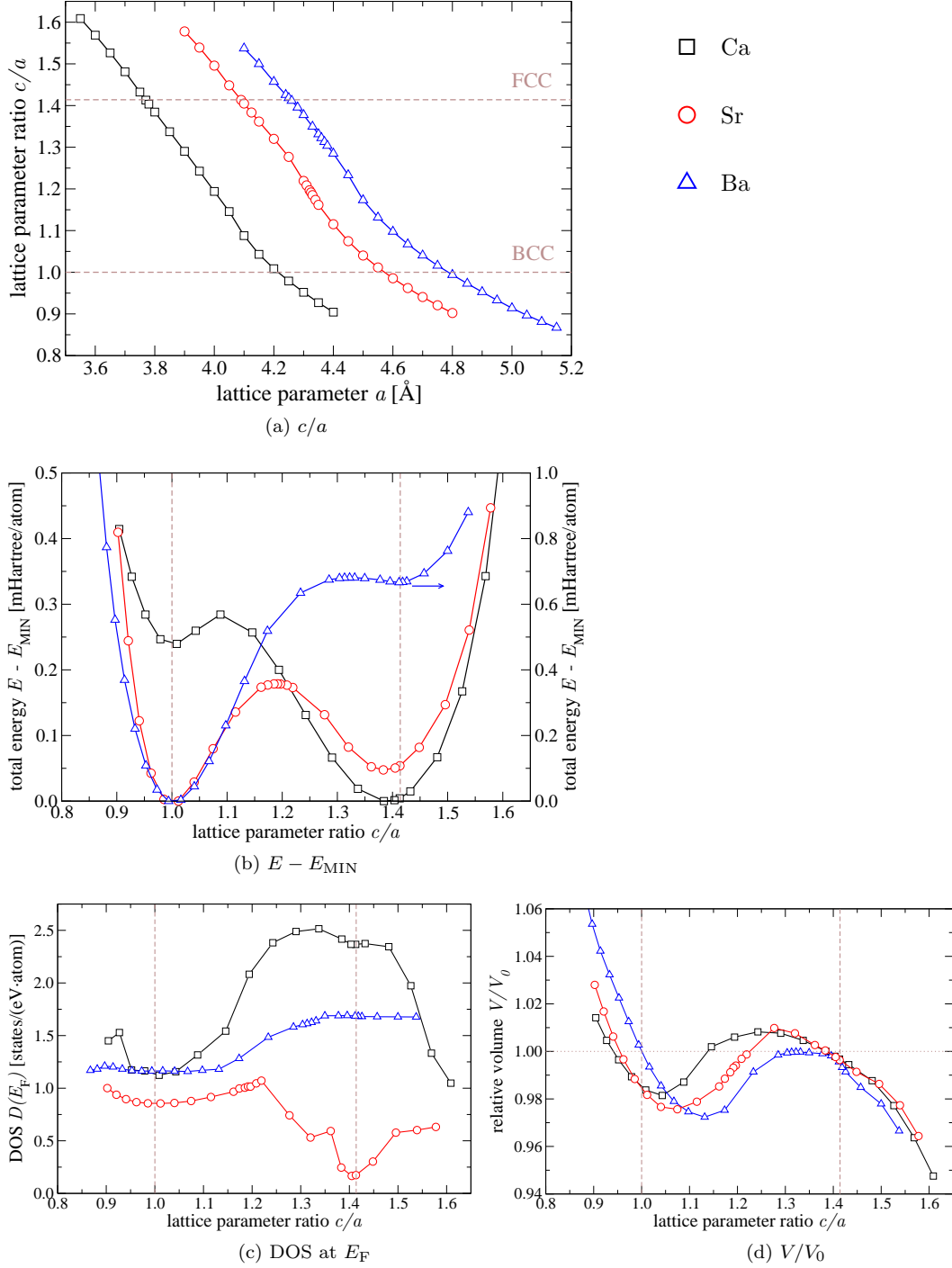


Figure 4.5: For the EBPs of **Ca**, **Sr**, and **Ba**: (a)  $c/a$ , (b)  $E - E_{\text{MIN}}$ , (c)  $D(E_F)$ , and (d)  $V/V_0$ . Numerical data in Table 4.3. Lines guide the eye.

## CHAPTER 4. TRANSITION METALS, SELECTED ALKALINE EARTH METALS AND LANTHANIDES

---

the symmetry dictated value could be due to lacking numerical precision other than the Brillouin zone integration mesh and the 3D-grid, because the position of the minimum is stable with respect to an increase of these two parameters. Among the elements studied in this thesis, it is rather an exceptional case, that both minima of  $E(a)$  are at cubic structures. Two minima at cubic structures were, however, found for the alkali metals Li, K, and Rb [206].

The LDA results of Ref. 131 for Sr agree very well with our findings (Table 4.3). This is different to results of GGA calculations [140], which found two energetically almost degenerate stationary points located at the BCC structure and at  $c/a = 0.71$ . There are no published data on non-volume conserving Bain paths employing LDA for Ca and Ba to the best of our knowledge. Total energy calculations for Ca based on PBE96 reported a maximum at the BCC structure and a minimum with  $c/a < 1$ , Ref. 140, contradictory to our results (minimum at BCC structure, Table 4.3). However, there is an overall agreement between our findings and the PBE96 results of Ref. 140 for Ba. The EBP of Ba exhibits a small energy difference between the minimum coinciding with the FCC structure and the adjacent maximum. In order to clearly determine this energy difference, we used a denser sampling mesh for the numerical integrals (3D-grid). This will be more elaborately discussed in the next paragraph.

The differences among the LDA results, as reported in Ref. 131 and this work, and the GGA results from Ref. 140 can likely be traced back to the XC functional, particularly for Sr, for which different XC functionals gave different GSs (cf. discussion above).

The overbinding effect of PW92 is very pronounced for Ca, Sr, and Ba. The calculated volume per atom in the experimentally determined GS crystal structure is in average 13% smaller than the measured one. We also computed the CVBP of Ca for several volumes in the range between the LDA equilibrium volume ( $\approx 0.87 \cdot V_{\text{EXP}}$ ) and the experimental volume,  $V_{\text{EXP}}$ , see Fig. 4.6. The CVBP at  $0.87 \cdot V_{\text{EXP}}$  resembles the extremum sequence of the EBP, i.e., two minima at cubic structures and a maximum in between. With increasing volume, the extremum sequence of the CVBP alters. At  $0.95 \cdot V_{\text{EXP}}$  and at  $V_{\text{EXP}}$ , BCC occupies the position of the maximum, and the secondary minimum has  $c/a < 1$ . The same sequence of extrema was computed in Ref. 140 within GGA (values from Ref. 140 are listed in Table 4.3).

**Small energy barrier for local minimum of Ba** The energy along the EBP of Ba possesses a local minimum at the FCC structure, which is only  $15 \mu\text{Hartree/atom}$  deeper in energy than the adjacent maximum at  $c/a = 1.33$ . Since the energies of both stationary points are almost indistinguishable in Fig. 4.5b, we present a more detailed picture in Fig. 4.7. We had to use the enhanced 3D-grid in order to compute a clear extremum sequence. With default numerical settings, a maximum - minimum sequence in  $E(c/a)$  is hardly seen ('plateau', Fig. 4.7). We found, that this plateau is stable with respect to a denser Brillouin zone integration mesh ( $48^3$  and  $96^3$   $k$ -points were checked, data are not shown). The  $15 \mu\text{Hartree/atom}$  high energy barrier, as obtained with the enhanced 3D-grid, is not affected by an increase of the  $k$ -points. Note that the enhanced 3D-grid shifts the energies in the plotted range upwards by approximately  $0.06 \text{ mHartree/atom}$ . Reference 140 found no evidence of a sec-

#### 4.5. EPITAXIAL BAIN PATH OF TRANSITION METALS, SELECTED ALKALINE EARTH METALS AND LANTHANIDES

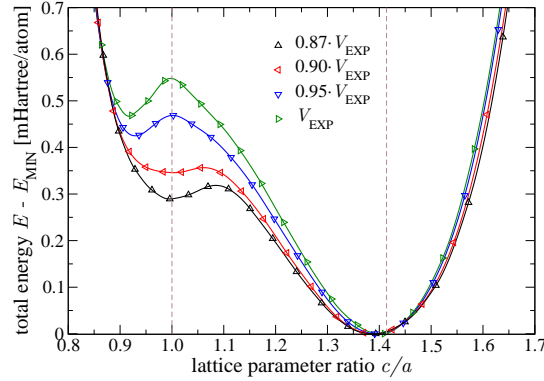


Figure 4.6: Total energy along the CVBP for **Ca** for various volumes as stated in the legend.  $V_{\text{EXP}}$  is the experimentally determined volume of FCC Ca. The value  $0.87 \cdot V_{\text{EXP}}$  is approximately the PW92 equilibrium volume. The total energy is given with respect to the lowest energy value for each curve,  $E_{\text{MIN}}$ . The BCC state changes from being a maximum to being a minimum of the curve with decreasing volume. The global minimum of all curves is unchanged, but does not coincide with  $c/a = \sqrt{2}$ . The position of the third stationary point relative to BCC is determined by the type of stationary point that BCC takes, because the existence of a stationary point at BCC is symmetry dictated. Solid lines are spline interpolation to the data (symbols) and guide the eye.

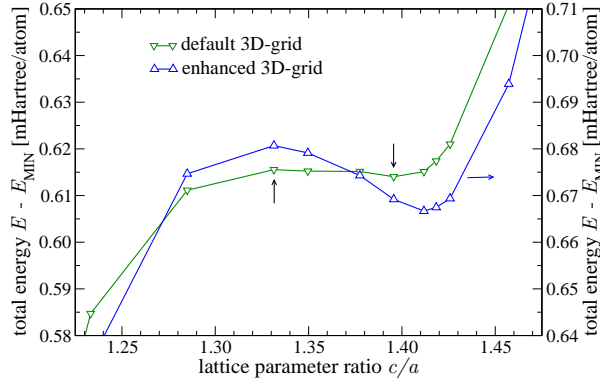


Figure 4.7: Enlarged picture of the plateau-like region from Fig. 4.5b for **Ba** with  $24^3$   $k$ -points with default (*left hand ordinate*) and enhanced 3D-grid (*right hand ordinate*). The scaling of both ordinates is identical, the right hand one was shifted by 0.06 mHartree/atom. The position of the extrema of the curve with default 3D-grid is indicated by black vertical arrows. Lines guide the eye.

ond minimum at  $c/a = \sqrt{2}$ . The (possible) local minimum and the adjacent maximum were reported to be degenerate in total energy.

#### 4.5.4 Group 3 elements: Sc, Y, La, and Lu

The elements Sc, Y, La, and Lu exist at RTP and below in hexagonal closed packed structures. La is DHCP (ABAC stacking), the other three elements are HCP (AB stacking). A high temperature BCC phase and a high pressure FCC phase are known for Sc and Y, respectively. The phase diagram of La features both structures at elevated temperatures [43, 256]. There are no cubic or tetragonal phases verified for Lu, but a phase transition to FCC is predicted to occur under pressure at approximately 100 GPa [144]. The atomic electron configuration both of lanthanum and of lutetium is  $5d^16s^2$ . The difference between both elements is the empty and full  $4f$ -shell for La and Lu, respectively. By arguments of simple canonical band theory, Duthie and Pettifor, and Skriver showed that the  $d$ -occupation number is the decisive parameter that controls the crystal structures of the lanthanides [46, 204]. Skriver substantiated this picture by LMTO calculations including hybridisation. Reference 204 also found the  $d$ -occupation number for Lu to be slightly smaller than for La, as calculated for the experimentally observed equilibrium volume and structure.

#### **Instability of the BCC structure of La and implications for the EBP**

We discuss below the instability of the BCC structure of La with respect to a small variation of the out-of-plane lattice parameter  $c$ . This instability effectively causes the EBP, and all quantities plotted along the EBP as function of  $c/a$  to be discontinuous. In case of La, one part of the EBP has  $c/a < 1$ , the other part has  $c/a > 1$ . This discussion holds general meaning.

The theoretical equilibrium lattice constant of BCC La is  $a_{\text{BCC}} = 4.051 \text{ \AA}$  (determined in  $Im\bar{3}m$  symmetry). The elastic constant  $c_{xxxx} = c_{zzzz} \propto \partial^2 E / \partial c^2$  at  $a_{\text{BCC}}$  is smaller than zero (see Table A.2 on Page 141), i.e., a small deformation of the cubic lattice into a tetragonal lattice lowers the total energy. (Only one cubic axis is involved in the deformation.) Hence,  $E(a = a_{\text{BCC}}, c = a_{\text{BCC}})$  is a (local) maximum of  $E(a_{\text{BCC}}, c)$  over all  $c$ , and the point  $(a_{\text{BCC}}, a_{\text{BCC}})$  in the tetragonal phase space does not belong to the EBP according to the Definition (3.7) on Page 13.

We sketch with the help of Fig. 4.8, how the EBP is modified by the unstable BCC structure of La. Since BCC La is not a singular case among the elements studied in this thesis, we discuss the effect more generally. Note that the curves  $E(c)$  in Fig. 4.8 (top row) represent cuts through  $E(a, c)$  for constant  $a$  from Fig. 3.6 on Page 19.

In what follows,  $(a', c')$  be an unstable point in the tetragonal phase space, i.e.  $c_{zzzz}|_{c'} < 0$ . Hence  $E(c)$  is maximal at  $c'$ , assuming  $a'$  is fixed, i.e., any small change of the lattice parameter  $c$  away from  $c'$  will result in a lowering of the energy. The decrease of the total energy by a variation of  $c$  is certainly counteracted by repulsive contributions to the total energy. Hence the overall decrease of the total energy with respect to  $c$  is limited. A double well in  $E(c)$  occurs, see the illustration in the middle figure in the top row in Fig. 4.8 for an illustration. The double well at  $a = a'$  has three stationary points (one is at  $c = c'$ ). Both minima of the double well need not be of equal depth (neither need the curve be symmetric at all), since a deformation related to a lattice expansion may have a different effect on the total energy than a lattice contraction. For simplicity of the discussion, we assume a symmetric energy curve  $E(c)$  exactly

#### 4.5. EPITAXIAL BAIN PATH OF TRANSITION METALS, SELECTED ALKALINE EARTH METALS AND LANTHANIDES

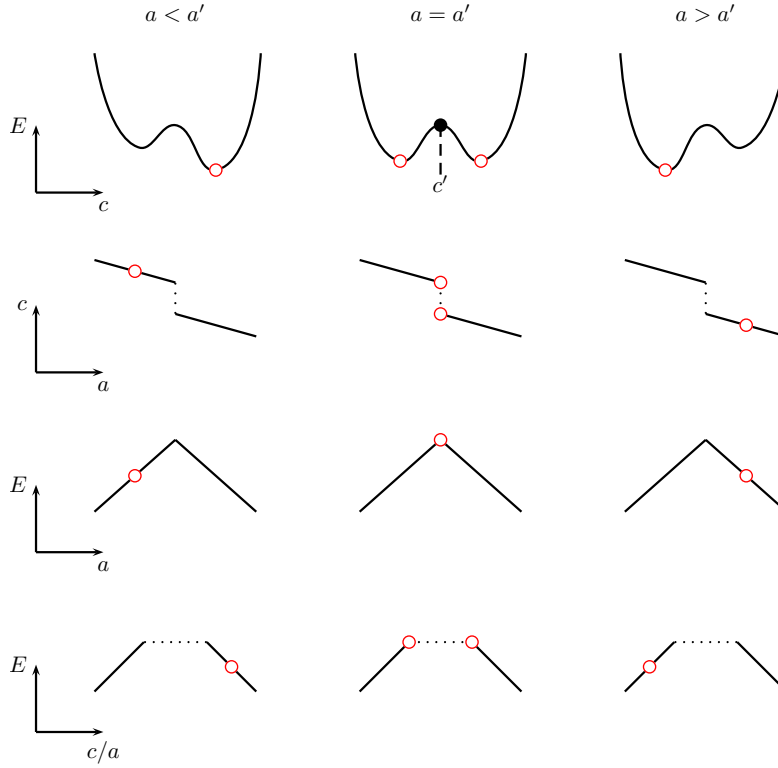


Figure 4.8: On the general occurrence of a double well in  $E(c)$  and its effect on the EBP. For  $a = a'$  (middle column, top row),  $E(c)$  at  $c'$  (black solid dot) is unstable towards a small change of  $c$ . The minimum positions of  $E(c)$  (red open dots) are assumed equally deep, hence both coordinates fulfil the minimum condition in Eq. (3.7) and are recorded for the EBP. The three subsequent figures in the middle column sketch how both minima show up in typical diagrams associated with the EBP:  $c(a)$  (second row),  $E(a)$  (third row) and  $E(c/a)$  (last row). Since both minima of  $E(c)$  have distinct  $c$ -coordinates, all quantities plotted along the EBP as function of  $c$  or  $c/a$  exhibit a gap (dotted lines) across the  $c$  or  $c/a$  values that are located in between both minima. If  $a$  is smaller (larger) than  $a'$ , only a single deepest minimum occurs, with has a minimum  $c$ -coordinate,  $\tilde{c}$ , larger (smaller) than  $c'$ . The position of the minimum  $\tilde{c}$  in the associated diagrams is illustrated in the leftmost (rightmost) column.

at  $a = a'$ . Moreover, there are double wells in  $E(c)$  for values of the lattice parameter  $a \neq a'$  with stationary points at slightly different positions (top row in Fig. 4.8). Assuming that  $c(a)$  is monotonically decreasing along the EBP for all considered metals, we note that for  $a < a'$  ( $a > a'$ ), the minimum of  $E(c)$  over all  $c$ , referred to as  $\tilde{c}$ , is larger (smaller) than  $c'$ .

By construction of the EBP, the minimum of  $E(c)$  over all  $c$  for each  $a$  is selected (cf. Eq. (3.7)). It is evident from Fig. 4.8, that the  $c$ -coordinate of the deeper minimum as function of  $a$  abruptly 'jumps' from one to the other minimum at the point, at which both valleys are equally deep. In the discussion

Table 4.4: Overview of calculated GS properties and numerical data of stationary points for the elements **Sc**, **Y**, **La**, and **Lu** in comparison to computations and experiments from the literature, if available. General remarks on this Table are given in Sec. 4.5.1.

element		this work				literature							
		structure			$E - E_0$ [mHa]	theory			Ref.	experiment			
		type	$a$ [Å]	$c/a$		structure		Ref.		structure			
					$a$ [Å]	$c/a$	[mHa]		setup [ML]	$a$ [Å]	$c/a$	Ref.	
<b>Sc</b>	GS	HCP	3.233	1.545	0	3.209	1.560	0	[201] <sup><math>\delta g</math></sup>	bulk	3.308	1.593	[237]
	SP	MIN	3.17	1.40	1.30								
		MAX	3.57	1.00	4.32								
		MIN	3.70	0.90	4.27								
<b>Y</b>	GS	HCP	3.547	1.557	0	3.528	1.567	0	[165] <sup><math>\beta d</math></sup>	bulk	3.647	1.576	[237]
	SP	MIN	3.47	1.41	0.38								
		MAX	3.92	1.00	4.71								
		MIN	4.07	0.88	4.17								
<b>La</b>	GS	DHCP	3.589	3.198	0	3.620	3.227	0	[159] <sup><math>\delta f \dagger</math></sup>	bulk	3.770	3.220	[237]
	SP	MIN	3.57	1.41	1.52								
		MAX	4.04	0.90, 1.11	6.57								
		MIN	4.28	0.83	4.72								
<b>Lu</b>	GS	HCP	3.377	1.548	0					bulk	3.503	1.585	[237]
	SP	MIN	3.30	1.41	0.69								
		MAX	3.73	1.00	5.60								
		MIN	3.88	0.87	5.14								

legend			
$\alpha$	L(S)DA [174] (PW92)	$abc$	FP-LAPW [16] ( <sup><math>a</math></sup> WIEN2K, <sup><math>b</math></sup> WIEN97, <sup><math>c</math></sup> WIEN95)
$\beta$	L(S)DA [30, 239]	$d$	FP-LMTO [141]
$\gamma$	GGA [172] (PBE96)	$e$	PAW [110] (VASP)
$\delta$	L(S)DA [76] (HL71)	$f$	FP-LAPW [249]
$\dagger$	scalar-relativistic	$g$	APW [137]



#### 4.5. EPITAXIAL BAIN PATH OF TRANSITION METALS, SELECTED ALKALINE EARTH METALS AND LANTHANIDES

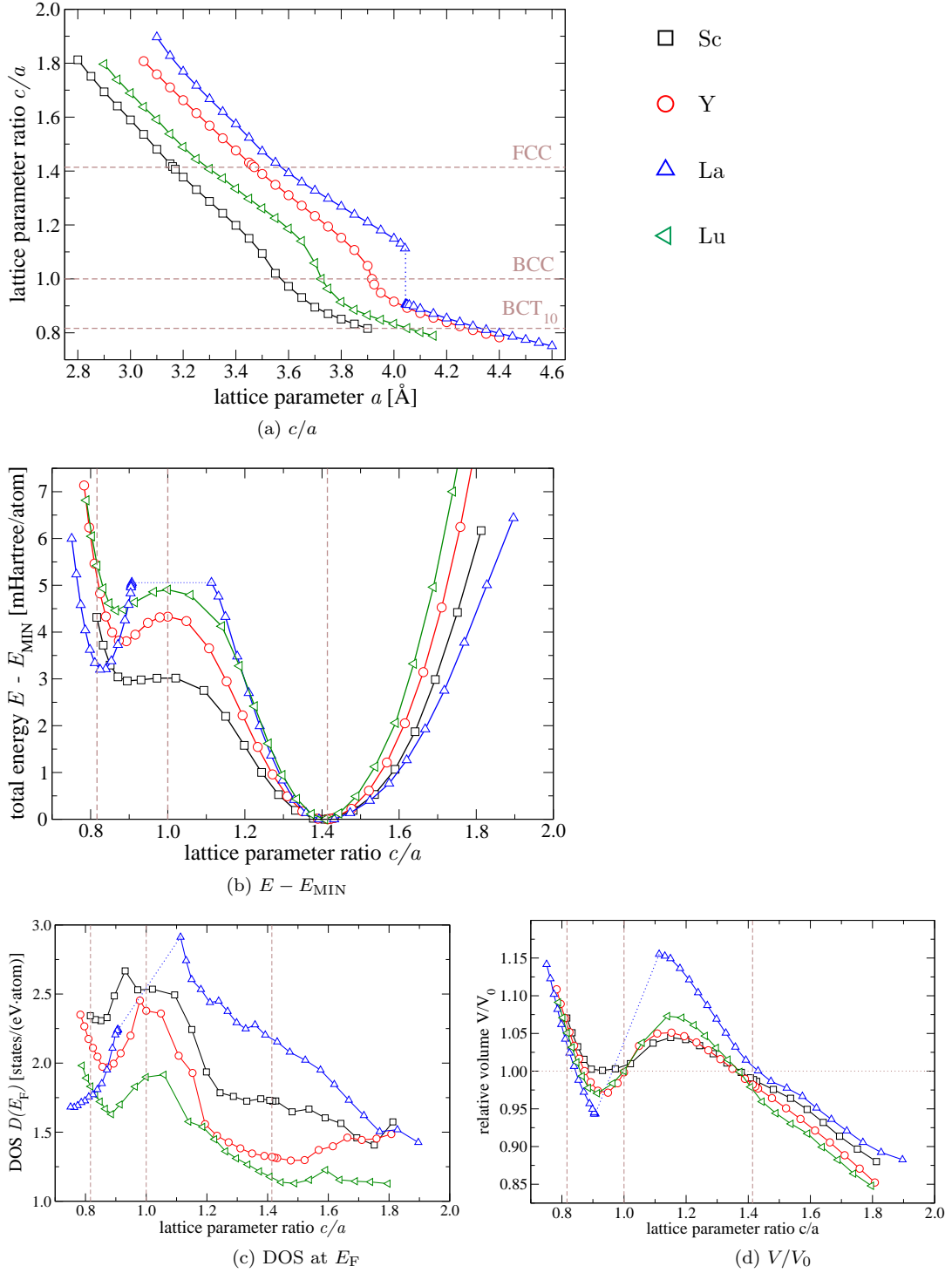


Figure 4.9: For the EBPs of **Sc**, **Y**, **La** and **Lu**: (a)  $c/a$ , (b)  $E - E_{\text{MIN}}$ , (c)  $D(E_F)$ , and (d)  $V/V_0$ . Numerical data in Table 4.4. Lines guide the eye.

## CHAPTER 4. TRANSITION METALS, SELECTED ALKALINE EARTH METALS AND LANTHANIDES

given here, this happens at  $a = a'$ . As a consequence of the fact, that we only record the position of the minimum of  $E(c)$ , the EBP and all related curves will either feature a kink or a gap (piece-wise graph). Representative quantities are  $c(a)$  (or  $c(a)/a$ ),  $E(a)$ , and  $E(c/a)$ , whose typical curve progression are sketched in the lower three rows in Fig. 4.8.

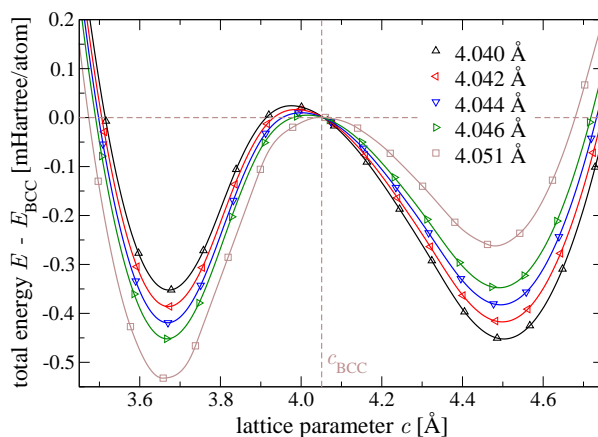


Figure 4.10: Double wells in the total energy as function of the lattice parameter  $c$ ,  $E(c)$ , for a set of in-plane lattice parameters  $a$  close to  $a_{\text{BCC}}$  of **La**. The values of  $a$  are stated in the legend. Total energies are given with respect to  $E_{\text{BCC}}$ . A horizontal dashed line indicates the zero-level. The lattice parameter of BCC **La** is  $a_{\text{BCC}} = c_{\text{BCC}} = 4.051 \text{ \AA}$ . For  $a \leq 4.042 \text{ \AA}$ , the deeper minimum is located on the right hand side of the vertical dashed line, which indicates  $c_{\text{BCC}}$ . For  $a \geq 4.044 \text{ \AA}$ , the deeper minimum is located on the left hand side of this line. The minimum's  $c$ -coordinate changes abruptly between  $a = 4.042 \text{ \AA}$  and  $a = 4.044 \text{ \AA}$ . At  $a_{\text{BCC}}$ , the position of the maximum of  $E(c)$  must coincide with the intersection point of both dashed lines, but the curve need not be symmetric (brown solid line). Solid lines are spline interpolation to the data (symbols) and guide the eye.  $D(E_{\text{F}})$  as function of  $c$  for three selected curves is depicted in Fig. 4.11.

As previously stated, we computed  $c_{zzzz} < 0$  for the BCC structure of **La** ( $a_{\text{BCC}} = c_{\text{BCC}} = 4.051 \text{ \AA}$ ). For a set of parameters  $a$  close to  $a_{\text{BCC}}$ , we plotted  $E(c) - E_{\text{BCC}}$  in Fig. 4.10.  $E_{\text{BCC}} = E(c_{\text{BCC}})$  is the total energy of BCC **La**, as determined in  $Im\bar{3}m$  symmetry. The results of our calculations clearly show a double well structure in  $E(c)$  and the transition from the minimum with  $\tilde{c} > c_{\text{BCC}}$  to the minimum with  $\tilde{c} < c_{\text{BCC}}$ , when  $a$  is increased from  $4.040 \text{ \AA}$  to  $4.046 \text{ \AA}$ . The transition point between both minima is thus not at exactly  $a_{\text{BCC}}$ .

Our calculations for further elements suggest, that the occurrence of such double wells in  $E(c)$  is rather rare, but it is not a singular case. We found them indeed for **La**, **V**, **Nb**, **Fe**, **Ru**, **Os**, and **Ir**. Our calculations also predict, that such double wells only occur in small ranges of  $a$  around  $a'$ . The energetically higher-lying minimum rapidly vanishes in a hump-like structure. This effect can be best seen using the example of **Ir**, see Fig. 4.31 on Page 90.

## 4.5. EPITAXIAL BAIN PATH OF TRANSITION METALS, SELECTED ALKALINE EARTH METALS AND LANTHANIDES

**Possible reason for the BCC La instability** The DOS at  $E_F$  of BCC La amounts to  $4.1/(\text{eV} \cdot \text{atom})$  and is due to a singularity in the electronic DOS (not shown). This value is considerable higher than any other value of BCC La along the EBP within the given limits of  $c/a$ , see Fig. 4.9c. For  $a_{\text{BCC}}$  and two lattice parameters  $a$  close to  $a_{\text{BCC}}$ , we plot the DOS at the Fermi energy as function of  $c$  in Fig. 4.11. With the help of this figure, we can analyse  $D(E_F)$  for three double wells from Fig. 4.10. We notice at first, that the three DOS curves are very similar to each other. We therefore concentrate on the curve belonging to  $a_{\text{BCC}} = 4.051 \text{ \AA}$ .  $D(E_F)$  as function of  $c$  peaks in the vicinity of  $c_{\text{BCC}}$  (the same  $c$  corresponds to the position of the maxima of  $E(c)$  in Fig. 4.10).  $D(E_F)$  is considerable smaller for both minima of  $E(c)$ , i.e., a distortion from BCC to BCT (increase or decrease of  $c$ ,  $a$  fixed) significantly reduces the DOS at the Fermi energy. Simultaneously to a reduction of  $D(E_F)$ , the total energy decreases in response to this tetragonal deformation until  $E(c)$  reaches a minimum value (Fig. 4.10). Thus, the high value of  $D(E_F)$  helps to destabilise the BCC structure of La [100]. A similar mechanism was suggested to occur in BCC Co [124].

A possible FM state of BCC La was tested for. We found, that there is a metamagnetic FM state of BCC La with a total moment of  $0.16 \mu_B/\text{atom}$ , but the FM state is not more stable than the NM state.

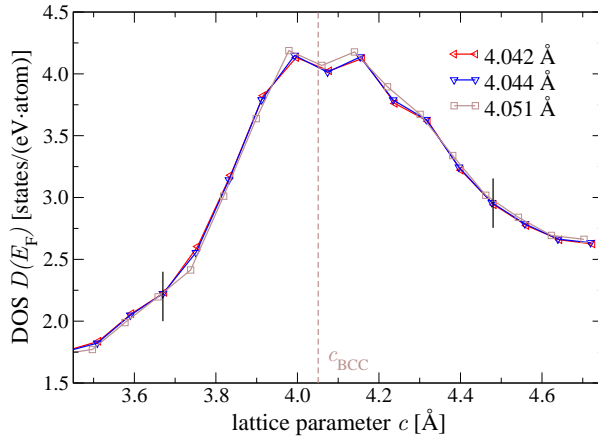


Figure 4.11: DOS at the Fermi energy,  $D(E_F)$ , as function of the lattice parameter  $c$  for  $a_{\text{BCC}} = c_{\text{BCC}} = 4.051 \text{ \AA}$  and two lattice parameters  $a$  close to  $a_{\text{BCC}}$  of **La**. The values of  $a$  are stated in the legend. The vertical dashed line indicates  $c_{\text{BCC}}$ . Two solid black lines indicate the DOS of the two minima of  $E(c)$  for  $a = 4.044 \text{ \AA}$ . The positions of both minima are approximately the same for the other two curves, see Fig. 4.10. Solid lines to the data guide the eye.

**Discussion of EBPs** The EBPs of the four elements from this group feature strong similarities. Their complete data are presented in Table 4.4 and Fig. 4.9. The global minimum at the FCC structure and a second, local minimum with  $c/a < 1$  is common to all four EBPs. The position and the energy barrier of the BCT minimum varies with the element. The  $c/a$ -ratio of the second minimum

## CHAPTER 4. TRANSITION METALS, SELECTED ALKALINE EARTH METALS AND LANTHANIDES

---

of  $E(a)$  of La, 0.83, is very close to the ratio of  $\text{BCT}_{10}$ . The maximum of  $E(a)$  is at the BCC structure for Sc, Y and Lu.

There are no published data on any non-volume conserving Bain path for one of the considered elements to the best of our knowledge. In agreement with our findings, Refs. 159 reported  $E_{\text{FCC}} - E_{\text{BCC}} = 5 \text{ mHartree/atom}$  for La (scalar-relativistic, FP-LAPW [249], LDA by Hedin and Lundqvist [76]). We computed  $5.49 \text{ mHartree/atom}$  for the same energy difference in the full-relativistic mode. Note that this particular energy difference cannot be extracted from the EBP (because BCC La is not on the EBP).

### 4.5.5 Group 4 elements: Ti, Zr, and Hf

The TM elements Ti, Zr, and Hf occur at RTP and below in the HCP configuration ( $\alpha$ -phase), and all three elements transform to BCC at higher temperatures and at RP ( $\beta$ -phase). The  $\beta$ -phase is denser than the  $\alpha$ -phase [43, 256]. High pressure at RT is an alternative route to induce a phase transition from HCP to BCC in Zr and Hf (via a simple hexagonal structure). A new route of fabricating BCC Zr was reported very recently by Ref. 176: simultaneously applied pressure and torsion induces a HCP to BCC shear transformation at RT resulting in stable BCC Zr at ambient conditions.

**Discussion of EBPs** The EBPs of Ti and Hf have many common features, while Zr constitutes an exception, see Table 4.7 and Fig. 4.12 for the complete data. The similarities of Ti and Hf are, that the global energy minimum is exactly at the FCC structure for Hf, and with  $c/a = 1.39$  close to the FCC structure for Ti. The second minimum possesses an axial ratio slightly larger than the one of  $\text{BCT}_{10}$  ( $\approx 0.816$ ). The total energy along the EBP of Hf scales approximately by a factor of three with the total energies of Ti. The BCC configurations coincide with the maximum of  $E(a)$  for both elements. Zirconium constitutes an exception, because  $E(a)$  exhibits three minima. The global minimum at  $c/a = 0.82$  is  $0.03 \text{ mHartree/atom}$  deeper in energy than the minimum at  $c/a = 1.40$ . The third minimum of  $E(a)$  is at  $c/a = 1$  (BCC).

There is good agreement between this work and Refs. 131, 132 about the EBP of Ti. Solely, the position of the maximum at  $c/a = 1.05$ , as reported by the latter references, disagrees with our calculations. Earlier, Ref. 93 published an EBP of Zr. The reported coordinates of stationary points (and thus the sequence of extrema) along the EBP are consistent with our findings (complete data in Table 4.7). There is, however, a striking disagreement on the energy differences between stationary points of  $E(a)$  and  $E_0$ . The most important discrepancy comes from the fact, that  $E(c/a = 1.40)$  is lower than  $E_{\text{BCC}}$  according to our calculations, while Ref. 93 reported the opposite. This discrepancy changes the shape of  $E(c/a)$ :  $E(c/a)$  after Ref. 93 is reminiscent of the solid curve in Fig. 4.3b on Page 38, while the dashed curve in the same figure resembles our  $E(c/a)$ . Other total energy calculations (LDA and GGA) generally underline  $E_{\text{FCC}} < E_{\text{BCC}}$  for Zr, as well as for Ti and Hf [1, 169]. These references thereby support our findings. Note that the PBE96 results of Ref. 93 for Zr are not compared to in this work. The calculated total energy along the EBP exhibits several kinks and humps, whose presence may be doubted. We are not aware of any published non-volume conserving Bain path for hafnium.

#### 4.5. EPITAXIAL BAIN PATH OF TRANSITION METALS, SELECTED ALKALINE EARTH METALS AND LANTHANIDES

Table 4.5:  $d$ -band occupation numbers for the elements **Ti**, **Zr**, and **Hf** in the FCC and the BCC configuration. The number is the gross occupation number in the (first) valence basis state with angular  $d$ -character ( $3d$  for Ti,  $4d$  for Zr,  $5d$  for Hf).

element	$d$ -occupation number	
	FCC	BCC
Ti	2.69	2.66
Zr	2.90	2.89
Hf	2.65	2.65

Table 4.6:  $d$ -band occupation numbers for a 'virtual' element in the FCC and in the BCC structure at the theoretical FCC equilibrium volume of **Zr**. The statement of the occupation numbers is identical to the one in Table 4.5.

charge	$d$ -occupation number	
	FCC	BCC
39.80	2.77	2.74
39.85	2.80	2.77
39.90	2.84	2.81
39.95	2.87	2.84
40.00 (Zr)	2.90	2.89

**EBP of Zr** We intend to gain more insight into the EBP of Zr, in particular the question, why there are three minima in  $E(a)$ . We notice at first, that the  $d$ -valence electron occupation number of Zr is generally higher than the one of Ti and of Hf. We selected the FCC structure and the BCC structure as representative states of the EBP and tabulate their occupation numbers in Table 4.5. The number of electrons in the (first)  $d$ -valence set is almost identical in the FCC state and in the BCC state. In general, the occupation numbers vary along the EBP.

We know from canonical band theory, that there is a crossover from close-packed structures to the BCC structure for a  $d$ -occupation number between two and three (Sec. 4.2). Self-consistent one-electron theory determined this transition point to lie between 2.5 and 3.5 [58, 165, 169, 204]. Evidently, there is a change in sign of  $E_{\text{BCC}} - E_{\text{FCC}}$  as function of the  $d$ -band filling, since this difference is positive for Ti, Zr, and Hf, and negative for V, Nb, and Ta, see also results of Sec. 4.5.6. The absolute value of  $E_{\text{BCC}} - E_{\text{FCC}}$  is significantly larger for V, Nb, and Ta than for Ti, Zr, and Hf. Hence, we can expect a sensible dependence of  $E_{\text{BCC}} - E_{\text{FCC}}$  on the filling of the  $d$ -band for an occupation number between the one of Ti (accordingly Zr and Hf) and the one of V (accordingly Nb and Ta), respectively.

In the following, we study the effect of the  $d$ -band filling on the EBP of Zr.

Table 4.7: Overview of calculated GS properties and numerical data of stationary points for the elements **Ti**, **Zr**, and **Hf** in comparison to computations and experiments from the literature, if available. General remarks on this Table are given in Sec. 4.5.1.

element		this work				literature								
		structure			$E - E_0$ [mHa]	theory			Ref.	experiment				
		type	$a$ [Å]	$c/a$		$a$ [Å]	$c/a$	$E - E_0$ [mHa]		structure				
					setup [ML]				$a$ [Å]	$c/a$		Ref.		
<b>Ti</b>	GS	HCP	2.867	1.596	0	2.839	1.589	0	[165] <sup><math>\beta d</math></sup>	bulk	2.951	1.588		[237]
	SP	MIN	2.85	1.39	1.97	2.84	1.40	$C$	[131, 132] <sup><math>\alpha c</math></sup>	Al{001} $\approx$ 12	2.86	1.495		[101]
		MAX	3.17	1.00	3.14	3.11	1.05	$1.30 + C$	[131, 132] <sup><math>\alpha c</math></sup>					
		MIN	3.33	0.86	2.64	3.34	0.85	$0.80 + C$	[131, 132] <sup><math>\alpha c</math></sup>					
<b>Zr</b>	GS	HCP	3.154	1.616	0	3.151	1.613	0	[165] <sup><math>\beta d</math></sup>	bulk	3.233	1.592		[237]
	SP	MIN	3.14	1.40	1.21	3.12	1.41	$1.33 + C$	[93] <sup><math>\alpha b</math></sup>	W{001} $\approx$ 17	3.17	$1.48 \pm 0.04$		[93]
		MAX	3.32	1.17	1.95	3.24	1.24	$1.55 + C$	[93] <sup><math>\alpha b</math></sup>	W{001} 50	3.17	1.46		[78]
		MIN	3.49	1.00	1.71	3.47	1.00	$0.80 + C$	[93] <sup><math>\alpha b</math></sup>					
		MAX	3.56	0.94	1.72	3.57	0.92	$0.85 + C$	[93] <sup><math>\alpha b</math></sup>					
		MIN	3.74	0.82	1.18	3.73	0.81	$C$	[93] <sup><math>\alpha b</math></sup>					
<b>Hf</b>	GS	HCP	3.119	1.586	0	3.178	1.620	0	[201] <sup><math>\delta f \dagger</math></sup>	bulk	3.198	1.583		[237]
	SP	MIN	3.09	1.41	2.28									
		MAX	3.44	1.00	5.27									
		MIN	3.64	0.85	4.24									

legend

$\alpha$	L(S)DA [174] (PW92)	$abc$	FP-LAPW [16] ( <sup><math>a</math></sup> WIEN2K, <sup><math>b</math></sup> WIEN97, <sup><math>c</math></sup> WIEN95)
$\beta$	L(S)DA [30, 239]	$d$	FP-LMTO [141]
$\gamma$	GGA [172] (PBE96)	$e$	PAW [110] (VASP)
$\delta$	L(S)DA [76] (HL71)	$f$	APW [137]
$\dagger$	scalar-relativistic		

#### 4.5. EPITAXIAL BAIN PATH OF TRANSITION METALS, SELECTED ALKALINE EARTH METALS AND LANTHANIDES

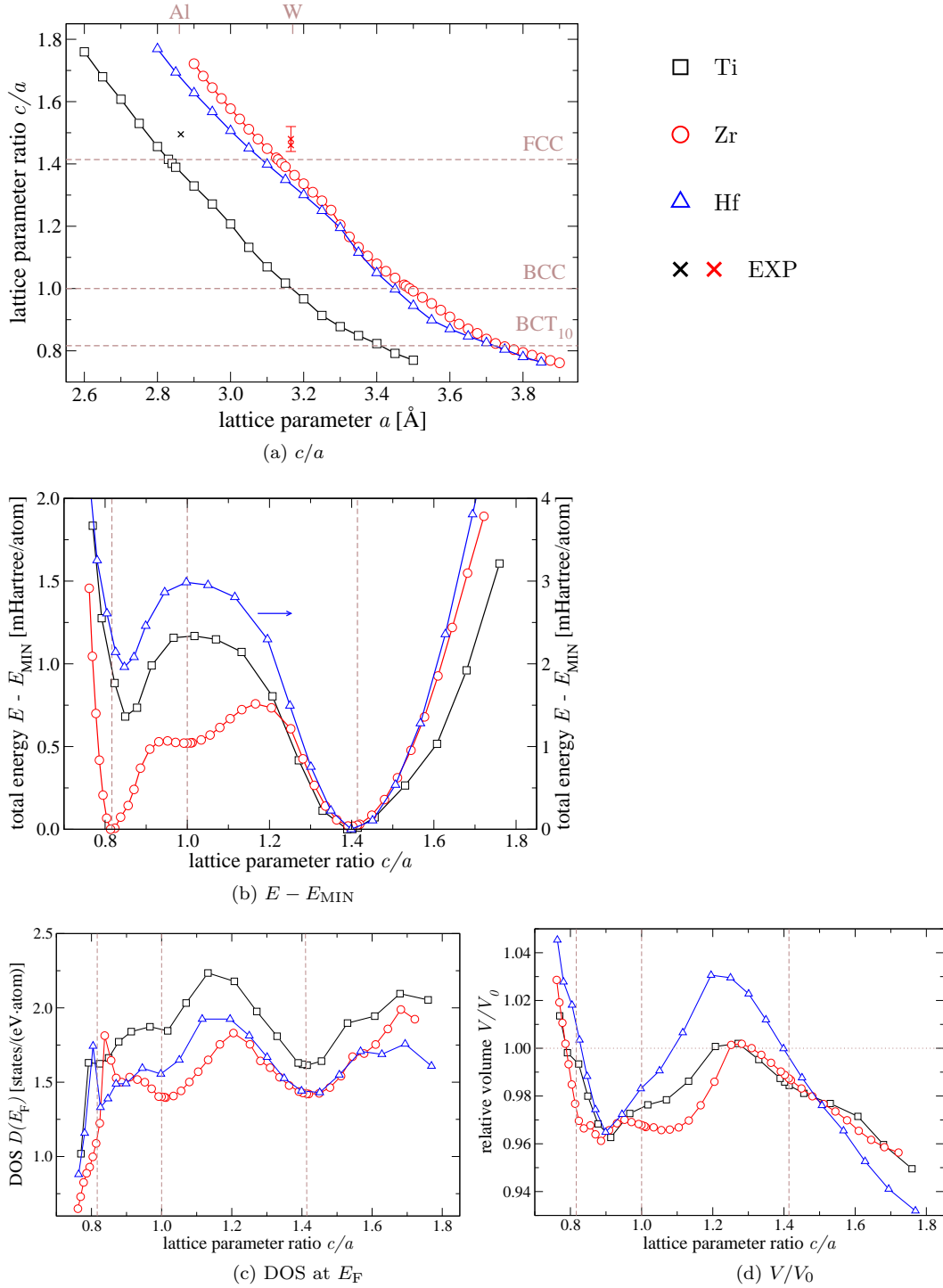


Figure 4.12: For the EBPs of **Ti**, **Zr**, and **Hf**: (a)  $c/a$ , (b)  $E - E_{\text{MIN}}$ , (c)  $D(E_F)$ , and (d)  $V/V_0$ . Numerical data in Table 4.7. Lines guide the eye.

## CHAPTER 4. TRANSITION METALS, SELECTED ALKALINE EARTH METALS AND LANTHANIDES

There are two simple approaches primarily known from alloy theory. The first way to invoke a change in the  $d$ -band filling is to use the rigid-band approximation, i.e., based on an initial self-consistent calculation, the Fermi energy in the obtained band structure and in the DOS is simply shifted in accordance to the electronic charge added or subtracted to the system. An improved approach is the virtual crystal approximation (VCA), see, e.g., Refs. 161, 234. Every atom in the crystal (every potential) is replaced by an 'average' atom (average potential). The charge of each 'average' or 'virtual' atom is a concentration weighted average of the charge of its constituents. Thus, a 'virtual' atom may have non-integer nuclear and electronic charge (charge neutrality is abided by). The crystal is still perfectly ordered. The Kohn-Sham equations are solved self-consistently in the VCA. The VCA for the description of disordered alloys is justified, if the chemical species have nearly identical properties [234].

We performed VCA calculations for Zr (40 electrons/atom) and a 'virtual' element with slightly smaller electron count. By doing so, we intend to effectively reduce the  $d$ -band filling and investigate its effect in the EBP. We imply, that the  $d$ -band filling mainly controls not only structural energy differences as mentioned earlier in this thesis, but also the alteration of the EBP. In order to reduce the effort, we calculated the CVBP at the theoretical FCC equilibrium volume,  $V_{\text{FCC}}$ , instead of the EBP. The volume along the EBP in the range between the minima of  $E(a)$  varies only by few percent (Fig. 4.12d), so that this CVBP is a fairly good approximation to the EBP of Zr. The energy along the CVBP at  $V_{\text{FCC}}$  in Fig. 4.13b (red line) indeed resembles remarkably well  $E(a)$  in Fig. 4.12b.

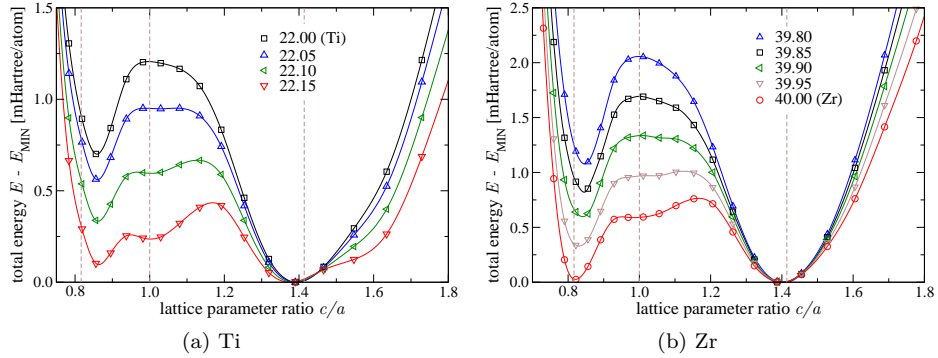


Figure 4.13: The CVBP of (a) **Ti** and of (b) **Zr** at the respective theoretical FCC equilibrium volume, and their alteration in response to a charge variation studied by means of the VCA. The virtual charge is stated in the legend. The energy zero is set to the minimum total energy of each individual curve,  $E_{\text{MIN}}$ . Lines are spline interpolation to the data (symbols) and guide the eye.

On a lowering of the charge, the energy along the CVBP of Zr transforms into a curve reminiscent on  $E(a)$  of Ti and of Hf, if one compares Figs. 4.12b and 4.13b. The resemblance is best for a virtual charge of 39.85, because the corresponding curve exhibits three stationary points, the BCC structure coincides with the position of the maximum, and the position of the BCT minimum with  $c/a < 1$  shifts to a slightly larger ratio, thereby approaching the ratio of the BCT minimum of Ti and Hf. Additionally, the energy difference between  $E_{\text{BCC}}$



## 4.5. EPITAXIAL BAIN PATH OF TRANSITION METALS, SELECTED ALKALINE EARTH METALS AND LANTHANIDES

---

and the minimum at  $c/a = 1.40$ , and the difference between the second BCT minimum with  $c/a < 1$  and the minimum at  $c/a = 1.40$  increase considerably. We also calculated the CVBP of Ti at the theoretical FCC equilibrium volume of Ti. The qualitative best agreement between the CVBP of Ti (black curve in Fig. 4.13a) and the CVBP of Zr is again for 39.85 electrons.

How does the reduction of the virtual electronic charge affect the  $d$ -band filling? As expected, the  $d$ -band occupation number decreases in response to a lowering of the amount of charge, see Table 4.6. If we reduce the number of electrons from 40.00 to 39.85, the  $4d$ -occupation number diminished by approximately 0.1. In other words, the CVBP for 39.85 electrons with approximately 2.8 electrons in the  $4d$ -band resembles qualitatively best the CVBP for Ti, which possesses approximately 2.7 electrons in the  $3d$ -band. There is a difference between the reduced virtual electronic charge and the number of electrons that are removed from the  $4d$ -band, because a fraction of the total number of electrons are also removed from other valence states, mainly the free-electron like bands, which contribute to the DOS in the region of  $E_F$ .

In the above discussion of the CVBP, we neglected the effect of volume relaxation on the equilibrium volume of a virtual element. The theoretical FCC equilibrium volume for a 'virtual element' with 39.85 electrons is almost 4% larger than for Zr. This is of the same order as the variation of the volume between the two minima of the EBP of Zr (Fig. 4.12d). We checked whether the 4% larger volume has an important effect on the shape of the CVBP curve with 39.85 electrons from Fig. 4.13b, which may spoil the previously drawn conclusions. We found that the VCA CVBP curves are qualitatively identical for both volumes. The extended volume increases the energy difference between the maximum at the BCC structure and  $E_{\text{MIN}}$ , and the energy difference between the second minimum at the BCT structure and  $E_{\text{MIN}}$ . Simultaneously, the number of electrons in the  $4d$ -band reduces by 0.03 for FCC as well as for BCC.

If the energy along the CVBP of Zr can be transformed into a shape approximately identical to the energy along the CVBP of Ti and Hf by a reduction of the  $d$ -band filling, the inverse approach to Ti or to Hf should work as well. We calculated CVBPs for Ti (22 electrons/atom) up to a charge of 22.15 electrons. Indeed, there is a conversion of the CVBP curve of Ti into a shape that is reminiscent of the EBP curve and the CVBP curve of Zr (Fig. 4.13a), although the agreement is less pronounced as the VCA curves generated from Zr.

### 4.5.6 Group 5 elements: V, Nb, and Ta

The experimental phase diagram of the refractory metals V, Nb, and Ta is simple. The only known solid phase is BCC, which is stable to highest applied pressures in shock experiments [43, 256]. In accordance, calculations found a large energy difference between BCC to closed packed structures [58, 165, 169, 204]. Donohue, Chopra, and Nnolim *et al.* alluded to two other forms of tantalum (complex tetragonal and FCC) and an FCC modification of V and Nb as seen in sputtering experiments [35, 43, 160]. These structures were most likely impurity stabilised.

Table 4.8: Overview of calculated GS properties and numerical data of stationary points for the elements **V**, **Nb**, and **Ta** in comparison to computations and experiments from the literature, if available. General remarks on this Table are given in Sec. 4.5.1.

element	this work				literature								
	structure			$E - E_0$	theory			Ref.	experiment			Ref.	
	type	$a$ [Å]	$c/a$	[mHa]	$a$ [Å]	$c/a$	[mHa]		structure				
								setup [ML]	$a$ [Å]	$c/a$			
<b>V</b>	GS	BCC	2.929	–	0	2.932	–	0	[226] <sup>aa</sup>	bulk	3.030	–	[237]
	SP	MIN	2.40	1.84	4.07	2.41	1.83	3.7	[4] <sup>ac</sup>				
						2.43	1.78	5.00	[131, 225] <sup>ac</sup>				
							1.799	3.67	[140] <sup>γa</sup>				
						2.47	1.80	3.45	[160] <sup>γb</sup>				
		MAX	2.64	1.27, 1.52	11.68	2.65	$\sqrt{2}$	10.7	[4] <sup>ac</sup>				
						2.64	1.43	10.4	[131] <sup>ac</sup>				
							$\sqrt{2}$	9.17	[140] <sup>γa</sup>				
	MIN	2.93	1.00	0	2.93	1	0	[4] <sup>ac</sup>					
					2.93	1.00	0	[131] <sup>ac</sup>					
					1	0	[140] <sup>γa</sup>						
				3.00	1	0	[160] <sup>γb</sup>						
<b>Nb</b>	GS	BCC	3.258	–	0	3.250	–	0	[226] <sup>aa</sup>	bulk	3.306	–	[237]
	SP	MIN	2.70	1.79	6.72		1.787	5.12	[140] <sup>γa</sup>				
						2.74	1.80	5.37	[160] <sup>γb</sup>				
		MAX	2.93	1.27, 1.50	14.55		$\sqrt{2}$	12.09	[140] <sup>γa</sup>				
							$\sqrt{2}$	14.0	[160] <sup>γb</sup>				
MIN	3.26	1.00	0		1	0	[140] <sup>γa</sup>						
				3.31	1	0	[160] <sup>γb</sup>						
<b>Ta</b>	GS	BCC	3.260	–	0	3.260	–	0	[226] <sup>aa</sup>	bulk	3.302	–	[237]
	SP	MIN	2.75	1.71	7.22	2.79	1.72	5.95	[160] <sup>γb†</sup>				
		MAX	2.93	1.41	11.09		$\sqrt{2}$	7.5	[160] <sup>γb†</sup>				
		MIN	3.26	1.00	0	3.32	1	0	[160] <sup>γb†</sup>				

legend

$\alpha$	L(S)DA [174] (PW92)	<sup>abc</sup>	FP-LAPW [16] ( <sup>a</sup> WIEN2K, <sup>b</sup> WIEN97, <sup>c</sup> WIEN95)
$\beta$	L(S)DA [30, 239]	<sup>d</sup>	FP-LMTO [141]
$\gamma$	GGA [172] (PBE96)	<sup>e</sup>	PAW [110] (VASP)
†	scalar-relativistic		

#### 4.5. EPITAXIAL BAIN PATH OF TRANSITION METALS, SELECTED ALKALINE EARTH METALS AND LANTHANIDES

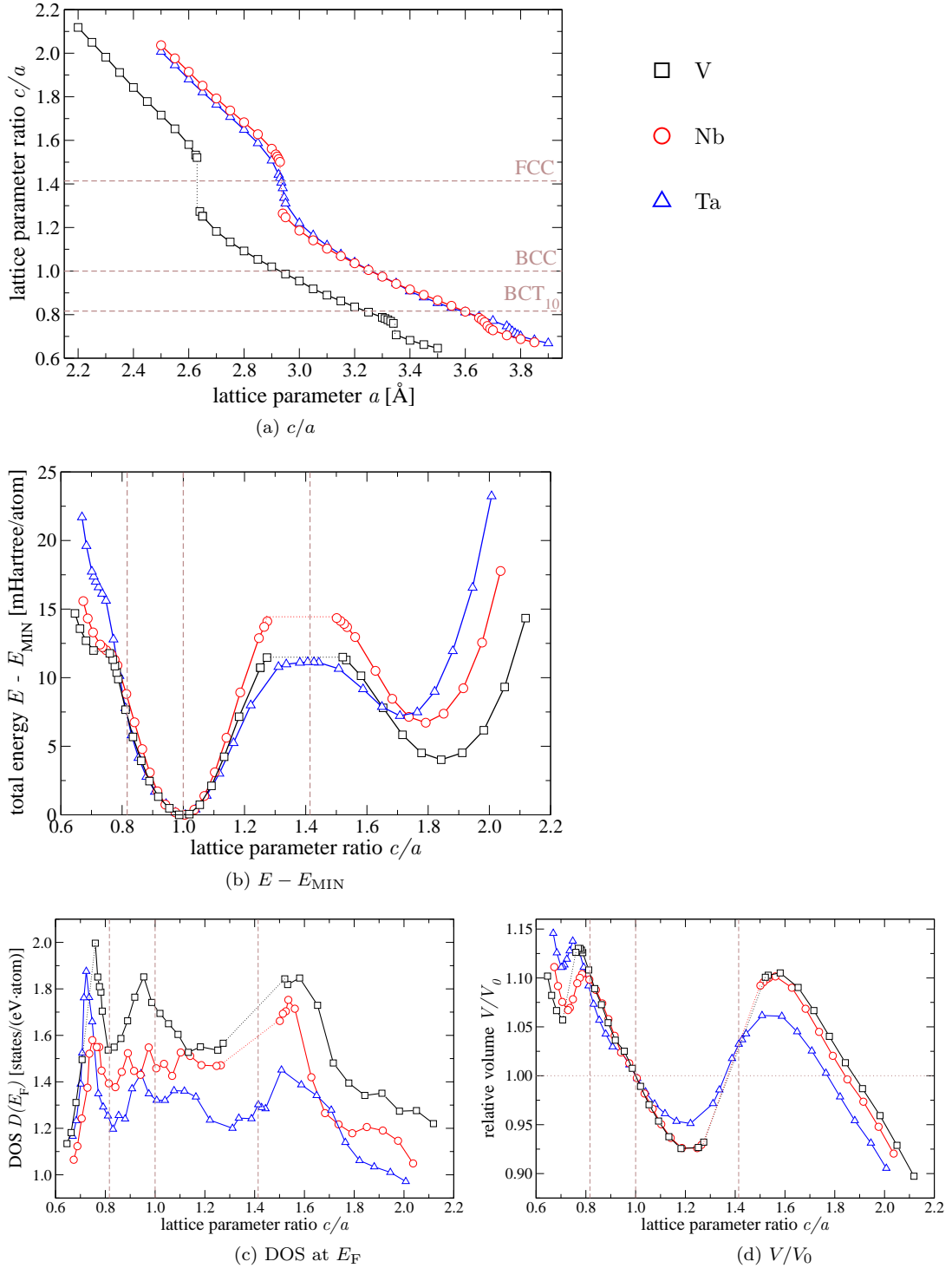


Figure 4.14: For the EBPs of **V**, **Nb**, and **Ta**: (a)  $c/a$ , (b)  $E - E_{\text{MIN}}$ , (c)  $D(E_F)$ , and (d)  $V/V_0$ . Numerical data in Table 4.8. Lines guide the eye.

## CHAPTER 4. TRANSITION METALS, SELECTED ALKALINE EARTH METALS AND LANTHANIDES

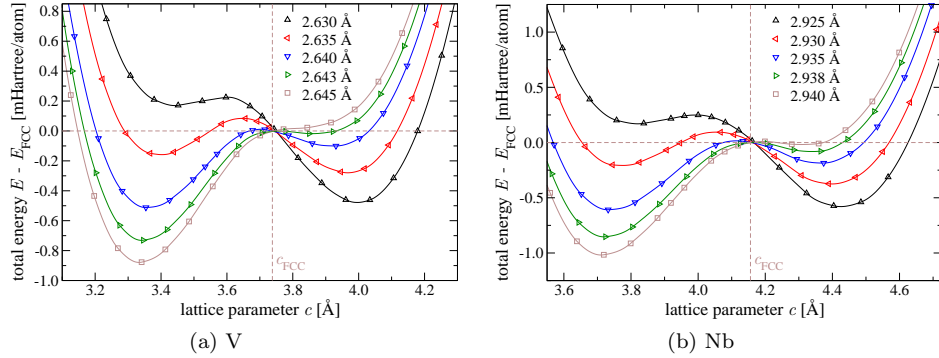


Figure 4.15: Double wells in the total energy as function of the lattice parameter  $c$ ,  $E(c)$ , for a set of in-plane lattice parameters  $a$  close to  $a_{\text{FCC}}$  for (a) **V** and (b) **Nb**. The values of  $a$  are stated in the legend. Total energies are given with respect to  $E_{\text{FCC}}$ . A horizontal dashed line indicates the zero-level. The lattice parameters of FCC V and FCC Nb are  $c_{\text{FCC}} = 3.738$  Å ( $a_{\text{FCC}} = 2.643$  Å) and  $c_{\text{FCC}} = 4.156$  Å ( $a_{\text{FCC}} = 2.938$  Å), respectively. For  $a \leq 2.635$  Å (V) and  $a \leq 2.930$  Å (Nb), the deeper minimum is located on the right hand side of the vertical dashed line, which indicates  $c_{\text{FCC}}$ . For  $a \geq 2.640$  Å (V) and  $a \geq 2.935$  Å (Nb), the minimum is located on the left hand side of this line. The  $c$ -coordinate of the global minimum of  $E(c)$  changes abruptly between 2.635 Å and 2.640 Å, and between 2.930 Å and 2.935 Å for V and Nb, respectively. At  $a_{\text{FCC}}$ , the position of the maximum of  $E(c)$  must coincide with the intersection point of both dashed lines. Solid lines are spline interpolation to the data (symbols) and guide the eye.

**Instability of the FCC structure of V and of Nb** The FCC structures of V and Nb violate the stability condition  $c_{zzzz} > 0$  (Table A.3.2 on Page 142). This situation resembles the instability of the BCC structure of La. The discussion for La can be straightforwardly applied to V and Nb.

The theoretical FCC lattice parameters, evaluated in  $Fm\bar{3}m$  symmetry, are  $c_{\text{FCC}} = 3.738$  Å ( $a_{\text{FCC}} = c_{\text{FCC}}/\sqrt{2} = 2.643$  Å) for V, and  $c_{\text{FCC}} = 4.156$  Å ( $a_{\text{FCC}} = 2.938$  Å) for Nb. The related total energies are denoted by  $E_{\text{FCC}} = E(c_{\text{FCC}})$ . We computed  $E(c)$  in the vicinity of  $a_{\text{FCC}}$ , Fig. 4.15, which shows the expected double wells. Two minima in  $E(c)$  can only be seen in a small range around  $a_{\text{FCC}}$ . Away from  $a_{\text{FCC}}$ , the minimum higher in energy disappears in a hump-like structure. In the case of La, a peak in the DOS at the Fermi energy might contribute to the instability of its BCC structure, see discussion of Fig. 4.11. We computed  $D(E_{\text{F}}) = 1.58/(\text{eV} \cdot \text{atom})$  for FCC V and  $D(E_{\text{F}}) = 1.54/(\text{eV} \cdot \text{atom})$  for FCC Nb. Both values are smaller than the value of  $D(E_{\text{F}})$  at the discontinuity of the EBP (Fig. 4.14c). That is, there is no peak in the DOS of neither V nor of Nb, that may contribute to the instability of their FCC structure.

**Discussion of EBPs** The EBPs of all three elements exhibit many common features, see Table 4.8 and Fig. 4.14 for the complete data. The position of the global minima is at the BCC structure, which is the GS phase. The second minima have somewhat different ratios  $c/a > \sqrt{2}$ . The FCC structure of Ta coincides with the position of the maximum of  $E(c/a)$ . According to our previous

#### 4.5. EPITAXIAL BAIN PATH OF TRANSITION METALS, SELECTED ALKALINE EARTH METALS AND LANTHANIDES

---

thoughts, the FCC structures of V and of Nb do not belong to the EBP.

At  $a = 3.340 \text{ \AA}$ , we find a second, small discontinuity in the  $c(a)/a$  curve of V due to the occurrence of another double well in  $E(c)$ . We argue in the next paragraph, that a van Hove singularity is likely to induce this discontinuity.

The agreement between the computed EBPs from this work and the ones from the available literature is good in so far as the sequence and position of stationary points, as well as energy differences between stationary points and  $E_0$  are fairly identical, see Table 4.8 for a detailed comparison. This is true for all results irrespective of the XC potential. However, none of the published EBPs of V and Nb accounted for the instability of their FCC structures: the FCC structure belongs to the EBP and its position coincides with the position of the maximum of  $E(c/a)$  in Refs. 4, 131, 133, 225.

**Origin of the discontinuity/shoulder in  $E(c/a)$**  The EBPs of V, Nb, and Ta consistently have a step-like feature in  $c(a)/a$  and a shoulder-like feature in  $E(c/a)$  at approximately  $c/a = 0.75$ . The step in  $c(a)/a$  is more clearly seen in the volume curve (Fig. 4.14c). There is also a prominent peak in  $D(E_F)$  at the same position. We are concerned with the origin of these features in the following.

We firstly analysed the total energy curves  $E(c)$  in the vicinity of the shoulder. These curves exhibit a double well only for V. According to our previous thoughts, this results in another discontinuity of  $E(c/a)$ , due to a discontinuous change of the minimum of  $E(c)$  for neighbouring  $a$ 's. The discontinuity happens between the lattice parameters  $a = 3.340 \text{ \AA}$  and  $a = 3.350 \text{ \AA}$ . The change of the  $c$ -coordinate across the discontinuity is approximately  $\Delta c = 0.2 \text{ \AA}$  (distance between the two minima of  $E(c)$ ). We notice a peaking  $D(E_F)$  of height  $2.0/(\text{eV} \cdot \text{atom})$  at  $a = 3.340 \text{ \AA}$  ( $c/a = 0.76$ ), however a considerable smaller value of  $1.5/(\text{eV} \cdot \text{atom})$  at  $a = 3.350 \text{ \AA}$  ( $c/a = 0.71$ ) (Fig. 4.14c). This likely hints at a distinguished singularity in the single particle DOS. The DOS, calculated at  $a = 3.340 \text{ \AA}$  of the EBP, indeed reveals a broad peak situated at the Fermi level, see Fig. 4.16 (black line). How does that peak alter when the  $c$ -coordinate is intentionally decreased but the  $a$ -coordinate is kept fixed? Upon decreasing the lattice parameter  $c$  by  $0.1 \text{ \AA}$ , i.e., one half of the distance between the two minima of  $E(c)$ , this broad peak sharpens considerably and leads to an increase of  $\approx 0.3/(\text{eV} \cdot \text{atom})$  in the DOS at  $E_F$ . The corresponding DOS is depicted in the inset of Fig. 4.16. This intentional decrease of  $c$  is accompanied by an increase of  $E$ , i.e., a high electronic DOS at the Fermi energy may be one reason, why this state is energetically not favourable. The point  $a = 3.350 \text{ \AA}$  on the EBP has a lattice parameter  $c$  smaller than the one of  $a = 3.340 \text{ \AA}$  ( $c(a)$  is monotonically decreasing). In order not to have the mentioned peak in the DOS in coincidence with the Fermi level, the lattice parameter  $c$  may relax considerably. In fact, we find such a pronounced relaxation to be energetically favourable. The relaxation of  $c$  is accompanied by a band broadening and a relative downshift of the prominent peak in the DOS, see Fig. 4.16 (red line).

Nb and Ta are partially different. For both metals,  $E(c)$  does not exhibit double wells in the vicinity of the shoulder of  $E(c/a)$ , although  $D(E_F)$  also peaks at the same  $c/a$  ratio (cf. Fig. 4.16). Instead, the energy landscape of  $E(c)$  is very flat and has a single minimum. The shape of  $E(c)$  can be described as a (more or less inclined) trough valley. The  $c$ -coordinate of the minimum of  $E(c)$

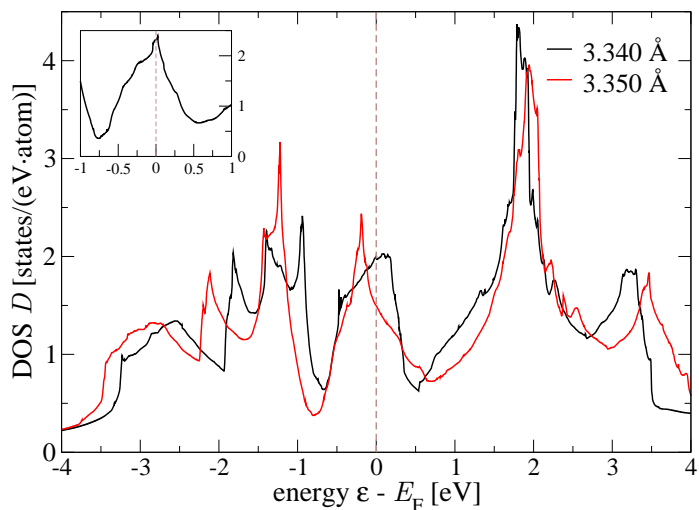


Figure 4.16: On the origin of the discontinuity in the EBP of  $\mathbf{V}$ . The main figure shows the total DOS for two adjacent states of the EBP:  $a = 3.340 \text{ \AA}$  with  $c/a = 0.76$  (black line), and  $a = 3.350 \text{ \AA}$  with  $c/a = 0.71$  (red line). The strong decrease of the lattice parameter  $c$  from  $a = 3.340 \text{ \AA}$  to  $3.350 \text{ \AA}$  by  $\Delta c = 0.2 \text{ \AA}$  leads to a band broadening, but also shifts a prominent peak below  $E_F$  (peak at  $0.2 \text{ eV}$  below  $E_F$ , red line). Without this pronounced relaxation, the peak would be situated at  $E_F$  (inset), which is accompanied by an increase of the total energy. Note the different scales of inset and main figure.

changes significantly in the flat energy landscape for adjacent lattice parameters  $a$ , while the total energy of the minima does not change significantly. This correlation causes the shoulder in  $E(c/a)$ . The DOS at the Fermi energy across this trough valley exhibits a pronounced peak at approximately the position of the minimum of  $E(c)$ , i.e., in the centre of the valley.

**Remark on experiments** Vanadium was grown pseudomorphically on the (001) surface of Fe [14] ( $a_{\text{EXP}} = 2.87 \text{ \AA}$ ) and Ni{001} [225] ( $a_{\text{EXP}} = 2.49 \text{ \AA}$ ). Coherency was, however, only obtained to a thickness of 7 MLs and 8 MLs on Fe and Ni, respectively, i.e., below the threshold defined by us (9 MLs). For this reason, both experiments are not listed in Table 4.8. The vanadium overlayers on Ni had an interlayer distance of  $(1.75 \pm 0.02) \text{ \AA}$  and exhibited a high density of defects.

#### 4.5.7 Group 6 elements: Cr, Mo, and W

The TMs Cr, Mo, and W resemble in various ways the preceding elements of the fifth group in the periodic table. At RTP, the elements appear in the BCC crystal structure. The experimental temperature-pressure phase diagram is simple, since it features no other than the BCC structure [43, 256]. Reports on solid-solid phase transitions for Cr and W at high temperatures remained

#### 4.5. EPITAXIAL BAIN PATH OF TRANSITION METALS, SELECTED ALKALINE EARTH METALS AND LANTHANIDES

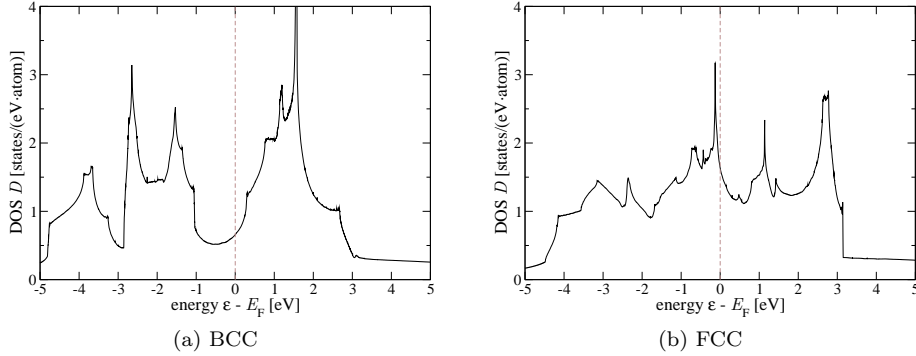


Figure 4.17: Total DOS of (a) BCC and (b) FCC Cr, which corresponds to the situation of a nearly half filled  $d$ -band. The number of electrons per atom in the  $3d$ -states are 4.71 for BCC and 4.75 for FCC, respectively. Both DOS were calculated with  $48^3$   $k$ -points. The ordinates in the two subfigure have equal range to simplify the comparison.

inconsistent [43]. Theory predicted a sequence of phase transitions from BCC  $\rightarrow$  HCP  $\rightarrow$  FCC under pressures of the order of 1 TPa for all three elements [208]. Structural energy differences peak at a  $d$ -band filling of approximately five electrons [58, 165, 169, 204].

Cr exhibits an incommensurate AFM GS (spin density wave (SDW)), which is not reproduced by LSDA [37]. The GS within LSDA is an NM one. For small volume expansion (approximately 5%), LSDA found AF1 order more stable than NM Cr [37, 135]. In contrast, GGA XC functionals gave an AFM GS, but also failed to reproduce the SDW GS, see for example Ref. 37. The occurrence of this rather unusual incommensurate AFM GS was attributed to Fermi surface nesting [57]. Recently a ‘nodon model’ (hole excitations in an AFM background) was suggested to reconcile theory and experiment [235]. Although LSDA failed to reproduce the magnetism of Cr in the GS, states of the EBP might exhibit magnetic order. Being aware of that, we calculated the EBP of Cr in due consideration of FM and AFM order.

**Is there a magnetic instability on the EBP of Cr?** The Fermi energy of BCC Cr (and of BCC Mo and W as well) falls in the pseudogap of the characteristically bimodal electronic DOS of BCC TMs, see Fig. 4.17a for Cr and the *Handbook of band structures* [167] for the other elements of this group. The pseudogap separates the DOS into predominantly  $T_{2g}$  bonding and  $E_g$  antibonding states. For approximately half band filling, e.g., the case of Cr, the DOS at the Fermi energy is comparatively low and does not favour FM order according to Stoner’s criterion for band ferromagnetism [219]. The Stoner criterion predicts spontaneous onset of ferromagnetism for a sufficiently high NM DOS at  $E_F$ . For the same amount of band filling, SDWs are however possible [111]. In detail, Sandratskii *et al.* showed that the static, enhanced,  $q$ -vector dependent susceptibility,  $\chi(\mathbf{q})$ , peaks around  $\mathbf{q} = (0, 0, 2\pi/a)^T$  for BCC Cr, which corresponds to AF1 order [193]. Spontaneous onset of AFM order

Table 4.9: Overview of calculated GS properties and numerical data of stationary points for the elements **Cr**, **Mo**, and **W** in comparison to computations and experiments from the literature, if available. General remarks on this Table are given in Sec. 4.5.1.

element	this work					literature							
	structure			$E - E_0$ [mHa]	theory			Ref.	experiment			Ref.	
	type	$a$ [Å]	$c/a$		$a$ [Å]	$c/a$	$E - E_0$ [mHa]		structure				
				setup [ML]				$a$ [Å]	$c/a$				
Cr	GS	BCC	2.791	–	0	2.794	–	0	[37] <sup>ab</sup>	bulk	2.884	–	[237]
	SP	MIN	2.31	1.81	10.83	2.36	1.80	10.0	[160] <sup>γb</sup>				
		MAX	2.51	1.41	16.14		$\sqrt{2}$	15.0	[160] <sup>γb</sup>				
		MIN	2.79	1.00	0	2.85	1	0	[160] <sup>γb</sup>				
Mo	GS	BCC	3.124	–	0	3.116	–	0	[226] <sup>ac</sup>	bulk	3.145	–	[237]
	SP	MIN	2.61	1.75	14.03		1.765	11.73	[140] <sup>γa</sup>				
						2.64	1.75	12.0	[160] <sup>γb</sup>				
		MAX	2.80	1.41	17.28		$\sqrt{2}$	15.15	[140] <sup>γa</sup>				
		MIN	3.12	1.00	0		$\sqrt{2}$	15.2	[160] <sup>γb</sup>				
					3.16	1	0	[160] <sup>γb</sup>					
W	GS	BCC	3.145	–	0	3.147	–	0	[226] <sup>ac</sup>	bulk	3.163	–	[237]
	SP	MIN	2.68	1.66	14.80		1.678	14.60	[140] <sup>γa†</sup>				
						2.69	1.70	14.1	[160] <sup>γb†</sup>				
		MAX	2.82	1.41	17.68		$\sqrt{2}$	18.24	[140] <sup>γa†</sup>				
		MIN	3.15	1.00	0		$\sqrt{2}$	18.0	[160] <sup>γb†</sup>				
					3.19	1	0	[160] <sup>γb†</sup>					

legend

$\alpha$	L(S)DA [174] (PW92)	$abc$	FP-LAPW [16] ( <sup>a</sup> WIEN2K, <sup>b</sup> WIEN97, <sup>c</sup> WIEN95)
$\beta$	L(S)DA [30, 239]	$d$	FP-LMTO [141]
$\gamma$	GGA [172] (PBE96)	$e$	PAW [110] (VASP)
$\dagger$	scalar-relativistic		



#### 4.5. EPITAXIAL BAIN PATH OF TRANSITION METALS, SELECTED ALKALINE EARTH METALS AND LANTHANIDES

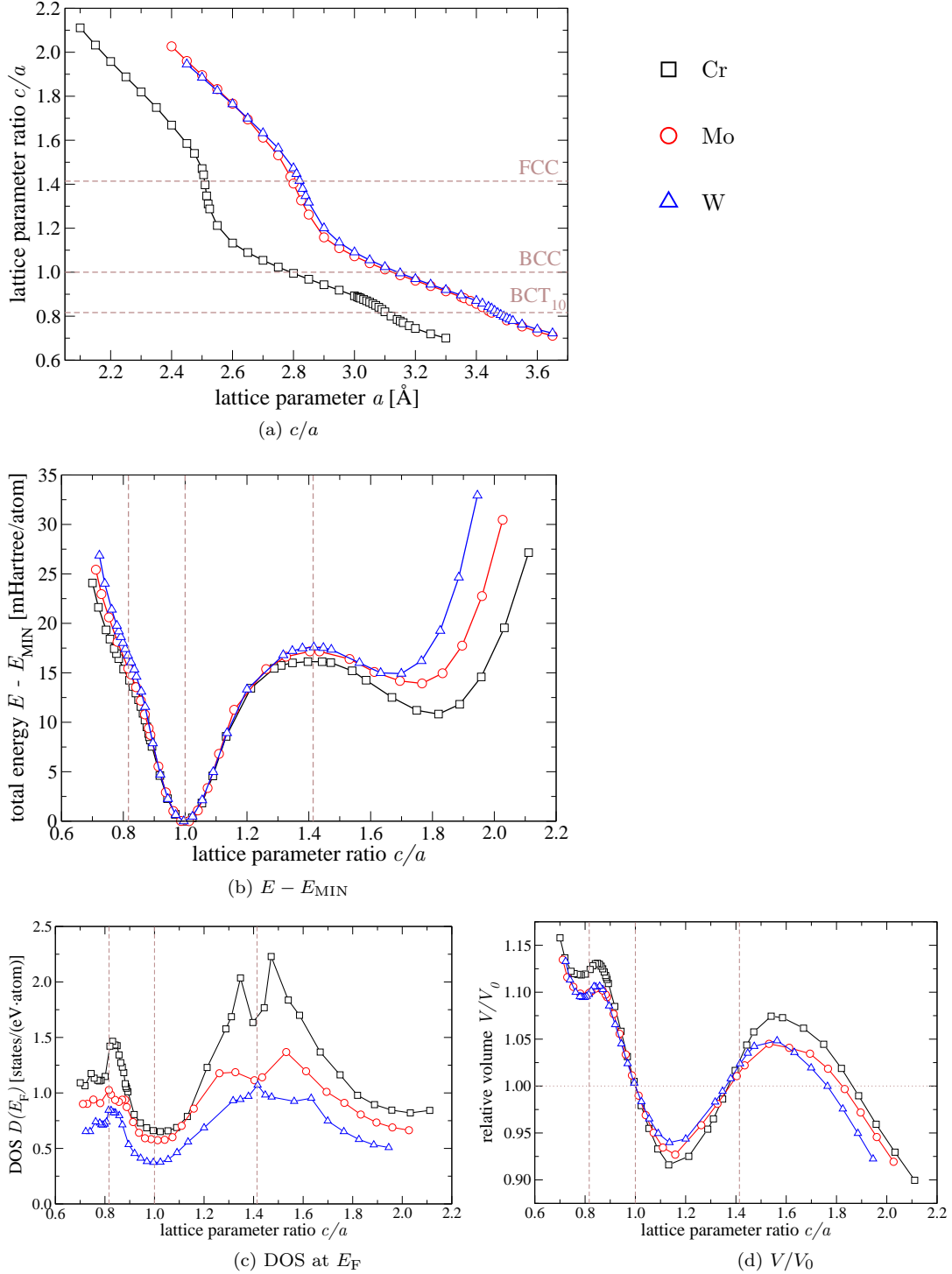


Figure 4.18: For the EBPs of **Cr**, **Mo**, and **W**: (a)  $c/a$ , (b)  $E - E_{\text{MIN}}$ , (c)  $D(E_F)$ , and (d)  $V/V_0$ . Numerical data in Table 4.9. Lines guide the eye.

## CHAPTER 4. TRANSITION METALS, SELECTED ALKALINE EARTH METALS AND LANTHANIDES

---

with a general  $q$ -vector is expected, if [111]

$$I\chi_0(\mathbf{q}) > 1, \quad (4.9)$$

with the unenhanced susceptibility,  $\chi_0$ , and the intra-atomic Stoner exchange integral,  $I$ , which is in general weakly structure dependent [89, 201].<sup>6</sup> For Cr,  $I$  is also weakly  $\mathbf{q}$ -dependent [193]. In the limit of  $\mathbf{q} \rightarrow \mathbf{0}$ ,

$$\chi_0(\mathbf{q} = \mathbf{0}) \propto D(E_F). \quad (4.10)$$

Thus the Stoner criterion,  $I \cdot D(E_F) > 1$ , for ferromagnetism is retained. We infer from  $D(E_F)(c/a)$  in Fig. 4.18c, that the DOS for some states of the EBP of Cr is a factor of two to three higher compared to  $D(E_F)$  of BCC Cr. This is the case for FCC Cr, and states whose  $c/a$  ratio is slightly larger or smaller than  $\sqrt{2}$ . Note that the DOS of the FCC structure is comparatively high, because the Fermi energy for approximately half  $d$ -band filling coincides with the central peak of the FCC DOS of Cr, see Fig. 4.17b. The peak originates from the bands with  $T_{2g}$  character. Following Stoner's criterion (Eq. (4.10)), spontaneous onset of FM order is expected at  $\approx 2.6 / (\text{eV} \cdot \text{atom})$  – the parameter  $I$  of Cr is  $0.35 \dots 0.38 \text{ eV}$  [89, 201]. The highest DOS along the EBP is  $2.22 / (\text{eV} \cdot \text{atom})$ , observed at  $a = 2.50 \text{ \AA}$  with  $c/a = 1.47$ , i.e., the Stoner criterion is not fulfilled. However, this does not rule out the possibility of a metamagnetic state (see also discussion in the next paragraph).

**Discussion of EBPs** Table 4.8 and Fig. 4.18 summarise our results for Cr, Mo, and W. For all three elements in common, the sequence of extrema of  $E(c/a)$  for increasing  $c/a$  ratio is: global minimum at the BCC structure - maximum at the FCC structure - local minimum at a BCT structure – identical to the elements in the fifth group. The shoulder in  $E(c/a)$  at very low  $c/a$  ratios, now fairly coinciding with  $c/a$  of BCT<sub>10</sub>, is strongly reduced compared to the elements in the vanadium group. A dip in the volume curve and a peak in  $D(E_F)$  is present at the same  $c/a$  ratio. The FCC structure has  $c_{zzzz} > 0$  in each case, the FCC structure is further exactly at the position of the maximum of  $E(c/a)$ . We found no double wells in  $E(c)$ . Figure 3.4 on Page 17 shows a contour plot of the total energy in the tetragonal parameter space,  $E(a, c)$ , and the EBP of Cr. The small shoulders in  $c(a)/a$  and in  $E(c/a)$  at  $a = 3.05 \text{ \AA}$  and  $c/a = 0.85$  (Figs. 4.18a and 4.18b) show up as buckling of the contour lines of  $E(a, c)$  in Fig. 3.4.

We carefully investigated the EBP of Cr taking into account FM, AF1 and AF2 order. We did not find any magnetic state on the EBP, i.e., all states of the EBP of Cr are NM in PW92. Also, we did not find a meta-magnetic state in Cr by FSM calculations.

There are no published EBPs of neither Cr, Mo, nor W. The published data on stationary points of Mo and W from Ref. 140, and of Cr, Mo, and W from Ref. 160 agree well with our findings. In addition, the energy differences are fairly independent of the XC functional.

---

<sup>6</sup>The calculations from Sigalas *et al.* for various elements in the BCC, the FCC, and the HCP structure showed, that  $I$  does not differ more than 10% among the three structures [201].

## 4.5. EPITAXIAL BAIN PATH OF TRANSITION METALS, SELECTED ALKALINE EARTH METALS AND LANTHANIDES

### 4.5.8 Group 7 elements: Mn, Tc, and Re

Mn adopts a complex crystal structure with 58 atoms in the unit cell at ambient conditions [43, 256]. It is paramagnetic at RTP, below 95 K it orders in a non-collinear magnetic structure [83]. The transition is accompanied by a tiny tetragonal distortion. Non-collinear magnetic structures cannot be calculated in FPLO. In what follows, we consider an NM cubic structure (space group  $I43m$ ) as GS crystal structure ( $\alpha$ -Mn). The Wyckoff positions are taken from Villars and Calvert [237], and only the lattice parameter is optimised. There exist an FCC ( $\gamma$ -Mn) and a BCC phase of Mn at elevated temperatures. The  $\gamma$ -Mn phase transforms into a BCT structure with  $a = 2.673 \text{ \AA}$  and  $c/a = 1.325$  as a result of quenching [43] and exhibits AF1 order [48].<sup>7</sup> Tc and Re exist in the HCP structure and no further allotropes are known. Both elements maintain the canonical pattern of GS crystal structures across the TM-series [169, 204].

According to our calculations, the (NM) FCC phase of Mn is lower in total energy than NM  $\alpha$ -Mn by an amount of  $\approx 3 \text{ mHartree/atom}$ . This is most likely due to the neglect of magnetic order in the GS and the rigid Wyckoff positions (only the lattice parameter was optimised). Literature to compare this issue with was not available.

**Discussion of EBPs** Consistently for all three elements,  $E(c/a)$  has a minimum at the FCC structure, see Table 4.10 and Fig. 4.19 for the complete results.  $E(c/a)$  of Tc and of Re has a maximum at the BCC structure and a shallow minimum at  $c/a = 0.90$ . The order of the stationary points is different for Mn: the BCC structure coincides with the position of the second, shallow minimum of  $E$ . Hence, the local maximum in between both minima of  $E$  has  $c/a > 1$ . We more clearly depict this shallow minimum in Fig. 4.20. The lattice constants of the quenched BCT structure of Mn ( $a = 2.673 \text{ \AA}$  and  $c/a = 1.325$ ) do not coincide with the ones of any stationary point of the EBP of Mn.

We predict FM order for a part of the EBP of Mn and discuss this more elaborately in the next paragraph.

Reference 133 reported on an EBP of Mn, for which only AF1 order was considered. However, neither figures, numerical data, nor the XC functional were published. Stationary points of  $E(c/a)$  with increasing  $c/a$  were stated to be at a non-cubic structure, at a cubic structure, and again at a non-cubic structure. (According to our considerations in Sec. 3.4, only  $c/a = 1$  is a symmetry dictated stationary point in total energy on an EBP with presumed AF1 order.) CVBP calculations at the experimentally determined volume of BCT Mn predicted predominant AF1 order for most states of this Bain path, irrespective of the employed XC functional [184]. Reference 184 found two minima of  $E(c/a)$ , the energetically deeper one is located at  $c/a = 1.358$ , the second minimum is at  $c/a = 0.849$ . The maximum between both minima is at the BCC structure. Total energy calculations using gradient corrected functionals and the respective theoretical equilibrium volume [47, 69] found AF2 order for the BCC structure of Mn, and AF1 order for the FCC structure. Reference [70] predicted three tetragonal configurations of Mn, whose energies are minima of  $E(a, c)$ . These states are located at  $a = 2.57 \text{ \AA}$  with  $c/a = 1.34$  (AF1 order), at  $2.48 \text{ \AA}$  with

<sup>7</sup>Lattice parameter values of the BCT structure are averaged over extrapolated data from miscellaneous Mn-alloys.

Table 4.10: Overview of calculated GS properties and numerical data of stationary points for the elements **Mn**, **Tc**, and **Re** in comparison to computations and experiments from the literature, if available. General remarks on this Table are given in Sec. 4.5.1.

element	this work				literature									
	structure			$E - E_0$	theory			Ref.	experiment				Ref.	
	type	$a$ [Å]	$c/a$	[mHa]	$a$ [Å]	$c/a$	$E - E_0$		structure					
							[mHa]	setup	[ML]	$a$ [Å]	$c/a$			
<b>Mn</b>	GS	CUB	8.371	–	0 (NM)	8.532	–	0 (NM)	[83] <sup><math>\gamma e</math></sup>	bulk		8.865	1.00	(PM) [255]
	SP	MIN	2.43	1.41	-2.97 (NM)	2.48	1.48	$C + 0.22$ (AFM <sup>‡</sup> )	[70] <sup><math>\delta e</math></sup>	Co(001)Cu(001)	50	2.55	1.49 ± 0.01	[106]
		MAX	2.69	1.03	0.81 (NM)	2.57	1.34	$C$ (AF1)	[70] <sup><math>\delta e</math></sup>	Cu <sub>3</sub> Au{001}	16	2.65	1.34	[196]
		MIN	2.72	1.00	0.73 (NM)	2.84	0.97	$C + 2.98$ (AFM <sup>‡</sup> )	[70] <sup><math>\delta e</math></sup>	Cu <sub>3</sub> Au{001}	35	2.65	1.35	[123]
										Pd{001}	21	2.75	1.25 ± 0.03	[224]
									Fe{001}	14	2.87	1.13 ± 0.02	[102]	
<b>Tc</b>	GS	HCP	2.722	1.597	0	2.689	1.604	0	[165] <sup><math>\beta d</math></sup>	bulk		2.743	1.604	[237]
	SP	MIN	2.71	1.41	3.19									
		MAX	3.05	1.00	10.74									
		MIN	3.14	0.90	10.55									
<b>Re</b>	GS	HCP	2.751	1.608	0	2.720	1.620	0	[165] <sup><math>\beta d \dagger</math></sup>	bulk		2.762	1.614	[237]
	SP	MIN	2.74	1.41	3.48									
		MAX	3.08	1.00	14.14									
		MIN	3.18	0.90	13.99									

## legend

$\alpha$	L(S)DA [174] (PW92)	$abc$	FP-LAPW [16] ( <sup><math>a</math></sup> WIEN2K, <sup><math>b</math></sup> WIEN97, <sup><math>c</math></sup> WIEN95)
$\beta$	L(S)DA [30, 239]	$d$	FP-LMTO [141]
$\gamma$	GGA [172] (PBE96)	$e$	PAW [110] (VASP)
$\delta$	GGA [173]		
$\dagger$	scalar-relativistic	$\ddagger$	(2 × 2) AFM order in the (001) plane

#### 4.5. EPITAXIAL BAIN PATH OF TRANSITION METALS, SELECTED ALKALINE EARTH METALS AND LANTHANIDES

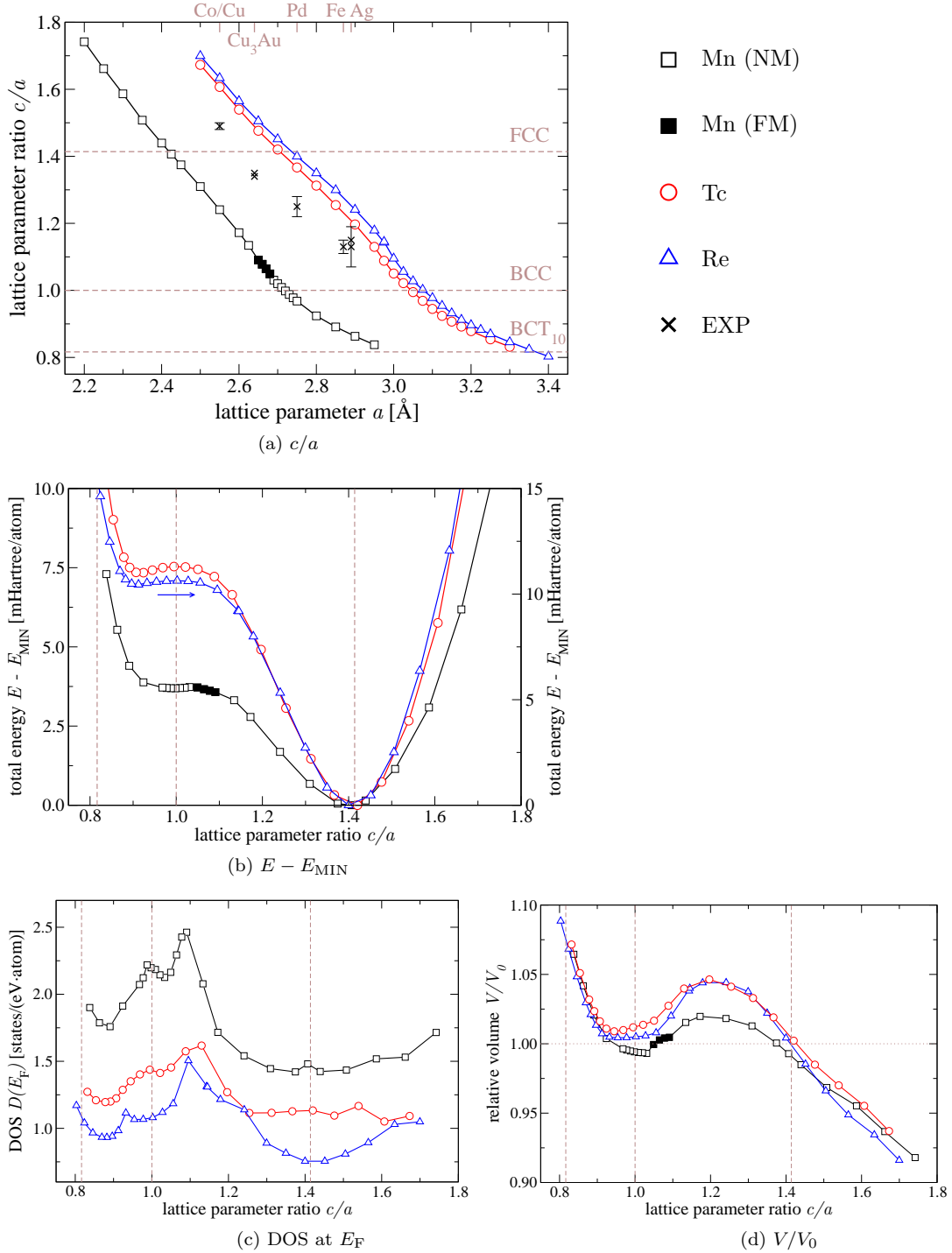


Figure 4.19: For the EBPs of Mn, Tc, and Re: (a)  $c/a$ , (b)  $E - E_{\text{MIN}}$ , (c)  $D(E_F)$ , and (d)  $V/V_0$ . Numerical data in Table 4.10. Lines guide the eye.

## CHAPTER 4. TRANSITION METALS, SELECTED ALKALINE EARTH METALS AND LANTHANIDES

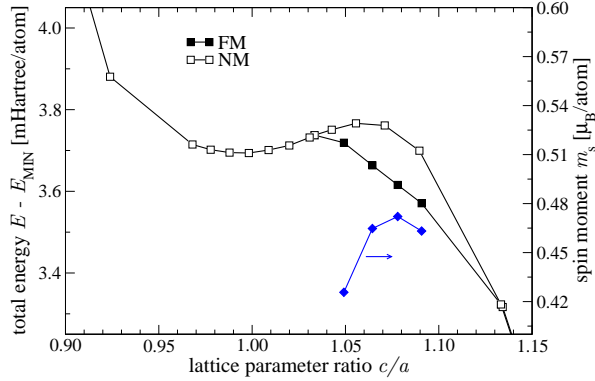


Figure 4.20: Enlarged picture of the plateau-like region of  $E(c/a)$  from Fig. 4.19b for **Mn** (*left hand ordinate*). A part of the EBP exhibits FM order (*solid symbols*). NM states of the EBP are depicted by *open symbols*. The energy difference between FM states and NM states (in the range where ferromagnetism occurs) equals the difference between the respective symbols. Due to a relaxation of the lattice parameter  $c$  in response to the occurrence of magnetic order, symbols representing FM order are displaced to different ratios  $c/a$  compared to symbols which indicate no magnetic order. The spin moment of the FM states of the EBP is plotted using the *right hand ordinate*. Lines guide the eye.

$c/a = 1.48$  and at  $2.84 \text{ \AA}$  with  $c/a = 0.97$ . The latter two states were found to have a  $(2 \times 2)$  AFM order in the (001) plane.

**Ferromagnetic states on the EBP of Mn** We considered FM, AF1, and AF2 order in the calculation of the EBP of Mn. We fixed the spin moment in the unit cell by virtue of the FSM method following the discussion on Page 35. FM states along the EBP of Mn occur in the limited range  $a = 2.65 \dots 2.68 \text{ \AA}$  with  $c/a \approx 1.09 \dots 1.05$ , see Fig. 4.19 for a global overview, and a more detailed picture in Fig. 4.20. If we do not allow for finite spin polarisation,  $E(c/a)$  has a maximum at  $c/a = 1.055$ . The presence of a finite spin polarisation reduces the total energy of all FM states of the EBP. The position of the maximum shifts to  $c/a = 1.034$ . The energy gain due to FM order amounts to at most  $0.1 \text{ mHartree/atom}$ , and the spin moment varies between  $0.42$  and  $0.47 \mu_B/\text{atom}$  (Fig. 4.20). The position of FM states on the EBP coincides with the peak in  $D(E_F)$  along the EBP, see Fig. 4.19c. The total energy vs. the spin moment for fixed lattice geometry,  $E(m_s)$ , reveals, that the onset of magnetism is spontaneous, i.e.,  $d^2E/dm_s^2|_{m_s=0} < 0$ .

We find the FCC and the BCC structure of Mn to be NM, which is in compliance with previous LSDA calculations from Eder *et al.* [47] (PAW [110] (VASP), XC functional proposed by Perdew and Zunger [175]). There is additionally very good agreement in the calculated lattice parameters: we find  $2.72 \text{ \AA}$  and  $3.44 \text{ \AA}$ , Eder *et al.*  $2.73 \text{ \AA}$  and  $3.43 \text{ \AA}$  for BCC and FCC Mn, respectively.

## 4.5. EPITAXIAL BAIN PATH OF TRANSITION METALS, SELECTED ALKALINE EARTH METALS AND LANTHANIDES

---

**Remark on magnetic structure in Mn films** Among the five experiments listed in Table 4.10, three attempted to determine the magnetic structure in these films [106, 123, 196]. For Mn on Cu<sub>3</sub>Au, Ref. [196] unequivocally excluded FM order, however conjectured AFM order. An AFM state in films can directly be measured by spin-polarised scanning tunnelling microscopy (SP-STM) [59], but not directly by, e.g., neutron diffraction due to lacking sensitivity. However, exchange effects on AFM/FM surfaces can be exploited by means of neutron diffraction [106]. Reference [123] substantiated AFM order for the Mn on Cu<sub>3</sub>Au epitaxial system, by detecting an exchange biased hysteresis loop in Fe capped Mn films. Similarly, Ref. [106] verified AFM order in Mn overlayers on Co(001)Cu(001).

### 4.5.9 Group 8 elements: Fe, Ru, and Os

The phase diagram of Fe has three cubic allotropes. These have a BCC structure ( $\alpha$ -Fe and  $\delta$ -Fe) and an FCC structure ( $\gamma$ -Fe) [43, 256]. The Curie temperature of  $\alpha$ -Fe is lower than the phase transition temperature from  $\alpha$ -Fe to  $\gamma$ -Fe at RP, i.e., BCC  $\alpha$ -Fe is the only magnetically ordered allotrope of Fe at RP. Non-collinear spin arrangements were measured in FCC Fe precipitates and in thin FCC Fe films [142, 228, 229]. Ru and Os crystallise in the HCP structure, no other phases are known [43, 256].

The possibility of non-collinear magnetic structures in BCC Fe was negated on the basis of the calculations of the  $q$ -vector dependent static susceptibility [193] and by spin spiral calculations [227]. FCC Fe is a more complicated case, because of its non-collinear magnetic structure, which is sensitive to the volume per atom and details of the method. For the ongoing discussion on the magnetic structure of  $\gamma$ -Fe, see, for example, Refs. 112, 229, 230. LSDA gives an NM GS for FCC Fe (at the theoretical equilibrium volume) [73, 134, 231]. Furthermore, LSDA finds the NM HCP phase energetically lower than the FCC phase, and the FCC phase lower in energy than the FM BCC phase of Fe [150, 231].

**Discussion of the EBP of Fe** The EBP of Fe is characterised by two discontinuities in  $c(a)/a$ , see Fig. 4.21 and Table 4.11 for the complete data. Their positions on the EBP are at  $c/a \approx 1.18$  and at  $c/a \approx 0.82$ . Both the BCC and the FCC structure minimise  $E(c/a)$ . The discontinuity at  $c/a \approx 1.18$  is due to a double well in  $E_{m_s}(a, c)$ ,  $a$  fixed, which is shown for  $a = 2.575 \text{ \AA}$  in Fig. 4.22.  $E_{m_s}(a, c)$  was defined as the minimum of  $E(a, c, m_s)$  with respect to the spin moment  $m_s$  with fixed lattice parameters  $a$  and  $c$ , see discussion at the end of Sec. 4.4. The  $c$ -coordinate of the minimum of  $E_{m_s}(a, c)$ ,  $a$  fixed, changes discontinuously between  $a = 2.575 \text{ \AA}$  and  $a = 2.580 \text{ \AA}$  analogously to previous considerations, e.g., discussion for La in Sec. 4.5.4. The associated change of  $c$  is  $\Delta c = 0.1 \text{ \AA}$ . Simultaneously, the spin moment changes by  $1 \mu_B/\text{atom}$  (Fig. 4.22). Thus, the discontinuity is related to a transition between two different FM states.

The total energy as function of the spin moment for fixed lattice,  $E(m_s)$ , in the vicinity of the discontinuity is depicted in Fig. 4.23. By means of this magnetisation curves, we elucidate the transition from a state with low spin moment at  $a = 2.570 \text{ \AA}$  to a state with high spin moment at  $a = 2.580 \text{ \AA}$ . We find a finite magnetic moment of  $0.77 \mu_B/\text{atom}$  at  $a = 2.570 \text{ \AA}$  as the state of lowest

Table 4.11: Overview of calculated GS properties and numerical data of stationary points for the elements **Fe**, **Ru**, and **Os** in comparison to computations and experiments from the literature, if available. General remarks on this Table are given in Sec. 4.5.1.

element		this work				literature								
		structure			$E - E_0$	theory			Ref.	experiment				Ref.
		type	$a$ [Å]	$c/a$	[mHa]	$a$ [Å]	$c/a$	[mHa]		setup	[ML]	$a$ [Å]	$c/a$	
Fe	GS	BCC	2.752	–	0 (FM)	2.753	–	0 (FM)	[226] <sup>αa</sup>	bulk	2.867	–	(FM) [237]	
	SP	MIN	2.39	1.41	–2.05 (NM)	2.47	1.55	3.21 (AF2)	[185] <sup>γb</sup>	Ni{001}	25	2.49	1.56	[126]
		MAX	2.58	1.16, 1.21	3.15 (FM)	2.59	1.36	6.50 (FM)	[185] <sup>γb</sup>	Cu{001}	10	2.55	1.41 ± 0.02	[90]
		MIN	2.75	1.00	0 (FM)	2.85	1.00	0 (FM)	[185] <sup>γb</sup>	Rh{001}	10	2.69	1.16	[12]
										Pd{001}	53	2.75	1.09 ± 0.02	[186]
									Ag{001}	25	2.89	1.00 ± 0.02	[118]	
Ru	GS	HCP	2.685	1.579	0	2.663	1.584	0	[165] <sup>βd</sup>	bulk	2.705	1.583	[237]	
	SP	MIN	2.66	1.41	4.58	2.71	√2	5	[247] <sup>γb</sup>					
		MAX	3.01	1.00	25.12	3.06	1	25	[247] <sup>γb</sup>					
		MIN	3.18	0.85	21.99 (FM)	3.25	0.83	21 (FM)	[247] <sup>γb</sup>					
Os	GS	HCP	2.726	1.579	0	2.707	1.588	0	[165] <sup>βd†</sup>	bulk	2.734	1.579	[237]	
	SP	MIN	2.70	1.41	4.98									
		MAX	3.06	0.99, 1.07	33.27									
		MIN	3.24	0.84	27.60									

legend

α	L(S)DA [174] (PW92)	<sup>abc</sup>	FP-LAPW [16] ( <sup>a</sup> WIEN2K, <sup>b</sup> WIEN97, <sup>c</sup> WIEN95)
β	L(S)DA [30, 239]	<sup>d</sup>	FP-LMTO [141]
γ	GGA [172] (PBE96)	<sup>e</sup>	PAW [110] (VASP)
†	scalar-relativistic		



#### 4.5. EPITAXIAL BAIN PATH OF TRANSITION METALS, SELECTED ALKALINE EARTH METALS AND LANTHANIDES

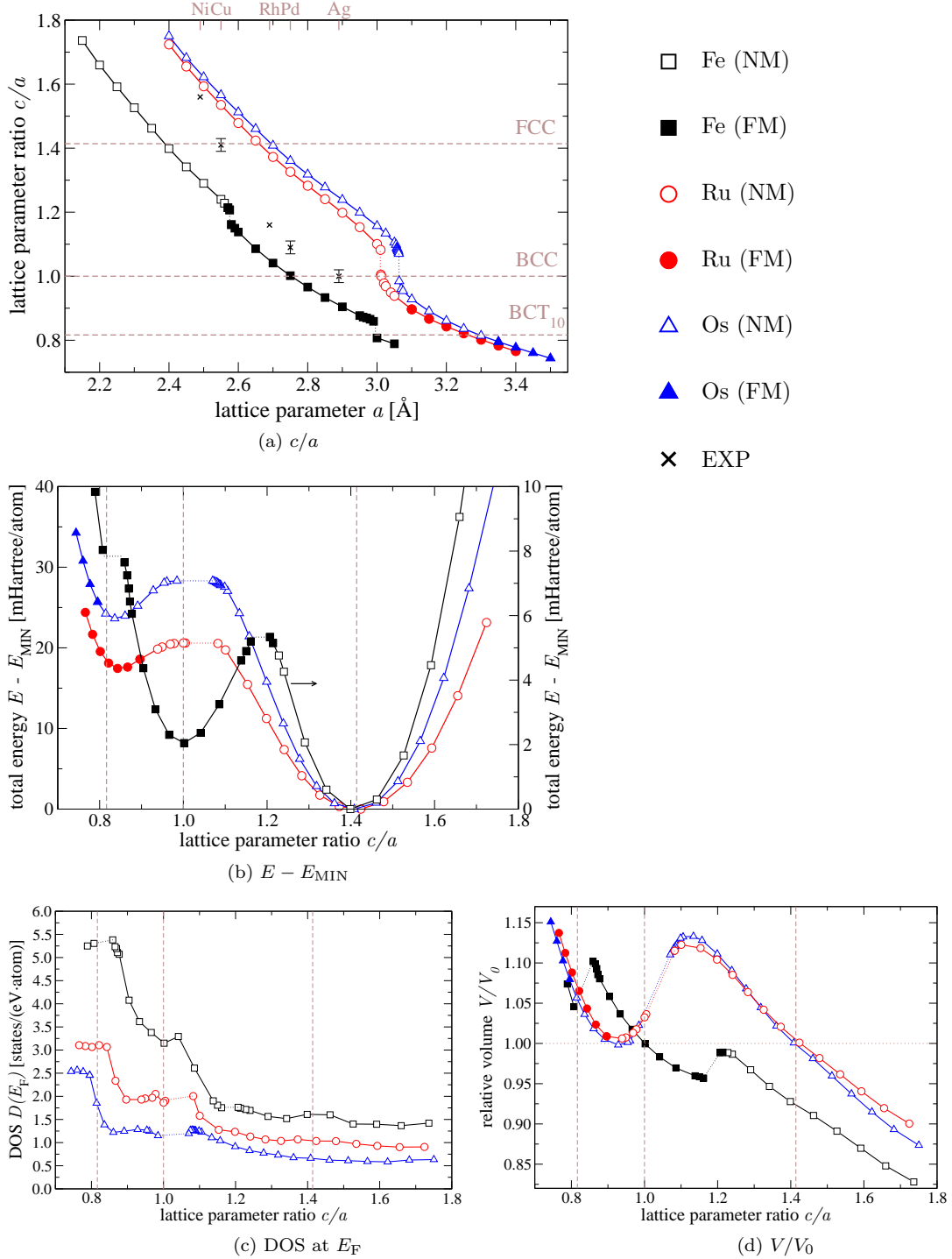


Figure 4.21: For the EBPs of **Fe**, **Ru**, and **Os**: (a)  $c/a$ , (b)  $E - E_{\text{MIN}}$ , (c)  $D(E_F)$ , and (d)  $V/V_0$ . Numerical data in Table 4.10. Lines guide the eye.

## CHAPTER 4. TRANSITION METALS, SELECTED ALKALINE EARTH METALS AND LANTHANIDES

---

energy over all spin moments. There is a metastable state with zero magnetic moment, since  $d^2E/dm_s^2|_{m_s=0} > 0$  (inset of Fig. 4.23). The state at  $a = 2.580 \text{ \AA}$  has a considerably smaller  $c$ -parameter and a considerably larger magnetic moment of  $1.78 \mu_B/\text{atom}$ . The maximum gain in total energy due to a finite spin polarisation,  $\max_{m_s} [E(m_s = 0 \mu_B) - E(m_s)]$ , is about  $0.2 \text{ mHartree/atom}$  for  $a = 2.570 \text{ \AA}$ , and already  $3.1 \text{ mHartree/atom}$  for  $a = 2.580 \text{ \AA}$ . The magnetisation curve for  $a = 2.560 \text{ \AA}$  reveals two energetically degenerate minima with zero and finite spin moment, respectively. The second discontinuity at  $c/a \approx 0.82$  is again due to a shallow double well in  $E_{m_s}(a, c)$ ,  $a$  fixed, with a difference of  $0.4 \mu_B/\text{atom}$  and  $\Delta c = 0.14 \text{ \AA}$  between the two minima of  $E_{m_s}(a, c)$  with  $a$  fixed.

**Magnetic properties of Fe along the EBP** States on the EBP of Fe are either NM or FM. We predict FM states on the EBP for  $a \geq 2.57 \text{ \AA}$  ( $c/a \leq 1.21$ ). All other states, including FCC Fe, are found to be NM, see Figs. 4.21b and 4.24. Note that we depict  $E(a)$  in Fig. 4.24 in contrast to previous figures, for which we used  $E(c/a)$ . This is because the functional dependence of  $c(a)$  is different for different magnetic order, and only the representation of the energies as function of  $a$  unambiguously depicts the magnetic order with the lowest total energy for a given  $a$ . AF1 and AF2 orders are never more stable than FM order on the EBP, since states with AF1 or AF2 orders have higher energies than the FM ones. The FCC structure coincides with the position of the global minimum of  $E(a)$ . The positions of the maximum and the second minimum of  $E(a)$  depend on the imposed magnetic pattern. Assuming FM order, the second minimum is situated at the BCC structure, but this structure coincides with the maximum of  $E(a)$  for the NM EBP. States with finite spin moment in AF1 order do not exist for BCC Fe (Fig. 4.24), hence the maxima of  $E(a)$  for NM states and AF1 order are at identical positions. AF2 order has no symmetry dictated stationary points. The maximum and the minimum of  $E(a)$  in terms of the structural unit cell are found at  $c/a = 1.07$  and  $c/a = 0.88$ , respectively (the magnetic unit cell has doubled  $c/a$  ratios). The secondary, tetragonal minimum along  $E(a)$  assuming AF1 order is located at  $c/a = 0.86$ .

According to Fig. 4.24, the energy gain due to magnetic order is larger for the AF2 arrangement than for the AF1 one with reference to the NM states. This is understandable, if we take the predominance of FM order over AF1 order for granted. AF1 order involves an anti-parallel orientation of the spin moment between every (001) layer, AF2 only between every second layer. By that argument, lesser anti-parallel orientations of the spin moment in adjacent planes, i.e., SDWs with shorter (commensurate)  $q$ -vectors, will possess an energy below that of AF2 order but still above that of FM Fe ( $\mathbf{q} = \mathbf{0}$ ). This argument may be oversimplified because it neglects any further details of the electronic structure, and must be supported by additional calculations. Reference [193] found this trend by means of spin spiral calculations for BCC Fe (theoretical equilibrium volume, augmented spherical wave method, LSDA in the parameterisation of Ref. 238). Finally, we show the modulus of the site resolved spin moments along the EBP for FM, AF1, and AF2 orders in Fig. 4.25. The spin moment of FM BCC Fe was determined to  $2.01 \mu_B/\text{atom}$  compared to the experimental value of  $(2.083 \pm 0.023) \mu_B/\text{atom}$  [187] (measured at 300 K).

To the best of our knowledge, there is no published EBP of Fe within the

#### 4.5. EPITAXIAL BAIN PATH OF TRANSITION METALS, SELECTED ALKALINE EARTH METALS AND LANTHANIDES

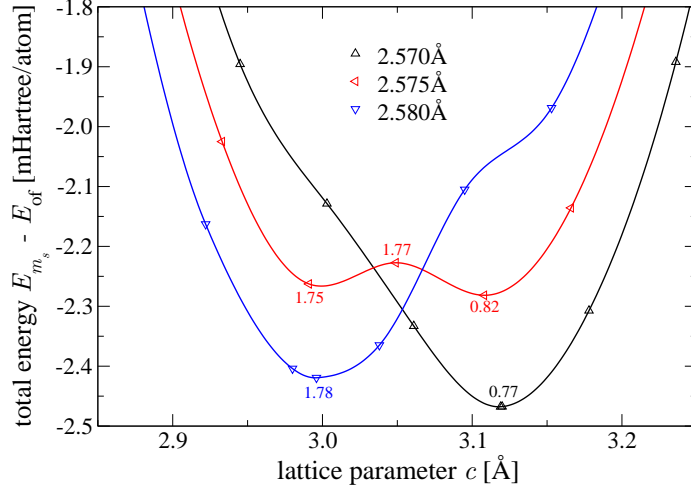


Figure 4.22: On the discontinuity of  $E(c/a)$ :  $E_{m_s}(a, c)$  versus the lattice parameter  $c$  of **Fe** for parameters  $a$  as stated in the legend. The value of the spin moment  $m_s$  for the extrema of  $E_{m_s}(a, c)$  are stated (values are in  $\mu_B/\text{atom}$ ). All energies are shifted by an offset,  $E_{\text{of}} = -1270.579$  Hartree/atom. Solid lines are spline interpolation to the data (symbols) and guide the eye.

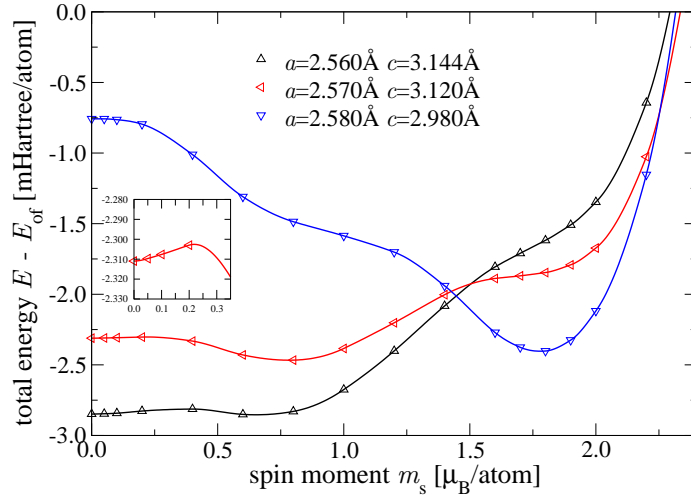


Figure 4.23: Total energy versus spin moment for three points of the EBP of **Fe**. The respective lattice parameters  $a$  and  $c$  are stated in the legend. There are significant changes of the corresponding out-of-plane lattice parameter and the spin moment between  $a = 2.570$  Å and  $a = 2.580$  Å, but the energy difference between the minima of each associated curve is small (cf. Fig. 4.22). All energies are shifted by an offset,  $E_{\text{of}} = -1270.579$  Hartree/atom. Solid lines are spline interpolation to the data (symbols) and guide the eye.

## CHAPTER 4. TRANSITION METALS, SELECTED ALKALINE EARTH METALS AND LANTHANIDES

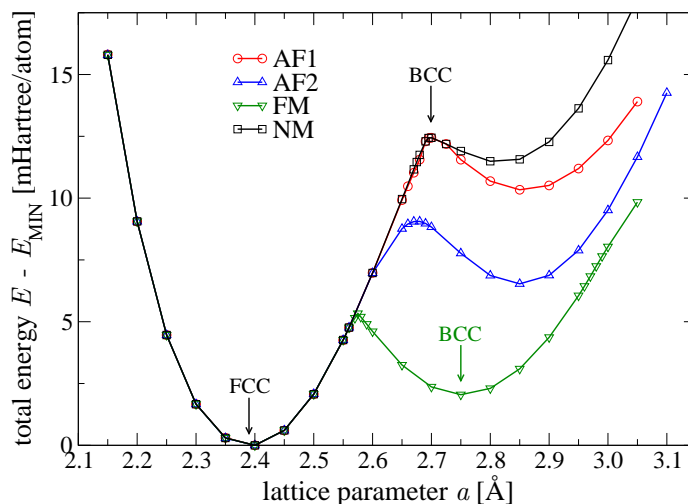


Figure 4.24: Total energy along the EBP of **Fe** considering FM and two kinds of AFM order.  $E - E_{\text{MIN}}$  is plotted with respect to  $a$ . If the FM or the AFM curves coincide with the NM curve, respective states (data points) possess zero spin moment per site (cf. Fig. 4.25 below). The positions of the FCC and the BCC structures on the NM EBP (black arrows), and the position of the BCC structure on the FM EBP (green arrow) are indicated. Solid lines guide the eye.

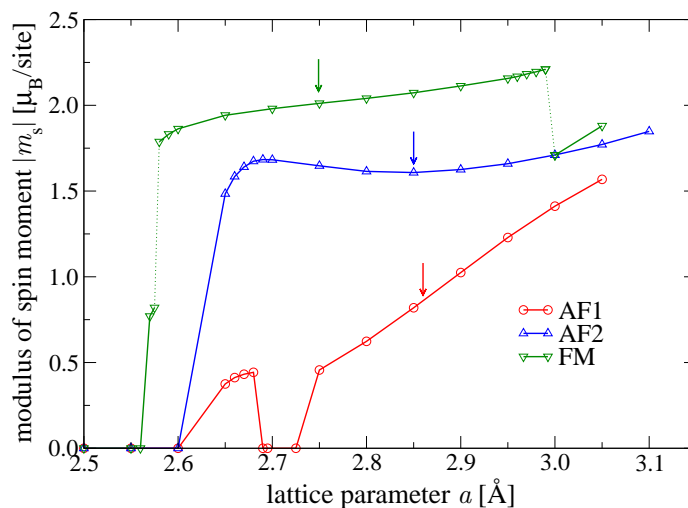


Figure 4.25: Modulus of the site resolved spin moment along the EBP of **Fe** in consideration of FM and two kinds of AFM order. For  $a < 2.5 \text{ \AA}$  all moments are identical zero. The arrows indicate the position of the local minima of the respective  $E(a)$  curves from Fig. 4.24 (minima obtained through spline fit to data). Lines guide the eye.

## 4.5. EPITAXIAL BAIN PATH OF TRANSITION METALS, SELECTED ALKALINE EARTH METALS AND LANTHANIDES

---

framework of LSDA. It was, however, studied within GGA. Bain paths obtained with constant volume exist for LSDA (Table 4.1). In the following, we review these results. Reference 62 calculated CVBPs at various atomic volumes to map the total energy in the tetragonal plane (for PW92 and for PBE96). The minimum energy contour plot with respect to FM, AF1, and AF2 orders defined magnetic phase boundaries between different magnetic states in the tetragonal plane (NM states were not considered in the contour plots). The positions of borderlines were found to be similar between both XC functionals, although phase boundaries in PW92 occurred at higher volumes. Furthermore, the positions of stationary points in the total energy along the CVBP at the experimental atomic volume were at identical  $c/a$  ratios for PW92 and PBE96, concordantly for NM, FM, AF1, and AF2 orders [62,184]. BCC Fe and FCC Fe were found to order ferromagnetically and anti-ferromagnetically (AF2), respectively, at the theoretical equilibrium volume of PBE96 [185] and at the experimental volume for PW92 and PBE96 [62,242]. Reference 242 included further AFM orders with  $q$ -vectors  $(1/2, 1/2, 0)^T$  and  $(0, 0, 1/3)^T$  (in units of  $2\pi(1/a, 1/a, 1/c)^T$ ) in the study of the CVBP at the experimental volume and employing PW92. According to this result, FCC Fe orders with AF2 arrangement, and AF1 order does not occur on the CVBP. Spin spirals with various  $q$ -vectors were predicted for a large part of the tetragonal parameter space around  $c/a = \sqrt{2}$  and in the range  $0.85 \leq V/V_{\text{EXP}} \leq 1.05$ , as studied by the LMTO method in ASA and PBE96 [227].

Evident from Fig. 4.21d, the FCC volume per atom is 8% smaller than the BCC one. We find an NM FCC phase at its equilibrium volume in agreement with Refs. 73, 134, 231. For a volume expansion of 3% with respect to the equilibrium volume, AF1 order in FCC Fe was predicted [134,231].

**Remark on experiments with Fe** None of the five experiments but Ref. 90 (Fe on Cu{001}) in Table 4.11 attempted to determine the magnetic structure of the epitaxial Fe films. FCC Fe on Cu{001} is an experimentally and theoretically vigorously investigated bilayer system, since this system exhibits a rich variety of structural and magnetic phases, e.g., Ref. 70,142,214,253. Early experiments with Fe on Cu{001} determined a strained FCC Fe overlayer with  $c/a \approx 1.40$  (BCT) [40,125], but later on, LEED pattern revealed thickness dependent superstructures ( $x \times 1$ ), typically  $x = 2, 4, 5$ , in thermally deposited Fe films [254]. Pseudomorphic Fe films in the FCC structure without any superstructures were reported in Ref. 90, which were grown by pulsed-laser-deposition. For thicknesses greater than 10 MLs, the film transformed to BCC. The layer resolved magnetic structure in FCC Fe films up to a thickness of 8 MLs [142] involves noncollinearity, i.e., layers tend to form pairs (blocks) with an almost antiparallel orientation of the spin moment in one block, and a noncollinear orientation between two adjacent blocks.

**Discussion of EBPs of Ru and Os** The EBPs of Ru and Os are similar to each other. The FCC structure coincides with the position of the global minimum of  $E(c/a)$ . The second, BCT minimum is at  $c/a = 0.85$  and at 0.84 for Ru and Os, respectively, see Fig. 4.19 and Table 4.11 for the complete data. The total energy along the EBP of Ru reaches a maximum at the BCC structure,

## CHAPTER 4. TRANSITION METALS, SELECTED ALKALINE EARTH METALS AND LANTHANIDES

---

but there is a discontinuity for  $c/a$  marginally larger than 1. In the case of Os, the EBP is also discontinuous, but the BCC point does not belong to the EBP.

The PW92 lattice parameter of BCC Ru amounts to  $a_{\text{BCC}} = 3.012 \text{ \AA}$ , and we computed  $c_{\text{zzzz}} \approx 80 \text{ GPa} > 0$  (cf. Sec. A.3.1). A plot of the function  $E(c)$  at  $a_{\text{BCC}}$  reveals a double well with the global minimum at  $c_{\text{BCC}} = a_{\text{BCC}}$ , Fig. 4.26a, i.e., the BCC point belongs to the EBP. The transition to the second minimum of  $E(c)$ , which causes the discontinuous EBP, takes place between  $a = 3.010 \text{ \AA}$  and  $a = 3.011 \text{ \AA}$  with  $c/a > 1$ . Figure 4.26b depicts  $D(E_{\text{F}})$  as function of  $c$  in the vicinity of  $a_{\text{BCC}}$ , from which we see a peak between the  $c_{\text{BCC}}$  and the minimum at approximately  $c = 3.25 \text{ \AA}$ . This peak may contribute to the occurrence of double wells in  $E(c)$  for BCC Ru, similar to the case of BCC La and of BCC Ir, see discussion in the text. For BCC Os,  $a_{\text{BCC}} = 3.061 \text{ \AA}$ , we computed  $c_{\text{zzzz}} \approx 30 \text{ GPa} > 0$ . The function  $E(c)$  at  $a_{\text{BCC}}$  exhibits a local minimum in energy at  $c_{\text{BCC}} = a_{\text{BCC}}$ , see Figs. 4.26c and 4.26d. The global minimum is at  $c = 3.332 \text{ \AA}$  and its energy difference to the local minimum is  $0.20 \text{ mHartree/atom}$ . Although  $c_{\text{zzzz}} > 0$ , BCC Os is metastable with an energy barrier of  $4 \mu\text{Hartree/atom}$  (Fig. 4.26d). We found, that this energy difference is stable with respect to an increase of the  $k$ -points from  $24^3$  to  $48^3$  and stable with respect to the use of default or enhanced 3D-grid. In fact, the curves in Fig. 4.26c were calculated with  $24^3 k$ -points, as determined from the convergence procedure of the Brillouin integration mesh, while the curve in Fig. 4.26d was obtained with  $48^3 k$ -points. The curvature of  $E(c)$  at  $a_{\text{BCC}}$  is larger than zero for  $|\epsilon_{zz}| < 0.01$  around the stationary point at  $\epsilon_{zz} = 0$ . A fit with a harmonic function following Eq. (A.7) on Page 138 to  $E(c)$  approximates  $E$  well only in a narrow range of  $|\epsilon_{zz}| < 0.005$  around the stationary point (Fig. 4.26d). Since the global minimum of  $E(c)$  for  $a_{\text{BCC}}$  is not at  $c_{\text{BCC}} = a_{\text{BCC}}$ , BCC Os is not a point of the EBP. The curves  $E(c)$  in the vicinity of  $a_{\text{BCC}}$  have two minima, the transition between both happens between  $a = 3.063 \text{ \AA}$  and  $a = 3.064 \text{ \AA}$  with  $c/a > 1$  (Fig. 4.26c). We do not find a prominent peak in the DOS at the Fermi energy as function of  $c$  in the vicinity of the discontinuity.

We predict FM states on the EBP for both Ru and Os. Magnetic order occurs for  $c/a \leq 0.90$  ( $a \geq 3.1 \text{ \AA}$ ) and  $c/a \leq 0.80$  ( $a \geq 3.35 \text{ \AA}$ ) for Ru and Os, respectively. In particular, BCT Ru with  $a = 3.18 \text{ \AA}$  and  $c/a = 0.85$ , for which  $E(c/a)$  is locally a minimum, orders ferromagnetically. The positions of the FM states on the EBP coincide with the positions of the highest NM DOS at  $E_{\text{F}}$ , see Fig. 4.21c.

**Magnetic properties of Ru along the EBP** We predict, that Ru orders ferromagnetically for states with  $a \geq 3.100 \text{ \AA}$ . The onset of magnetic order is accompanied with a reduction of the total energy of at most  $340 \mu\text{Hartree/atom}$  for the state at  $a = 3.250 \text{ \AA}$ , see Fig. 4.27. The spin moment amounts to  $0.4 - 0.5 \mu_{\text{B}}/\text{atom}$  depending on the in-plane lattice parameter. The local minimum of  $E(c/a)$  at  $a = 3.18 \text{ \AA}$  and  $c/a = 0.85$  possesses a spin moment of  $0.43 \mu_{\text{B}}/\text{atom}$ . AFM order is never more stable than FM order on the EBP. States that order with AF2 arrangement are in fact lower in total energy than NM states, but are energetically higher than states with FM order, Fig. 4.27. The decrease in total energy due to AF2 order relative to the NM states amounts to at most  $230 \mu\text{Hartree/atom}$  at  $a = 3.30 \text{ \AA}$ . The absolute value of the site resolved spin moment for AF2 order is generally smaller than for FM order (Fig. 4.27). None

#### 4.5. EPITAXIAL BAIN PATH OF TRANSITION METALS, SELECTED ALKALINE EARTH METALS AND LANTHANIDES

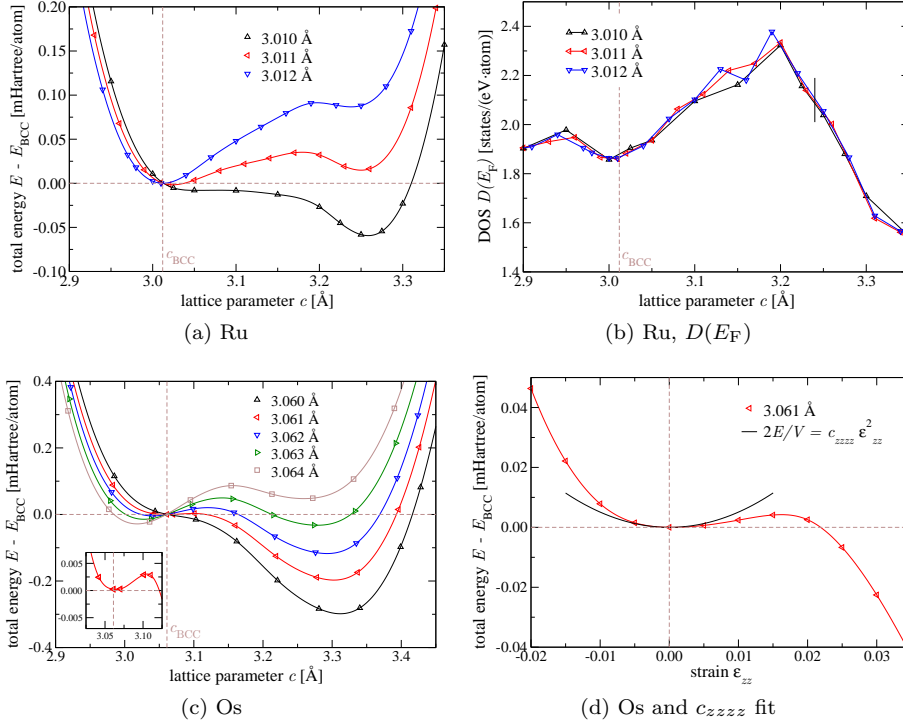


Figure 4.26: On the discontinuities of the EBP of **Ru** and **Os**. (a) depicts  $E(c)$  for three parameters  $a$ . Their values are stated in the legend.  $E(c)$  at  $a_{\text{BCC}} = 3.012$  Å has the global minimum at  $a_{\text{BCC}} = c_{\text{BCC}}$ . A vertical dashed line indicates  $c_{\text{BCC}}$ . The transition from the minimum with high  $c/a$  to the minimum with small  $c/a$  takes place between  $a = 3.010$  Å and  $a = 3.011$  Å. (b)  $D(E_F)$  as function of  $c$  for the same parameters  $a$  as in (a). A solid black line indicates the DOS of the second minimum of  $E(c)$  for  $a = 3.011$  Å. (c) Similar plot for Os as for Ru in (a).  $E(c)$  at  $a_{\text{BCC}} = 3.061$  Å has a local minimum at  $a_{\text{BCC}}$  (red curve and inset), the global minimum is found at  $3.332$  Å. The transition from the minimum with high  $c/a$  to the minimum with small  $c/a$  happens between  $a = 3.063$  Å and  $a = 3.064$  Å. (d) More detailed figure of  $E(c)$  at  $a = 3.061$  Å from (c).  $E$  is plotted as function of strain,  $\epsilon_{zz}$ . The black solid curve is a harmonic fit to five data points within  $|\epsilon_{zz}| \leq 0.01$ . The curvature of the fit function is the elastic constant  $c_{zzzz}$ . In subfigures (a), (c), and (d), the total energy is given with respect to  $E_{\text{BCC}}$ . A horizontal dashed line indicates the zero-level. Solid lines are spline interpolation to the data (symbols) and guide the eye.

of the calculations with assumed AF1 order converged into a solution with a finite spin moment on each site, i.e., the self-consistency cycle resulted in NM states. The onset of ferromagnetism in Ru happens spontaneously, since the curvature of  $E(m_s)$  at  $m_s = 0 \mu_B$ , as studied by FSM calculations, is negative (curves are not shown). Thus, the Stoner criterion is fulfilled.

Reference 247 calculated the CSBP for Ru and found a local energy minimum of  $E(a, c)$  at  $c/a \simeq 0.83$ . This state was predicted to order ferromagnetically with a spin moment equal to  $0.4 \mu_B/\text{atom}$  [247] (FP-LAPW [16], PBE96). It was further predicted, that Ru orders ferromagnetically along the CSBP for

## CHAPTER 4. TRANSITION METALS, SELECTED ALKALINE EARTH METALS AND LANTHANIDES

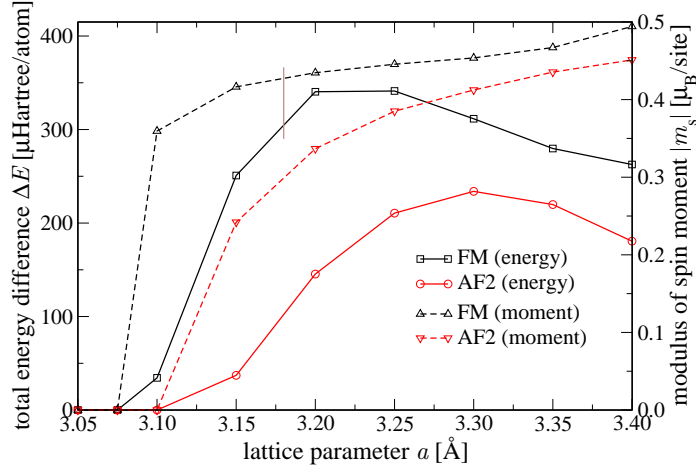


Figure 4.27: Total energy difference between NM states and magnetically ordered states along the EBP of **Ru**,  $\Delta E = E_{\text{non-spin-polarised}} - E_{\text{spin-polarised}}$ , assuming FM and AF2 order (*left hand ordinate and solid lines*). The modulus of the site resolved spin moment is plotted with *dashed lines using the right hand ordinate*. A grey vertical line indicates the position of the BCT structure which minimises  $E(a)$  at  $a = 3.18 \text{ \AA}$  ( $c/a = 0.85$ ). Lines guide the eye.

$c/a < 1$ . This work and Ref. 247 thus consistently predict an FM BCT state of Ru, whose energy corresponds to a local minimum of  $E(a, c)$ .

**Remark on experiments with Ru** Shiiki and Hio reported on BCT Ru as sputtered on a (110) oriented single-crystalline Mo substrate (lattice constant  $3.147 \text{ \AA}$ ) [200]. Lattice parameters of the 'single crystal like' Ru film, as determined by electron beam diffraction, were measured to  $a = 3.24 \text{ \AA}$  and  $c = 2.69 \text{ \AA}$  ( $c/a = 0.83$ ). Possible magnetic order was not investigated. The epitaxial relationship between BCT Ru and BCC Mo, Ru(110) ( $1 \times 1$ ) Mo(110), indicates that the EBP model does not apply to this epitaxial system, because the in-plane directions of the Ru film on Mo are [110] and [001], and the out-of-plane direction of the Ru film is  $[\bar{1}\bar{1}0]$  (for the EBP, in-plane directions are [100] and [010], and the out-of-plane direction is [001]).

**Magnetic properties of Os along the EBP** We predict ferromagnetism of Os on the EBP for states with  $a \geq 3.35 \text{ \AA}$ . The onset of magnetic order is accompanied by a reduction of the total energy. The largest energy difference between an NM and an FM state of the EBP amounts to  $21 \mu\text{Hartree/atom}$  at  $a = 3.40 \text{ \AA}$ , see Fig. 4.28. All values in Fig. 4.28 were obtained with  $48^3 k$ -points to verify the stability of the magnetic solution.  $24^3 k$ -points stabilised the total energy at a level lower than  $10 \mu\text{Hartree/atom}$  as determined from the convergence procedure of the Brillouin zone integration mesh. Because Os was calculated in the full-relativistic mode, we can analyse the spin, orbital, and total moments. The total moment is the sum of spin moment and orbital moment. In case of Os, the latter two couple parallel (Fig. 4.28). The quantisation axis



## 4.5. EPITAXIAL BAIN PATH OF TRANSITION METALS, SELECTED ALKALINE EARTH METALS AND LANTHANIDES

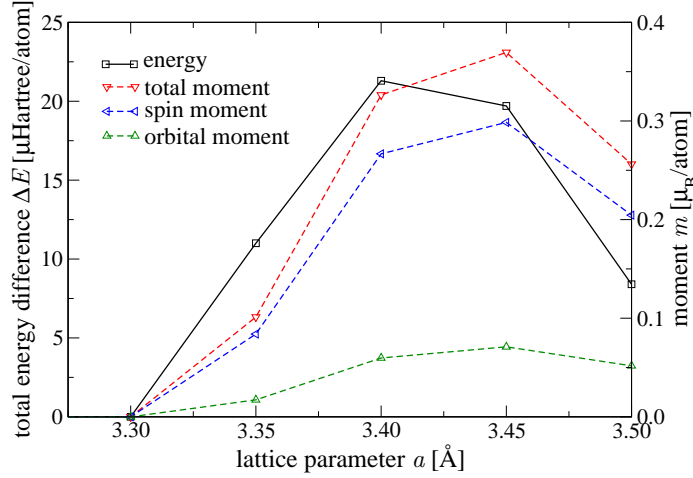


Figure 4.28: Total energy difference between NM and FM states along the EBP of **Os**,  $\Delta E = E_{\text{NM}} - E_{\text{FM}}$ , assuming FM order (*left hand ordinate and solid line*). The total, spin, and orbital moments are plotted with *dashed lines using the right hand ordinate*. Lines guide the eye.

was assumed parallel to the tetragonal axis ( $[001]$ ). The largest total moment among all FM states is  $0.37 \mu_B/\text{atom}$  at  $3.45 \text{ \AA}$  (Fig. 4.28). The Stoner criterion for ferromagnetism is not fulfilled. The Stoner parameter for Os is  $0.28 \text{ eV}$  [201]. Evident from Fig. 4.21c, the DOS at  $E_F$  is at most  $2.6/(\text{eV} \cdot \text{atom})$  (at  $c/a = 0.76$ ).

None of the states on the EBP exhibits neither AF1 nor AF2 order. In fact, all calculations with assumed AFM order converged into a solution with zero site-projected total moment, i.e., the self-consistency cycle resulted in NM states.

### 4.5.10 Group 9 elements: Co, Rh, and Ir

At RTP and below, Co is HCP. A martensitic transformation to FCC occurs at  $696 \text{ K}$  [43,256]. Both phases are FM below the critical temperature of  $1388 \text{ K}$  [7]. Rh and Ir are FCC; there are no further phases known.

**Discussion of the EBP of Co** Stationary points of  $E(c/a)$  with decreasing axial ratio are: global minimum at the FCC structure, maximum at the BCC structure, and a second minimum at  $c/a = 0.92$ . All states on the EBP order ferromagnetically, see Fig. 4.29 and Table 4.12 for the complete data.

An earlier total energy calculation excluded the possibility of AF1 and AF2 orders in the range  $0.8 \leq c/a \leq 1.5$  and  $0.8 \leq V/V_{\text{EXP}} \leq 1.1$  of the tetragonal parameter space [258] (calculations were done with FP-LAPW [16] and PBE96).  $V_{\text{EXP}}$  is the experimentally determined volume per atom of HCP Co. There is no publication on a similar calculation employing an LSDA functional to the best of our knowledge. From calculations of the  $q$ -dependent susceptibility for FCC Co (assumed lattice constant  $c_{\text{FCC}} = 3.412 \text{ \AA}$ ), Sandratskii and Kübler

Table 4.12: Overview of calculated GS properties and numerical data of stationary points for the elements **Co**, **Rh**, and **Ir** in comparison to computations and experiments from the literature, if available. General remarks on this Table are given in Sec. 4.5.1.

element	this work					literature								
	structure			$E - E_0$	theory			Ref.	experiment				Ref.	
	type	$a$ [Å]	$c/a$	[mHa]	$a$ [Å]	$c/a$	$E - E_0$		structure					
							[mHa]	setup	[ML]	$a$ [Å]	$c/a$			
Co	GS	HCP	2.433	1.612	0 (FM)	2.433	1.615	0 (FM)	[216] <sup><math>\delta f</math></sup>	bulk	2.506	1.624	(FM) [237]	
	SP	MIN	2.42	1.41	0.92 (FM)	2.48	$\sqrt{2}$	0.6 (FM)	[258] $\gamma^a$	Ni{001}	30	2.48	1.45	[32]
						2.50	$\sqrt{2}$	$C$ (NM)	[4] $\alpha^c$	Cu{001}	10	2.55	1.36	[31]
		MAX	2.74	1.00	5.30 (FM)		1	3.5 (FM)	[258] $\gamma^a$	Rh{001}	10	2.69	1.19 $\pm$ 0.02	[13]
		MIN	2.81	0.92	5.05 (FM)	2.83	1	2.65 + $C$ (NM)	[4] $\alpha^c$	Pd{001}	30	2.75	1.13 $\pm$ 0.04	[67]
					2.91	0.92	3.0 (FM)	[258] $\gamma^a$	Pt{001}	20	2.77	1.07	[233]	
							(NM)	[4] $\alpha^c$						
Rh	GS	FCC	3.769	–	0	3.759	–	0	[226] $\alpha^a$	bulk	3.803	–	[237]	
	SP	MIN	2.67	1.41	0		$\sqrt{2}$	0	[140] $\gamma^a$					
		MAX	3.02	1.00	14.41		1	13.24	[140] $\gamma^a$					
		MIN	3.22	0.82	9.26		0.814	7.81	[140] $\gamma^a$					
Ir	GS	FCC	3.820	–	0	3.834	–	0	[226] $\alpha^a$	bulk	3.839	–	[237]	
	SP	MIN	2.70	1.41	0		$\sqrt{2}$	0	[140] $\gamma^{a\dagger}$					
		MAX	3.08	0.94, 1.05	25.10		1	24.50	[140] $\gamma^{a\dagger}$					
		MIN	3.30	0.80	13.88		0.80	12.66	[140] $\gamma^{a\dagger}$					

## legend

$\alpha$	L(S)DA [174] (PW92)	$abc$	FP-LAPW [16] ( <sup><math>a</math></sup> WIEN2K, <sup><math>b</math></sup> WIEN97, <sup><math>c</math></sup> WIEN95)
$\beta$	L(S)DA [30, 239]	$d$	FP-LMTO [141]
$\gamma$	GGA [172] (PBE96)	$e$	PAW [110] (VASP)
$\delta$	L(S)DA [76] (HL71)	$f$	FP-LAPW [202]
$\dagger$	scalar-relativistic		

#### 4.5. EPITAXIAL BAIN PATH OF TRANSITION METALS, SELECTED ALKALINE EARTH METALS AND LANTHANIDES

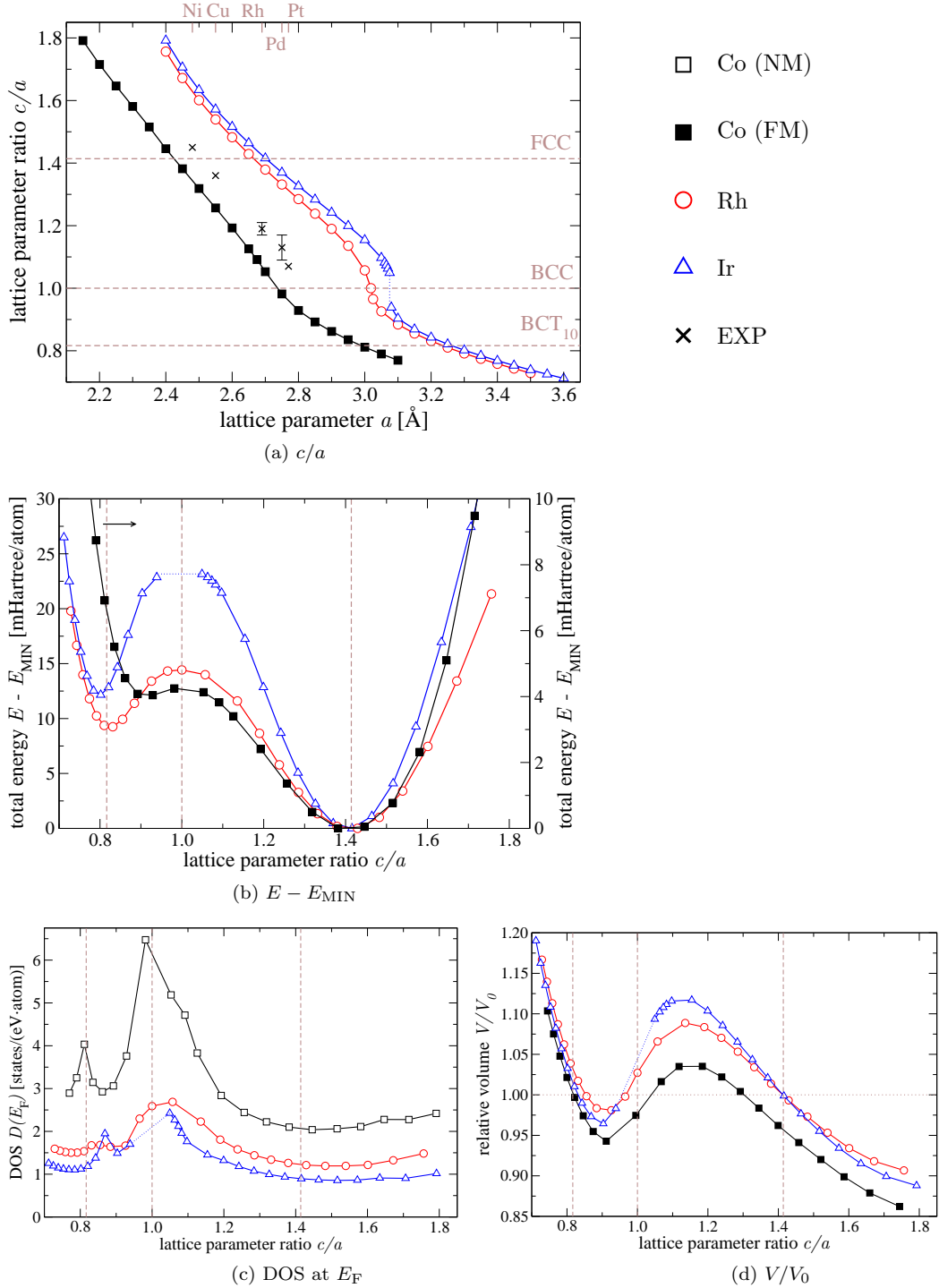


Figure 4.29: For the EBPs of **Co**, **Rh**, and **Ir**: (a)  $c/a$ , (b)  $E - E_{\text{MIN}}$ , (c)  $D(E_F)$ , and (d)  $V/V_0$ . Numerical data in Table 4.12. Lines guide the eye.

## CHAPTER 4. TRANSITION METALS, SELECTED ALKALINE EARTH METALS AND LANTHANIDES

reported the absence of local moments for  $q \geq 0.6$  in terms of the  $q$ -vector,  $(2\pi/c_{\text{FCC}})(0, 0, q)^T$  [193]. This includes AF1 order with  $q = 1$ . Band structure calculations with LSDA and GGA XC functionals consistently found, that an FM state of Co is always lower in energy than an NM one in the whole part of the aforementioned phase space [60, 258]. Based on the results of Refs. 193, 258, we limited ourselves to the investigation of NM and FM states along the EBP of Co. A possible AF1 or AF2 order was tested for as precaution at selected points on the EBP, but we found, that both orders are never more stable than FM order.

Table 4.13: Spin moment of Co in various structures as calculated in this work, and in comparison to theoretical and experimental references. All literature calculations were done for bulk in LSDA in the parameterisation of Ref. 238. Experimental values were determined at RT. Moments are per atom in units of  $\mu_{\text{B}}$ .

system	method	spin moment	Ref.
bulk HCP	FP-LCLO	1.51	this work
	FP-LAPW	1.45	[60]
	LMTO	1.63	[144]
	LMTO	1.57	[209]
	EXP	1.52	[21]
bulk FCC	FP-LCLO	1.54	this work
	FP-LAPW	1.51	[60]
	LMTO	1.64	[144]
	EXP	$1.523 \pm 0.015$	[187]
bulk BCC	FP-LCLO	1.65	this work
	FP-LAPW	1.62	[60]
	LMTO	1.74	[144]
	LCAO	1.64	[8]
250 MLs Co/GaAs ( $c/a = 1.00$ )	EXP	$1.38 \pm 0.01^{\text{a}}$	[182]
	EXP	$1.35^{\text{b}}$	[99]
bulk BCT ( $c/a = 0.92$ )	FP-LCLO	1.63	this work

<sup>a</sup> estimated value; total moment measured:  $(1.53 \pm 0.01) \mu_{\text{B}}/\text{atom}$ ; estimated orbital moment from HCP/FCC Co:  $0.15 \mu_{\text{B}}/\text{atom}$  [21, 187]

<sup>b</sup> estimated value (see table note a); total moment measured:  $1.50 \mu_{\text{B}}$  per atom

**Magnetic properties of Co along the EBP** The variation of the spin moment of Co along the EBP is depicted in Fig. 4.30. There is a trend to higher spin moments for small  $c/a$  ratio compared to lower spin moments for large  $c/a$  ratio. We computed a spin moment of  $1.51 \mu_{\text{B}}/\text{atom}$  for Co in the HCP structure at the theoretical equilibrium volume. This value is marginally smaller than the spin moment of FCC Co,  $1.54 \mu_{\text{B}}/\text{atom}$ . Both theoretical values are in reasonable agreement with experimentally determined spin moments in both

#### 4.5. EPITAXIAL BAIN PATH OF TRANSITION METALS, SELECTED ALKALINE EARTH METALS AND LANTHANIDES

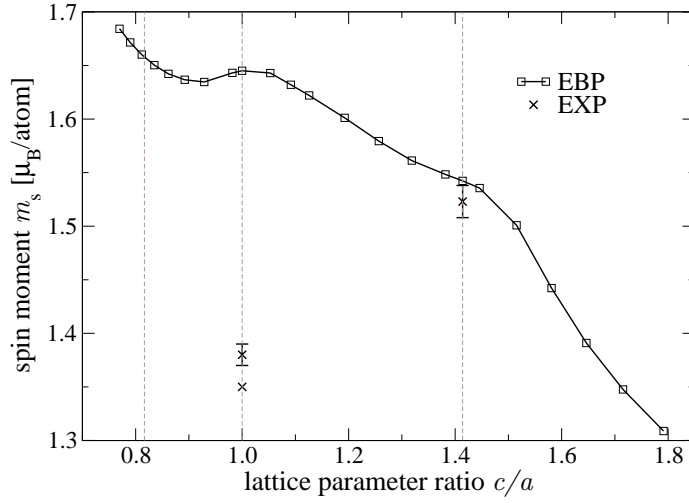


Figure 4.30: Calculated spin moment of **Co** along the EBP, and in comparison to experiments. Experimental data were taken from references as listed in Table 4.13. Lines guide the eye.

Co phases at RT, see Table 4.13. We also contrast our calculated spin moments with values from other band structure calculations. The agreement is best for the results of Fox *et al.* [60].

BCC Co was grown by means of epitaxial growth on GaAs [99, 182]. The measured total moment in a 250 MLs thick film was determined to  $(1.53 \pm 0.01) \mu_B/\text{atom}$  [182] and  $1.50 \mu_B/\text{atom}$  [99]. In order to estimate the contribution of the spin moment to the total moment, we assume the orbital moment in BCC Co to be identical to the orbital moment in bulk HCP Co or bulk FCC Co. The orbital moments of FCC and HCP Co, which are aligned parallel to the spin moments, were obtained to  $(0.147 \pm 0.003) \mu_B/\text{atom}$  [187] and  $0.147 \mu_B/\text{atom}$  [21], respectively. Hence, the experimental spin moment in BCC Co is estimated to  $\approx 1.35 - 1.38 \mu_B/\text{atom}$ , which is considerably smaller than our calculated value,  $1.65 \mu_B/\text{atom}$ , and values from comparable calculations (see Table 4.13). The significantly smaller experimental value of the spin moment of BCC Co may be due to structural defects or impurities in the Co film [99, 124, 153] (also see comments in the experiment below). Note that, for HCP and FCC Co, the calculated spin moments are in good agreement with experiments.

HCP Co is a strong ferromagnet, i.e., the majority *d*-band spin channel is fully occupied. In a good approximation, majority and minority spin projected DOS are identical, however rigidly shifted by an exchange splitting, which is proportional to the magnetisation [20, 219]. The spin moment of HCP Co amounts to  $1.51 \mu_B/\text{atom}$  in our calculation. According to Fig. 4.30, the spin moments in the FCC and BCC structures, as well as the spin moment of the second BCT minimum are of the same size or even larger than in HCP Co.

The calculated number of electrons per atom in *3d*-states is in a good approximation almost constant along the EBP, and almost the same as that of

## CHAPTER 4. TRANSITION METALS, SELECTED ALKALINE EARTH METALS AND LANTHANIDES

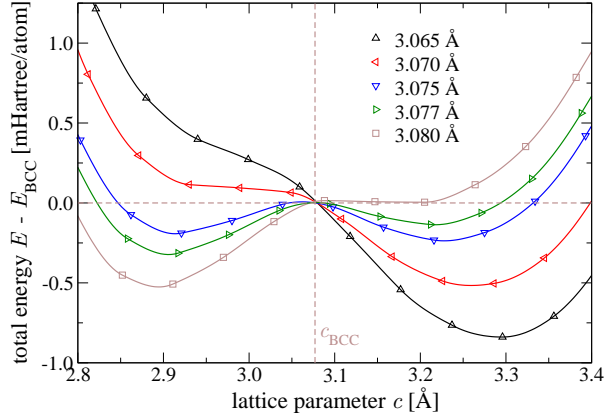


Figure 4.31: Double wells in the total energy as function of the lattice parameter  $c$ ,  $E(c)$ , for a set of in-plane lattice parameters  $a$  close to  $a_{\text{BCC}}$  for **Ir**. The values of  $a$  are stated in the legend. Total energies are given with respect to  $E_{\text{BCC}}$ . A horizontal dashed line indicates the zero level. The lattice parameter of BCC Ir is  $c_{\text{BCC}} = 3.077 \text{ \AA}$ . For  $a \leq 3.075 \text{ \AA}$ , the deeper minimum is located on the right hand side of the vertical dashed line, which indicates  $c_{\text{BCC}}$ . For  $a \geq 3.077 \text{ \AA}$ , the minimum is located on the left hand side of this line. The  $c$ -coordinate of the global minimum of  $E(c)$  changes abruptly between  $3.075 \text{ \AA}$ , and  $3.077 \text{ \AA}$ . At  $a_{\text{BCC}}$ , the position of the maximum of  $E(c)$  must coincide with the intersection point of both dashed lines. Solid lines are spline interpolation to the data (symbols) and guide the eye.

HCP Co. In fact, the number of  $d$ -electrons varies by 0.05 along the EBP in the limits  $2.15 \text{ \AA} \leq a \leq 3.00 \text{ \AA}$ . Based on the calculated DOS, we conclude that BCC and FCC Co, as well as BCT Co with  $c/a = 0.92$ , are strong ferromagnets. For BCT structures with small in-plane lattice parameter, hence large axial ratios, the spin moment gets considerable smaller compared to that of HCP Co (Fig. 4.30). The spin moment of BCT Co with  $c/a = 1.80$  is approximately  $1.3 \mu_{\text{B}}/\text{atom}$ . For this state we find that the majority spin  $d$ -band is not fully occupied anymore (weak ferromagnetism).

There is no published EBP of Co to the best of our knowledge, for which magnetic order was incorporated and for which an LSDA functional was employed. There is qualitative agreement between our findings and the EBP published by Ref. 258, which employed PBE96. In particular, the positions of the stationary points of  $E(c/a)$  are identical. The spin moments along the EBP from Ref. 258 are throughout approximately  $0.2 \mu_{\text{B}}/\text{atom}$  larger than the values obtained in this work. Alippi *et al.* calculated the EBP of Co using PW92 but neglected spin-polarisation [4]. Their reported  $a$ -coordinates of the stationary points of  $E(a, c)$  are systematically larger than our values, although there is an agreement in the  $c/a$  ratio (all values are listed for comparison in Table 4.12).

**Remark on experiments with Co** Among the experiments listed in Table 4.12, only Ref. 233 proved an FM state of the Co overlayer. The magnetic moment was, however, not published. The structure and magnetic properties of

#### 4.5. EPITAXIAL BAIN PATH OF TRANSITION METALS, SELECTED ALKALINE EARTH METALS AND LANTHANIDES

thick (250 MLs) films of BCC Co on GaAs{110}, grown by means of molecular beam epitaxy, were studied in Refs. 99,182. The epitaxial relationship between BCC Co and GaAs, Co(110) (1 × 1) GaAs(110), indicates that the EBP model does not apply to this epitaxial system, because the in-plane directions of the Co film on GaAs are [110] and [001], and the out-of-plane direction of the Co film is [1 $\bar{1}$ 0] (for the EBP, in-plane directions are [100] and [010], and the out-of-plane direction is [001]). Further, coherent epitaxial growth was not proven in Refs. 99,182.

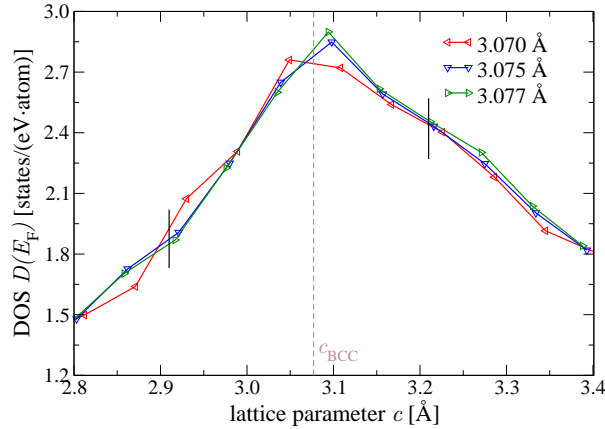


Figure 4.32: DOS at the Fermi energy,  $D(E_F)$ , as function of the lattice parameter  $c$  for  $a_{\text{BCC}} = c_{\text{BCC}} = 3.077 \text{ \AA}$  and two lattice parameters  $a$  close to  $a_{\text{BCC}}$  of **Ir**. The vertical dashed line indicates  $c_{\text{BCC}}$ . Two solid black lines indicate the DOS of the two minima of  $E(c)$  for  $a = 3.077 \text{ \AA}$ . The positions of both minima for the other two curves can be seen from Fig. 4.31. Solid lines to the data guide the eye.

**Discussion of EBPs of Ru and Ir** The global minimum of  $E(c/a)$  is the FCC configuration, the second, local minimum resides at  $c/a = 0.82$  and  $0.80$  for Rh and Ir, respectively, i.e., their ratios are close to that of BCT<sub>10</sub>, see Fig. 4.29 and Table 4.12 for the complete data. The BCC structure of Rh coincides with the maximum of  $E(c/a)$ . The BCC configuration of Ir has an elastic constant  $c_{zzzz} < 0$  (Section A.3.2) and is therefore not a point of the EBP. The lattice parameter of BCC Ir, evaluated in  $Im\bar{3}m$  symmetry, is  $c_{\text{BCC}} = 3.077 \text{ \AA}$ . The function  $E(c)$  in the vicinity of  $a_{\text{BCC}} = a_{\text{BCC}}$  shows double wells, see Fig. 4.31. The transition from the minimum with large  $c$ -lattice parameter to the minimum with small  $c$ -lattice parameter is between  $a = 3.075 \text{ \AA}$  and  $a = 3.077 \text{ \AA}$ . The change of  $c$  across the discontinuity amounts to  $\Delta c = 0.30 \text{ \AA}$ . We computed for BCC Ir  $D(E_F) = 2.80 / (\text{eV} \cdot \text{atom})$ . This value is higher than  $D(E_F)$  at the discontinuity of the EBP, see Fig. 4.29c. From Fig. 4.32 we see, that  $D(E_F)$  as function of  $c$  peaks in the vicinity of  $c_{\text{BCC}}$ , and that  $D(E_F)$  is significantly smaller than the peak value for both minima of  $E(c)$  around  $a_{\text{BCC}}$ . That is, similar to La, a distortion from BCC to BCT (increase or decrease of  $c$ ,  $a$  fixed) reduces the DOS at the Fermi energy, and thus, the high value of  $D(E_F)$  may help to destabilise the BCC structure of Ir.

## CHAPTER 4. TRANSITION METALS, SELECTED ALKALINE EARTH METALS AND LANTHANIDES

---

There are no published EBPs of Rh and Ir to the best of our knowledge. Published data on stationary points of  $E(a, c)$  within PBE96 agree with our results—in particular the position of the local BCT minimum—and there is agreement in the energy differences between the stationary points and  $E_0$  [140], see Table 4.12 for complete data. The instability of FCC Ir was not a point of discussion in Ref. 140.

### 4.5.11 Group 10 elements: Ni, Pd, and Pt

Ni is FCC at RTP, and FM below the Curie temperature of 627 K [7, 43]. Pd and Pt are FCC as well. The phase diagrams do not exhibit any further solid phase with different crystal structure. The FCC phase of Pt was found stable in shock compression experiments up to 660 GPa. The stability is attributed to a weak  $d \rightarrow s$  electron transfer inhibiting phase transitions [86].

**Discussion of the EBPs** The EBPs of Ni, Pd, and Pt consistently locate the FCC structure and the BCC structure at the position of the global minimum and the global maximum of  $E(c/a)$ , respectively, see Table 4.15 and Figs. 4.34 for the elaborate results. The positions of the local minimum of Ni and Pd are found at  $c/a = 0.87$  and  $c/a = 0.88$ , respectively. The depth of the local minimum in energy relative to the BCC–FCC energy barrier is similar for both elements. The EBP of Pt is different, because the BCT minimum is located at a position with smaller axial ratio,  $c/a = 0.81$ , and the depth of the local minimum in energy is larger than in the other two cases.

**Magnetic properties of Ni along the EBP** The magnetic properties of BCT Ni in a large part of the tetragonal parameter space,  $0.8 \leq c/a \leq 1.5$  and  $0.7 \leq V/V_{\text{EXP}} \leq 1.5$ , were recently studied within PBE96 [258].  $V_{\text{EXP}}$  is the experimentally determined equilibrium volume of FCC Ni. The dominant magnetic order in this part of the phase space is FM one. NM states occur for  $V/V_{\text{EXP}} < 0.85$  in a for this work not interesting part of the phase space. Ni with assumed AF1 and AF2 orders had throughout higher energies in the whole part of the studied phase space. From calculations of the  $q$ -dependent susceptibility for FCC Ni (assumed lattice constant  $c_{\text{FCC}} = 3.466 \text{ \AA}$ ), Sandratskii and Kübler reported the absence of local moments for  $q \geq 0.5$  in terms of the  $q$ -vector,  $(2\pi/c_{\text{FCC}})(0, 0, q)^T$  [193]. This includes AF1 order with  $q = 1$  and AF2 order with  $q = 0.5$ . Based on the results of Refs. 193, 258, we limited ourselves to the investigation of NM and FM states along the EBP of Ni. A possible AF1 or AF2 order was tested for as precaution for selected points of the EBP, but we found, that both orders are never more stable than FM order.

All states on the EBP of Ni are FM. The maximum spin moment is  $0.60 \mu_{\text{B}}$  per atom for the state with  $c/a = 1.38$ , see Fig. 4.33. The calculated spin moment of FCC Ni is only slightly smaller,  $0.59 \mu_{\text{B}}/\text{atom}$ . This value is larger than the experimental value at RT,  $0.510 \pm 0.006 \mu_{\text{B}}/\text{atom}$  [187], but agrees with a previous calculations [50]. The spin moment of BCC Ni,  $0.44 \mu_{\text{B}}/\text{atom}$ , is smaller than the one of FCC Ni. We note a characteristic dip in the spin moment along the EBP, which is centred around BCC Ni (Fig. 4.33). The spin moment of the BCT minimum at  $c/a = 0.87$ ,  $0.55 \mu_{\text{B}}/\text{atom}$ , is almost as large as



## 4.5. EPITAXIAL BAIN PATH OF TRANSITION METALS, SELECTED ALKALINE EARTH METALS AND LANTHANIDES

Table 4.14: Spin moment of **Ni** in various structures as calculated in this work, in comparison to theoretical and experimental references. References 50 and 150 used the Vosko-Wilk-Nusair [239] and the von Barth-Hedin [238] parameterisation (LSDA), respectively. Experimental values were determined at RT [187] and at 5 K [222, 223]. Moments are per atom in units of  $\mu_B$ .

system	method	spin moment	Ref.
bulk FCC	FP-LCLO	0.59	this work
	LMTO	0.59	[50]
	EXP	$0.518 \pm 0.006$	[187]
bulk BCC	FP-LCLO	0.44	this work
	PAW	0.5	[150]
25 ML Ni/GaAs ( $c/a = 1.00$ )	EXP	$0.48 \pm 0.08^a$	[222, 223]
bulk BCT ( $c/a = 0.87$ )	FP-LCLO	0.55	this work

<sup>a</sup> estimated value; total moment measured:  $(0.53 \pm 0.08) \mu_B/\text{atom}$ , estimated orbital moment from FCC Ni:  $\approx 0.05 \mu_B/\text{atom}$  [187]

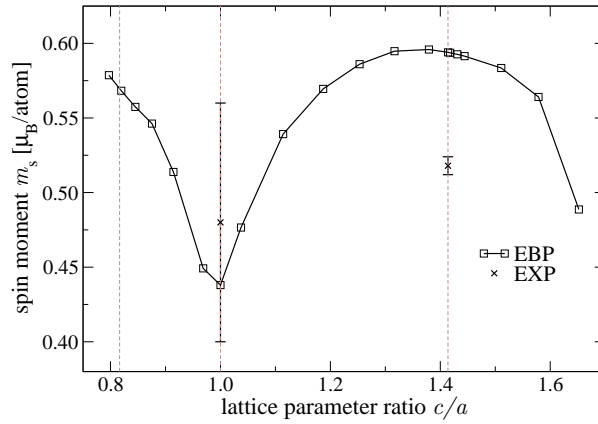


Figure 4.33: Calculated spin moment of **Ni** along the EBP, and in comparison to experiments. Experimental data were taken from references as listed in Table 4.14. Lines guide the eye.

in the FCC structure. In Table 4.14 we compiled experimental and theoretical references.

References 222, 223 reported a total moment of  $(0.53 \pm 0.08) \mu_B/\text{atom}$  measured in 25 MLs thick films with BCC structure epitaxially grown on GaAs(001). We estimated the experimental spin moment by subtracting the experimental bulk orbital moment value of FCC Ni,  $(0.0508 \pm 0.0012) \mu_B/\text{atom}$  [187]. The measured orbital moment of BCC Ni was not available. The error bar of the experimentally determined total moment of Ni films in the BCC structure ( $0.08 \mu_B/\text{atom}$ ) is larger than the estimated orbital moment.

The EBP of Ni was considered in Ref. 258 using PBE96. These findings

Table 4.15: Overview of calculated GS properties and numerical data of stationary points for the elements **Ni**, **Pd**, and **Pt** in comparison to computations and experiments from the literature, if available. General remarks on this Table are given in Sec. 4.5.1.

element		this work				literature								
		structure			$E - E_0$	theory			Ref.	experiment				Ref.
		type	$a$ [Å]	$c/a$	[mHa]	$a$ [Å]	$c/a$	[mHa]		setup	[ML]	$a$ [Å]	$c/a$	
Ni	GS	FCC	3.428	–	0 (FM)	3.423	–	0 (FM)	[226] <sup>αα</sup>	bulk	3.535	–	(FM) [237]	
	SP	MIN	2.42	1.41	0 (FM)	2.49	$\sqrt{2}$	0 (FM)	[258] <sup>γa</sup>	Pd{001}	12	2.75	1.11 ± 0.04	[180]
		MAX	2.73	1.00	3.80 (FM)	2.80	1	3.7 (FM)	[258] <sup>γa</sup>	GaAs{001}	25	2.82	1.00	[222, 223]
		MIN	2.86	0.87	3.19 (FM)	2.95	0.87	3.1 (FM)	[258] <sup>γa</sup>					
Pd	GS	FCC	3.852	–	0	3.848	–	0	[226] <sup>αα</sup>	bulk	3.890	–	[237]	
	SP	MIN	2.72	1.41	0	2.77	1.41	0	[96] <sup>αb</sup>	W{001} ≈ 13	3.17	(0.92 or 0.95)±0.03	[94]	
						2.80	1.41	0	[96] <sup>γb</sup>					
		MAX	3.07	1.00	2.36	3.07	1.00	1.85	[96] <sup>αb</sup>					
						3.12	1.00	2.05	[96] <sup>γb</sup>					
	MIN	3.20	0.88	2.17	3.20	0.92	1.75	[96] <sup>αb</sup>						
					3.29	0.88	1.85	[96] <sup>γb</sup>						
Pt	GS	FCC	3.913	–	0	3.923	–	0	[226] <sup>αα</sup>	bulk	3.923	–	[237]	
	SP	MIN	2.77	1.41	0									
		MAX	3.11	1.00	4.48									
		MIN	3.34	0.81	1.47									

legend

<sup>α</sup>	L(S)DA [174] (PW92)	<sup>abc</sup>	FP-LAPW [16] ( <sup>a</sup> WIEN2K, <sup>b</sup> WIEN97, <sup>c</sup> WIEN95)
<sup>β</sup>	L(S)DA [30, 239]	<sup>d</sup>	FP-LMTO [141]
<sup>γ</sup>	GGA [172] (PBE96)	<sup>e</sup>	PAW [110] (VASP)
†	scalar-relativistic		

#### 4.5. EPITAXIAL BAIN PATH OF TRANSITION METALS, SELECTED ALKALINE EARTH METALS AND LANTHANIDES

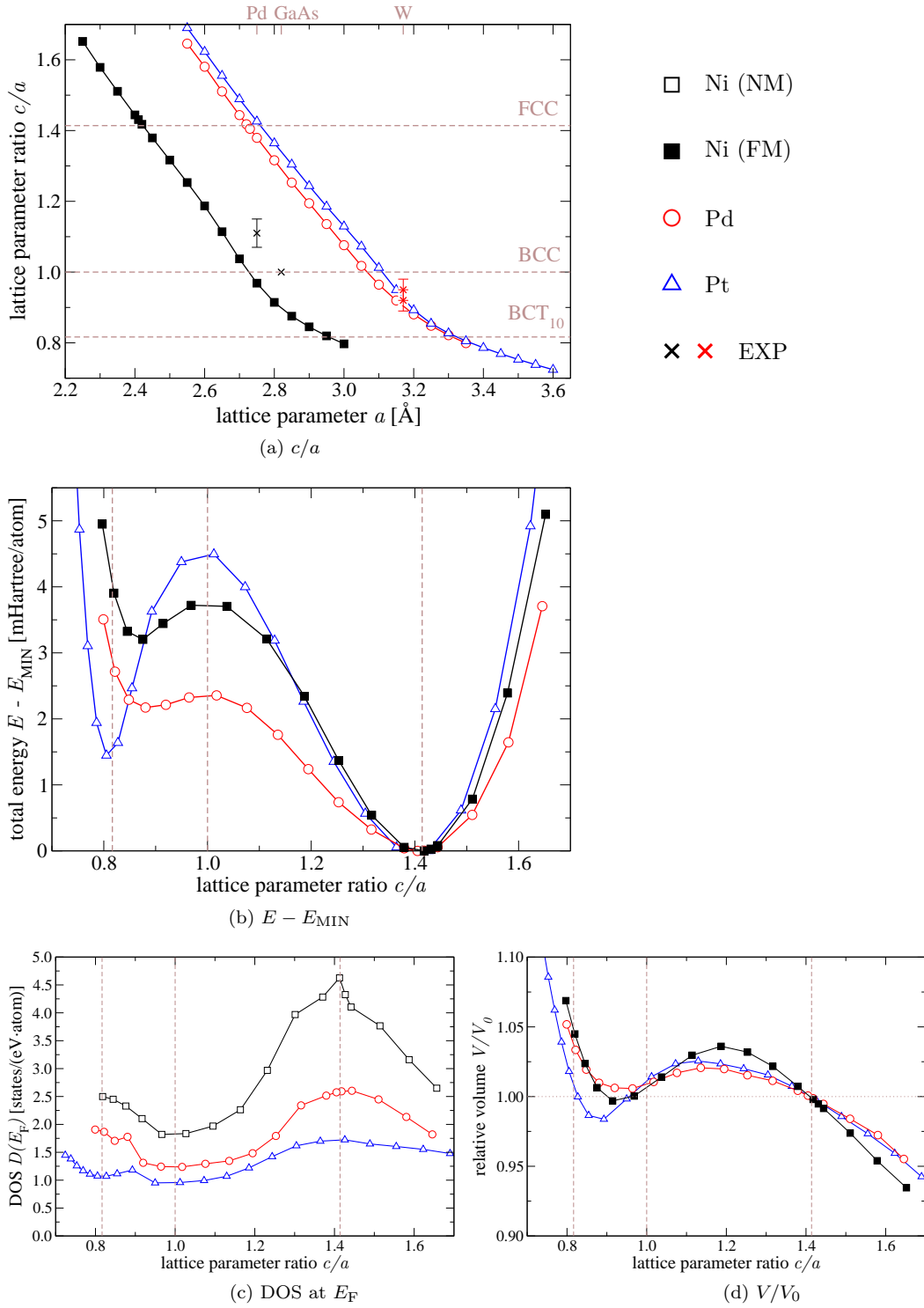


Figure 4.34: For the EBPs of Ni, Pd, and Pt: (a)  $c/a$ , (b)  $E - E_{\text{MIN}}$ , (c)  $D(E_F)$ , and (d)  $V/V_0$ . Numerical data in Table 4.15. Lines guide the eye.

## CHAPTER 4. TRANSITION METALS, SELECTED ALKALINE EARTH METALS AND LANTHANIDES

---

are in reasonable agreement with our results, see Table 4.15 for the numerical comparison. The spin moments are throughout larger than our values, but the characteristic dip in the spin moment along the EBP at  $c/a = 1$  was also found. The  $a$ -lattice parameter of the stationary points of  $E(a, c)$ , as reported in the latter reference, are throughout larger than our computed values, which can be attributed to the stronger overbinding effect of PW92. Jona *et al.* computed the EBP of Pd with PW92 and with PBE96 [96] (Table 4.15). They predicted a local minimum in  $E(c/a)$  at  $c/a = 0.92$  and  $c/a = 0.88$  for PW92 and PBE96, respectively (our value is 0.88). The Fermi energy of FCC Pd is directly located above a distinctive van Hove singularity in the DOS. If the lattice parameter of palladium is expanded by 5%, it is predicted to order ferromagnetically [34]. Reference 197 ruled out the possibility of FM order in bulk Pd for the tetragonal states of the EBP. Haftel and Gall computed the UBP of Pt in Ref. 72, in which we did not find published numerical data on stationary points of  $E(a, c)$ , nor allowed the presented graphical material to extract such data.

**Remark on experiments with Pd** An approximately 25 MLs thick Pd film was pseudomorphically grown on W{001} (lattice constant 3.16 Å) [94]. The Pd overlayer was highly defective. On the basis of the LEED data, the interlayer distance could not be unambiguously determined ( $c/a \approx 0.92$  or 0.95). The authors of Ref. 94 concluded, that the overlayer structure is ‘probably a strained state of the BCT phase’ which was prior predicted in Ref. 96.

### 4.5.12 Group 11 elements: Cu, Ag, and Au

The noble metals Cu, Ag, and Au are FCC at RTP, and there are no further reported solid phases [43, 256]. Although the copper-group’s nominal electronic configuration states a filled  $d$ -shell, namely  $s^1d^{10}$ , thus suggesting a nearly-free electron metal, it was shown, that the  $d$ -band has an important effect on the bonding by  $s-d$  hybridisation [204]. Theory predicts a stable FCC phase under pressure due to  $d \rightarrow s$  electron transfer [148], similar to Pt [86].

**Discussion of EBPs** The EBPs of all three elements exhibit many common features, for example, small energy differences between the stationary points of  $E(c/a)$  and  $E_0$ , see Figs. 4.36 and Table 4.16 for the complete data. The global minimum of  $E$  is at the FCC structure, which is the GS crystal structure. The maximum of  $E(c/a)$  coincides with the BCC structure, whose energy is typically  $\approx 1$  mHartree/atom higher than  $E_0$ . The second BCT minimum is at  $c/a < 1$ , the exact position varies with the element. The energy differences between the maximum and the second minimum of Ag and Au amount to about 0.1 mHartree/atom. The related value for Cu is 0.01 mHartree/atom, shown more clearly in an enlarged picture in Fig. 4.35.

Inspired by an earlier experimental success on the epitaxial growth of a ‘somewhat distorted’ metastable BCC configuration of Cu [245], pseudopotential total energy calculations of  $E(a, c)$  predicted a new, non-cubic BCT equilibrium structure for Cu ( $a = 2.76$  Å,  $c/a = 1.2$ ) [151], which is referred to as  $\alpha$ -BCT. This prediction attracted interest, both experimental [119, 121] and theoretical [108, 127]. The all-electron calculations from Refs. 108, 127 consistently disproved the existence of the  $\alpha$ -BCT phase, and suggested computational errors

## 4.5. EPITAXIAL BAIN PATH OF TRANSITION METALS, SELECTED ALKALINE EARTH METALS AND LANTHANIDES

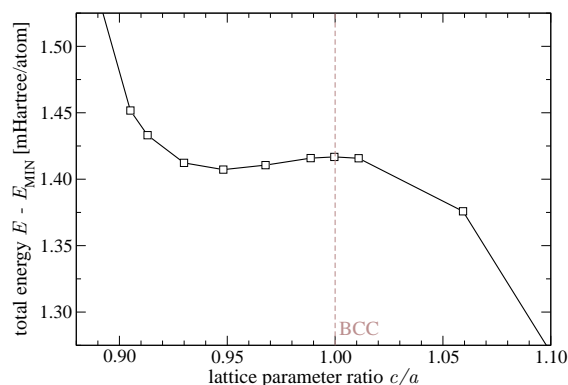


Figure 4.35: Enlarged picture detail of Fig. 4.36b for **Cu** highlighting the local BCT minimum at  $c/a = 0.95$  and the adjacent maximum at the BCC structure. Lines guide the eye.

in Ref. 151. In fact, a BCT minimum at  $c/a = 1.2$  was not confirmed in recent calculations of stationary points in the tetragonal parameter space [4, 95, 140]. Experiments [119, 121], initially aimed at pseudomorphic epitaxial growth of the predicted  $\alpha$ -BCT metastable phase, identified the structures in the BCT films with  $c/a = 1.17$  and  $c/a = 1.18$  as strained from FCC (complete data are in Table 4.16).

We can compare our own findings with available literature (see Table 4.16). Reference 95 published two EBPs of Cu, one calculated with PW92 and one with PBE96. There is no striking difference between both EBPs, only the lattice parameters of stationary points obtained with PW92 are smaller than the ones obtained with PBE96, which is attributed to the known LSDA overbinding. We find good agreement in the position of stationary points and in the energy differences of all stationary points with respect to  $E_0$  with the PW92 results from Ref. 95. For Ag and Au, there are only literature results from total energy calculations employing the PBE96 parameterisation [95, 140]. The  $c/a$ -coordinates of the second minima of Ag and Au from the latter references agree with our findings. We confirm the small energy difference between the BCC configuration and the local minimum of  $E(c/a)$  of Cu, which was earlier mentioned in Refs. 95, 140. In contrast, Ref. 4 reported two energetically degenerate states. Haftel and Gall performed UBP calculations for all three elements [72], but we did not find published numerical data on stationary points in  $E(a, c)$ , nor allowed the presented graphical material to extract such data.

### 4.5.13 Group 12 elements: Zn, Cd, and Hg

Zn and Cd are HCP at RTP with unusually large  $c/a$  ratios compared to early TMs or elements past the middle of the TM series. No other solid phases are known [43, 256]. The GS of Hg is BCT with  $c/a = 0.707$  (known as  $\beta$ -Hg) [43]. At 79 K at RP, there is a phase transition to rhombohedral Hg, known as  $\alpha$ -Hg. The PW92 parameterisation of the XC functional was recently shown to yield the correct lattice structure of  $\alpha$ -Hg (with moderate overbinding), in contrast to

Table 4.16: Overview of calculated GS properties and numerical data of stationary points for the elements **Cu**, **Ag**, and **Au** in comparison to computations and experiments from the literature, if available. General remarks on this Table are given in Sec. 4.5.1.

element	this work					literature								
	structure			$E - E_0$ [mHa]	theory			Ref.	experiment				Ref.	
	type	$a$ [Å]	$c/a$		$a$ [Å]	$c/a$	$E - E_0$ [mHa]		structure					
				setup				[ML]	$a$ [Å]	$c/a$				
<b>Cu</b>	GS	FCC	3.523	–	0	3.522	–	0	[226] <sup>αα</sup>	bulk	3.613	–	[237]	
	SP	MIN	2.49	1.41	0	2.53	$\sqrt{2}$	0	[4] <sup>ab</sup>	Pd{001}	10	2.75	1.18	[119]
						2.51	1.42	0	[95] <sup>αc</sup>	Pt{001}	15	2.78	1.17 ± 0.02	[121]
						2.57	1.42	0	[95] <sup>γc</sup>					
							$\sqrt{2}$	0	[140] <sup>γa</sup>					
		MAX	2.80	1.00	1.42	2.80	1	1.65	[95] <sup>αc</sup>					
						2.91	1	1.48	[95] <sup>γa</sup>					
							1	1.35	[140] <sup>γa</sup>					
MIN	2.85	0.95	1.41	2.89	0.94	1.6	[95] <sup>αc</sup>							
				2.97	0.93	1.43	[95] <sup>γa</sup>							
					0.95	1.34	[140] <sup>γa</sup>							
<b>Ag</b>	GS	FCC	4.016	–	0	4.007	–	0	[226] <sup>αα</sup>	bulk	4.060	–	[237]	
	SP	MIN	2.84	1.41	0		$\sqrt{2}$	0	[140] <sup>γa</sup>					
		MAX	3.20	1.00	1.39		1	1.20	[140] <sup>γa</sup>					
		MIN	3.31	0.90	1.33		0.89	1.12	[140] <sup>γa</sup>					
<b>Au</b>	GS	FCC	4.052	–	0	4.066	–	0	[226] <sup>αα</sup>	bulk	4.072	–	[237]	
	SP	MIN	2.87	1.41	0		$\sqrt{2}$	0	[140] <sup>γa†</sup>					
		MAX	3.22	1.00	1.05		1	0.89	[140] <sup>γa†</sup>					
		MIN	3.39	0.86	0.92	3.42	0.84	0.66	[64, 72] <sup>γe†</sup>					
					0.85	0.74	[140] <sup>γa†</sup>							

legend

<sup>α</sup>	L(S)DA [174] (PW92)	<sup>abc</sup>	FP-LAPW [16] ( <sup>a</sup> WIEN2K, <sup>b</sup> WIEN97, <sup>c</sup> WIEN95)
<sup>β</sup>	L(S)DA [30, 239]	<sup>d</sup>	FP-LMTO [141]
<sup>γ</sup>	GGA [172] (PBE96)	<sup>e</sup>	PAW [110] (VASP)
<sup>†</sup>	scalar-relativistic		

#### 4.5. EPITAXIAL BAIN PATH OF TRANSITION METALS, SELECTED ALKALINE EARTH METALS AND LANTHANIDES

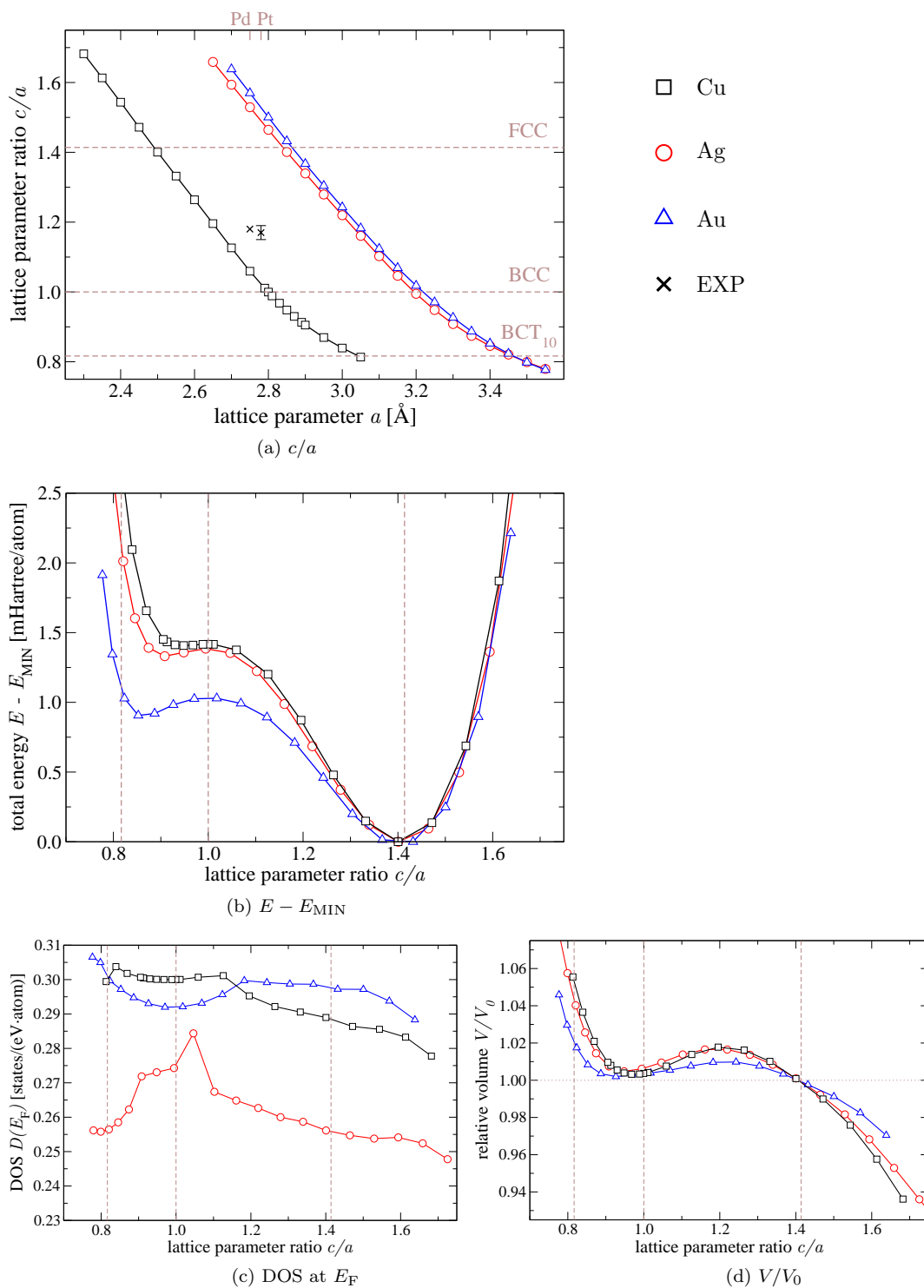


Figure 4.36: For the EBPs of **Cu**, **Ag**, and **Au**: (a)  $c/a$ , (b)  $E - E_{\text{MIN}}$ , (c)  $D(E_F)$ , and (d)  $V/V_0$ . Numerical data in Table 4.16. Lines guide the eye.

Table 4.17: Overview of calculated GS properties and numerical data of stationary points for the elements **Zn**, **Cd**, and **Hg** in comparison to computations and experiments from the literature, if available. General remarks on this Table are given in Sec. 4.5.1.

element		this work				literature							
		structure			$E - E_0$	theory			Ref.	experiment			Ref.
		type	$a$ [Å]	$c/a$	[mHa]	$a$ [Å]	$c/a$	[mHa]		setup [ML]	$a$ [Å]	$c/a$	
<b>Zn</b>	GS	HCP	2.574	1.842	0	2.56	1.91	0	[248] <sup><math>\beta f</math></sup>	bulk	2.665	1.856	[237]
	SP	MIN	2.68	1.41	0.99								
		MAX	3.02	1.00	3.61								
		MIN	3.30	0.77	1.08								
<b>Cd</b>	GS	HCP	2.926	1.852	0	2.93	1.78	0	[248] <sup><math>\beta f</math></sup>	bulk	2.979	1.886	[237]
	SP	MIN	3.05	1.41	0.52								
		MAX	3.44	1.00	2.97								
		MIN	3.78	0.76	0.44								
<b>Hg</b>	GS	BCT	3.928	0.728	0			0		bulk	3.995	0.707	[43]
	SP	MIN	2.98	1.69	0.249								
		MAX	3.07	1.51, 1.53	0.436								
		MIN	3.14	1.41	0.401								
		MAX	3.55	1.00	0.492								
MIN	3.93	0.73	0										

legend

$\alpha$	L(S)DA [174] (PW92)	$abc$	FP-LAPW [16] ( <sup><math>a</math></sup> WIEN2K, <sup><math>b</math></sup> WIEN97, <sup><math>c</math></sup> WIEN95)
$\beta$	L(S)DA [30, 239]	$d$	FP-LMTO [141]
$\gamma$	GGA [172] (PBE96)	$e$	PAW [110] (VASP)
$\dagger$	scalar-relativistic	$f$	LCAO [195] (CRYSTAL03)



#### 4.5. EPITAXIAL BAIN PATH OF TRANSITION METALS, SELECTED ALKALINE EARTH METALS AND LANTHANIDES

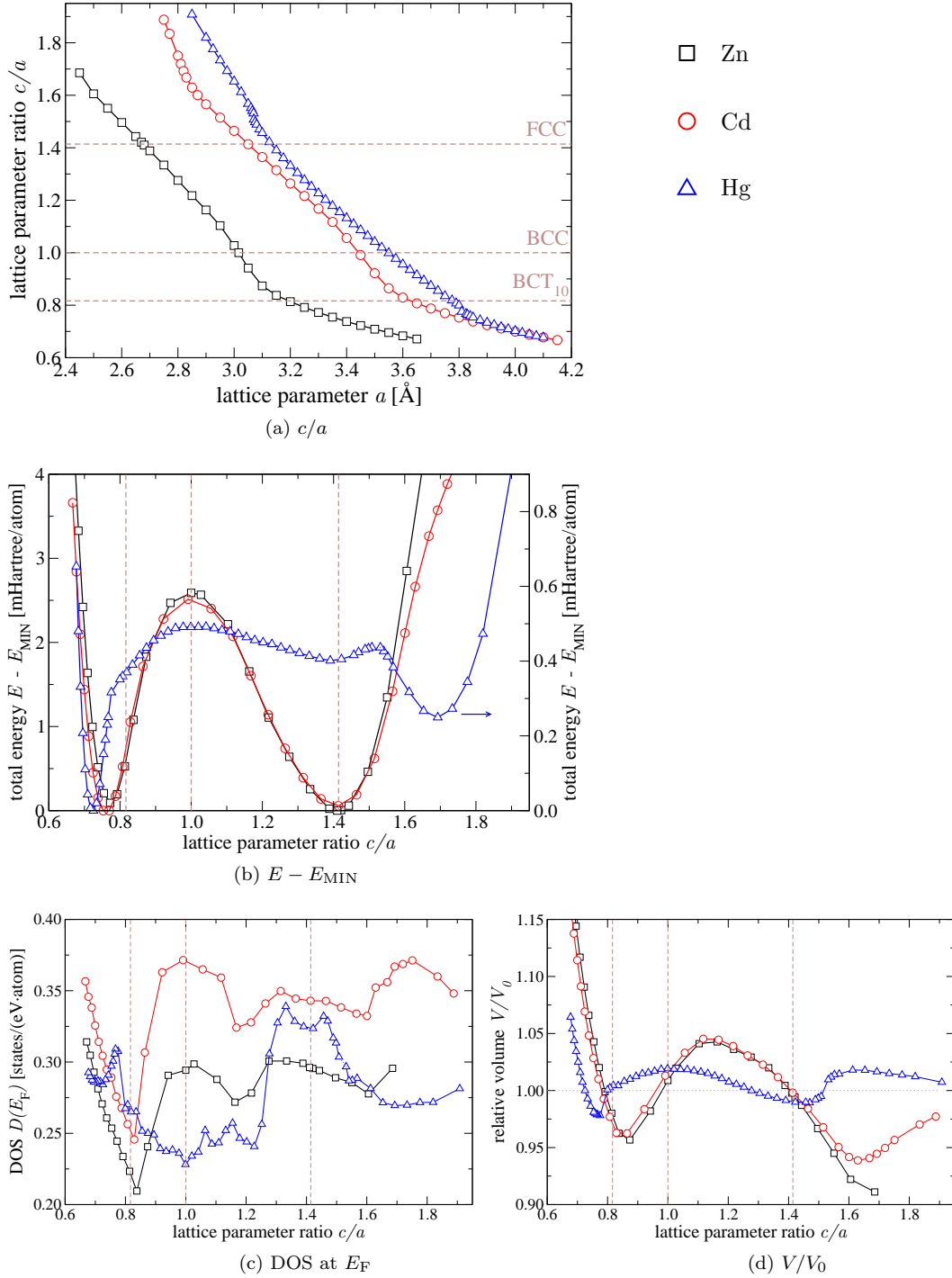


Figure 4.37: For the EBPs of **Zn**, **Cd**, and **Hg**: (a)  $c/a$ , (b)  $E - E_{\text{MIN}}$ , (c)  $D(E_{\text{F}})$ , and (d)  $V/V_0$ . Numerical data in Table 4.17. Lines guide the eye.

## CHAPTER 4. TRANSITION METALS, SELECTED ALKALINE EARTH METALS AND LANTHANIDES

---

gradient corrected functionals (such as PBE96), which predicted FCC to be the minimum energy structure accompanied by strongly underbound lattice parameters [65] (the  $\beta$ -phase was not considered in this reference). Moreover, relativistic effects on the level of the scalar-relativistic approximation were shown to be essential to yield a stable BCT structure of Hg [149]. In a purely non-relativistic treatment, LDA predicted otherwise a HCP GS [65, 149].

**Discussion of the EBP of Zn and of Cd** Common for both elements is the maximum of  $E(c/a)$ , which coincides with the BCC structure. The FCC structure is at the minimum of the energy along the EBP. In the case of Zn it is the global minimum. In the case of Cd, FCC is the local minimum with an energy 0.06 mHartree/atom above the energy of the global BCT minimum at  $c/a = 0.76$ . At  $c/a = 0.77$ , we find the local minimum of Zn with an energy 0.09 mHartree/atom above the energy of the FCC structure, see Fig. 4.37 and numerical data in Table 4.17. There are no published data on non-volume conserving Bain paths for Zn and Cd to the best of our knowledge.

**Discussion of the EBP of Hg** The experimental GS of Hg is BCT with  $a = 3.995 \text{ \AA}$  and  $c/a = 0.707$  [43]. We calculated  $a = 3.928 \text{ \AA}$  in good agreement with the experiment. We overestimate the  $c/a$  ratio of the GS by 3%, since our calculated value is  $c/a = 0.728$ . This tetragonal state is the global minimum of  $E(c/a)$ , see Fig. 4.37 and numerical data in Table 4.17. The energy along the EBP has two additional local minima, one coincides with the FCC structure and one is located at  $c/a = 1.69$ . One maximum of  $E(c/a)$  is found at the BCC structure. In the vicinity of  $a = 3.069 \text{ \AA}$ , the function  $E(c)$  exhibits a double well with  $\Delta c = 0.06 \text{ \AA}$  between both minima. The transition from the minimum with higher  $c/a$  to the minimum with lower  $c/a$  takes place between  $a = 3.069 \text{ \AA}$  and  $a = 3.070 \text{ \AA}$ .  $E(a)$  peaks at this position. We found a small shoulder in the total energy curve at  $c/a \approx 0.80$ . Both features are also apparent as shoulders in the plots of  $c(a)/a$  and  $V/V_0$  in Figs. 4.37a and 4.37d, respectively.

To the best of our knowledge, there are neither a published EBP of Hg nor any data of stationary points from any other non-volume conserving Bain path calculation. In an earlier work using pseudopotentials, assuming a filled  $d$ -band, and including scalar-relativistic effects, Moriarty calculated a CVBP of Hg at  $V/V_{\beta\text{-Hg}} = 0.824$  [149].  $V_{\beta\text{-Hg}}$  is the experimentally determined equilibrium volume of  $\beta$ -Hg. This CVBP did not possess a minimum in  $E$  at  $c/a = 1.69$ , however another minimum with  $1 \leq c/a \leq \sqrt{2}$  appeared (FCC was situated at a saddle point). The computed energy differences as function of the volume in Ref. 149 suggest, that the new minimum disappears for volumes  $V/V_{\beta\text{-Hg}} > 0.824$ .

### 4.6 Trends and regularities in epitaxial Bain paths

We conclude from the results in Sec. 4.5, that there are at least two minima in  $E(a, c)$  for each of the 34 considered elements. Special cases are Zr and Hg, which have three minima each. If we trace the total energy along the EBP ( $E(a)$ ), it is clear that, there is a (finite) energy barrier between each adjacent pair of minima. The related energy maximum can either be found at a stationary

## 4.6. TRENDS AND REGULARITIES IN EPITAXIAL BAIN PATHS

point or at a discontinuity of the EBP. One may ask, if there are regularities among the 34 elements. Those could be, for example,

- the energy differences among stationary points of  $E(a)$ ,
- the symmetry and position of stationary points in the tetragonal parameter space,
- the (in)stability of minima in terms of elastic constants.

Regularities are in principle expected to occur for elements of the same group and among the three periods of elements, if we keep in mind, that many properties of the TM series are related to the filling of the  $d$ -band (see discussion in Sec. 4.2). Concerning the symmetry of stationary points, we know from considerations in Secs. 3.3 and 3.4, that the energy of the BCC structure and the one of the FCC structure are stationary points of  $E(a)$  (provided they belong to the EBP).

We study possible trends in the following three sections.

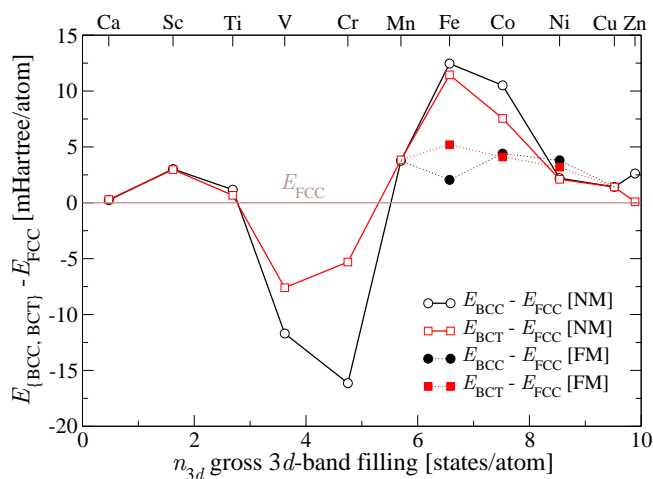
### 4.6.1 Structural energy differences

In Sec. 4.2 we elucidated energy differences among common crystal structures of TMs (FCC, BCC, HCP) as function of the  $d$ -electron occupation. Figure 4.2 on Page 29 is, through derived from a canonical model, a characteristic depiction of trends in energy differences in NM TM series, which to a large extent agrees with results from one-electron theory [58, 165, 169, 204]. If we presume for each element, that one extremal point of  $E(a)$  is at the BCC structure and that another extremal point of  $E(a)$  is the FCC structure, then the third extremum of  $E(a)$  (and each additional one) has BCT symmetry. In that case, we can investigate the total energy difference between the BCC state and the FCC state and between the extremal points with BCT symmetry and the FCC state for all elements, that belong to the same series, say, as functions of the number of electrons in the  $d$ -valence basis states (band filling).

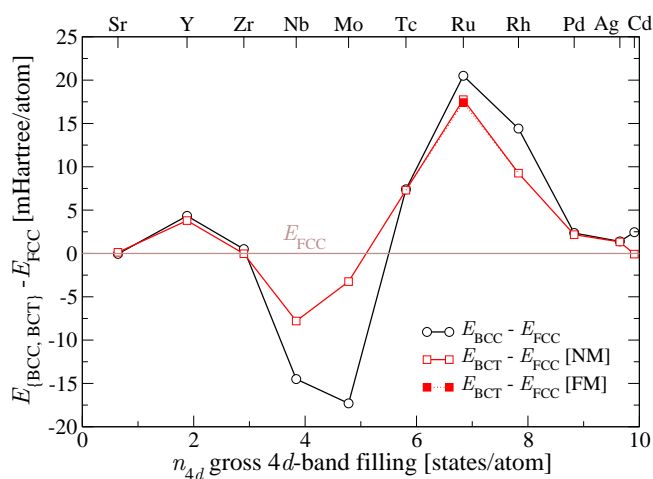
This consideration is hampered by the fact that, first of all, the BCC lattice is not a point of the EBPs of La, Os, and Ir, as well as the FCC lattice is not a point of the EBPs of V and Nb, due to the instability of these cubic structures with respect to a deformation associated with  $c_{zzzz} = c_{xxxx} < 0$ . Also, the maximum of the EBP of Fe, which is BCT, is unstable. Secondly, we computed minima of  $E(c/a)$ , which possess  $c/a$  ratios that deviate from the exact ratios  $c/a = \sqrt{2}$  for FCC and  $c/a = 1$  for BCC. These ratios were determined from  $E(c/a)$  with two digits precision. Within the two digits precision, the 'ideal' ratios are 1.41 for FCC and 1.00 for BCC. The complete list of elements with deviating  $c/a$  ratio, stated in parentheses, is: Ca (1.39), Sr (1.39), Sc (1.40), Ti (1.39), and Zr (1.40). The deviation from the 'ideal' ratio is at most  $|0.02|$ , and may be related to lacking numerical accuracy.

In the course of this section, structural energy differences were obtained with the following arrangements. The reference structure is FCC, i.e., all energy differences are given with respect to the total energy in the FCC configuration. If the FCC structure of a particular element is unstable with respect to a deformation associated with  $c_{zzzz}$ , (i.e., FCC would not be a point of the EBP)

## CHAPTER 4. TRANSITION METALS, SELECTED ALKALINE EARTH METALS AND LANTHANIDES



(a) fourth period



(b) fifth period

Figure 4.38: Total energy differences for elements in the (a) fourth, (b) fifth, (c) and sixth period of the periodic table of elements as function of  $3d$ ,  $4d$ , and  $5d$ -band filling, respectively. Each figure depicts the BCC – FCC energy differences, as well as the difference of the third extremum, ‘BCT’, on the EBP with respect to FCC. These differences are plotted for two cases: firstly, all states are assumed to be NM, and secondly, FM order is taken into account (if present). Treatment of special cases with more than one BCT extremum on the EBP (Zr, Hg) is discussed in the text. *Continued on Page 105.*

#### 4.6. TRENDS AND REGULARITIES IN EPITAXIAL BAIN PATHS

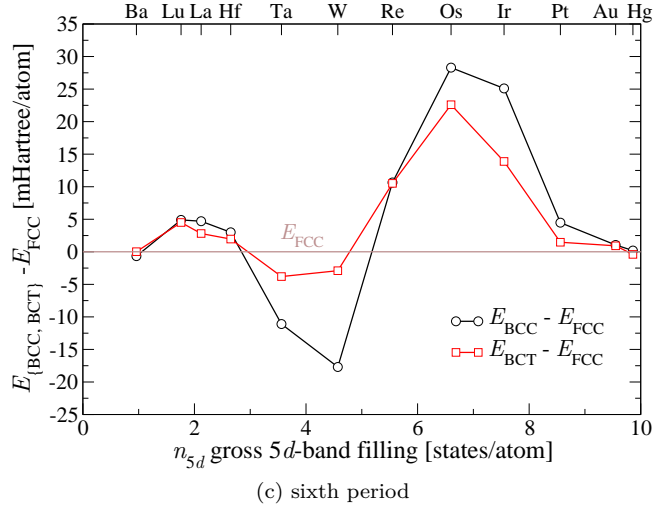


Figure 4.38: Continued figure from Page 104.

then the reference total energy is derived from the equilibrium FCC structure evaluated with cubic symmetry, i.e., in the space group  $Fm\bar{3}m$ . BCC unstable points are subject to the same procedure (space group is  $Im\bar{3}m$ ). If the  $c/a$  ratio of a particular extremum does not coincide with the 'ideal' ratio of a symmetry dictated extremum, i.e.,  $c/a$  is not equal to 1.41 for FCC or  $c/a$  is not equal to 1.00 for BCC (see discussion above, largest error is  $|0.02|$ ), then we nevertheless refer to that extremum as FCC or as BCC. We read off the total energy of that particular extremum from the curve  $E(c/a)$  (taking the actual  $c/a$ -ratio).

These arrangements are justified, because they do not introduce significant sources of errors, especially when trends are object of investigation. This is, on the one hand, for EBPs with an unstable cubic point, due to the smallness of the energy difference between the maximum of  $E(a)$  (which is not exactly at the cubic point) and the energy derived from the equilibrium cubic structure evaluated with cubic symmetry compared to typical energy differences of stationary points of  $E(a)$ . To make this point more clear, let us have a look on the curves  $E(c)$  of La in Fig. 4.10 on Page 54 again. The maximum of  $E(a)$  is at  $a'$ , i.e., at the position at which both minima of the double well in  $E(c)$  are degenerate in energy. For La,  $a' \approx 4.043 \text{ \AA}$ . Due to the double wells in  $E(c)$ , the BCC structure of La is not a point of the EBP. From Fig. 4.10 we infer, that the energy of the equilibrium BCC structure evaluated with cubic symmetry,  $E_{\text{BCC}}$ , is approximately 0.4 mHartree/atom higher than  $E(a')$ . Energy differences between extremal points of  $E(a)$  are much larger than  $E_{\text{BCC}} - E(a')$ , e.g.,  $E(a') - E(a = 4.28 \text{ \AA}) = 5.05 \text{ mHartree/atom}$  (see Table 4.4). Thus, this arrangement does not spoil our conclusion on trends.<sup>8</sup> On the other hand, the energy difference between extrema with non-ideal  $c/a$ -ratio, as read off the

<sup>8</sup>Similar conclusions to La can be drawn for the other EBPs, which feature a discontinuity in  $c(a)$ , see Fig. 4.15 on Page 64 (V and Nb), Figs. 4.22 and 4.23 on Page 79 (Fe), Fig. 4.26 on Page 83 (Os), and Fig. 4.31 on Page 90 (Ir), and by comparison to the energy differences of extremal points of  $E(a)$  in the respective tables.

## CHAPTER 4. TRANSITION METALS, SELECTED ALKALINE EARTH METALS AND LANTHANIDES

---

EBP, and the energy derived from the equilibrium cubic structure evaluated with cubic symmetry is small compared to typical energy differences of stationary points of  $E(a)$ . The total energy along the EBP can be expanded around any extremal point in terms of the deviation (strain). The first, non-vanishing term is of second order in the strain. The expansion coefficient is the curvature at the stationary point (Eq. (4.15)). For a deviation of  $|\Delta(c/a)| = 0.02$  from the ideal ratio, the energy difference is in the order of  $10 \mu\text{Hartree/atom}$  and hence negligible compared to typical structural energy differences.<sup>9</sup>

Within these assumptions, we computed total energy differences between pairs of extrema of the EBP for each element. These energy differences are then plotted for all elements that are counted to the same period. The independent variable is the gross occupation number in the first set of valence states with  $d$ -orbital character,  $n_d$  (cf. definition of the basis in Sec. 4.4). For elements of the fourth period in the periodic table of elements, these are the  $3d$ -orbitals. For elements of the fifth and sixth periods these are the  $4d$  and  $5d$ -orbitals, respectively. In general, the value of  $n_d$  is not the same for the FCC structure, for the BCC structure, and the extremum/extrema with BCT symmetry, because the occupation number is not constant for the states of the EBP. The variation of  $n_d$  is greatest for refractory metals—elements, for which we also computed the largest variation of  $V/V_0$  along the EBP.  $n_d$  varies by at most 0.1 states/atom along the EBP in the range between the minima of  $E(a)$ . This variation is considerable smaller than the difference in the  $d$ -occupation number for two adjacent elements of the same period (we expect  $\Delta n_d \approx 1$  electron/atom for TMs). Without loss of generality, we chose the occupation number of the FCC structure for the presentation.

The EBPs of Zr and Hg have three minima with BCT symmetry each. We took the BCT minimum that is lowest in total energy in order to calculate its energy difference with respect to the energy of the FCC structure. The choice of that particular extremum does not spoil statements about the trend, because the energy differences of all BCT extrema with respect to the FCC structure are of the same order for Zr as well as for Hg (few 0.1 mHartree/atom).

States of some elements (Fe, Co, Ni, and Ru), that correspond to stationary points of  $E(a)$ , order ferromagnetically. Structural energy difference were first of all determined from stationary points that exhibit FM order. Since we also gained the EBPs for purely NM states in the course of this work—not allowing for FM order on the EBP—we also calculated structural energy differences from stationary points, which are exclusively NM states. By doing so, we can study trends across a period of NM elements, as well as modifications due to magnetism.

We denote the total energy of an extremal point of  $E(a)$  by  $E_{\text{FCC}}$ ,  $E_{\text{BCC}}$ , and  $E_{\text{BCT}}$  if the symmetry of the state is FCC, BCC, and BCT, respectively. Structural energy differences as function of the  $d$ -occupation number are denoted

---

<sup>9</sup>Without loss of generality, we estimate this energy for Ti. We may expand the total energy along the EBP (, defined per volume of the primitive unit cell,) around the stationary point,  $a_0$ ,  $E_0 = E(a_0)$ , and  $c_0/a_0 = 1.39$ , up to second order in  $\epsilon_{xx}$  to obtain with the help of Eq. (4.14):  $E(a) - E_0 = Y\epsilon_{xx}^2 + o(\epsilon_{xx}^3)$ , with  $\epsilon_{xx} = (a - a_0)/a_0$ . Assume, that the point  $(\tilde{a}, \tilde{c})$  has  $\tilde{c}/\tilde{a} = \sqrt{2}$ . For Ti,  $|\Delta(c/a)| = |\tilde{c}/\tilde{a} - c_0/a_0| = 0.02$ ,  $\tilde{a} = 2.831 \text{ \AA}$ ,  $\rightarrow \epsilon_{xx} \approx 0.014$ . With the elastic constants of Ti (Table A.4),  $E(\tilde{a}) - E_0 = 6 \mu\text{Hartree/atom}$ .

#### 4.6. TRENDS AND REGULARITIES IN EPITAXIAL BAIN PATHS

by  $(E_{\text{BCC}} - E_{\text{FCC}})(n_d)$  and  $(E_{\text{BCT}} - E_{\text{FCC}})(n_d)$ , or in short

$$\Delta E_{\text{BCC}} \equiv (E_{\text{BCC}} - E_{\text{FCC}})(n_d),$$

$$\Delta E_{\text{BCT}} \equiv (E_{\text{BCT}} - E_{\text{FCC}})(n_d).$$

The modulus,  $(|E_{\text{BCC}} - E_{\text{FCC}}|)(n_d)$ , is denoted by  $|\Delta E_{\text{BCC}}|$  etc. We plotted structural energy differences for elements across the fourth, the fifth, and the sixth period in three Figs. 4.38a – 4.38c.

The trend in  $\Delta E_{\text{BCC}}$  for NM states, Fig. 4.38 (black lines), resembles curves for all three periods from published total energy calculations [58, 165, 169, 204]. That is,  $\Delta E_{\text{BCC}} > 0$  for low band fillings with a maximum corresponding to the band fillings of the elements Sc, Y, and Lu, and  $\Delta E_{\text{BCC}} < 0$  for nearly half band fillings with minimum values for the elements Cr, Mo, and W.  $\Delta E_{\text{BCC}}$  reaches its largest values for  $n_d$  approximately 6.5 electrons/atom. These are the elements of the eighth group, Fe, Ru, and Os. The modulus of  $\Delta E_{\text{BCC}}$  is the smallest for low band fillings (second group) and high band fillings (eleventh and twelfth group), as well as for elements whose  $d$ -occupancy is close to zero-crossings of  $\Delta E_{\text{BCC}}$  (fourth group).  $\Delta E_{\text{BCC}}$  reduces by several mHartree/atom for the FM states of Fe and Co, however increases by approximately 2 mHartree/atom for Ni (Fig. 4.38a).  $\Delta E_{\text{BCC}}$  for FM order has its largest value for Co.

$\Delta E_{\text{BCT}}$  for NM states, Fig. 4.38 (red lines), has a similar trend as  $\Delta E_{\text{BCC}}$ , but the peak positions shift to different groups. The largest negative values of  $\Delta E_{\text{BCT}}$  appear throughout for elements of the fifth group, in contrast to the minima of  $\Delta E_{\text{BCC}}$  which occurred for the elements of the sixth group.

At first sight,  $|\Delta E_{\text{BCT}}|$  is always smaller than  $|\Delta E_{\text{BCC}}|$ , i.e., the red curve is always closer to the zero line than the black curve. Indeed, this holds for all elements but Ca, Sr, Ba, Mn, and Hg. Hence, for elements except the previous five, the BCC structure and the FCC structure occupy the position of the maximum and minimum of  $E(a)$ , respectively, or vice versa. In a good approximation, also  $(E_{\text{BCT}} - E_{\text{BCC}})(n_d)$  (the difference between the red and the black curve) is subject to the same trend for all three depicted periods. Further,  $\Delta E_{\text{BCT}}$  for FM states is again by several mHartree/atom smaller than  $\Delta E_{\text{BCT}}$  for the NM states in case of Fe and Co, however larger for Ni. In case of Fe, the extremum at the BCC structure and the extremum at the BCT structure swap their positions on the EBP, hence their types of stationary point: the BCC structure coincides with the position of the maximum and with the position of the minimum on the purely NM EBP and on the EBP with FM states, respectively. The BCT structure behaves vice versa. The gain in total energy due to FM order for the Ru BCT state is comparatively small and does not alter the curve progression significantly.

To conclude, the structural energy differences associated with the extrema of the EBP,  $\Delta E_{\text{BCC}}$  and  $\Delta E_{\text{BCT}}$ , follow a similar trend in all three periods as function of the number of electrons in the  $d$ -band. Our previous observation, that the global minimum and the maximum on the EBP almost always coincide with either the FCC structure or the BCC structure, is looked at in more detail in the following section.

## CHAPTER 4. TRANSITION METALS, SELECTED ALKALINE EARTH METALS AND LANTHANIDES

	2	3	4	5	6	7	8	9	10	11	12
4	20 <b>Ca</b> FCC	21 <b>Sc</b> HCP	22 <b>Ti</b> HCP	23 <b>V</b> BCC	24 <b>Cr</b> BCC	25 <b>Mn</b> CUB	26 <b>Fe</b> BCC	27 <b>Co</b> HCP	28 <b>Ni</b> FCC	29 <b>Cu</b> FCC	30 <b>Zn</b> HCP
5	38 <b>Sr</b> FCC	39 <b>Y</b> HCP	40 <b>Zr</b> HCP	41 <b>Nb</b> BCC	42 <b>Mo</b> BCC	43 <b>Tc</b> HCP	44 <b>Ru</b> HCP	45 <b>Rh</b> FCC	46 <b>Pd</b> FCC	47 <b>Ag</b> FCC	48 <b>Cd</b> HCP
6	56 <b>Ba</b> BCC	57,71 <b>La,Lu</b> DHCP,HCP	72 <b>Hf</b> HCP	73 <b>Ta</b> BCC	74 <b>W</b> BCC	75 <b>Re</b> HCP	76 <b>Os</b> HCP	77 <b>Ir</b> FCC	78 <b>Pt</b> FCC	79 <b>Au</b> FCC	80 <b>Hg</b> BCT

Figure 4.39: Mapping of types of EBP on the elements in the periodic table. **Green** and **blue** colouring represent Type I and Type II EBP, respectively, which are standard EBPs with two minima of  $E(a)$  of which the global minimum, and the maximum of  $E(a)$  are at cubic symmetry. Type III EBPs are coloured in **red** and indicate standard EBPs which do not belong to Type I nor Type II. Type IV, coloured in grey, comprise non-regular EBPs ( $E(a)$  has more than two minima). General organisation of this table as in Table 4.1 on Page 26.

### 4.6.2 Classification of epitaxial Bain paths

If not stated otherwise we use the results obtained in the previous section, particularly total energies of the BCC, the FCC, and the BCT structures and FM order.

FCC and BCC structures are frequently occurring GS crystal structures for the 34 elements considered in this chapter, see Fig. 4.1 on Page 26. The most frequently (11 times) occurring crystal structure is HCP. The amplitude of the HCP – FCC structural energy difference,  $\Delta E_{\text{HCP}} \equiv (E_{\text{HCP}} - E_{\text{FCC}})(n_d)$ , is in general smaller than the amplitude of  $\Delta E_{\text{BCC}}$ . This is true for the three periods considered here, see the canonical structure difference in Fig 4.2 on Page 29 as well as more accurate results in Refs. 169, 204. In a good approximation,  $\Delta E_{\text{HCP}}$  is anti-cyclical to  $\Delta E_{\text{BCC}}$ , if we neglect FM order, i.e., if  $\Delta E_{\text{BCC}} > 0$  then  $\Delta E_{\text{HCP}} < 0$  and vice versa. In other words, an element with an HCP GS has  $\Delta E_{\text{BCC}} > 0$ .

We noticed in the previous section, that the global minimum and the maximum on the EBP almost always coincide with either the FCC or the BCC structure.  $E(a)$  possesses three extrema for the majority of all EBPs; we refer to such an EBP as a *standard* EBP. Without loss of generality, we define four types of EBPs:

**Type I:** standard;  $E(a)$  with global minimum at the FCC structure, maximum at the BCC structure;

**Type II:** standard;  $E(a)$  with global minimum at the BCC structure, maximum at the FCC structure;

**Type III:** standard, but neither Type I nor Type II;

Type IV: non-standard.

It is clear, that a Type I EBP and a Type II EBP have a local BCT minimum with  $c/a < 1$  and  $c/a > \sqrt{2}$ , respectively. Type I and Type II are referred



## 4.7. STABILITY OF EXTREMAL POINTS: PREDICTION OF METASTABLE PHASES

---

to as being regular. Type III comprises all other standard EBPs, for example the case when both minima have cubic symmetry. Type IV comprises all other EBPs, which are referred to as non-standard, i.e.,  $E(a)$  possesses more than two minima.

Figure 4.39 summarises the distribution of Type I–IV EBPs in the set of elements which are considered in this Chapter. Evidently, Type II is present for elements in the fifth and sixth group, which all possess a BCC GS. The majority of the remaining elements, which in most cases have FCC or HCP GSs, are of Type I. Type III EBPs are located in the second group (one minimum has cubic symmetry, maximum has BCT symmetry), and in the twelfth group, of which Cd has a BCT global minimum. The EBPs of Fe and Mn are also Type III with both minima coinciding with cubic symmetry. The EBP of purely NM Fe, Co, Ni, and Ru are of Type I. Zr and Hg do not fit the standard EBP model, because there are more than two minima of  $E(a)$ .

## 4.7 Stability of extremal points: prediction of metastable phases

So far nothing has been said about the (meta) stability of cubic or tetragonal structures whose energies minimise  $E(a)$ . Structures are metastable if there is no small deformation that can further decrease their total energy. The underlying theory, the computation, and detailed results of this analysis are given in App. A of this thesis. Here we elucidate, if there are metastable cubic or tetragonal phases; if unstable, which are the violated stability conditions that cause the instability and which are common to certain elements (which even may show a trend), and possible trends of elastic constants. For several elements, these considerations will allow us to predict metastable phases not yet observed in experiment.

### 4.7.1 Connection between structural stability and curvature of $E(a)$

In the following we derive an expression for the curvature of  $E(a)$  at extremal points [133].

The coordinates of a stationary point of  $E(a, c)$  be  $(a_0, c_0)$ , its energy is  $E_0 = E(a_0, c_0) \equiv 0$ .  $E(a)$  has an extremum at  $a_0$ . We expand the total energy  $E(a, c)$  up to second order in terms of normal strains,  $\epsilon_{ii}$ ,  $i = \{x, y, z\}$ , around the stationary point, i.e., tetragonal symmetry is conserved. The strain energy in Eq. (A.3) for this deformation reads:

$$E = (c_{xxxx} + c_{xyyy})\epsilon_{xx}^2 + \frac{1}{2}c_{zzzz}\epsilon_{zz}^2 + 2c_{xxzz}\epsilon_{xx}\epsilon_{zz}. \quad (4.11)$$

For every state of the EBP holds by definition:  $c_{zzzz} > 0$ . The stress for every state of the EBP in out-of-plane direction,  $\sigma_{zz}$ , must be identical zero. Using Hook's law, Eq. (A.2), we obtain for the same tetragonal deformation,

$$\sigma_{zz} = 2c_{xxzz}\epsilon_{xx} + c_{zzzz}\epsilon_{zz} \stackrel{!}{=} 0. \quad (4.12)$$

## CHAPTER 4. TRANSITION METALS, SELECTED ALKALINE EARTH METALS AND LANTHANIDES

---

Eliminating  $\epsilon_{zz}$  in Eq. (4.11) by the previous relation and differentiating  $E$  with respect to  $\epsilon_{xx}$  leads to

$$\begin{aligned} \frac{dE}{d\epsilon_{xx}} &= 2Y\epsilon_{xx} \\ Y &= c_{xxxx} + c_{xxyy} - \frac{2c_{xxzz}^2}{c_{zzzz}} \end{aligned} \quad (4.13)$$

$$\frac{d^2E}{d\epsilon_{xx}^2} = 2Y. \quad (4.14)$$

The curvature of  $E(a)$  at an extremal point is  $2Y$ .  $Y \cdot c_{zzzz} > 0$  is identical to a particular stability condition (SC) for tetragonal lattices, Eq. (A.6),  $c_{zzzz}(c_{xxxx} + c_{xxyy}) - 2c_{xxzz}^2 > 0$ . Since  $c_{zzzz} > 0$  for all points of the EBP, Inequality (A.6) is fulfilled (not fulfilled), if the curvature of  $E(a)$  is positive (negative). In case of cubic symmetry,  $Y$  in Eq. (4.13) simplifies to  $Y'$ ,

$$Y' = \frac{(c_{xxxx} - c_{xxyy})(c_{xxxx} + 2c_{xxyy})}{c_{xxxx}} \quad (4.15)$$

$$\stackrel{(A.11)}{=} \frac{3B}{c_{xxxx}} (c_{xxxx} - c_{xxyy}). \quad (4.16)$$

The latter relation made use of the definition of the bulk modulus,  $B$ , in Sec. A.2. The curvature of  $E(a)$  at an extremal point with cubic symmetry is  $2Y'$ .  $Y'$  is the product of a positive prefactor,  $3B/c_{xxxx} > 0$ ,<sup>10</sup> and the value of  $c_{xxxx} - c_{xxyy}$ , which is related to another SC for cubic lattices,  $c_{xxxx} - c_{xxyy} > 0$  (SC (III) in Sec. A.3.1). If  $c_{xxxx} - c_{xxyy} > 0$  then SC (III) is fulfilled and  $Y'$  is positive, if  $c_{xxxx} - c_{xxyy} < 0$  then SC (III) is violated and  $Y'$  is negative [38].

The above analysis leads to interesting consequences for extremal points with cubic symmetry. There are four SCs for cubic lattices, see Sec. A.3.1. SC (I) and SC (IV) are always fulfilled. SC (III) is always fulfilled for minima because  $Y' > 0$ . Hence, the violation of SC (II),  $c_{xyxy} > 0$ , is the only SC, that causes the elastic instability of a cubic structure, whose total energy is a minimum in the tetragonal phase space, with respect to a deformation that breaks cubic symmetry. For a maximum, SC (III) is never fulfilled because  $Y' < 0$ . SC (II) may or may not be violated. This analysis can not be straightforwardly applied to extremal points of  $E(a)$  with BCT symmetry, because there are in total five SCs (Sec. A.3.3).

We checked all SCs for all stationary points of  $E(a)$  for all elements in Sec. A.3. The results underline the above statement, that SC (III) is fulfilled (not fulfilled) for all minima of  $E(a)$  (for all maxima of  $E(a)$ ).

### 4.7.2 Elastic properties of cubic structures

The bulk moduli and elastic constants of various elements, and trends based on those data are often calculated only for the true GS crystal structure [152,

<sup>10</sup> $c_{xxxx}$  is positive for cubic structures according to the definition of the EBP ( $c_{xxxx} = c_{zzzz}$  for cubic structures).  $B$  is positive for constrained (=cubic) geometries at equilibrium, because the energy is minimised.

## 4.7. STABILITY OF EXTREMAL POINTS: PREDICTION OF METASTABLE PHASES

211, 251]. A trend across a TM series for example, then comprises different crystal structures, which allows for a comparison with experiments, but does not allow to study the progression of elastic properties for a fixed structure across the series. In the course of this work, we computed the bulk modulus and the three elastic constants of the BCC structure and the FCC structure for every element. Both structures regularly occupy the position of a minimum of  $E(a)$ . By evaluating the elastic constants of cubic structures, we can then directly check the stability conditions of minima of  $E(a)$  for a large number of elements.

The sum of our results are depicted in eight subfigures of Fig. 4.40. The bulk moduli for BCC and FCC structures across each series have a parabolic but slightly skewed shape, which reach their peak values for elements of the seventh and eighth groups. These trends are interrupted by the presence of ferromagnetism, which is most prominently seen for BCC Fe, but also for FCC Co. In all cases, structures with FM order have lower bulk moduli than the NM counterparts.

The elastic constants  $c_{xxxx}$ ,  $c_{xxyy}$ , and  $c_{xyxy}$  are different between the BCC structure and the FCC structure, but follow the same principal trend among the three periods for the same structure. FM configurations for  $3d$ -TMs alter the trends.  $c_{xxxx}$  and  $c_{xxyy}$  are the largest for elements of the sixth group and of the eighth/ninth group for NM states in the BCC structure, respectively. This is vice versa for the FCC structure., i.e.,  $c_{xxxx}$  and  $c_{xxyy}$  are the largest for elements of the eighth/ninth group and of the sixth group, respectively. Consistent for both structures,  $c_{xyxy}$  is the largest for the eighth group without magnetic order. The signs of  $c_{xxxx}$ ,  $c_{xxxx} - c_{xxyy}$ , and  $c_{xyxy}$  define the stability of the structure, see Sec. A.3.<sup>11</sup> The structure is stable or metastable, if all three values are positive. If a cubic structure has  $c_{xxxx} < 0$ , it is unstable with respect to a tetragonal deformation, and not a point of the EBP. This is true for BCC La, BCC Ir, FCC V and FCC Nb (second row in Fig. 4.40). If a cubic structure on the EBP has  $c_{xxxx} - c_{xxyy} < 0$ , it is unstable towards an orthorhombic deformation, and the structure is a maximum of  $E(a)$  since  $Y' < 0$  (fourth row in Fig. 4.40).  $c_{xyxy}$  involves a change of the angle between two adjacent sides of the cubic unit cell, but the highest symmetry is still orthorhombic, i.e.,  $c_{xyxy} < 0$  also signals an instability towards an orthorhombic distortion. Evidently from Fig. 4.40, elements from the fifth and sixth group with a BCC GS have an unstable FCC phase, and elements with an FCC or HCP GS phase from the eighth or ninth group possess an unstable BCC phase. In all these cases,  $c_{xxxx} - c_{xxyy} > 0$  is not fulfilled.

We predict, that the following elements with an (D)HCP GS may have a metastable FCC phase: Sc, Ti, Zr, Tc, Ru, Lu, Hf, Re, and Os. Up to now, an FCC phase of these metals is not known from their phase diagram to the best of our knowledge. According to our calculations, the FCC phases of Zn and Cd are unstable. This is in agreement with Ref. 133, and both phases have not been observed either [43, 256]. We find, that the FCC phases of Y and La are metastable. Both phases were observed [43, 256]. We also find the possibility of a metastable BCC phase of Ca, Sr, Zr, and of Mn, and a metastable FCC phase of Mn and of Ba, of which all but FCC Ba are known from their phase

<sup>11</sup>The fourth stability condition is always fulfilled, because it is related to the bulk modulus, which is always greater than zero (Sec. A.3).

**CHAPTER 4. TRANSITION METALS, SELECTED ALKALINE EARTH METALS AND LANTHANIDES**

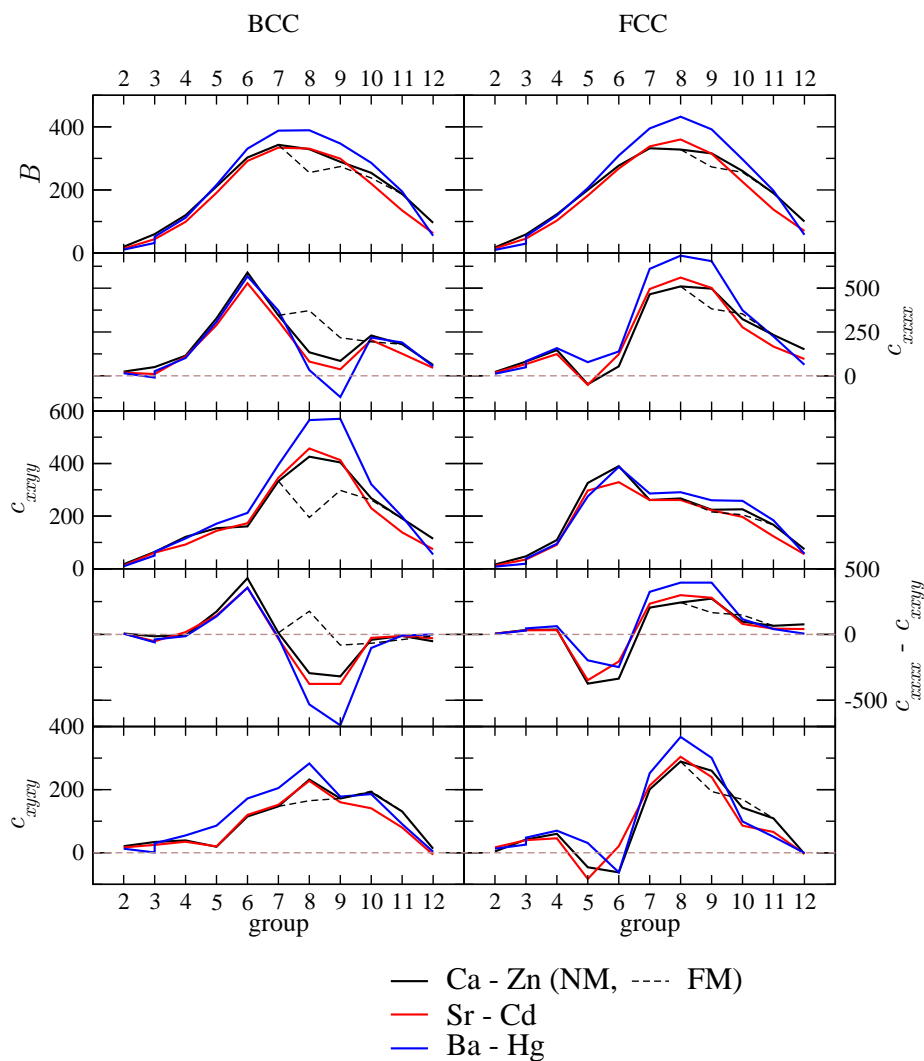


Figure 4.40: Bulk moduli and elastic constants of BCC and FCC structures for elements of the fourth (Ca–Zn), the fifth (Sr–Cd), and the sixth (Ba–Hg) period and the second to twelfth group of the period table.  $c_{xxxx} - c_{xxyy}$  defines SC (III). The structures are unstable if  $c_{xxxx} < 0$ ,  $c_{xxyy} < 0$ , or  $c_{xxxx} - c_{xxyy} < 0$ . The elastic properties are plotted for two cases: firstly, all states are assumed to be NM, and secondly, FM order is taken into account (if present). The two columns of each row show the same quantity and have identically scaled ordinates. All values are in GPa. Horizontal grey dashed lines indicate the zero level.

## 4.7. STABILITY OF EXTREMAL POINTS: PREDICTION OF METASTABLE PHASES

diagrams. In the case of Fe, ferromagnetism stabilises the BCC phase, i.e.,  $c_{xxxx} - c_{xyyy} > 0$ , which is not the case for NM BCC Fe.

$c_{xxxx} - c_{xyyy}$  across each series has zero-crossings at approximately the fourth group and the seventh group for the BCC structure, and between the fourth and fifth group and between the sixth and seventh group for the FCC structure (fourth row in Fig. 4.40). If we assume that the trend of  $c_{xxxx} - c_{xyyy}$  across each TM series is again determined by the  $d$ -electron number, this difference may be tuned to vanishingly small values by changing the average number of  $d$ -electrons per atom, i.e., by alloying. This is indeed used in so-called gum metals, which are high strength, ductile alloys. Gum metals are multicomponent solid solutions based on the binary alloys Ti-V and Ti-Nb in the BCC structure [120,191], and alloys with similar properties were proposed for binary alloys of few group 6 and group 7 elements (Mo, Tc, W, Re) [213]. For a certain alloy composition in gum metals, Young's modulus in the [100] direction and shear moduli in various directions on various crystal planes in the BCC crystal simultaneously approach zero (these specific moduli are proportional to  $c_{xxxx} - c_{xyyy}$ ) [120,191].

### 4.7.3 Elastic stability of minima of $E(a)$

The minima of  $E(a)$  are (meta)stable in the constraint tetragonal phase space. Some minima could correspond to (meta)stable phases. The global minimum of  $E(a)$  is stable, if the underlying structure is identical to the (LSDA) GS crystal structure, i.e., if the GS crystal structures is either FCC, BCC, or BCT. The global minimum of  $E(a)$  and each additional one is metastable, if the underlying structure is locally stable, but not identical to the GS.

We analyse the elastic constants and SCs separately for the global minimum of  $E(a)$  and the local minimum (local minima) of  $E(a)$ . The analysis benefits from the fact that most elements have a standard EBP, that elements from the same group in most cases have the same type of EBP, and that the  $c/a$ -ratio of the local minimum of  $E(a)$  of standard EBPs from the same group is similar (Sec. 4.6.2). Also, structural energy difference curves, if divided by the modulus of the largest energy difference, lie fairly on top of each other (Sec. 4.6.1). We therefore expect to find similarities in the elastic properties of the states that minimise  $E(a)$  as we found them for the FCC and the BCC structure.

The highest lattice symmetry underlying each minimum of  $E(a)$  changes across each series, i.e., cubic structures and tetragonal structures alternate along a series and, thus, the type and the number of elastic constants and SCs. In order to have a consistent view on trends, we depict the elastic constants in the BCT reference frame, i.e.,  $c_{xxxx}$ ,  $c_{xyyy}$ , and  $c_{xyxy}$  are back-transformed from the FCC reference frame to the BCT reference frame according to Eqs. (A.12) in Sec. A.2.

The final results for the global minimum of  $E(a)$  and the local minimum of  $E(a)$  are depicted in Fig. 4.41 and Fig. 4.42, respectively. Each figure shows five of a total of six elastic constants for BCT lattices and allows to analyse four of a total of five SCs for BCT lattices. We forwent to plot the elastic constant  $c_{xyyy}$  and preferred to show the difference  $c_{xxxx} - |c_{xyyy}|$  instead. The SC  $c_{zzzz}(c_{xxxx} - c_{xyyy}) - 2c_{xxzz}^2 > 0$  is always fulfilled for minima of  $E(a)$  and is therefore not depicted, see discussion in Sec. 4.7.1. Note that, for Zr and Hg, which possess two local minima of  $E(a)$ , we only depict the data of the local

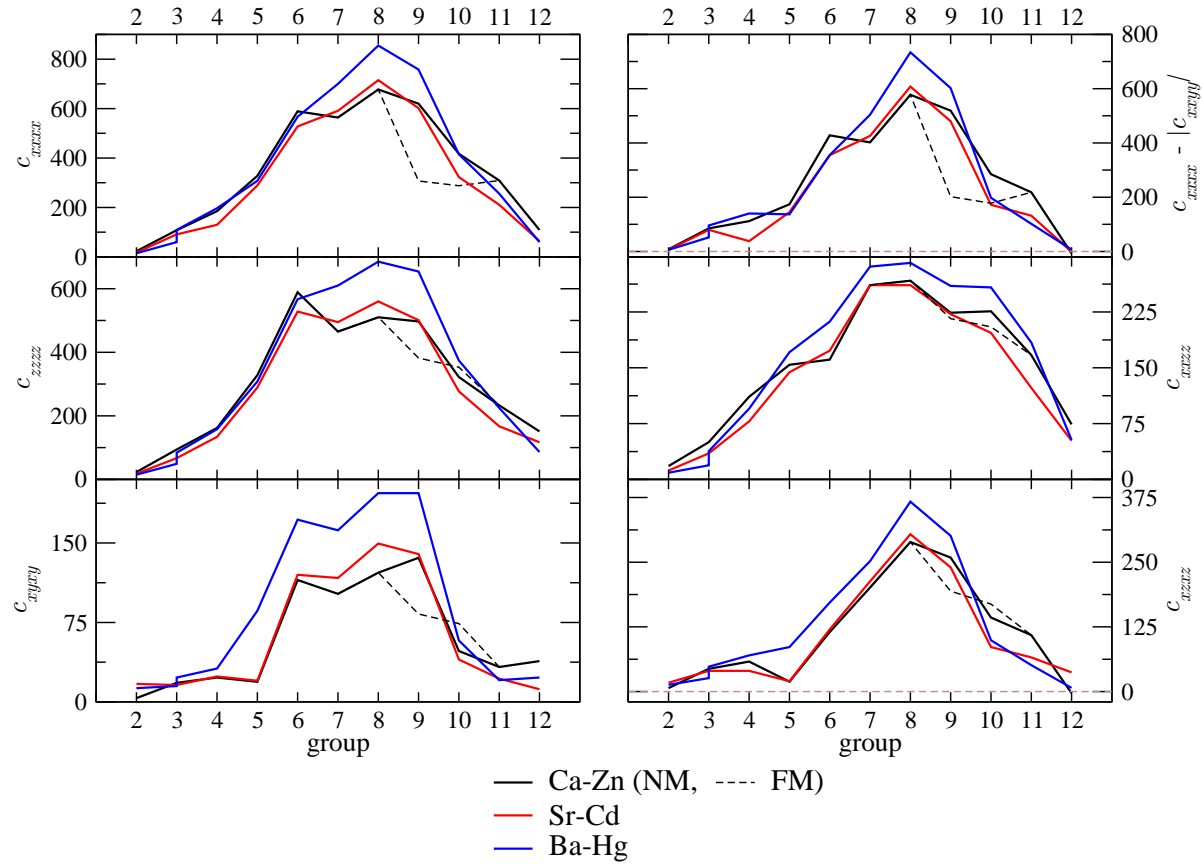


Figure 4.41: Elastic constants of the structure **globally** minimising  $E(a)$  in the BCT reference frame for elements of the fourth (Ca-Zn), the fifth (Sr-Cd), and the sixth (Ba-Hg) period and the second to twelfth group of the period table. If  $c_{xxxx} < 0$ ,  $c_{xxxx} - |c_{xyxy}| < 0$ ,  $c_{xyxy} < 0$  or  $c_{xzzz} < 0$ , then the structure is unstable. SC (V),  $c_{zzzz}(c_{xxxx} - c_{xyxy}) - 2c_{xzzz}^2 > 0$ , is always fulfilled and not shown. All values are in GPa. Horizontal dashed lines indicate the zero level.

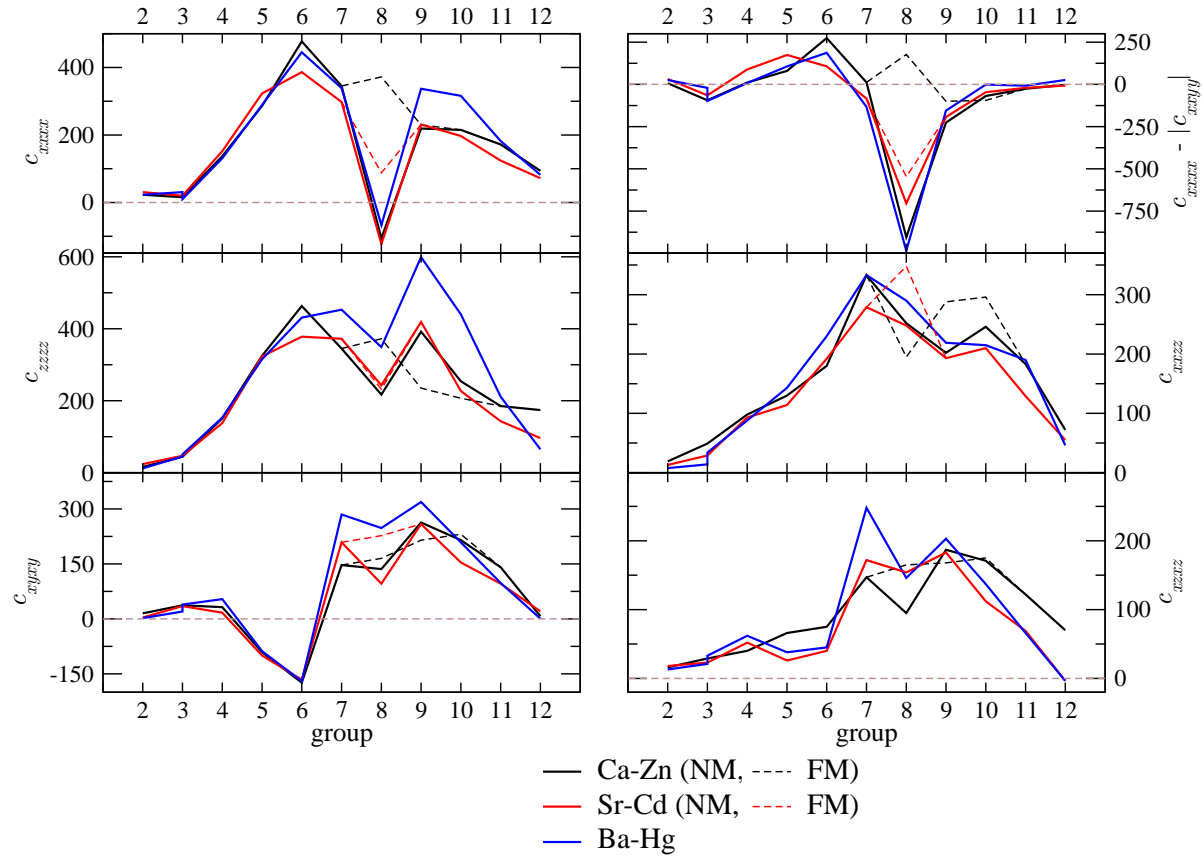


Figure 4.42: Elastic constants of the structure **locally** minimising  $E(a)$  in the BCT reference frame for elements of the fourth (Ca-Zn), the fifth (Sr-Cd), and the sixth (Ba-Hg) period and the second to twelfth group of the period table. If  $c_{xxxx} < 0$ ,  $c_{xxxx} - |c_{xyxy}| < 0$ ,  $c_{xyxy} < 0$  or  $c_{zzzz} < 0$ , then the structure is unstable. SC (V),  $c_{zzzz}(c_{xxxx} - c_{xyxy}) - 2c_{zzz}^2 > 0$ , is always fulfilled and not shown. All values are in GPa. Horizontal dashed lines indicate the zero level.

## CHAPTER 4. TRANSITION METALS, SELECTED ALKALINE EARTH METALS AND LANTHANIDES

---

minimum, which is deepest in total energy. The other, energetically higher-lying local minimum is at BCC and at FCC for Zr and Hg, respectively. BCC Zr is metastable, while FCC Hg is unstable due to  $c_{xxxx} < c_{xyxy}$  (see previous subsection).

Considering only NM states, there is an identical global trend for each of the three series of elements for every elastic constant. That is, prominent kinks, peaks, and valleys for each of the three series appear in many cases at the same position (for the same group). But there are also 'missing features', e.g.,  $c_{xyxy}$  and  $c_{zzz}$  of the global minimum have a dip for V and Nb, but not for Ta. The presence of ferromagnetism for the global minimum (Co and Ni) and for the local minimum (Fe, Co, Ni, and Ru) clearly changes the trend set by NM states. Magnetic order stabilises the structure locally minimal in  $E(a)$  of Fe (BCC Fe), see topmost charts in Fig. 4.42. The local minimum of Ru has  $c_{xxxx} < 0$  and  $c_{xxxx} > 0$  if the state is NM and FM, respectively. The shear,  $c_{xxxx} - |c_{xyxy}|$ , is always negative for this state, i.e., the local minimum of Ru is not stabilised by magnetic order.

We predict, that the following tetragonal states may be metastable:

- BCT Ti with  $a = 3.33 \text{ \AA}$  and  $c/a = 0.86$
- BCT Zr with  $a = 3.74 \text{ \AA}$  and  $c/a = 0.82$
- BCT Hf with  $a = 3.64 \text{ \AA}$  and  $c/a = 0.85$

The three elements from the fourth group (Ti, Zr, and Hf) are thus exceptional, because we predict for each element a metastable BCT state according to the previous list, but also a metastable FCC state (see previous subsection). Reference 133 finds, that the BCT minimum on the EBP of Ti with lattice parameter  $a = 3.34 \text{ \AA}$  and  $c/a = 0.85$  is unstable due to  $c_{xxxx} - |c_{xyxy}| < 0$ . The BCT minimum on the EBP of Zr with  $a = 3.73 \text{ \AA}$  and  $c/a = 0.81$  from Ref. 93 was predicted to be metastable in agreement with our findings. Our predicted metastable BCT phase of Hf has not been reported before.

Elements with a Type II EBP (fifth and sixth group) consistently have a local minimum in  $E(a)$ , which is unstable, since  $c_{xyxy} < 0$ . Elements with a Type I EBP and an FCC GS (groups 9–11 but not Co) have a local minimum in  $E(a)$ , which is unstable, since  $c_{xxxx} - |c_{xyxy}| < 0$ . This correlation was earlier disclosed in Ref. 140, which we confirm by our calculations and extend to a larger set of elements. Elements with a Type I EBP and an (D)HCP GS from the groups 3, 7, and 8 have a local minimum in  $E(a)$ , which is also unstable due to a violation of  $c_{xxxx} - |c_{xyxy}| > 0$ .

### 4.8 Summary of main results

We obtained the EBPs of 34 elements of the periodic table of elements by means of density functional calculations employing the PW92 parameterisation of the XC potential. We allowed for FM and two types of AFM order to study the magnetic structure of the FM elements Fe, Co, and Ni on the EBP, but we also investigated the possibility of a magnetic instability for several, normally NM metals. Most of the elements under consideration are TMs and many GS



## 4.8. SUMMARY OF MAIN RESULTS

---

properties of TMs (and particularly common features among the TM series) are attributed to the filling of the  $d$ -band. We were interested in whether there are features of the EBP that can be explained on the basis of a filling of the  $d$ -band as well.

Our findings show, that each investigated element except Zr and Hg possesses two minima of the total energy in the tetragonal parameter space, i.e., at least one minimum does not correspond to the GS. Only the elements Zr and Hg have three minima each. The exceptional number of minima for Zr in comparison to the isoelectronic elements Ti and Hf was attributed to a higher  $d$ -electron occupation in bulk Zr compared to bulk Ti and Hf. FM states with tetragonal symmetry on the EBP were found for Fe, Co, Ni, Ru, and Os. AF1 order and AF2 order are never more stable than FM order on the EBP for none of the considered elements. In case of Fe, Co, Ni, and Ru, FM order is found at the energetically higher lying minimum of the EBP. The occurrence of FM order for Ru and Os is due to an increase of the DOS at the Fermi energy in the NM state for certain  $c/a$  ratios, which is seen in the isoelectronic Fe as well. FM order on the EBPs of Ru and Os has not been reported before, but FM order was predicted to occur on the CSBP of Ru in Ref. 247.

The BCC structures of La, Os, Ir and the FCC structures of V and Nb have an elastic constant  $c_{zzzz} < 0$  and belong therefore not to their EBPs, i.e, these structures can never be stabilised on a quadratic interface. Associated with these particular unstable structures are kinks and discontinuities in quantities which are plotted as function of  $a$  and as function of  $c/a$  along the EBP, respectively. This has not been taken into account in any published EBP so far. By evaluating SCs based on elastic constants, we conclude that 13 FCC, four BCC, and three BCT structures may be metastable. From this set of structures, ten FCC and all three BCT structures are not known from the respective phase diagrams.

We classified the EBPs into four types according to the number of minima of  $E(a)$  and the lattice symmetry of stationary point of  $E(a)$ . There are two regular EBP types which frequently occur in the set of considered elements (the types were referred to as Type I and Type II). For both types,  $E(a)$  has two minima and only one minimum of  $E(a)$  coincides with either the FCC or the BCC structure. There is an almost identical distribution of regular EBPs types across each of the three TM series. Irregular EBPs, i.e., Type III and Type IV, occur in the set of TMs for Zr (three minima), Mn (both cubic structures at minima), and Fe (both cubic structures at minima, due to presence of magnetic order). Irregular EBPs also occur for alkaline earth metals and post-TMs of the second and twelfth group of the periodic table, respectively.

We analysed structural energy differences among extremal points of  $E(a)$ .  $\Delta E_{\text{BCT}}$  follows hereby the same trend as  $\Delta E_{\text{BCC}}$  as function of the  $d$ -band filling for each series. Clear similarities among the three periods of elements are reflected in the bulk moduli and in the elastic constants of the cubic and tetragonal structures that define the minima of  $E(a)$ .





# 5

## Uranium

Ferromagnetism is a rare GS among the elements in the periodic table. There are six stable elements known to show FM order in their GSs: Fe, Co, and Ni from the  $3d$  TM series, and Gd, Dy, and Tb from the  $4f$  series. At ambient conditions, only the three TM elements and Gd remain FM [91]. Uranium has a paramagnetic GS [114]. Magnetism among uranium compounds is, however, not unusual [194]. Indeed, uranium compounds exhibit different types of magnetic order ranging from FM order in, e.g., in  $\text{UNi}_2$  and  $\text{US}$ , over AF1 order in, e.g., the mononitride  $\text{UN}$ , to canted order in  $\text{U}_3\text{X}_4$ ,  $X = \{\text{P, As}\}$  [194]. All these magnetic phenomena reflect the active role of uranium  $5f$ -electrons in forming a broken-symmetry GS [147, 194].

The majority of single-crystalline, metallic overlayers manufactured so far by means of epitaxial growth belong to the TM series and the rare-earth-metal series. The growth and study of single crystal uranium films in the GS crystal structure and the stabilisation of in a new HCP structure offers new research opportunities. The properties of the charge density wave in thick uranium films (5000 Å) are different compared to its properties in bulk; the HCP structure was predicted to be FM [215, 246].

The purpose of the present chapter is to calculate the EBP of uranium, to identify possible metastable BCT states, and to investigate the possibility of an FM state in bulk-like uranium films.

### 5.1 Introduction

Bulk elemental uranium has an orthorhombic low temperature crystal structure with four atoms in the conventional unit cell ( $\alpha$ -uranium), see Fig. 5.1 for a sketch. The  $\alpha$ -phase is stable up to temperatures of 940 K at ambient pressure [11], and stable up to pressures of 100 GPa at ambient temperature [3, 116]. Apart from a complex tetragonal high temperature phase, experiments revealed a BCC phase stable above 1045 K, which has an extrapolated RT-value of the lattice parameter of 3.474 Å [43]. At temperatures below 43 K,  $\alpha$ -uranium undergoes three successive structural phase transitions manifesting themselves in charge density waves (CDW), as seen in X-ray and neutron diffraction experiments [114, 136, 147]. The structural transition locking in at the highest temperature has a commensurate wave vector and corresponds to a doubling of

## CHAPTER 5. URANIUM

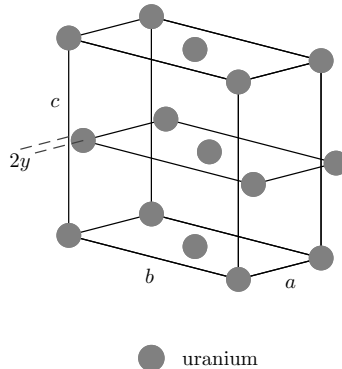


Figure 5.1: Conventional unit cell of  $\alpha$ -uranium corresponding to the arrangement of atoms at 50 K. The experimentally determined lattice parameters at 50 K are:  $a = 2.836 \text{ \AA}$ ,  $b = 5.867 \text{ \AA}$ ,  $c = 4.936 \text{ \AA}$  ( $V = 20.535 \text{ \AA}^3/\text{atom}$ ), and  $y = 0.1018 \text{ \AA}$  [11]. The shift of the centre plane with respect to the basal plane by an amount  $2y$  is not drawn to scale.

the unit cell in  $a$ -direction [114].<sup>1</sup> This transition and the doubled unit cell is referred to as  $\alpha_1$  and  $\alpha_1$ -uranium, respectively. Neutron scattering experiments found a softening of an optical phonon branch associated with the occurrence of  $\alpha_1$ , see, e.g., Ref. 114. Recent experimental progress has been achieved in the field of epitaxial growth of uranium films, including the manufacture of HCP films [15, 146, 215]. An HCP structure is notably not known from the conventional pressure-temperature phase diagram of uranium [43].

The picture that has evolved for elemental uranium by comparison of experimental data with DFT supports itinerant  $5f$ -electrons in a dominant valence band of width approximately 3 eV, which is pinned at the Fermi energy [114, 147, 166]. In turn, the low-symmetric, open crystal structure of  $\alpha$ -uranium was attributed to the narrow  $f$ -band, which is considerably smaller than the  $d$ -bandwidth in a TM [207, 210, 251]. The mechanism that stabilises such open structures in systems with narrow bands is considered to be similar to a Peierls distortion. That is, there can be an energy gain for metals with narrow bands and degenerate energy levels close to the Fermi energy due to a crystal structure distortion from high symmetric structures (cubic ones) towards low symmetric crystal structures. Such a distortion can lift degeneracies in the band structure and effectively lower one-electron energy contributions to the total energy (there are counteracting contributions, like electrostatic interactions, which prefer high symmetry structures).

Density functional calculations confirmed the magnitude of the  $\alpha_1$  lattice distortion ( $0.028 \text{ \AA}$ ) in agreement with the experimental value ( $0.027 \text{ \AA}$ ) [56]. The occurrence of the  $\alpha_1$  structural distortion was attributed to nesting features of the Fermi surface [56]. Recent full-relativistic DFT calculations employing the PBE96 parameterisation of the XC functional predicted, that surface atoms of bulk  $\alpha$ -uranium are FM [115, 217]. The size of the total magnetic moment

<sup>1</sup>lock-in = the CDW wave vector gets temperature independent with decreasing temperature

## 5.2. COMPUTATIONAL DETAILS

was reported to be  $0.54 \mu_B/\text{atom}$  (Ref. 115) and  $0.65 \mu_B/\text{atom}$  (Ref. 217). The occurrence of magnetism was traced back to a fulfilled Stoner criterion caused by band narrowing and the increased DOS at the surface compared to the bulk counterpart. DFT calculations for bulk HCP-uranium predicted the possibility of ferromagnetism [215]. These predictions of magnetism in HCP-uranium and surface magnetism in  $\alpha$ -uranium have not been confirmed hitherto. We investigate HCP-uranium in Sec. 5.3.2.

The success of LDA and GGA in describing bulk uranium was recently argued to be due to its low  $5f$ -occupation (about three electrons per atom) [33]. In their quasi particle GW calculations for  $\alpha$ -uranium, Chantis *et al.* show that correlations mainly predominate the unoccupied part of the band structure. Within GW, the uranium  $f$ -bands shift up by 0.5 eV relative to  $s - d$  bands, and the  $f$ -band width in GW is narrower than in LDA. Properties of the GS and the occupied part of the band structure around the Fermi level are not significantly different between the GW calculation and the LDA calculation.

## 5.2 Computational details

The band-structure calculations in this chapter were done throughout in the full-relativistic implementation of the FPLO program package, version 9.00 – 34. In version 9, the GGA XC potential in the parameterisation of PBE96 is available and was used in all cases. Details of the band structure code and principal numerical settings were reported in Sec. 4.4 on Page 32 *et. seqq.* Here we only state settings specific to the calculation of the EBP of uranium. The orthorhombic lattice of  $\alpha$ -uranium, and uranium in the BCT and HCP structures were calculated with a Brillouin zone integration mesh ( $k$ -mesh) of  $24^3$  points. This mesh was found sufficient to stabilise the total energy at a level of  $50 \mu\text{eV}/\text{atom}$  and  $180 \mu\text{eV}/\text{atom}$  for BCT and HCP, respectively, compared to a mesh with  $48^3 k$ -points. The reported DOS and magnetic moments, were obtained using a mesh with  $48^3 k$ -points. We checked the completeness of the valence basis with the procedure described in Sec. 4.4.2 on Page 35. The default basis is sufficient and comprised  $5df$ ,  $6spdf$ ,  $7spd$ , and  $8s$  states. All calculations were done with spin-polarisation allowed for. The quantisation axis was chosen along [001] (parallel to the tetragonal axis).

**Orthorhombic GS of uranium** We considered the orthorhombic crystal structure, as present for temperatures between 43 K and 940 K, as GS crystal structure of uranium (Fig. 5.1). We did not take into account the lattice distortions due to the low temperature structural phase transitions, because of their tiny energy scale ( $< 1 \text{ meV}/\text{atom}$ ) compared to typical structural energy differences, e.g., the energy differences between BCC uranium and  $\alpha$ -uranium ( $200 \text{ meV}/\text{atom}$ ). Reference 56 calculated in fact a total energy decrease of  $0.6 \text{ meV}/\text{atom}$  with respect to the energy of  $\alpha$ -uranium, which is accompanied by the onset of  $\alpha_1$ . The absolute atomic displacement of  $\alpha_1$  is one order of magnitude larger than the one of the other two structural phase transitions [114]. The temperature, at which the CDWs lock in, is further the highest for  $\alpha_1$ . Thus, the energy scale of the other two CDWs is certainly less than or at most in the order of  $1 \text{ meV}/\text{atom}$ .

## CHAPTER 5. URANIUM

Table 5.1: Structural and energetic details of all stationary points of  $E$  along the EBP of uranium ordered by increasing  $a$  (decreasing  $c/a$ ). The points are referred to as their highest symmetry indicates, BCT structures are consecutively numbered. Type defines the type of stationary point of the total energy (MIN=minimum and MAX=maximum). Differences in energy with respect to the GS are given per atom, and compared to values available in the literature.

label	type	$a$ [Å]	$c/a$	$E - E_\alpha$ [meV]
BCT <sup>(1)</sup>	MIN	2.80	1.89	142
FCC	MAX	3.16	1.41	300, 259 <sup>a</sup>
BCT <sup>(2)</sup>	MIN	3.38	1.07	197
BCC	MAX	3.45, 3.46 <sup>a</sup>	1.00	200, 223 <sup>a</sup>
BCT <sup>(3)</sup>	MIN	3.70	0.82	106, 92.5 <sup>ab</sup>

<sup>a</sup> PBE96 values from Ref. 166 (FP-LMTO)

<sup>b</sup> with fixed  $c/a = 0.825$

The space group of the orthorhombic GS is  $CMCM$ . The only Wyckoff position is  $(0\ y\ 0.25)$  [237]. This structure has four independent parameters, which must be optimised (three lattice parameters, one internal parameter, cf. Fig. 5.1). The parameter ratios  $b/a$  and  $c/a$ , and the parameter  $y$  were earlier reported to be moderately volume dependent in the range of the theoretical equilibrium volume [3]. Starting from the fixed lattice parameter ratios  $b/a$  and  $c/a$ , and the parameter  $y$  as determined in experiments, we optimised the volume in a first step. Then we subsequently optimised one of the ratios or  $y$ , keeping the volume in the unit cell constant (keeping the volume constant during the lattice parameter optimisation decreased the total energy generally stronger than with fixed parameter ratios and variable volume). We always chose to adjust the parameter, that lowered the total energy the most during the optimisation, and continued the total energy optimisation with respect to the other parameters. Each of the four parameters was optimised at least once during the procedure. We found for the completely relaxed orthorhombic structure (deviation from experimental value is stated in parentheses)  $a = 2.840$  Å (0.14% too large),  $b = 5.829$  Å (0.53% too small),  $c = 4.962$  Å (0.53% too large), and  $y = 0.1008$  Å (0.99% too small). These value agree well with the experimental ones which were stated in the caption of Fig. 5.1. The theoretical equilibrium volume,  $V_\alpha$ , is  $20.537$  Å<sup>3</sup>/atom. The total energy per atom of  $\alpha$ -uranium in the theoretical equilibrium configuration is referred to as  $E_\alpha$ .

## 5.3 Results and discussion

### 5.3.1 The epitaxial Bain path of uranium

We calculated the EBP of uranium and found three minima and two maxima in the total energy along the EBP ( $E(a)$ ). Thus, the EBP of uranium can be classified as non-standard according to the scheme proposed in Sec. 4.6.2 on Page 108. The extrema are labelled according to the symmetry of the under-

### 5.3. RESULTS AND DISCUSSION

lying lattice and are consecutively numbered, cf. Fig. 5.2 and Table 5.1 for the complete data. The positions of both maxima in total energy coincide with structures of cubic symmetry. The FCC structure has the higher energy. There is a shallow, local minimum (BCT<sup>(2)</sup>) between the maxima of the cubic geometries. The extrapolated room temperature lattice parameter of BCC uranium, 3.474 Å [43], agrees well with our calculated value, 3.45 Å. The tetragonal state BCT<sup>(3)</sup>, which is lowest in total energy, possesses an axial ratio  $c/a = 0.82$ . This ratio is close to the value of BCT<sub>10</sub> ( $\sqrt{2/3} \approx 0.816$ ). The second lowest minimum in total energy is BCT<sup>(1)</sup> at 2.80 Å ( $c/a = 1.89$ ). The structural energy differences of the five distinguished states with respect to the GS are given in Table 5.1. Our values fairly agree with published energy differences from Ref. 166, which are stated in the table as well.

The observed GS crystal structure of protactinium is BCT with  $c/a = 0.825$ . Protactinium precedes uranium in the periodic table of elements. A predicted transformation of  $\alpha$ -uranium under pressure is  $\alpha$ -U  $\rightarrow$  BCT-U ( $c/a = 0.82$ )  $\rightarrow$  BCC-U [207], but has not been confirmed hitherto [116].

We calculated the EBP of uranium in due consideration of magnetic order, whereat we focused on FM and AF1 order only. A possible relaxation of  $c$  due to presence of magnetism was accounted for. The FSM method is not available in the full-relativistic calculation method. All spin-polarised calculations were therefore done with an ISS. At first we note, that  $\alpha$ -uranium did not show a stable FM or AFM GS (calculations with assumed FM and AFM order converged into a solution with zero total moment on each site). However, the EBP reveals surprisingly states that order ferromagnetically. These states are highlighted by filled red triangles in Fig. 5.2. According to that picture, there are two ranges of states with FM order to be distinguished: a first range is limited to  $a = 2.875 \dots 3.18$  Å, hereafter called ‘R1’. The second range ‘R2’ begins at  $a = 4.05$  Å and extends beyond the limit of the present calculation, 4.10 Å. FCC uranium orders ferromagnetically and is situated in R1.

We plotted the total energy differences between NM and FM states of R1 in Fig. 5.3. The magnitude of the energy difference of at most 13 meV/atom suggests, that an FM state might be stable at temperatures of several 10 K. Figure 5.3 also gives a detailed picture of total, spin, and orbital magnetic moments for the FM states of R1. Both spin and orbital moments are of considerable size, but couple anti-parallel and almost cancel their values to a surviving total magnetic moment of about 0.17 to 0.33  $\mu_B$ /atom depending on  $a$ . Approximate cancellation of spin and orbital magnetic moments at the uranium site is, for example, known from the itinerant uranium compound UNi<sub>2</sub> [199]. The large orbital moment originates from the strong spin-orbit coupling in the narrow 5*f*-band of uranium [24]. FCC uranium has a total moment of 0.34  $\mu_B$ /atom (spin moment: 0.94  $\mu_B$ /atom, orbital moment:  $-0.60 \mu_B$ /atom).

In Fig. 5.4, we plotted total, spin, and orbital moments, as well as the total energy difference between NM and FM states of the EBP for R2. In what follows, we neglect the discussion of R2, since states in that region are high in energy compared to the GS (cf. Fig. 5.2), and also exhibit much larger in-plane stresses than states in R1. The in-plane stress along the EBP,  $\sigma = \sigma(a)$ , is given by [133, 163]

$$\sigma(a) = \frac{2}{ac} \frac{\partial E}{\partial a} \quad (5.1)$$

## CHAPTER 5. URANIUM

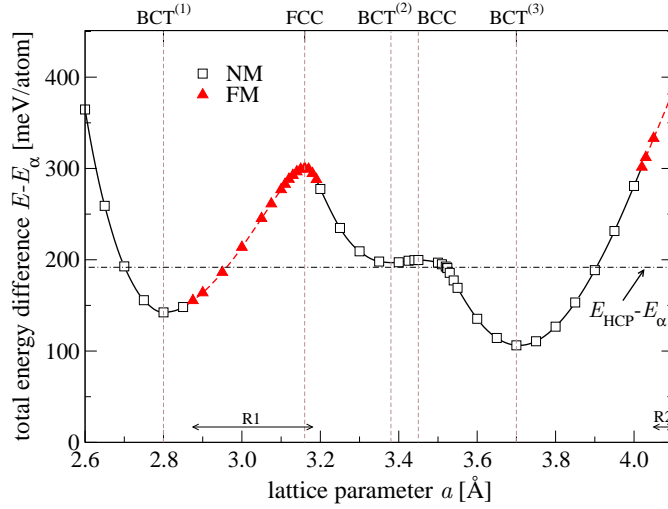


Figure 5.2: Total energy along the EBP of uranium with respect to  $E_\alpha$ . NM and FM states are distinguished. FM order occurs in two ranges on the EBP, R1 and R2. The horizontal dot-dashed line indicates the energy difference between HCP-uranium and  $\alpha$ -uranium. Vertical dashed lines highlight positions of extrema, and are referred to according to the labels on top. Lines to the data (symbols) are spline fits and guide the eye.

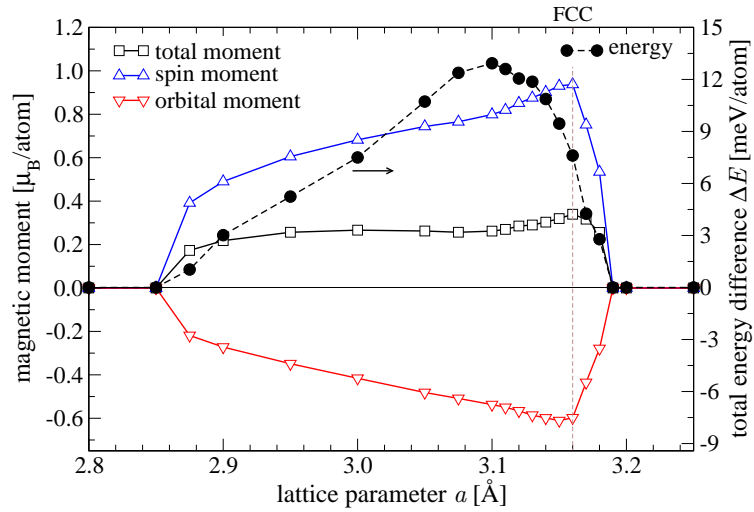


Figure 5.3: Total, spin, and orbital moments for the magnetic states in R1 along the EBP (*left hand ordinate*), and total energy difference,  $\Delta E = E_{\text{NM}} - E_{\text{FM}}$ , (*right hand ordinate*). If  $\Delta E > 0$ , FM order is preferred. The vertical dashed line highlights the FCC structure on the EBP. Lines to the data (symbols) guide the eye.



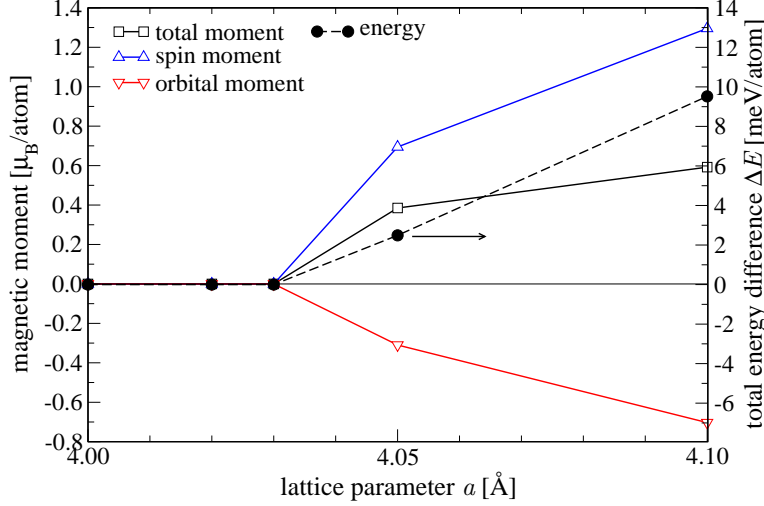


Figure 5.4: Total, spin, and orbital moments for the magnetic states in R2 along the EBP (left hand ordinate), and total energy difference  $\Delta E$  (right hand ordinate).  $\Delta E$  is defined in Fig. 5.3. Lines guide the eye.

$\sigma$  is larger in R2 than in R1, mainly due to the steeper slope of  $E(a)$  (the product of the prefactors  $a$  and  $c$  has nearly the same weight, due to their reciprocal ratio, see Fig. 5.5 for the functional dependence of  $c$  upon  $a$ ). From the experimental point of view, the feasibility of epitaxial growth depends on the size of both parameters,  $E - E_\alpha$  and  $\sigma$ , whereat high feasibility is achieved for low energies and small stresses [253]. Thus from an experimental point of view, R1 is to be preferred over R2.

We also checked the possibility of a layerwise AFM order (AF1) exemplarily for  $a = 3.00, 3.10, 3.15, 4.10$  Å. The AF1 energy is in all cases well above the FM energy (by about 5 meV/atom) but also below the energy of the NM state. Since AFM order is not the ruling magnetic GS order we neglect it in the ongoing discussion.

A closer look on the structural properties of the tetragonal states constituting the EBP is worthwhile. In Fig. 5.5 we plotted  $c(a)/a$ , from which we realise a monotonic decrease with increasing  $a$ , and two pronounced drops in the curve progression. The larger drop approximately coincides with the position of the FCC structure on the EBP, which is an instable maximum. The second drop is a discontinuity in  $c$ , and occurs between  $a = 3.523$  Å and  $3.534$  Å. This case is identical to the discontinuity that we found for, e.g., La and V in the previous chapter of this thesis, and was discussed on more general grounds in Sec. 4.5.4. The change of  $c$  across the discontinuity is  $\Delta c = 0.08$  Å accompanied by a pronounced decrease of the DOS at  $E_F$  by  $0.7/(eV \cdot \text{atom})$  (Fig. 5.6).

Both drops are clearly seen in the volume curve along the EBP,  $V(a)$ , see Figure 5.5, where we depict the unit volume relative to the volume per atom of  $\alpha$ -uranium,  $V_\alpha$ . Magnetism occurs in a range where the relative volume is slightly to moderately larger (3 to 12% in R1) or considerably larger ( $> 15\%$  in

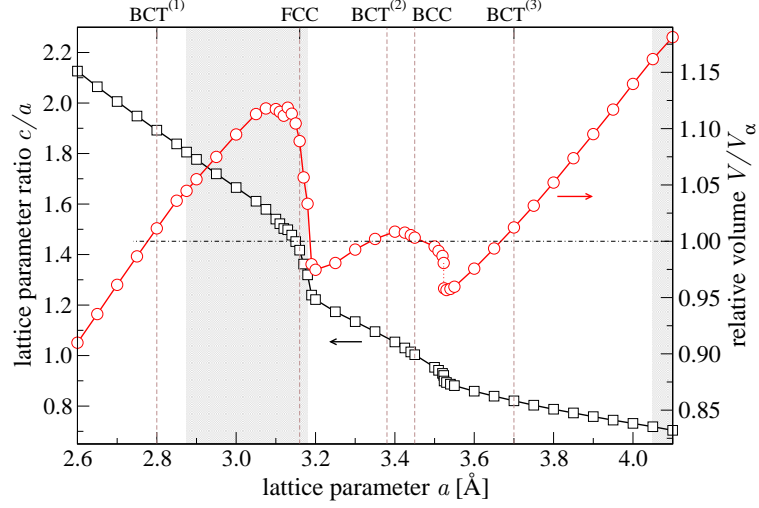


Figure 5.5: Lattice parameter ratio (*left hand ordinate*), and relative volume (*right hand ordinate*) along the EBP of uranium. The volume is given relative to  $V_\alpha$ . The horizontal dot-dashed line corresponds to  $V/V_\alpha = 1$ . The grey bars indicate the region of FM states of the EBP in conformance with Fig. 5.2. Vertical dashed lines highlight positions of extrema in the total energy. Solid lines to the data (symbols) guide the eye.

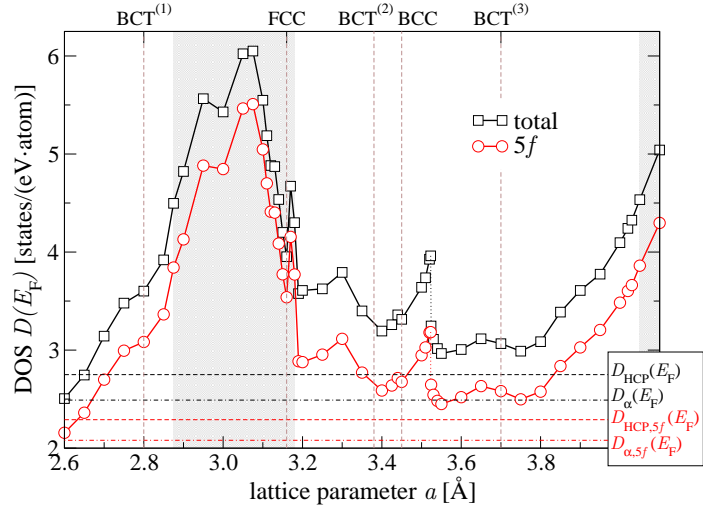


Figure 5.6: Total DOS and contributions from  $5f$ -states at the Fermi energy along the EBP of uranium calculated without spin-polarisation. The grey bars indicate the region of FM states of the EBP in conformance with Fig. 5.2. Horizontal dot-dashed and dashed lines indicate total and  $5f$ -values of HCP-uranium and  $\alpha$ -uranium, respectively. Vertical dashed lines highlight positions of extrema in the total energy. Solid lines to the data (symbols) guide the eye.

### 5.3. RESULTS AND DISCUSSION

R2) than the one of  $\alpha$ -uranium.

The nearest distance between two uranium atoms along the EBP can be derived with the help of Fig. 3.7 on Page 20 and Fig. 5.5. The former states the nearest neighbour pair in reduced lattice parameters, and the latter relates  $c$  to  $a$  according to the EBP of uranium. It turns out, that the largest distance,  $d_{\max}$ , between two nearest neighbours along the EBP is  $d_{\max} = a_{\text{FCC}} = 3.16 \text{ \AA}$ , hence well below the Hill distance of uranium ( $\approx 3.5 \text{ \AA}$ ) [79, 147].

To answer the question what drives the onset of magnetism in certain tetragonal states, we evaluated the DOS, using a non-polarised calculation method, but took the geometry that was optimised in the spin-polarised calculations. Figure 5.6 shows the total DOS at the Fermi level and contributions from the  $5f$ -orbitals along the EBP. The difference between the two curves can be almost exclusively attributed to  $6d$ -states. The DOS at  $E_{\text{F}}$  shows great volatility along the EBP with peak values more than twice as large as the DOS at  $E_{\text{F}}$  in the GS,  $D_{\alpha}(E_{\text{F}})$ , for which we evaluated  $D_{\alpha}(E_{\text{F}}) = 2.49 / (\text{eV} \cdot \text{atom})$ . The  $5f$ -fraction to the total DOS,  $D_{\alpha, 5f}(E_{\text{F}})$ , is  $2.08 / (\text{eV} \cdot \text{atom})$ . Both values are indicated in Fig. 5.6. A similar value for  $D_{\alpha}$  was reported from Ref. 166:  $2.5 / (\text{eV} \cdot \text{atom})$  at the theoretical equilibrium volume, calculated within PBE96 and FP-LMTO. A slightly higher value,  $2.75 / (\text{eV} \cdot \text{atom})$ , was found in Ref. 33 at the experimental atomic volume with PBE96 and FP-LAPW. We note from Fig. 5.6, that the  $5f$ -contribution to the total DOS at the Fermi level in the FM regions R1 and R2 is larger than about  $3.5 / (\text{eV} \cdot \text{atom})$ . The Stoner criterion for the onset of FM, introduced in Eq. (4.10) on Page 70, with the Stoner exchange integral  $I \approx 0.2 \text{ eV}$  [115, 188] for uranium  $5f$ -states is not fulfilled in the FM regions, but only in the centre of R1, where  $D_{\alpha, 5f}(E_{\text{F}}) > 5 / (\text{eV} \cdot \text{atom})$ . In the other parts of the FM region, a non-trivial situation with a metastable NM and a stable FM state is obviously present.

It is instructive to compare the total DOS of  $\alpha$ -uranium with that of BCT-uranium, Fig. 5.7. Without loss of generality, we chose the tetragonal state at  $a = 3.00 \text{ \AA}$  (with  $c/a = 1.67$ ). The predominant contributions to the presented DOS originate from  $5f$ -states. The bandwidth of uranium in the BCT structure is narrower than in  $\alpha$ -uranium, an effect that can be understood from the 10% larger atomic volume of the BCT structure compared to  $V_{\alpha}$ . Clearly, the DOS of BCT-U has sharper features, particularly in the unoccupied part, than the DOS of  $\alpha$ -U. This was shown to be generally the case for the  $5f$ -partial DOS of uranium in higher symmetric structures, such as the FCC and the Pa structure, than in the lower symmetric orthorhombic structure, despite the bandwidth being approximately the same in those structures [251]. As mentioned in the introduction, Sec. 5.1, a crystal structure distortion from high symmetric structures to low symmetric structures can avoid a high degeneracy of energy levels around the Fermi energy in narrow band systems. We suggest, that a converse argument is valid in the present case. We impose a higher symmetry than orthorhombic on uranium, by modelling BCT films clamped to a substrate. This brings along a DOS with generally sharper features (Ref. 251), and particularly high DOS in BCT lattices for certain values of the (substrate) lattice parameter  $a$  (Fig. 5.6). A likely energy lowering mechanism in such cases is the onset of ferromagnetism, since the lattice symmetry is constrained.

We are not aware of any published non-volume conserving Bain path of U, especially there is no published EBP of uranium to the best of our knowledge.

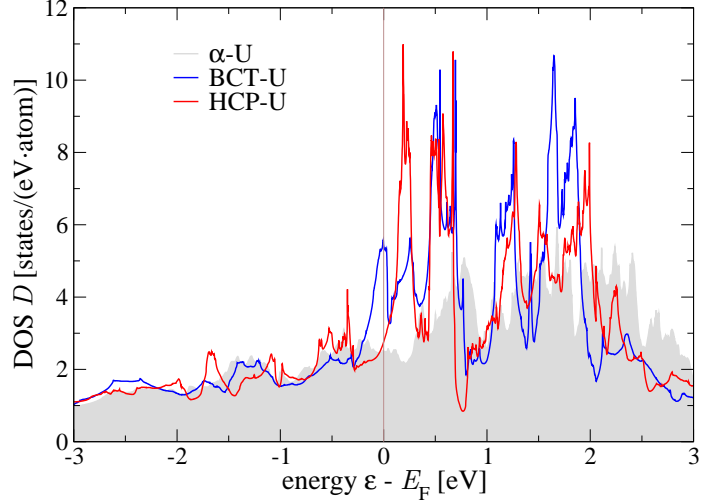


Figure 5.7: Total DOS for  $\alpha$ -uranium, and uranium in the BCT and HCP structure. The BCT state corresponds to  $a = 3.00 \text{ \AA}$  on the EBP and was calculated without spin-polarisation. The Fermi energy is indicated by a vertical line. The  $5f$ -occupation per atom for  $\alpha$ -uranium is 3.00 states, for the BCT and HCP structure 2.90 states and 2.92 states, respectively.

We feel however bound to mention a CVBP for uranium, where the unit volume per atom along the transformation path was fixed to  $V_{\text{CVBP}} = 20.75 \text{ \AA}^3$  [207]. This value is slightly larger than the experimental volume per atom of  $\alpha$ -uranium ( $20.535 \text{ \AA}^3$ ). The CVBP, as depicted in Ref. 207, has qualitatively the same structure as our EBP, i.e., an identical sequence of extrema with increasing  $c/a$ , whereat the FCC and the BCC structure are points of maxima of the energy, and the global minimum of  $E$  has  $c/a = 0.82$ . Reference 207 did not report on any magnetic order.

We calculated the properties along the CVBP at the experimentally determined equilibrium volume of  $\alpha$ -uranium (at 50 K),  $V_{\alpha, \text{EXP}}$ . The CVBP is close to the EBP whenever  $V/V_{\alpha} \simeq V_{\alpha, \text{EXP}}/V_{\alpha} \approx 1$ . According to Fig. 5.5, this is the case for the BCC structure and all three BCT extrema. We also calculated the properties along the CVBP at the theoretical equilibrium volume of uranium in the FCC structure,  $V_{\text{FCC}} = 22.37 \text{ \AA}^3$  (per atom). The results are summarised in Fig. 5.8. Both CVBPs must have total energies equal or above those of the EBP, due to the relaxation of the out-of-plane lattice parameter, which is only done for the EBP (Fig. 5.8a). The  $a$ -coordinate of the extrema between the CVBPs and the EBP differs the more, the larger the volume difference between the CVBPs and the EBP is. CVBPs also have stationary points in total energy at cubic structures [38, 133]. Large volume differences go along with large energy differences. The CVBP at  $V_{\text{FCC}}$  adapts the EBP in R1 and at  $a = 3.90 \text{ \AA}$ , when  $V = V_{\text{FCC}}$ . Similarly, the CVBP at  $V_{\alpha, \text{EXP}}$  adapts the EBP in  $a_{\text{FCC}} < a < a_{\text{BCT}^{(3)}}$  and at  $a = 2.78 \text{ \AA}$ , when  $V = V_{\alpha, \text{EXP}}$  (cf. volume along the EBP in Fig. 5.5).

### 5.3. RESULTS AND DISCUSSION

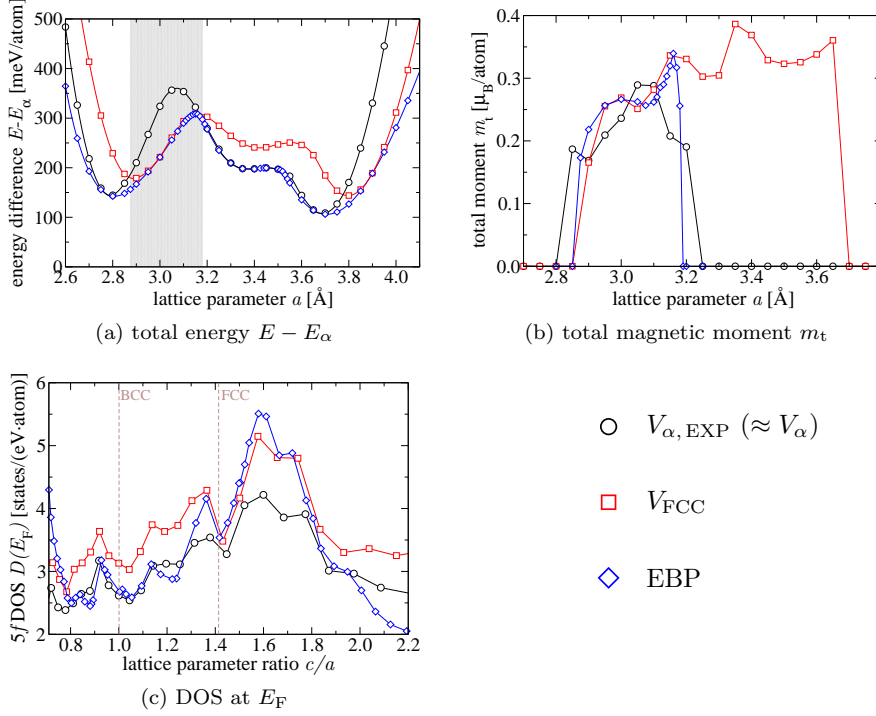


Figure 5.8: Comparison of the EBP with the CVBP at the experimental volume of  $\alpha$ -uranium,  $V_{\alpha, \text{EXP}}$ , and the CVBP at the theoretical volume of FCC uranium,  $V_{\text{FCC}}$ . The total energy, in (a), and the total magnetic moment, in (b), along the Bain paths are plotted versus the lattice parameter  $a$ , while the DOS at the Fermi energy, in (c), is depicted as function of  $c/a$ . The DOS was computed without spin-polarisation. In order not to overload the figures, FM states on the Bain paths are not distinguished from NM states. The grey bar in (a) indicates R1 for the EBP. Solid lines guide the eye. The total energy data were interpolated by splines.

The total moment,  $m_t$ , along the EBP and the CVBPs exhibits a similar trend for all three curves in the region identical to R1,  $2.875 \text{ \AA} < a < 3.180 \text{ \AA}$ , despite the different atomic volumes, see Fig. 5.8b. Ferromagnetism for the CVBP with  $V_{\text{FCC}}$  persists up to  $a = 3.65 \text{ \AA}$ . In order to study the influence of the volume and the symmetry, we plot the DOS at the Fermi level, evaluated without spin-polarisation, in Fig. 5.8c. Note that the DOS is plotted as function of  $c/a$ . Although the three curves differ in their absolute height, there are evidently similar characteristics for all curves. At first, there is the pronounced, broad peak in the DOS centred around  $c/a = 1.6$  adjacent to a dip at approximately the position of FCC. There is a strong decrease of the DOS for  $c/a > 1.75$ . Further, there are minor peaks at approximately  $c/a = 0.9$  and  $1.35$ , which are visible in all three curves. The occurrence of the aforementioned features at identical  $c/a$  ratios, in particular the major peak at  $c/a = 1.6$ , suggest that the general structure (but not the absolute height) of the DOS along the CVBPs and the EBP is mainly determined by the axial ratio alone. The absolute

height, however, is mainly determined by the volume. In favour of this argument is the fact, that the DOS for the CVBP at  $V_{\text{FCC}}$  is always larger than the corresponding DOS of the CVBP at  $V_{\alpha, \text{EXP}}$ , and  $V_{\text{FCC}} > V_{\alpha, \text{EXP}}$ . The volume along the EBP curve is strongly varying. Accordingly, the DOS along the EBP relative to the DOS along the CVBPs scales inversely with the volume along the EBP relative to the fixed volume of the CVBPs.

Itinerant magnetic uranium compounds like  $\text{UFe}_2$ ,  $\text{UNi}_2$ , and UN exhibit a substantial orbital and spin magnetic moment [24, 199, 252]. A close agreement of DFT calculations and experiments in  $\text{UNi}_2$  could only be achieved [199], if an orbital polarisation correction (OPC) [51, 162] was employed. OPC is a way to incorporate Hund's second rule in weakly correlated systems, and orbital polarisation in solids originates from spin-orbit coupling, but is exchange-enhanced [55]. The use of OPC in total energy calculations can be considered to give an upper estimate on orbital moments, while full-relativistic calculations without OPC supply a lower estimate to it [157]. The presence of a large orbital magnetic moment in the aforementioned compounds was conducted from 'anomalous'  $f$ -magnetic form factors [147], as measured in neutron scattering experiments. The form factors were called anomalous, since the measured total moment were small, but an analysis of the  $\mathbf{q}$ -vector (scattering vector) indicated a large orbital contribution to the total moments [199]. This is explained by an antiparallel orientation of spin and orbital moment, which compensate each other at the uranium site (Hund's third rule) [24]. In contrast, the field induced magnetic form factor of  $\alpha$ -uranium showed a rather 'normal' behaviour [130]. Normal, because the  $\mathbf{q}$ -dependence of the measured scattering amplitude in an external field indicated a small orbital moment, as it does for  $3d$  magnetic elements. References 81, 82 provided an explanation of the 'normal' magnetic form factor of  $\alpha$ -uranium by incorporating a Zeeman term in the electronic structure calculations, which coupled to the spin and the orbital moment. The external field destroys the Hund's rule GS, i.e. in a field induced state, orbital moment and spin moment are parallel. The best agreement with the experimentally determined, induced total magnetic moment and the magnetic form factor was achieved, if OPC was employed. The modulus of the calculated ratio of orbital and spin moment,  $|m_o/m_s|$ , for bulk uranium in an external magnetic field of 7 T is 3.5 and 1.3 with OPC and without OPC, respectively, i.e.,  $|m_o| > |m_s|$  [81]. This ratio for the magnetic states of the EBP is at most 0.67 without OPC (at 3.10 Å, this ratio can be inferred from the values in Fig. 5.8b). We employed spin dependent OPC according to Ref. 162 for  $5f$ -states, as implemented in FPLO. The application of OPC leads to increased orbital and spin moments, Fig. 5.9. The range R1 with applied OPC,  $2.85 \text{ \AA} \leq a \leq 3.18 \text{ \AA}$ , is slightly larger than without OPC (lower boundary was 2.875 Å, upper boundary is identical). While for the range  $a \geq 2.95 \text{ \AA}$ , the orbital moment exceeds the spin moment in its absolute value, the cancellation of both contribution to the total moment is almost perfect in the range  $2.85 \text{ \AA} \leq a \leq 2.95 \text{ \AA}$ . The largest ratio  $|m_o/m_s|$  with OPC amounts to 1.24 at  $a = 3.13 \text{ \AA}$ .

### 5.3.2 Bulk-like uranium overlayer with HCP structure

Originally, our interest in uranium arose from recent epitaxy experiments with uranium in a new HCP structure [15, 146, 215]. The lattice parameters, as

### 5.3. RESULTS AND DISCUSSION

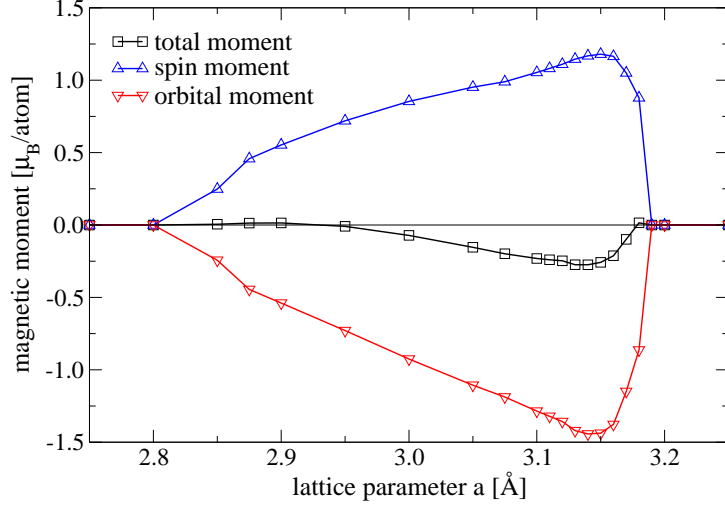


Figure 5.9: Total, spin, and orbital moment for the magnetic states in R1 along the EBP, calculated with OPC. Lines guide the eye.

determined in 50 nm thick HCP films, are  $a = 2.96 \text{ \AA}$  and  $c/a = 1.90 \pm 0.01$  [215]. Moreover, FP-LMTO calculations predicted FM order in bulk HCP uranium [215], although uranium in the GS crystal structure does not order magnetically. The predicted total magnetic moment in the HCP structure is  $0.12 \mu_B/\text{atom}$  at the theoretical equilibrium volume.

We argue in what follows, that bulk HCP-uranium should not order magnetically. Furthermore, we investigate a strained HCP structure of uranium to simulate a lattice mismatch between a hexagonal (0001) oriented substrate and a pseudomorphic bulk-like HCP film. Also strained HCP-uranium does not favour an FM state for in-plane strains smaller than  $|0.045|$ .

All calculations were done with spin-polarisation, and initially started with a finite ISS of  $2 \mu_B/\text{atom}$ . We denote the theoretical lattice constants of the HCP structure with  $a_{\text{HCP}}$  and  $c_{\text{HCP}}$ . The space group is  $P6_3/mmc$ . We obtained for both in equilibrium:  $a_{\text{HCP}} = 3.009 \text{ \AA}$  and  $c_{\text{HCP}}/a_{\text{HCP}} = 1.820$ . The corresponding total energy,  $E_{\text{HCP}}$ , with respect to the GS energy is  $E_{\text{HCP}} - E_\alpha = 192 \text{ meV/atom}$ . We find, that HCP-uranium with the mentioned lattice parameters does not exhibit a finite magnetic moment. Our calculated lattice parameters and the energy difference agree with respective values from Ref. 215, which reported  $a_{\text{HCP}} = 2.98 \text{ \AA}$ ,  $c_{\text{HCP}}/a_{\text{HCP}} = 1.84$ , and  $E_{\text{HCP}} - E_\alpha = 210 \text{ meV/atom}$ .

The experimentally determined in-plane lattice parameter of HCP-uranium,  $a = 2.96 \text{ \AA}$ , is smaller than our calculated value,  $a_{\text{HCP}} = 3.009 \text{ \AA}$ . Also, the measured  $c/a$ -ratio ( $c/a = 1.90 \pm 0.01$ ) is larger than our calculated ratio. This could point to small negative in-plane strain of the uranium film which was deposited on a gadolinium substrate. We expect, that the out-of-plane lattice parameter  $c$  increases in response to a decrease of  $a$  away from the equilibrium state. We relaxed the  $c/a$  ratio for  $a$  fixed to  $a = 2.96 \text{ \AA}$ , and obtained  $c/a = 1.864$  closer to the measured value.

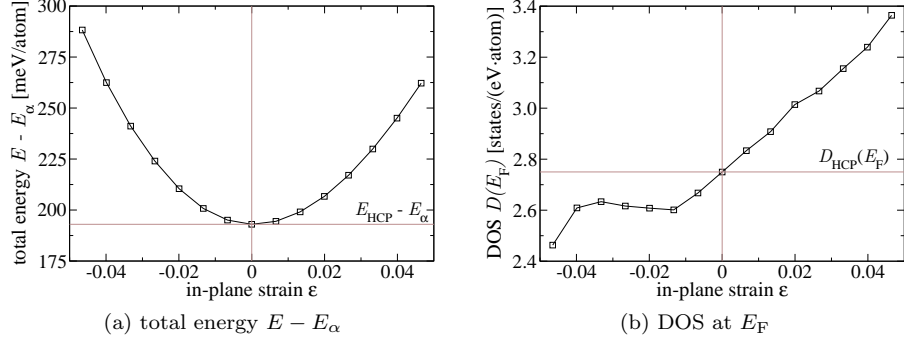


Figure 5.10: (a) Total energy  $E - E_\alpha$  and (b) DOS at  $E_F$  for epitaxially strained uranium in a HCP structure. Grey lines indicate the unstrained HCP state/values. Lines to the data (symbols) guide the eye.

In order to compare the HCP equilibrium state with the stationary states of the EBP, we indicated the energy difference  $E_{\text{HCP}} - E_\alpha$  in Fig. 5.2 (Page 124). The total energy of HCP-uranium is comparable with that of uranium in the BCC structure, while the energies of BCT<sup>(1)</sup> and BCT<sup>(3)</sup> are well below  $E_{\text{HCP}}$ . The total DOS at the Fermi level and contribution from 5*f*-states to the total DOS at the Fermi level of HCP-uranium are 2.75/(eV · atom) and 2.29/eV per atom, respectively. Both values are indicated in Fig. 5.6 (Page 126). Evident from Fig. 5.6, the DOS at  $E_F$  in HCP-uranium is considerably smaller than the DOS of all BCT states of the EBP which support ferromagnetism ( $> 3.5$ /(eV · atom)).

The DOS of HCP uranium exhibits a significant peak centred approximately 0.2 eV above  $E_F$ , see Fig. 5.7, which could become crucial for a strained HCP structure. The Fermi level may then coincide with the position of the peak, which may lead to an increase of the DOS in the vicinity of the Fermi level, and possibly render uranium FM. We therefore modelled strained HCP structures pseudomorphically grown on a (0001) oriented hexagonal substrate. The concept and the calculation is analogous to the EBP for tetragonal structures. We minimised the total energy by relaxing the out-of-plane lattice parameter  $c$  for each selected in-plane lattice parameter  $a$ . Hence,  $c$  is a function of  $a$ . In fact, the procedure allows for a straightforward definition of a hexagonal EBP [97]. We applied an in-plane strain,  $\epsilon = (a - a_{\text{HCP}})/a_{\text{HCP}}$ , up to  $|\epsilon| = 0.045$  on the relaxed HCP structure in the described manner. The applied strain was both compressive and tensile, and all calculations allowed for FM order.

Within the strain limits given, we did not find an FM state of HCP uranium, although the DOS at the Fermi level exhibits a pronounced increase for tensile in-plane strain, see Fig. 5.10. The DOS at  $E_F$  reaches 3.36/(eV · atom) at  $\epsilon = 0.045$ . An inspection of the DOS for that state signals a broadening and a height diminution of the aforementioned peak in the DOS. An FM state for even larger strains could be possible, but requires further calculations. Such a state would require to stabilise a film at the cost of a higher energy and a further increase of the in-plane stress  $\sigma \propto \partial E/\partial a$  (cf. Eq. (5.1)).



## 5.4 Summary of main results

The purpose of the density functional calculations in this chapter was to study structural and magnetic properties of bulk-like uranium overlayers in the BCT structure. The EBP provides a model therefor. We determined three prominent tetragonal structures (BCT<sup>(1)</sup>, BCT<sup>(2)</sup>, BCT<sup>(3)</sup>), whose energies in the tetragonal parameter space are locally minimised, i.e., these states exhibit no in-plane stresses. All three states are NM. The energies of the FCC and the BCC structure are maxima of  $E(a)$ .

We predict, that some BCT states on the EBP order ferromagnetically. Those states have a lattice parameter  $a$  in the range of  $2.875 \leq a \leq 3.180 \text{ \AA}$  or in the range of  $a \geq 4.050 \text{ \AA}$ . They exhibit a finite in-plane stress with the exception of the FCC state. All other BCT states are NM. The orbital moment couples antiparallel to the spin moment in the FM states. The largest predicted total moments amount to  $0.2 \mu_{\text{B}}/\text{atom}$  and  $0.3 \mu_{\text{B}}/\text{atom}$  without and with OPC, respectively. The occurrence of FM order in itinerant BCT uranium is due to a high  $5f$ -DOS in the vicinity of the Fermi level, which is not present in the GS. We argue, that the increase of the DOS is mainly due to particular, imposed  $c/a$  ratios of the BCT structure.

Concerning the possibility of FM order in unstrained HCP-uranium, our results disagree with an earlier literature work. We predict, that FM order in HCP uranium does not occur in epitaxially strained HCP-structures in the range  $|\epsilon| \leq 0.045$ .





# 6

## Summary and outlook

Epitaxial growth is an important technique for the fabrication of film structures with good crystalline quality, e.g., monoatomic overlayers, multilayers, compound materials, and ordered alloys. Such epitaxially grown films are technologically important materials with, e.g., adjustable electronic, magnetic, and optical properties. Epitaxial growth makes it possible to study fundamental aspects of low-dimensional structures and interfacial effects, and it can stabilise strained structures that are unstable in the bulk.

This thesis was concerned with a theoretical prediction of bulk-like properties in thick overlayers, which adopt the BCT crystal structure and grow coherently on a suitable substrate with quadratic surface symmetry. The employed model of the EBP provides a description of all possible, coherently grown bulk-like overlayers in the BCT structure, and the knowledge of the EBP therefore allows to study properties of the overlayer as function of the substrate lattice parameter. In particular, strain effects on the film material, magnetic order in the overlayer, and the existence of possible metastable states were investigated by means of DFT in the LSDA, and in the singular case of uranium, employing GGA. The knowledge of the EBP of a material may replace the procedure known as strain analysis, which is based on the assumption of a linear elastic response of the film material due to strain, since the EBP relates the out-of-plane lattice parameter of the film to the in-plane lattice parameter of the substrate without any such approximation.

Our definition of the EBP (Eq. (3.7)) has two, previously not considered consequences for EBPs in general: an EBP can be discontinuous, and the high symmetry cubic structures (FCC and BCC) need not be points on the EBP. Both cases occurred for several elements considered in this thesis. If, however, a cubic structure is a point on the EBP, then a symmetry property guarantees that  $E(a)$  is stationary at this cubic structure.

In Chapters 4 and 5 of this thesis, we computed the EBPs of all TMs, the post TMs Zn, Cd, and Hg, the alkaline earth metals Ca, Sr, and Ba, the lanthanides La and Lu, and the actinide U (35 elements were treated in total). For each element but Zr, Hg, and U, there are exactly two structures whose energies are minima on the EBP, and which exhibit neither in-plane nor out-of-plane stresses; for Zr, Hg, and U there are three minima each. All other states on the EBP exhibit in-plane stresses because they are a strained form of the stress-free structures. The possibility of metastability of these particular, stress-free structures, i.e., stabilisation of these structures without bonding to

## CHAPTER 6. SUMMARY AND OUTLOOK

---

the substrate, was investigated by stability conditions based on linear elasticity theory (except for U). We predict, that ten FCC structures and three BCT structures not known from the respective phase diagrams may be metastable.

We studied the properties of FM states on the EBP for the elements Fe, Co, and Ni, and moreover predict, that Mn, Ru, Os, and U order ferromagnetically for certain states of the EBP. The latter three elements are paramagnetic in the GS. The onset of ferromagnetism in Os and U is not accompanied by a simultaneously fulfilled Stoner criterion. According to our results, AF1 and AF2 orders are never more stable than FM order on any EBP for any element investigated.

On the basis of our comprehensive results for all TMs, we analysed trends across each of the three TM series and similarities among the three series. We demonstrated, that the type of the EBP (a classification of extrema of  $E(a)$  by symmetry into types) follows a characteristic trend across each of the three TM series. We discussed exceptions (Mn, Fe, and Zr) to this trend. Another trend, identical for the three series, is seen in the function  $\Delta E_{\text{BCT}}$ , which follows a similar trend as the well studied function  $\Delta E_{\text{BCC}}$ . Clear similarities among the three periods of elements are also reflected in the bulk moduli and in the elastic constants of the cubic or tetragonal structures, that define the global and local minima of  $E(a)$ . The mentioned similarities suggest, that many properties which are associated with the EBPs of TMs, can be attributed to the occupation of the  $d$ -band, which is the most dominant feature of the electronic structure of TMs.

A direct extension of this work could be to study the predictive character of a simple canonical  $d$ -band model for BCT lattices (with all relevant  $c/a$ -ratios) for the following quantities as function of the  $d$ -occupation number, i.e., across the TM series: firstly, the  $c/a$ -ratio of all extrema of  $E(a)$ , in particular the one of the secondary minimum, secondly, the trend  $\Delta E_{\text{BCT}}$ , and based on the latter two, the evolution of  $E(c/a)$ . Results of such a model may provide a simple picture of some of the trends that we found in this thesis. First attempts in this direction exist [211]. Using the example of Ti and Zr, we demonstrated the alteration of  $E(a)$  (number of extrema and general shape) in response to a change of the number of  $d$ -electrons per atom, thereby showing that the irregular number of extrema on the EBP of Zr is not a particular feature of the fourth period. The averaged electron number per atom can be influenced by alloying, i.e., it may be of interest to study the EBP and its energy landscape for alloys in general and as function of the alloy composition in particular. First results in this direction exist for  $\text{Fe}_{70}\text{Pd}_{30}$  [29] and for Fe-Co alloys [158].



# A

## Elastic constants

The total energy,  $E$ , is defined per volume of the primitive unit cell,  $V$ . Note the conversion of units:  $1 \cdot \text{Hartree} \cdot \text{\AA}^{-3} = 4378.311 \cdot \text{GPa}$ .

### A.1 Theoretical considerations

We consider the harmonic long wavelength limit of acoustical phonons to evaluate the elastic constants of crystals [22, 52]. Without the presence of external forces, the total energy has a stationary value at equilibrium. The total energy is a quadratic form of the components of the strain tensor (strain energy),  $\epsilon_{ij}$ ,

$$E = \frac{1}{2} \sum_{ijkl} c_{ijkl} \epsilon_{ij} \epsilon_{kl} \quad i, j, k, l = \{x, y, z\}, \quad (\text{A.1})$$

and elastic constants,  $c_{ijkl}$ , which are independent of  $\epsilon$  in the harmonic approximation. For the lattice to be (meta)stable, the total energy must be positive definite for any small strain. Hook's law relates stress  $\sigma$  and strain  $\epsilon$  by

$$\sigma_{ij} = \sum_{kl} c_{ijkl} \epsilon_{kl}. \quad (\text{A.2})$$

We consider the tetragonal crystal class  $I4/mmm$ , the  $z$ -axis be the tetragonal axis (for the orientation of the BCT lattice, see Sec. 3.2). This lattice symmetry reduces the number of independent elastic constants to six:  $c_{xxxx}$ ,  $c_{zzzz}$ ,  $c_{xyxy}$ ,  $c_{xxzz}$ ,  $c_{xyxy}$ , and  $c_{xzzx}$  [113, 163]. Thus, Eq. (A.1) becomes

$$\begin{aligned} E = & \frac{1}{2} c_{xxxx} (\epsilon_{xx}^2 + \epsilon_{yy}^2) + \frac{1}{2} c_{zzzz} \epsilon_{zz}^2 + c_{xxzz} (\epsilon_{xx} \epsilon_{zz} + \epsilon_{yy} \epsilon_{zz}) \\ & + c_{xyxy} \epsilon_{xx} \epsilon_{yy} + 2c_{xyxy} \epsilon_{xy}^2 + 2c_{xzzx} (\epsilon_{xz}^2 + \epsilon_{yz}^2), \end{aligned} \quad (\text{A.3})$$

since  $c_{xxxx} = c_{yyyy}$ ,  $c_{xxzz} = c_{yyzz}$ ,  $c_{xzzx} = c_{yzyz}$  due to crystal symmetry and further general symmetry properties of  $(c_{ijkl})$  [113]. The quadratic form (A.3) (and (A.1) in general) is positive definite, if all principal minors of  $(c_{ijkl})$  are positive (Sylvester's criterion) [87]. For the considered crystal class, the criterion leads to five stability conditions (SCs) in terms of the elastic constants [163, 197],

$$c_{xxxx}, c_{xyxy}, c_{xzzx} > 0 \quad (\text{A.4})$$

$$c_{xxxx} > |c_{xyxy}| \quad (\text{A.5})$$

$$c_{zzzz} (c_{xxxx} + c_{xyxy}) > 2c_{xzzx}^2. \quad (\text{A.6})$$

## APPENDIX A. ELASTIC CONSTANTS

---

The remaining task is to calculate the six elastic constants for stationary points of the EBP and check the above stability conditions. The number of elastic constants reduces to three for cubic (FCC, BCC) structures:  $c_{xxxx}$ ,  $c_{xxyy}$  and  $c_{xyxy}$ . Also, the SCs (A.4) – (A.6) simplify.

### A.2 Technical considerations

The approach pursued in this work is to directly calculate the total energy change with respect to the stationary reference state for small strains according to Eq. (A.3). The BCT unit cell is distorted in such a way, that the deformations correspond to a single applied strain or two simultaneously applied strains. This procedure simplifies Eq. (A.3). For example, if all strains but  $\epsilon_{zz}$  are defined zero, then

$$E = \frac{1}{2} c_{zzzz} \epsilon_{zz}^2$$

and

$$c_{zzzz} = \frac{d^2 E}{d \epsilon_{zz}^2}. \quad (\text{A.7})$$

Similar expressions hold for the other elastic constants. Values of elastic constants can also be gained from combined strains. Let  $\epsilon_{xx}$  and  $\epsilon_{yy}$  be the only non-vanishing components of the strain tensor. Without loss of generality, we set in case ‘1’ (subscript ‘1’)  $\epsilon_{xx} = \epsilon_{yy} = \epsilon/\sqrt{2}$  and in the second case (subscript ‘2’)  $\epsilon_{xx} = -\epsilon_{yy} = \epsilon/\sqrt{2}$  (the choice of the strains comes from the side condition  $\epsilon^2 = \epsilon_{xx}^2 + \epsilon_{yy}^2$ ), and obtain

$$E_1 = \frac{1}{2} c_{xxxx} \left( \frac{\epsilon^2}{2} + \frac{\epsilon^2}{2} \right) + c_{xxyy} \frac{\epsilon^2}{2}$$

$$E_1 = \frac{c_{xxxx} + c_{xxyy}}{2} \epsilon^2$$

and

$$\frac{d^2 E_1}{d \epsilon^2} = c_{xxxx} + c_{xxyy}.$$

Similarly for  $E_2$  we get

$$\frac{d^2 E_2}{d \epsilon^2} = c_{xxxx} - c_{xxyy}.$$

It is straightforward to see, that the superposition of both equations gives

$$c_{xxxx} = \frac{1}{2} \left( \frac{d^2 E_1}{d \epsilon^2} + \frac{d^2 E_2}{d \epsilon^2} \right) \quad (\text{A.8})$$

$$c_{xxyy} = \frac{1}{2} \left( \frac{d^2 E_1}{d \epsilon^2} - \frac{d^2 E_2}{d \epsilon^2} \right). \quad (\text{A.9})$$

## A.2. TECHNICAL CONSIDERATIONS

The bulk modulus,  $B$ , of a stationary structure can be derived from a differentiation of the total energy with respect to the volume [113],

$$B = V_0^2 \left. \frac{d^2 E}{dV^2} \right|_{V_0}, \quad (\text{A.10})$$

whereat  $V_0$  is the volume at the stationary point. Alternatively, we set  $\epsilon_{xx} = \epsilon_{yy} = \epsilon_{zz} = \epsilon/\sqrt{3}$ , and  $\epsilon_{ik} = 0$  for  $i \neq k$ , in Eq. (A.3), discard higher order than linear terms in  $V = V(\epsilon)$  with  $V(\epsilon) = V_0 (1 + \epsilon/\sqrt{3})^3 \approx V_0(1 + \sqrt{3}\epsilon)$  and use  $\frac{d^2 E}{d\epsilon^2} = \frac{d^2 E}{dV^2} \left(\frac{dV}{d\epsilon}\right)^2$  to obtain

$$B = \frac{c_{xxxx} + 2c_{xxyy}}{3}. \quad (\text{A.11})$$

We used both ways to compute  $B$  in order to check the consistency of our calculations.

The evaluation of each elastic constant requires different settings (space group, lattice parameters, angles, Wyckoff positions). For our specific problem, namely the distortion of a BCT Bravais lattice ( $I4/mmm$ , one Wyckoff position at 000), we list the space groups and Wyckoff position in Table A.1.

Table A.1: Setups appropriate for the calculation of elastic constants of BCT cells with  $I4/mmm$  symmetry.

elastic constant	space group (no.)	(symmetry)	Wyckoff position
$c_{xxxx}$	$Immm$ (71)	(orthorhombic)	000
$c_{zzzz}$	$I4/mmm$ (139)	(tetragonal)	000
$c_{xxyy}$	$Immm$ (71)	(orthorhombic)	000
$c_{xxzz}$	$Immm$ (71)	(orthorhombic)	000
$c_{xyxy}$	$Fmmm$ (69) <sup>a</sup>	(orthorhombic)	000
$c_{xzxz}$	$C2/m$ (12) <sup>b</sup>	(monoclinic)	000

<sup>a</sup> quadratic reference plane

<sup>b</sup> rectangular reference plane

$c_{xyxy}$  and  $c_{xzxz}$  involve a change of the included angle between two adjacent sides. If the lengths of both sides are identical (as for the basal plane of the BCT lattice), the space group is face-centred orthorhombic, otherwise monoclinic.

**Remark on cubic structures** The Bulk modulus according to Eq. (A.10) for the FCC structure and the BCC structure is evaluated in the space group  $Fm\bar{3}m$  and  $Im\bar{3}m$ , respectively. Relation (A.11) requires the knowledge of elastic constants, which in general are calculated based on the tetragonal delineation (cf. Fig. 3.1 on Page 9). That is, we impose deformations on the tetragonal lattice (using tetragonal axes) in order to calculate the elastic constants of BCC and FCC. However, the elastic constants of the FCC phase are defined with respect to the cubic axes. Both coordinate systems are rotated against each other by  $|\pi/4|$ . Thus, the elastic constants, obtained in the tetragonal setup, must

## APPENDIX A. ELASTIC CONSTANTS

---

be transformed from the BCT reference system to the FCC reference system according to tensor transformation rules [95,190]. Accordingly,

$$\begin{aligned} \epsilon_{ij}^{\text{FCC}} &= Q_{im}Q_{jn}\epsilon_{mn}^{\text{BCT}} \\ c_{ijkl}^{\text{FCC}} &= Q_{im}Q_{jn}Q_{kq}Q_{lp}c_{mnqp}^{\text{BCT}}, \end{aligned} \quad (\text{A.12})$$

with the transformation matrix,  $Q_{ij}$ , which for a rotation around [001] by  $\pi/4$  takes the form

$$Q_{ij} = \frac{1}{\sqrt{2}} \begin{pmatrix} 1 & -1 & 0 \\ 1 & 1 & 0 \\ 0 & 0 & \sqrt{2} \end{pmatrix}.$$

Above Eqs. (A.12) simplify to

$$c_{xxxx}^{\text{FCC}} = \frac{1}{2} (c_{xxxx}^{\text{BCT}} + c_{xxyy}^{\text{BCT}} + 2c_{xyxy}^{\text{BCT}}) \quad (\text{A.13})$$

$$c_{xxyy}^{\text{FCC}} = \frac{1}{2} (c_{xxxx}^{\text{BCT}} + c_{xxyy}^{\text{BCT}} - 2c_{xyxy}^{\text{BCT}}) \quad (\text{A.14})$$

$$c_{xyxy}^{\text{FCC}} = \frac{1}{2} (c_{xxxx}^{\text{BCT}} - c_{xxyy}^{\text{BCT}}). \quad (\text{A.15})$$

The back transformation is the same with superscript indices interchanged. All other elastic constants are equal in the FCC and the BCT reference frame for this particular transformation.

For an actual calculation, it is necessary to keep the distortion small enough, such that the harmonic form of the strain energy, Eq. (A.3), is valid. However, distortions should be accompanied by a large enough change in total energy, such that a reliable precision is guaranteed. A typical strain in the order of  $\epsilon = 0.005 \dots 0.010$  causes an energy change per atom in the order of  $10 \dots 100 \mu\text{Hartree}$ . A converged Brillouin zone integration mesh ensures stability of the total energies in the aforementioned range. The  $k$ -mesh was converged in space groups of low symmetry. We found that the values as obtained in Sec. 4.4 are sufficient to guarantee the stability of the total energy. We checked the stability of the computed elastic constants with respect to a doubling of the strain ( $\epsilon = 0.010 \dots 0.020$ ) and found that elastic constants did not change by more than 5%.

## A.3 Tables

### A.3.1 BCC structures

Table A.2 lists the theoretical equilibrium lattice parameter,  $c$ , and the bulk modulus,  $B$ , obtained via Eq. (A.10). Both values were calculated in  $Im\bar{3}m$  symmetry. We tabulate further  $c_{xxxx}$  and  $c_{xxyy}$ , which were evaluated by combining strains (following Eqs. (A.8) and (A.9)). The value of  $c_{xxxx}$  was checked for consistency with the one obtained from a single strain according to Eq. (A.7)



### A.3. TABLES

( $c_{xxxx} = c_{zzzz}$ ). We also computed the bulk modulus from the values of  $c_{xxxx}$  and  $c_{xxyy}$  (Eq. (A.11)) to check the consistency of our data. We also list  $c_{xyxy}$ , which was calculated both in the orthorhombic and the monoclinic symmetry to check its consistency ( $c_{xyxy} = c_{xzxz}$ , cf. Table A.1). The largest applied strains for the different distortions were (modulus values given):  $\epsilon(B) = 0.005$ ,  $\epsilon(c_{xxxx}) = 0.005 = \epsilon(c_{xxyy})$ , and  $\epsilon(c_{xyxy}) = 0.750^\circ$ . All computed elastic constant were consistent. Data from consistency checks are not listed in Table A.2.

The SCs for cubic lattices can be deduced from Inequalities (A.4) to (A.6) by symmetry arguments [163]. They read<sup>1</sup>

$$\text{SC (I)} \quad c_{xxxx} > 0$$

$$\text{SC (II)} \quad c_{xyxy} > 0$$

$$\text{SC (III)} \quad c_{xxxx} > c_{xxyy}$$

$$\text{SC (IV)} \quad c_{xxxx} + 2c_{xxyy} > 0.$$

We indicate by '+' and '-' if the SCs are fulfilled and violated, respectively. Note that, with Eq. (A.11), SC (IV) reads  $3B = c_{xxxx} + 2c_{xxyy} > 0$ . Since the bulk modulus is obtained for equilibrium geometries in the parameter space of cubic lattices,  $B$  is always positive and SC (IV) is always fulfilled. We forwent to show it in Table A.2.

Table A.2: Elastic constants and bulk moduli of various elements in the BCC configuration. Symbols and SCs as explained in the text ('+' fulfilled, '-' not fulfilled). SC (IV) is always fulfilled. Elements are sorted according to their atomic numbers. FM order is indicated.

element	$c$	$B$	$c_{xxxx}$	$c_{xxyy}$	$c_{xyxy}$	SC		
	[Å]	[GPa]	[GPa]	[GPa]	[GPa]	(I)	(II)	(III)
Ca	4.214	20	24	17	21	+	+	+
Sc	3.570	60	50	64	34	+	+	-
Ti	3.167	120	115	121	39	+	+	-
V	2.929	211	328	154	19	+	+	+
Cr	2.791	303	589	161	115	+	+	+
Mn	2.728	343	345	333	147	+	+	+
Fe (FM)	2.752	255	372	195	165	+	+	+
Co (FM)	2.736	274	217	298	172	+	+	-
Ni (FM)	2.725	238	194	261	195	+	+	-
Cu	2.800	187	180	191	131	+	+	-
Zn	3.016	96	62	114	13	+	+	-
Sr	4.571	14	18	12	17	+	+	+
Y	3.917	44	10	61	25	+	+	-
Zr	3.490	99	110	92	35	+	+	+
Nb	3.258	191	289	144	20	+	+	+
Mo	3.124	292	528	173	120	+	+	+
Tc	3.045	334	313	346	152	+	+	-

*continued on next page*

<sup>1</sup>Note that the statement of inequalities based on  $c_{xxxx}$  and  $c_{xxyy}$ , SC (I), SC (III) and SC (IV), can be combined to two SCs:  $c_{xxxx} > |c_{xxyy}|$  and SC (IV). We express the conditions for stability of cubic structures in four inequalities, because the sign of  $c_{xxxx} - c_{xxyy}$  determines the sign of the curvature of  $E(a)$  at stationary points with cubic symmetry, see Sec. 4.7.

## APPENDIX A. ELASTIC CONSTANTS

continued from previous page

element	$c$	$B$	$c_{xxxx}$	$c_{xxyy}$	$c_{xyxy}$	SC		
	[Å]	[GPa]	[GPa]	[GPa]	[GPa]	(I)	(II)	(III)
Ru	3.012	331	81	457	228	+	+	-
Rh	3.019	299	37	413	160	+	+	-
Pd	3.066	220	204	230	141	+	+	-
Ag	3.195	135	126	138	80	+	+	-
Cd	3.443	63	45	74	-6	+	-	-
Ba	4.780	11	15	9	13	+	+	+
La	4.051	32	-10	50	0.9	-	+	-
Lu	3.725	52	26	64	30	+	+	-
Hf	3.444	112	102	115	55	+	+	-
Ta	3.259	216	308	171	86	+	+	+
W	3.145	331	567	212	172	+	+	+
Re	3.081	388	372	395	205	+	+	-
Os <sup>2</sup>	3.061	389	33	565	283	+	+	-
Ir	3.077	347	-121	570	178	-	+	-
Pt	3.117	286	218	321	186	+	+	-
Au	3.220	195	190	198	91	+	+	-
Hg	3.549	54	53	54	3.3	+	+	-

### A.3.2 FCC structures

Table A.3 lists data for FCC structures. SC (IV) is *always* fulfilled as explained in the previous section. We forwent to show it in Table A.3. The theoretical equilibrium constants and bulk moduli were calculated in  $Fm\bar{3}m$  symmetry, the other quantities according to the explanations in the previous section. The applied strains in the BCT reference systems were (modulus values given):  $\epsilon(B) = 0.005$ ,  $\epsilon^{\text{BCT}}(c_{xxxx}) = 0.005 = \epsilon^{\text{BCT}}(c_{xxyy})$ , and  $\epsilon^{\text{BCT}}(c_{xyxy}) = 0.750^\circ$ .

Table A.3: Elastic constants and bulk moduli of various elements in the FCC configuration. Symbols and SCs as explained in the text ('+' fulfilled, '-' not fulfilled). SC (IV) is always fulfilled. Elements are sorted according to their atomic numbers. FM order is indicated.

element	$c$	$B$	$c_{xxxx}$	$c_{xxyy}$	$c_{xyxy}$	SC		
	[Å]	[GPa]	[GPa]	[GPa]	[GPa]	(I)	(II)	(III)
Ca	5.336	18	22	16	4.1	+	+	+
Sc	4.477	59	81	47	42	+	+	+
Ti	4.006	123	147	109	60	+	+	+
V	3.738	200	-48	326	-46	-	-	-
Cr	3.549	277	54	390	-62	+	-	-
Mn	3.434	332	465	261	201	+	+	+
Fe	3.378	328	510	267	289	+	+	+
Co (FM)	3.429	273	382	216	194	+	+	+
Ni (FM)	3.428	256	353	205	169	+	+	+

continued on next page

<sup>2</sup>unstable for  $\epsilon > 0.015$ , cf. Fig. 4.26 and discussion

### A.3. TABLES

*continued from previous page*

element	$c$	$B$	$c_{xxxx}$	$c_{xyyy}$	$c_{xyxy}$	SC		
	[Å]	[GPa]	[GPa]	[GPa]	[GPa]	(I)	(II)	(III)
Cu	3.523	190	233	167	109	+	+	+
Zn	3.787	100	151	74	-3.1	+	-	+
Sr	5.790	15	18	12	17	+	+	+
Y	4.912	46	67	35	40	+	+	+
Zr	4.429	103	124	91	46	+	+	+
Nb	4.156	182	-51	297	-83	-	-	-
Mo	3.956	268	123	329	21	+	+	-
Tc	3.828	338	495	261	213	+	+	+
Ru	3.762	360	560	261	304	+	+	+
Rh	3.769	315	501	222	240	+	+	+
Pd	3.852	226	277	197	86	+	+	+
Ag	4.016	138	167	123	66	+	+	+
Cd	4.314	70	96	55	-3.4	+	-	+
Ba	6.019	10	12	7.7	13	+	+	+
La	5.046	30	49	19	26	+	+	+
Lu	4.661	53	84	38	48	+	+	+
Hf	4.363	119	158	95	70	+	+	+
Ta	4.151	206	78	275	31	+	+	-
W	3.990	309	139	387	-62	+	-	-
Re	3.875	395	610	286	252	+	+	+
Os	3.817	432	685	291	367	+	+	+
Ir	3.830	392	654	260	301	+	+	+
Pt	3.913	297	374	258	99	+	+	+
Au	4.052	198	225	184	51	+	+	+
Hg	4.429	58	63	57	-0.5	+	-	+

#### A.3.3 BCT structures

All stationary points in energy on the EBP, that possess tetragonal symmetry, are listed in Table A.4. Both pairs  $c_{xxxx}$  and  $c_{xyyy}$ , and  $c_{zzzz}$  and  $c_{xzzz}$  were determined by combined strains following Eqs. (A.8) and (A.9). The applied strains were (modulus values given):  $\epsilon(c_{xxxx}) = \epsilon(c_{zzzz}) = 0.005 = \epsilon(c_{xyyy}) = \epsilon(c_{xzzz})$ , and  $\epsilon(c_{xyxy}) = 0.750^\circ = \epsilon(c_{xzzz})$ .

The following five SCs (already mentioned in Eqs. (A.4) – (A.6)) are checked for and the results are also tabulated in Table A.4:

$$\text{SC (I)} \quad c_{xxxx} > 0$$

$$\text{SC (II)} \quad c_{xyxy} > 0$$

$$\text{SC (III)} \quad c_{xzzz} > 0$$

$$\text{SC (IV)} \quad c_{xxxx} > |c_{xyyy}|$$

$$\text{SC (V)} \quad c_{zzzz}(c_{xxxx} + c_{xyyy}) > 2c_{xzzz}^2.$$

## APPENDIX A. ELASTIC CONSTANTS

Table A.4: Elastic constants and bulk moduli of various elements in the BCT configuration. Symbols and SCs as explained in the text ('+' fulfilled, '-' not fulfilled). Elements are sorted according to their atomic numbers and in-plane lattice parameters  $a$ . FM order is indicated.

element	$a$ [Å]	$c_{xxxx}$ [GPa]	$c_{xyxy}$ [GPa]	$c_{xyxy}$ [GPa]	$c_{zzzz}$ [GPa]	$c_{xxzz}$ [GPa]	$c_{xzzx}$ [GPa]	SC				
								(I)	(II)	(III)	(IV)	(V)
Ca	3.79	23	15	3.6	23	18	6.8	+	+	+	+	+
Ca	4.09	23	16	15	16	19	16	+	+	+	+	-
Sc	3.17	108	23	18	94	50	44	+	+	+	+	+
Sc	3.70	16	110	37	44	49	29	+	+	+	-	+
Ti	2.85	185	73	23	162	111	58	+	+	+	+	+
Ti	3.33	137	126	32	151	98	40	+	+	+	+	+
V	2.40	286	206	-91	325	130	66	+	-	+	+	+
Cr	2.31	477	203	-174	463	180	75	+	-	+	+	+
Mn	2.69	369	331	164	336	367	156	+	+	+	+	-
Co (FM)	2.81	230	330	215	235	288	168	+	+	+	-	-
Ni (FM)	2.86	215	310	231	207	296	175	+	+	+	-	-
Cu	2.85	172	198	141	185	183	122	+	+	+	-	+
Zn	3.30	94	97	7.3	174	72	70	+	+	+	+	+
Sr	4.12	31	-0.5	3.6	24	13	18	+	+	+	+	+
Sr	4.32	23	5.9	8.3	16	16	18	+	+	+	+	-
Y	4.07	20	85	35	47	29	23	+	+	+	-	+
Zr	3.14	152	64	17	138	93	52	+	+	+	+	+
Zr	3.32	82	135	24	73	102	43	+	+	+	-	-
Zr	3.56	103	77	35	100	109	35	+	+	+	+	-
Zr	3.74	130	92	24	134	78	40	+	+	+	+	+
Nb	2.70	323	149	-100	323	114	26	+	-	+	+	+
Mo	2.61	386	279	-166	378	192	40	+	-	+	+	+
Tc	3.14	298	382	209	372	279	172	+	+	+	-	+
Ru (FM)	3.18	88	634	227	232	348	154	+	+	+	-	-
Rh	3.22	231	424	259	419	193	183	+	+	+	-	+
Pd	3.20	197	243	154	227	210	112	+	+	+	-	+
Ag	3.31	124	145	96	143	129	69	+	+	+	-	+
Cd	3.78	64	65	12	117	52	37	+	+	+	-	+
Ba	4.35	20	-1.9	4.2	14	12	13	+	+	+	+	-
La	4.28	31	52	20	45	14	21	+	+	+	-	+
Lu	3.88	10	108	39	51	34	33	+	+	+	-	+
Hf	3.64	131	123	54	153	88	62	+	+	+	+	+
Ta	2.75	289	183	-88	315	143	38	+	-	+	+	+
W	2.68	445	258	-170	431	230	45	+	-	+	+	+
Re	3.18	339	472	285	453	333	248	+	+	+	-	+
Os	3.24	-67	918	248	349	290	146	-	+	+	-	+
Ir	3.30	337	492	319	599	219	203	+	+	+	-	+
Pt	3.34	316	317	209	440	215	137	+	+	+	-	+
Au	3.39	182	190	98	211	190	66	+	+	+	-	+
Hg	2.98	82	56	0.7	65	46	-3.7	+	+	-	+	+
Hg	3.93	60	53	23	86	53	7.2	+	+	+	+	+

# Bibliography

- [1] AGUAYO, A., MURRIETA, G., AND DE COSS, R. Elastic stability and electronic structure of fcc Ti, Zr, and Hf: a first-principles study. *Phys. Rev. B* 65 (2002), 092106.
- [2] AHUJA, R., WILLS, J. M., JOHANSSON, B., AND ERIKSSON, O. Crystal structure of Ti, Zr, and Hf under compression: theory. *Phys. Rev. B* 48 (1993), 16269.
- [3] AKELLA, J., WEIR, S., WILLS, J. M., AND SÖDERLIND, P. Structural stability in uranium. *J. Phys.: Condens. Matter* 9 (1997), L549.
- [4] ALIPPI, P., MARCUS, P. M., AND SCHEFFLER, M. Strained tetragonal states and Bain paths in metals. *Phys. Rev. Lett.* 78 (1997), 3892.
- [5] ANDERSEN, O. K., JEPSEN, O., AND GLÖTZEL, D. *Highlights of condensed-matter physics*. Proceedings of the international school of physics 'Enrico Fermi'. North-Holland, Bassani, F., Fumi, F., and Tossi, M. P., Eds., Amsterdam, 1985, ch. Canonical description of the band structure of metals, pp. 59–176.
- [6] ANDERSSON, K. M., JOHNSTON, R. L., AND MURRELL, J. N. Empirical potential-energy function for calcium solids and clusters. *Phys. Rev. B* 49 (1994), 3089.
- [7] ASHCROFT, N. W., AND MERMIN, N. D. *Solid state physics*. Thomson Learning, 1976.
- [8] BAGAYOKO, D., ZIEGLER, A., AND CALLAWAY, J. Band structure of bcc cobalt. *Phys. Rev. B* 27 (1983), 7046.
- [9] BAIN, E. C. The nature of martensite. *Transactions of the American Institute of Mining and Metallurgical Engineers* 70 (1924), 25.
- [10] BAIN, E. C. *Functions of the alloying elements in steel*. American Society for Metals, Cleveland, Ohio, 1939.
- [11] BARRETT, C. S., MUELLER, M. H., AND HITTERMAN, R. L. Crystal structure variations in alpha uranium at low temperatures. *Phys. Rev.* 129 (1963), 625.
- [12] BEGLEY, A. M., KIM, S. K., JONA, F., AND MARCUS, P. M. Growth mode and atomic structure of ultrathin Fe films on Rh{001} determined by quantitative low-energy electron diffraction. *Phys. Rev. B* 48 (1993), 1786.
- [13] BEGLEY, A. M., KIM, S. K., JONA, F., AND MARCUS, P. M. Low-energy electron diffraction study of the growth of ultrathin films of face-centred cubic Co on Rh{001}. *J. Phys.: Condens. Matter* 5 (1993), 7307.
- [14] BENCOK, P., ANDRIEU, S., ARCADE, P., RICHTER, C., ILAKOVAC, V., HECKMANN, O., VESELY, M., AND HRICOVINI, K. Growth of vanadium ultrathin films on Fe(100) studied by RHEED. *Surf. Sci.* 402-404 (1998), 327.
- [15] BERBIL-BAUTISTA, L., HÄNKE, T., GETZLAFF, M., WIESENDANGER, R., OPAHLE, I., KOEPERNIK, K., AND RICHTER, M. Observation of 5f states in U/W(110) films by means of scanning tunneling spectroscopy. *Phys. Rev. B* 70 (2004), 113401.
- [16] BLAHA, P., SCHWARZ, K., SORATIN, P., AND TRICKEY, S. B. Full-potential, linearized augmented plane wave programs for crystalline systems. *Comput. Phys. Commun.* 59 (1990), 399.
- [17] BLAND, J. A. C., AND HEINRICH, B., Eds. *Ultrathin magnetic structures*. Springer-Verlag, Berlin, 1994.
- [18] BLÜGEL, S. *Magnetische Schichtsysteme*. 30. Ferienkurs des Instituts für Festkörperforschung. Forschungszentrum Jülich GmbH, Jülich, 1999, ch. C1: Magnetische Anisotropie und Magnetostriktion (Theorie).

## BIBLIOGRAPHY

---

- [19] BLÜGEL, S. *Probing the nanoworld: microscopies, scattering and spectroscopies of the solid state*. 38<sup>th</sup> IFF spring school. Forschungszentrum Jülich GmbH, Jülich, 2007, ch. A5: electronic structure: reduced dimensions.
- [20] BLUNDELL, S. *Magnetism in condensed matter*. Oxford University Press, Oxford, 2003.
- [21] BONNENBERG, D., HEMPEL, K. A., AND WIJN, H. P. J. *Magnetic properties of 3d, 4d, and 5d elements, alloys and compounds*. No. III/19a in Landolt-Bornstein, New Series. Springer Verlag, Berlin, 1986, p. 178.
- [22] BORN, M., AND HUANG, K. *Dynamical theory of crystal lattices*. Oxford University Press, Oxford, 1954.
- [23] BRAUN, A. Quantitative model for anisotropy and reorientation thickness of the magnetic moment in thin epitaxially strained metal films. *Physica B* 373 (2006), 346.
- [24] BROOKS, M. S. S., AND KELLY, P. J. Large orbital-moment contribution to 5f band magnetism. *Phys. Rev. Lett.* 51 (1983), 1708.
- [25] BRUNO, E., GINATEMPO, B., AND GIULIANO, E. S. Fermi surfaces and electronic topological transitions in metallic random alloys. II. Ag<sub>c</sub>Pd<sub>1-c</sub>. *Phys. Rev. B* 52 (1995), 14557.
- [26] BURKERT, T., ERIKSSON, O., JAMES, P., SIMAK, S. I., JOHANSSON, B., AND NORDSTRÖM, L. Calculation of uniaxial magnetic anisotropy energy of tetragonal and trigonal Fe, Co, and Ni. *Phys. Rev. B* 69 (2004), 104426.
- [27] BURKERT, T., ERIKSSON, O., SIMAK, S. I., RUBAN, A. V., SANYAL, B., NORDSTRÖM, L., AND WILLS, J. M. Magnetic anisotropy of L1<sub>0</sub> FePt and Fe<sub>1-x</sub>Mn<sub>x</sub>Pt. *Phys. Rev. B* 71 (2005), 134411.
- [28] BURKERT, T., NORDSTRÖM, L., ERIKSSON, O., AND HEINONEN, O. Giant magnetic anisotropy in tetragonal FeCo alloys. *Phys. Rev. Lett.* 93 (2004), 027203.
- [29] BUSCHBECK, J., OPAHLE, I., RICHTER, M., RÖSSLER, U. K., KLAER, P., KALLMAYER, M., ELMERS, H. J., JAKOB, G., SCHULTZ, L., AND FÄHLER, S. Full tunability of strain along the fcc-bcc Bain path in epitaxial films and consequences for magnetic properties. *Phys. Rev. Lett.* 103 (2009), 216101.
- [30] CEPERLEY, D. M., AND ALDER, B. J. Ground state of the electron gas by a stochastic method. *Phys. Rev. Lett.* 45 (1980), 566.
- [31] CERDÁ, J. R., DE ANDRES, P. L., CEBOLLADA, A., MIRANDA, R., NAVAS, E., SCHUSTER, P., SCHNEIDER, C. M., AND KIRSCHNER, J. Epitaxial growth of cobalt films on Cu(100): a crystallographic LEED determination. *J. Phys.: Condens. Matter* 5 (1993), 2055.
- [32] CHAMBERS, S. A., ANDERSON, S. B., CHEN, H.-W., AND WEAVER, J. H. Growth of metastable fcc Co on Ni(001). *Phys. Rev. B* 35 (1987), 2592.
- [33] CHANTIS, A. N., ALBERS, R. C., JONES, M. D., VAN SCHILFGAARDE, M., AND KOTANI, T. Many-body electronic structure of metallic  $\alpha$ -uranium. *Phys. Rev. B* 78 (2008), 081101(R).
- [34] CHEN, H., BRENER, N. E., AND CALLAWAY, J. Electronic structure, optical and magnetic properties of fcc palladium. *Phys. Rev. B* 40 (1989), 1443.
- [35] CHOPRA, K. L. Metastable thin film epitaxial structures. *phys. stat. sol.* 32 (1969), 489.
- [36] CLATTERBUCK, D. M., CHRZAN, D. C., AND MORRIS JR., J. W. The ideal strength of iron in tension and shear. *Acta Mater.* 51 (2003), 2271.

## BIBLIOGRAPHY

- [37] COTTENIER, S., DE VRIES, B., MEERSSCHAUT, J., AND ROTS, M. What density-functional theory can tell us about the spin-density wave in Cr. *J. Phys.: Condens. Matter* 14 (2002), 3275.
- [38] CRAIEVICH, P. J., WEINERT, M., SANCHEZ, J. M., AND WATSON, R. E. Local stability of nonequilibrium phases. *Phys. Rev. Lett.* 72 (1994), 3076.
- [39] CYROT-LACKMANN, F. Sur le calcul de la cohésion et de la tension superficielle des métaux de transition par une méthode de liaisons fortes. *J. Phys. Chem. Solids* 29 (1968), 1235.
- [40] DARICI, Y., MARCANO, J., MIN, H., AND MONTANO, P. A. LEED measurements of Fe epitaxially grown on Cu(100). *Surf. Sci.* 182 (1987), 477.
- [41] DEDERICHS, P. H., BLÜGEL, S., ZELLER, R., AND AKAI, H. Ground states of constrained systems: application to cerium impurities. *Phys. Rev. Lett.* 53 (1984), 2512.
- [42] DIAO, J., GALL, K., AND DUNN, M. L. Surface-stress-induced phase transformation in metal nanowires. *Nat. Mater.* 2 (2003), 656.
- [43] DONOHUE, J. *The structures of the elements*. John Wiley and Sons, Inc., New York, 1974.
- [44] DREIZLER, R. M., AND GROSS, E. K. U. *Density functional theory, an approach to the quantum many-body problem*. Springer Verlag, 1990.
- [45] DUCASTELLE, F., AND CYROT-LACKMANN, F. Moments developments and their application to the electronic charge distribution of *d* bands. *J. Phys. Chem. Solids* 31 (1970), 1295.
- [46] DUTHIE, J. C., AND PETTIFOR, D. G. Correlation between *d*-band occupancy and crystal structure in the rare earths. *Phys. Rev. Lett.* 38 (1977), 564.
- [47] EDER, M., HAFNER, J., AND MORONI, E. G. Structural, electronic, and magnetic properties of thin Mn/Cu(100) films. *Phys. Rev. B* 61 (2000), 11492.
- [48] ENDOH, Y., AND ISHIKAWA, Y. Antiferromagnetism of  $\gamma$  iron manganese alloys. *J. Phys. Soc. Jpn.* 30 (1971), 1614.
- [49] ENTEL, P., HOFFMANN, E., MOHN, P., SCHWARZ, K., AND MORUZZI, V. L. First-principles calculations of the instability leading to the Invar effect. *Phys. Rev. B* 47 (1993), 8706.
- [50] ERIKSSON, O., BORING, A. M., ALBERS, R. C., FERNANDO, G. W., AND COOPER, B. R. Spin and orbital contributions to surface magnetism in 3*d* elements. *Phys. Rev. B* 45 (1992), 2868.
- [51] ERIKSSON, O., BROOKS, M. S. S., AND JOHANSSON, B. Orbital polarization in narrow-band systems: application to volume collapses in light lanthanides. *Phys. Rev. B* 41 (1990), 7311.
- [52] ESCHRIG, H. *Ergebnisse in der Elektronentheorie der Metalle*. Ziesche, P., and Lehmann, G., Eds., Springer-Verlag, Berlin, 1983, ch. 8.
- [53] ESCHRIG, H. *The fundamentals of density functional theory*. Edition am Gutenbergplatz Leipzig, Leipzig, 2003.
- [54] ESCHRIG, H.  $T > 0$  ensemble-state density functional theory via Legendre transform. *Phys. Rev. B* 82 (2010), 205120.
- [55] ESCHRIG, H., RICHTER, M., AND OPAHLE, I. *Relativistic electronic structure theory, part 2: applications*, vol. 14 of *Theoretical and Computational Chemistry*. Schwerdtfeger, P., Ed., Elsevier B. V., 2004, ch. 12, pp. 723–776.
- [56] FAST, L., ERIKSSON, O., JOHANSSON, B., WILLS, J. M., STRAUB, G., ROEDER, H., AND NORDSTRÖM, L. Theoretical aspects of the charge density wave in uranium. *Phys. Rev. Lett.* 81 (1998), 2978.

## BIBLIOGRAPHY

---

- [57] FAWCETT, E. Spin-density-wave antiferromagnetism in chromium. *Rev. Mod. Phys.* *60* (1988), 209.
- [58] FERNANDO, G. W., WATSON, R. E., WEINERT, M., WANG, Y. J., AND DAVENPORT, J. W. Cohesion and lattice stabilities in the 5d transition metals: full versus muffin-tin potentials. *Phys. Rev. B* *41* (1990), 11813.
- [59] FERRIANI, P., VON BERGMANN, K., VEDMEDENKO, E. Y., HEINZE, S., BODE, M., HEIDE, M., BIHLMAYER, G., BLÜGEL, S., AND WIESENDANGER, R. Atomic-scale spin spiral with a unique rotational sense: Mn monolayer on W(001). *Phys. Rev. Lett.* *101* (2008), 027201. Erratum *ibid.* *102* (2009), 019901.
- [60] FOX, S., AND JANSEN, H. J. F. Total energy of trigonal and tetragonal cobalt. *Phys. Rev. B* *60* (1999), 4397.
- [61] FREUND, L. B., AND SURESH, S. *Thin film materials: stress, defect formation and surface evolution*. Cambridge University Press, Cambridge, 2004.
- [62] FRIÁK, M., ŠOB, M., AND VITEK, V. Ab initio calculation of phase boundaries in iron along the bcc-fcc transformation path and magnetism of iron overlayers. *Phys. Rev. B* *63* (2001), 052405.
- [63] FRIEDEL, J. *The physics of metals: 1. Electrons*. Ziman, M. J., Ed., Cambridge University Press, London, 1969, ch. 8: Transition metals. Electronic structure of the d-band. Its role in the crystalline and magnetic structures.
- [64] GALL, K., DIAO, J., DUNN, M. L., HAFTEL, M., BERNSTEIN, N., AND MEHL, M. J. Tetragonal phase transformation in gold nanowires. *J. Eng. Mater. Technol.* *127* (2005), 417.
- [65] GASTON, N., PAULUS, B., ROSCISZEWSKI, K., SCHWERDTFEGER, P., AND STOLL, H. Lattice structure of mercury: influence of electronic correlation. *Phys. Rev. B* *74* (2006), 094102.
- [66] GELATT, JR., C. D., EHRENREICH, H., AND WATSON, R. E. Renormalized atoms: cohesion in transition metals. *Phys. Rev. B* *15* (1977), 1613.
- [67] GIORDANO, H., ATREI, A., TORRINI, M., BARDI, U., GLEESON, M., AND BARNES, C. Evidence for a strain-stabilized bct phase of cobalt deposited on Pd{100}: an x-ray photoelectron diffraction study. *Phys. Rev. B* *54* (1996), 11762.
- [68] GLADSTONE, G., JENSEN, M. A., AND SCHRIEFFER, J. R. *Superconductivity*, vol. 2. Marcel Dekker, Parks, R. D., Ed., New York, 1969, ch. 13.
- [69] HAFNER, J., AND HOBBS, D. Understanding the complex metallic element Mn. II. Geometric frustration in  $\beta$ -Mn, phase stability, and phase transitions. *Phys. Rev. B* *68* (2003), 014408.
- [70] HAFNER, J., AND SPIŠÁK, D. Ab initio investigation of the magnetism of tetragonal Mn: bulk, surface, ultrathin films, and multilayers. *Phys. Rev. B* *72* (2005), 144420.
- [71] HAFNER, R., SPIŠÁK, D., LORENZ, R., AND HAFNER, J. Does density-functional theory predict a spin-density-wave ground state for Cr? *J. Phys.: Condens. Matter* *13* (2001), L239.
- [72] HAFTEL, M. I., AND GALL, K. Density functional theory investigation of surface-stress-induced phase transformations in fcc metal nanowires. *Phys. Rev. B* *74* (2006), 035420.
- [73] HÄGLUND, J. Fixed-spin-moment calculations on bcc and fcc iron using the generalized gradient approximation. *Phys. Rev. B* *47* (1993), 566.
- [74] HAHN, T., Ed. *International tables for crystallography*, fourth ed., vol. A: space group symmetry. Kluwer Academic Publishers, Dordrecht, 1995.



## BIBLIOGRAPHY

- [75] HARRISON, W. A. *Electronic structure and the properties of solids: the physics of the chemical bond*, 2nd ed. Dover Publications, Inc., 1989.
- [76] HEDIN, L., AND LUNDQVIST, B. L. Explicit local exchange-correlation potentials. *J. Phys. C: Solid State Phys.* *4* (1971), 2064.
- [77] HEUSER, H. *Lehrbuch der Analysis*, 11. ed., vol. 2. B. G. Teubner, Leipzig, 2000.
- [78] HILL, G. E., MARKLUND, I., MARTINSON, J., AND HOPKINS, B. J. Simultaneous LEED and RHEED studies of the growth of zirconium on the tungsten (100) surface. *Surf. Sci.* *24* (1971), 435.
- [79] HILL, H. H. *Plutonium 1970 and other actinides*. The Metallurgical Society of the AIME, Miner, W. N., Ed., New York, 1970.
- [80] HIRSCH, A. The era of carbon allotropes. *Nat. Mat.* *9* (2010), 868.
- [81] HJELM, A., ERIKSSON, O., AND JOHANSSON, B. Breakdown of Hund's third rule for induced magnetism in U metal. *Phys. Rev. Lett.* *71* (1993), 1459.
- [82] HJELM, A., TRYGG, J., ERIKSSON, O., JOHANSSON, B., AND WILLS, J. Field-induced magnetism in itinerant *f*-electron systems: U, Pu, and Ce. *Phys. Rev. B* *50* (1994), 4332.
- [83] HOBBS, D., HAFNER, J., AND SPIŠÁK, D. Understanding the complex metallic element Mn. I. Crystalline and noncollinear magnetic structure of  $\alpha$ -Mn. *Phys. Rev. B* *68* (2003), 014407.
- [84] HOFMANN, P. *Solid state physics, an introduction*. Wiley-VCH, Berlin, 2008.
- [85] HOHENBERG, P., AND KOHN, W. Inhomogeneous electron gas. *Phys. Rev.* *136* (1964), B864.
- [86] HOLMES, N. C., MORIARTY, J. A., GATHERS, G. R., AND NELLIS, W. J. The equation of state of platinum to 660 GPa (6.6 Mbar). *J. Appl. Phys.* *66* (1989), 2962.
- [87] HORN, R. A., AND JOHNSON, C. R. *Matrix analysis*. Cambridge University Press, Cambridge, 1990.
- [88] JAHNÁTEK, M., HAFNER, J., AND KRAJČÍ, M. Shear deformation, ideal strength, and stacking fault formation of fcc metals: a density-functional study of Al and Cu. *Phys. Rev. B* *79* (2009), 224103.
- [89] JANAK, J. F. Uniform susceptibilities of metallic elements. *Phys. Rev. B* *16* (1977), 255.
- [90] JENNICHES, H., SHEN, J., MOHAN, C., SUNDAR MANOHARAN, S., BARTHEL, J., OHRESSER, P., KLAUA, M., AND KIRSCHNER, J. Structure and magnetism of pulsed-laser-deposited ultrathin films of Fe on Cu(100). *Phys. Rev. B* *59* (1999), 1196.
- [91] JENSEN, J., AND MACKINTOSH, A. R. *Rare earth magnetism: structures and excitations*. Clarendon Press, Oxford, 1991.
- [92] JEONG, S. Structural properties of bulk copper: pseudopotential plane-wave-basis study. *Phys. Rev. B* *53* (1996), 13973.
- [93] JI, X. Y., JONA, F., AND MARCUS, P. M. Metastable tetragonal states of zirconium: theory and experiment. *Phys. Rev. B* *68* (2003), 075421.
- [94] JI, X. Z., TIAN, Y., AND JONA, F. Tetragonal states of palladium II. Experiment. *Phys. Rev. B* *65* (2002), 155404.
- [95] JONA, F., AND MARCUS, P. M. Structural properties of copper. *Phys. Rev. B* *63* (2001), 094113.
- [96] JONA, F., AND MARCUS, P. M. Tetragonal states of palladium: I. Theory. *Phys. Rev. B* *65* (2002), 155403.

## BIBLIOGRAPHY

---

- [97] JONA, F., AND MARCUS, P. M. Metastable phases of silver and gold in hexagonal structure. *J. Phys.: Condens. Matter* 16 (2004), 5199.
- [98] JONA, F., AND MARCUS, P. M. Computational study of Ca, Sr and Ba under pressure. *J. Phys.: Condens. Matter* 18 (2006), 4623.
- [99] KARANIKAS, J. M., SOORYAKUMAR, R., PRINZ, G. A., AND JONKER, B. T. Thermal magnons in bcc cobalt-itinerancy and exchange stiffness. *J. Appl. Phys.* 69 (1991), 6120.
- [100] KATSNELSON, M. I., NAUMOV, I. I., AND TREFILOV, A. V. Singularities of the electronic structure and pre-martensitic anomalies of lattice properties in  $\beta$ -phases of metals and alloys. *Phase Transitions* 49 (1994), 143.
- [101] KIM, S. K., JONA, F., AND MARCUS, P. M. Growth of face-centred-cubic titanium on aluminium. *J. Phys.: Condens. Matter* 8 (1996), 25.
- [102] KIM, S. K., TIAN, Y., MONTESANO, M., JONA, F., AND MARCUS, P. M. Simple structure and soft elastic behavior of Mn on Fe{001}. *Phys. Rev. B* 54 (1996), 5081.
- [103] KOEPERNIK, K. FPLO8.65-32 – an all purpose DFT code. Lecture at workshop ‘DFT meets solid state chemistry’, 2009. available at [www.fplo.de](http://www.fplo.de).
- [104] KOEPERNIK, K., AND ESCHRIG, H. Full-potential nonorthogonal local-orbital minimum-basis band-structure scheme. *Phys. Rev. B* 59 (1999), 1743.
- [105] KOHANOFF, J., AND GIDOPOULOS, N. I. Density functional theory: basics, new trends and applications. In *Handbook of molecular physics and quantum chemistry*, S. Wilson, Ed., vol. 2. John Wiley & Sons, Chichester, 2003.
- [106] KOHLHEPP, J. T., AND DE JONGE, W. J. M. Stabilization of metastable expanded face-centered-tetragonal manganese. *Phys. Rev. Lett.* 96 (2006), 237201.
- [107] KOHN, W., AND SHAM, L. J. Self-consistent equations including exchange and correlation effects. *Phys. Rev.* 140 (1965), A1133.
- [108] KRAFT, T., MARCUS, P. M., METHFESSEL, M., AND SCHEFFLER, M. Elastic constants of Cu and the instability of its bcc structure. *Phys. Rev. B* 48 (1993), 5886.
- [109] KRASKO, G. L., AND OLSON, G. B. Energetics of bcc-fcc lattice deformation in iron. *Phys. Rev. B* 40 (1989), 11536.
- [110] KRESSE, G., AND FURTHMÜLLER, J. Efficient iterative schemes for ab initio total-energy calculations using a plane-wave basis set. *Phys. Rev. B* 54 (1996), 11169.
- [111] KÜBLER, J. *Theory of itinerant electron magnetism*. Clarendon Press, Oxford, 2000.
- [112] KURZ, P., FÖRSTER, F., NORDSTRÖM, L., BIHLMAYER, G., AND BLÜGEL, S. Ab initio treatment of noncollinear magnets with the full-potential linearized augmented plane wave method. *Phys. Rev. B* 69 (2004), 024415.
- [113] LANDAU, L. D., AND LIFSHITZ, E. M. *Elastizitätstheorie*, 6 ed., vol. 7 of *Lehrbuch der Theoretischen Physik*. Akademie-Verlag, Berlin, 1989.
- [114] LANDER, G. H., FISHER, E. S., AND BADER, S. D. The solid-state properties of uranium: a historical perspective and review. *Adv. Phys.* 43 (1994), 1–111.
- [115] LAREF, A., ŞAŞIOĞLU, E., AND SANDRATSKII, L. M. First-principles investigation of magnetism of U films and U(001)<sub>1</sub>/Fe(110)<sub>3</sub> multilayers. *J. Phys.: Condens. Matter* 18 (2006), 4177.
- [116] LE BIHAN, T., HEATHMAN, S., IDIRI, M., LANDER, G. H., WILLS, J. M., LAWSON, A. C., AND LINDBAUM, A. Structural behavior of  $\alpha$ -uranium with pressures up to 100 GPa. *Phys. Rev. B* 67 (2003), 134102.

## BIBLIOGRAPHY

- [117] LEVY, M. Electron densities in search of Hamiltonians. *Phys. Rev. A* 26 (1982), 1200.
- [118] LI, H., LI, Y. S., QUINN, J., TIAN, D., SOKOLOV, J., JONA, F., AND MARCUS, P. M. Quantitative low-energy electron-diffraction study of the epitaxy of Fe on Ag{001}: questions about the growth mode. *Phys. Rev. B* 42 (1990), 9195.
- [119] LI, H., WU, S. C., TIAN, D., QUINN, J., LI, Y. S., JONA, F., AND MARCUS, P. M. Epitaxial growth of body-centered-tetragonal copper. *Phys. Rev. B* 40 (1989), 5841.
- [120] LI, T., MORRIS, JR., J. W., NAGASAKO, N., KURAMOTO, S., AND CHRZAN, D. C. "Ideal" engineering alloys. *Phys. Rev. Lett.* 98 (2007), 105503.
- [121] LI, Y. S., QUINN, J., LI, H., TIAN, D., JONA, F., AND MARCUS, P. M. Large strains in the epitaxy of Cu on Pt{001}. *Phys. Rev. B* 44 (1991), 8261.
- [122] LIEB, E. H. Density functionals for coulomb systems. *Int. J. Quant. Chem.* 24 (1983), 243.
- [123] LIN, W. C., LIN, L. C., CHEN, T. Y., WANG, B. Y., SONG, K.-J., AND LIN, M.-T. Growth, structure, and magnetism of  $\gamma$ -phase Mn ultrathin films on Cu<sub>3</sub>Au(100). *J. Appl. Phys.* 97 (2005), 10K112.
- [124] LIU, A. Y., AND SINGH, D. J. Elastic instability of bcc cobalt. *Phys. Rev. B* 47 (1993), 8515.
- [125] LU, S. H., QUINN, J., TIAN, D., JONA, F., AND MARCUS, P. M. Structural properties of epitaxial films of Fe on Cu and Cu-based surface and bulk alloys. *Surf. Sci.* 209 (1989), 364.
- [126] LU, S. H., WANG, Z. Q., TIAN, D., LI, Y. S., JONA, F., AND MARCUS, P. M. Epitaxial growth of  $\gamma$ -Fe on Ni{001}. *Surf. Sci.* 221 (1989), 35.
- [127] LU, Z. W., WEI, S.-W., AND ZUNGER, A. Absence of volume metastability in bcc copper. *Phys. Rev. B* 41 (1990), 2699.
- [128] LUO, W., ROUNDY, D., COHEN, M. L., AND MORRIS, JR., J. W. Ideal strength of bcc molybdenum and niobium. *Phys. Rev. B* 66 (2002), 094110.
- [129] LYUBINA, J., GUTFLEISCH, O., KUZ'MIN, M. D., AND RICHTER, M. La(Fe,Si)<sub>13</sub>-based magnetic refrigerants obtained by novel processing routes. *J. Magn. Magn. Mater.* 321 (2009), 3571.
- [130] MAGLIC, R. C., LANDER, G. H., MUELLER, M. H., AND KLEB, R. Induced magnetization density in  $\alpha$ -uranium. *Phys. Rev. B* 17 (1978), 308.
- [131] MARCUS, P. M., AND ALIPPI, P. Tetragonal states from epitaxial strain on metal films. *Phys. Rev. B* 57 (1998), 1971.
- [132] MARCUS, P. M., AND JONA, F. Identification of metastable phases: face-centred cubic Ti. *J. Phys.: Condens. Matter* 9 (1997), 6241.
- [133] MARCUS, P. M., JONA, F., AND QIU, S. L. Epitaxial Bain paths and metastable phases from first-principles total-energy calculations. *Phys. Rev. B* 66 (2002), 064111.
- [134] MARCUS, P. M., MORUZZI, V. L., AND QIU, S.-L. Tetragonal equilibrium states of iron. *Phys. Rev. B* 60 (1999), 369.
- [135] MARCUS, P. M., QIU, S.-L., AND MORUZZI, V. L. The mechanism of antiferromagnetism in chromium. *J. Phys.: Condens. Matter* 10 (1998), 6541.
- [136] MARMEGGI, J. C., LANDER, G. H., VAN SMAALEN, S., BRÜCKEL, T., AND ZEYEN, C. M. E. Neutron-diffraction study of the charge-density wave in  $\alpha$ -uranium. *Phys. Rev. B* 42 (1990), 9365.

## BIBLIOGRAPHY

---

- [137] MATTHEISS, L. F., WOOD, J. H., AND SWITENDICK, A. C. *title not available. Methods Comput. Phys.* 8 (1968), 63.
- [138] MATTHEWS, J. W., Ed. *Epitaxial growth, part B*. Academic Press, New York, 1975, ch. 9.
- [139] MCNAUGHT, A. D., AND WILKINSON, A., Eds. *IUPAC. Compendium of chemical terminology*, 2nd ed. Blackwell Scientific Publications, Oxford, 1997.
- [140] MEHL, M. J., AGUAYO, A., BOYER, L. L., AND DE COSS, R. Absence of metastable states in strained monoatomic cubic crystals. *Phys. Rev. B* 70 (2004), 014105.
- [141] METHFESSEL, M., RODRIGUEZ, C. O., AND ANDERSEN, O. K. Fast full-potential calculations with a converged basis of atom-centered linear muffin-tin orbitals: structural and dynamic properties of silicon. *Phys. Rev. B* 40 (1989), 2009.
- [142] MEYERHEIM, H. L., TONNERRE, J.-M., SANDRATSKII, L., TOLENTINO, H. C. N., PRZYBYLSKI, M., GABI, Y., YILDIZ, F., FU, X. L., BONTEMPI, E., GRENIER, S., AND KIRSCHNER, J. New model for magnetism in ultrathin fcc Fe on Cu(001). *Phys. Rev. Lett.* 103 (2009), 267202.
- [143] MILSTEIN, F., FANG, H. E., AND MARSCHALL, J. Mechanics and energetics of the Bain transformation. *Phil. Mag. A* 70 (1994), 621.
- [144] MIN, B. I., OGUCHI, T., JANSEN, H. J. F., AND FREEMAN, A. J. Electronic and structural properties of Lu under pressure: relation to structural phases of the rare-earth metals. *Phys. Rev. B* 34 (1986), 654.
- [145] MOHN, P., SCHWARZ, K., AND WAGNER, D. Magnetoelastic anomalies in Fe-Ni Invar alloys. *Phys. Rev. B* 43 (1991), 3318.
- [146] MOLODTSOV, S. L., BOYSEN, J., RICHTER, M., SEGOVIA, P., LAUBSCHAT, C., GOROVIKOV, S. A., IONOV, A. M., PRUDNIKOVA, G. V., AND ADAMCHUK, V. K. Dispersion of 5f electron states: angle-resolved photoemission on ordered films of U metal. *Phys. Rev. B* 57 (1998), 13241.
- [147] MOORE, K. T., AND VAN DER LAAN, G. Nature of the 5f states in actinide metals. *Rev. Mod. Phys.* 81 (2009), 235.
- [148] MORIARTY, J. A. Density-functional formulation of the generalized pseudopotential theory. III. Transition-metal interatomic potentials. *Phys. Rev. B* 38 (1988), 3199.
- [149] MORIARTY, J. A. High-pressure structural phase stability in Hg to 1 TPa (10 Mbar). *Phys. Lett. A* 131 (1988), 41.
- [150] MORONI, E. G., KRESSE, G., HAFNER, J., AND FURTHMÜLLER, J. Ultrasoft pseudopotentials applied to magnetic Fe, Co, and Ni: from atoms to solids. *Phys. Rev. B* 56 (1997), 15629.
- [151] MORRISON, I. A., KANG, M. H., AND MELE, E. J. First-principles determination of the bulk phase diagram for body-centered-tetragonal copper: application to epitaxial growth of Cu on Fe{100}. *Phys. Rev. B* 39 (1989), 1575.
- [152] MORUZZI, V. L., AND MARCUS, P. M. Trends in bulk moduli from first-principles total-energy calculations. *Phys. Rev. B* 48 (1993), 7665.
- [153] MORUZZI, V. L., MARCUS, P. M., SCHWARZ, K., AND MOHN, P. Total energy surfaces in the  $M - V$  plane for bcc and fcc cobalt. *J. Magn. Magn. Mater.* 54-57 (1986), 955.
- [154] MORUZZI, V. L., WILLIAMS, A. R., AND JANAK, J. F. Local density theory of metallic cohesion. *Phys. Rev. B* 15 (1977), 2854.

## BIBLIOGRAPHY

- [155] MÜLLER, M., ERHART, P., AND ALBE, K. Analytic bond-order potential for bcc and fcc iron—comparison with established embedded-atom method potentials. *J. Phys.: Condens. Matter* 19 (2007), 326220.
- [156] NAGASAKO, N., JAHNÁTEK, M., ASAHI, R., AND HAFNER, J. Anomalies in the response of V, Nb, and Ta to tensile and shear loading: ab initio density functional theory calculations. *Phys. Rev. B* 81 (2010), 094108.
- [157] NEISE, C., KOEPERNIK, K., RICHTER, M., ESCHRIG, H., SARGOLZAEI, M., AND OPAHLE, I. Exchange-only orbital polarization corrections to local approximations in density functional theory. *to be submitted*, see also Ph.D. thesis of Carsten Neise.
- [158] NEISE, C., SCHÖNECKER, S., RICHTER, M., KOEPERNIK, K., AND ESCHRIG, H. The effect of chemical disorder on the magnetic anisotropy of strained Fe-Co films. *submitted to phys. stat. sol.*, see also Ph.D. thesis of Carsten Neise.
- [159] NIXON, L. W., PAPACONSTANTOPOULOS, D. A., AND MEHL, M. J. Electronic structure and superconducting properties of lanthanum. *Phys. Rev. B* 78 (2008), 214510.
- [160] NNOLIM, N. O., TYSON, T. A., AND AXE, L. Theory of the structural phases of group 5B–6B metals and their transport properties. *J. Appl. Phys.* 93 (2003), 4543.
- [161] NORDHEIM, L. Zur Elektronentheorie der Metalle. *Ann. Physik* 9 (1931), 607 and 641.
- [162] NORSTRÖM, L., BROOKS, M. S. S., AND JOHANSSON, B. Calculation of orbital magnetism and magnetocrystalline anisotropy energy in YCo<sub>5</sub>. *J. Phys.: Condens. Matter* 4 (1992), 3261.
- [163] NYE, J. F. *Physical properties of crystals: their representation by tensors and matrices*. Oxford University Press, Oxford, 1960.
- [164] OPAHLE, I. *Dichtefunktionalberechnungen für Seltenerd- und Übergangsmetall-Verbindungen*. PhD thesis, Technische Universität Dresden, 2001.
- [165] OZOLIDŠ, V., AND KÖRLING, M. Full-potential calculations using the generalized gradient approximation: structural properties of transition metals. *Phys. Rev. B* 48 (1993), 18304.
- [166] P. SÖDERLIND. First-principles elastic and structural properties of uranium metal. *Phys. Rev. B* 66 (2002), 085113.
- [167] PAPACONSTANTOPOULOS, D. A. *Handbook of the band structure of elemental solids*. Plenum Press, New York, 1986.
- [168] PARR, R. G., AND YANG, W. *Density-functional theory of atoms and molecules*. Oxford University Press, 1989.
- [169] PAXTON, A. T., METHFESSEL, M., AND POLATOGLU, H. M. Structural energy-volume relations in first-row transition metals. *Phys. Rev. B* 41 (1990), 8127.
- [170] PENG, S., AND JANSEN, H. J. F. Electronic structure of face-centered tetragonal iron. *J. Appl. Phys.* 67 (1990), 4567.
- [171] PENG, S. S., AND JANSEN, H. J. F. Antiferromagnetism in face-centered-tetragonal iron. *J. Appl. Phys.* 69 (1991), 6132.
- [172] PERDEW, J. P., BURKE, K., AND ERNZERHOF, M. Generalized gradient approximation made simple. *Phys. Rev. Lett.* 77 (1996), 3865. Erratum *ibid.* 78 (1997), 1396.
- [173] PERDEW, J. P., CHEVARY, J. A., VOSKO, S. H., JACKSON, K. A., PEDERSON, M. R., SINGH, D. J., AND FIOUHAIS, C. Atoms, molecules, solids, and surfaces: applications of the generalized gradient approximation for exchange and correlation. *Phys. Rev. B* 46 (1992), 6671. Erratum *ibid.* 48 (1993), 4978.

## BIBLIOGRAPHY

---

- [174] PERDEW, J. P., AND WANG, Y. Accurate and simple analytic representation of the electron-gas correlation energy. *Phys. Rev. B* 45 (1992), 13244.
- [175] PERDEW, J. P., AND ZUNGER, A. Self-interaction correction to density-functional approximations for many-electron systems. *Phys. Rev. B* 23 (1981), 5048.
- [176] PÉREZ-PRADO, M. T., AND ZHILYAEV, A. P. First experimental observation of shear induced hcp to bcc transformation in pure Zr. *Phys. Rev. Lett.* 102 (2009), 175504.
- [177] PETTIFOR, D. G. *Metallurgical chemistry*. Her Majesty's Stationery Office, London, 1972, p. 191.
- [178] PETTIFOR, D. G. *A quantum-mechanical critique of the Miedema rules for alloy formation*, vol. 40 of *Solid state physics: advances in research and applications*. Academic Press, Inc., 1987, pp. 43–92.
- [179] PETTIFOR, D. G. *Bonding and structure of molecules and solids*. Oxford University Press, Oxford, 1995.
- [180] PETUKHOV, M., RIZZI, G. A., SAMBI, M., AND GRANOZZI, G. An XPD and LEED study of highly strained ultrathin Ni films on Pd(001). *Appl. Surf. Sci.* 212-213 (2003), 264.
- [181] PHUSITTRAKOOL, A., BOVORNATANARAKS, T., AHUJA, R., AND PINSOOK, U. High pressure structural phase transitions in Sr from ab initio calculations. *Phys. Rev. B* 77 (2008), 174118.
- [182] PRINZ, G. A. Stabilization of bcc Co via epitaxial growth on GaAs. *Phys. Rev. Lett.* 54 (1985), 1051.
- [183] QIU, S. L., AND MARCUS, P. M. Phases of Ca from first principles. *J. Phys.: Condens. Matter* 21 (2009), 435403.
- [184] QIU, S. L., MARCUS, P. M., AND MA, H. Tetragonal equilibrium states of Mn and Fe. *J. Appl. Phys.* 87 (2000), 5932.
- [185] QIU, S. L., MARCUS, P. M., AND MA, H. Epitaxial Bain path of tetragonal Fe. *Phys. Rev. B* 64 (2001), 104431. Erratum: *ibid.* 64 (2001), 229902.
- [186] QUINN, J., LI, Y. S., LI, H., TIAN, D., JONA, F., AND MARCUS, P. M. Atomic and electronic structure of Fe films grown on Pd{001}. *Phys. Rev. B* 43 (1991), 3959.
- [187] RECK, R. A., AND FRY, D. L. Orbital and spin magnetization in Fe-Co, Fe-Ni, and Ni-Co. *Phys. Rev.* 184 (1969), 492.
- [188] RICHTER, M. *Density functional theory applied to 4f and 5f elements and metallic compounds*, vol. 13 of *Handbook of magnetic materials*. Elsevier, Buschow, K. H. J., Ed., Amsterdam, 2001, ch. 2, pp. 87–228.
- [189] RICHTER, M., KOEPERNIK, K., AND ESCHRIG, H. *Condensed matter physics in the prime of the 21st century*. World Scientific, Singapore, 2008, ch. Full-potential local-orbital approach to the electronic structure of solids and molecules, pp. 271–291.
- [190] SADD, M. H. *Elasticity, theory, application, and numerics*. Elsevier Butterworth-Heinemann, Oxford, 2005.
- [191] SAITO, T., FURUTA, T., HWANG, J.-H., KURAMOTO, S., NISHINO, K., SUZUKI, N., CHEN, R., YAMADA, A., ITO, K., SENO, Y., NONAKA, T., IKEHATA, H., NAGASAKO, N., IWAMOTO, C., IKUHARA, Y., AND SAKUMA, T. Multifunctional alloys obtained via a dislocation-free plastic deformation mechanism. *Science* 300 (2003), 464.

## BIBLIOGRAPHY

- [192] SAKURAI, J. J. *Advanced quantum mechanics*, 10th ed. Addison-Wesley Publishing Company, Inc., 1984.
- [193] SANDRATSKII, L. M., AND KÜBLER, J. Static non-uniform magnetic susceptibility of selected transition metals. *J. Phys.: Condens. Matter* 4 (1992), 6927.
- [194] SANTINI, P., LÉMANSKI, R., AND ERDÖS, P. Magnetism of actinide compounds. *Adv. Phys.* 48 (1999), 537–653.
- [195] SAUNDERS, V. R., DOVESI, R., ROETTI, C., ORLANDO, R., ZICOVICH-WILSON, C. M., HARRISON, N. M., DOLL, K., CIVALLERI, B., BUSH, I., D'ARCO, P., AND LLUNELL, M. *Crystal2003 user's manual*. University of Torino, Torino, 2003.
- [196] SCHIRMER, B., FELDMANN, B., SOKOLL, A., GAUTHIER, Y., AND WUTTIG, M. Tetragonal distortion of Mn films on Cu<sub>3</sub>Au(100). *Phys. Rev. B* 60 (1999), 5895.
- [197] SCHÖNECKER, S. Calculation of the epitaxial Bain path of palladium. Master's thesis, Technical University Dresden, 2007.
- [198] SCHWARZ, K., AND MOHN, P. Itinerant metamagnetism in YCo<sub>2</sub>. *J. Phys. F: Met. Phys.* 14 (1984), L129.
- [199] SEVERIN, L., NORDSTRÖM, L., BROOKS, M. S. S., AND JOHANSSON, B. Theoretical study of the ferromagnetism in UNi<sub>2</sub>. *Phys. Rev. B* 44 (1991), 9392.
- [200] SHIIKI, K., AND HIO, O. Formation of a new phase in Ru films by sputtering based on band structure calculation prediction. *Jpn. J. Appl. Phys.* 36 (1997), 7360.
- [201] SIGALAS, M. M., AND PAPACONSTANTOPOULOS, D. A. Calculations of the total energy, electron-phonon interaction, and Stoner parameter for metals. *Phys. Rev. B* 50 (1994), 7255.
- [202] SINGH, D. J. *Planewaves, pseudopotentials and the LAPW method*. Kluwer Academic Publishers, 1994.
- [203] SKRIVER, H. L. Calculated structural phase transitions in the alkaline earth metals. *Phys. Rev. Lett.* 49 (1982), 1768.
- [204] SKRIVER, H. L. Crystal structure from one-electron theory. *Phys. Rev. B* 31 (1985), 1909.
- [205] SLATER, J. C., AND KOSTER, G. F. Simplified LCAO method for the periodic potential problem. *Phys. Rev.* 94 (1954), 1498.
- [206] SLIWKO, V. L., MOHN, P., SCHWARZ, K., AND BLAHA, P. The fcc–bcc structural transition: I. A band theoretical study for Li, K, Rb, Ca, Sr, and the transition metals Ti and V. *J. Phys.: Condens. Matter* 8 (1996), 799.
- [207] SÖDERLIND, P. Theory of the crystal structures of cerium and the light actinides. *Adv. Phys.* 47 (1998), 959.
- [208] SÖDERLIND, P., AHUJA, R., ERIKSSON, O., JOHANSSON, B., AND WILLS, J. M. Theoretical predictions of structural phase transitions in Cr, Mo, and W. *Phys. Rev. B* 49 (1994), 9365.
- [209] SÖDERLIND, P., ERIKSSON, O., JOHANSSON, B., ALBERS, R. C., AND BORING, A. M. Spin and orbital magnetism in Fe-Co and Co-Ni alloys. *Phys. Rev. B* 45 (1992), 12911.
- [210] SÖDERLIND, P., ERIKSSON, O., JOHANSSON, B., WILLS, J. M., AND BORING, A. M. A unified picture of the crystal structures of metals. *Nature* 374 (1995), 524.
- [211] SÖDERLIND, P., ERIKSSON, O., WILLS, J. M., AND BORING, A. M. Theory of elastic constants of cubic transition metals and alloys. *Phys. Rev. B* 48 (1993), 5844.

## BIBLIOGRAPHY

---

- [212] SÖDERLIND, P., AND MOORE, K. T. When magnetism can stabilize the crystal structure of metals. *Scripta Materialia* 59 (2008), 1259.
- [213] SOUVATZIS, P., KATSNELSON, M. I., SIMAK, S., AHUJA, R., ERIKSSON, O., AND MOHN, P. First-principles prediction of superplastic transition-metal alloys. *Phys. Rev. B* 70 (2004), 012201.
- [214] SPIŠÁK, D., AND HAFNER, J. Complex reconstruction of  $\gamma$ -iron multilayers on Cu(100): ab initio local-spin-density investigations. *Phys. Rev. B* 61 (2000), 16129.
- [215] SPRINGELL, R., DETLEFS, B., LANDER, G. H., WARD, R. C. C., COWLEY, R. A., LING, N., GOETZE, W., AHUJA, R., LUO, W., AND JOHANSSON, B. Elemental engineering: epitaxial uranium thin films. *Phys. Rev. B* 78 (2008), 193403.
- [216] STEINLE-NEUMANN, G., STIXRUDE, L., AND COHEN, R. E. First-principles elastic constants for the hcp transition metals Fe, Co, and Re at high pressure. *Phys. Rev. B* 60 (1999), 791. Erratum *ibid.* 60 (2004), 219903.
- [217] STOJÍĆ, N., DAVENPORT, J. W., KOMELJ, M., AND GLIMM, J. Surface magnetic moment in  $\alpha$ -uranium by density-functional theory. *Phys. Rev. B* 68 (2003), 094407.
- [218] STOKES, H. T., AND HATCH, D. M. FINDSYM, 2004. [stokes.byu.edu/isotropy.html](http://stokes.byu.edu/isotropy.html).
- [219] STONER, E. C. Collective electron ferromagnetism II. Energy and specific heat. *Proc. R. Soc. A* 169 (1939), 339.
- [220] STURM, K. *Magnetismus von Festkörpern und Oberflächen*, vol. 24 of *IFF-Ferienkurs*. Forschungszentrum Jülich GmbH, Jülich, 1993, ch. 16. Grundlagen der Elektronentheorie des Festkörpers, p. 16.1.
- [221] SUTTON, A. P. *Electronic structure of materials*. Oxford University Press, Oxford, 1993.
- [222] TANG, W. X., QIAN, D., WU, D., WU, Y. Z., DONG, G. S., JIN, X. F., CHEN, S. M., JIANG, X. M., ZHANG, X. X., AND ZHANG, Z. Growth and magnetism of Ni films on GaAs(001). *J. Magn. Magn. Mater.* 240 (2002), 404.
- [223] TIAN, C. S., QIAN, D., WU, D., HE, R. H., WU, Y. Z., TANG, W. X., YIN, L. F., SHI, Y. S., DONG, G. S., JIN, X. F., JIANG, X. M., LIU, F. Q., QIAN, H. J., SUN, K., WANG, L. M., ROSSI, G., QIU, Z. Q., AND J. SHI. Body-centered-cubic Ni and its magnetic properties. *Phys. Rev. Lett.* 94 (2005), 137210.
- [224] TIAN, D., WU, S. C., JONA, F., AND MARCUS, P. M. Epitaxy of Mn on Pd{001}. *Solid State Commun.* 70 (1989), 199.
- [225] TIAN, Y., JONA, F., AND MARCUS, P. M. Metastable phase of vanadium. *Phys. Rev. B* 58 (1998), 14051.
- [226] TRAN, F., LASKOWSKI, R., BLAHA, P., AND SCHWARZ, K. Performance on molecules, surfaces, and solids of the Wu-Cohen GGA exchange-correlation energy functional. *Phys. Rev. B* 75 (2007), 115131.
- [227] TSETSERIS, L. Noncollinear magnetism of iron along the tetragonal Bain transformation. *Phys. Rev. B* 72 (2005), 012411.
- [228] TSUNODA, Y. Spin-density wave in cubic  $\gamma$ -Fe and  $\gamma$ -Fe<sub>100-x</sub>Co<sub>x</sub> precipitates in Cu. *J. Phys.: Condens. Matter* 1 (1989), 10427.
- [229] TSUNODA, Y., NOGAMI, H., AND TAKASAKA, M. Lattice symmetry of the spiral spin-density-wave state in  $\gamma$ -Fe precipitates in Cu. *Phys. Rev. B* 76 (2007), 054419.



## BIBLIOGRAPHY

- [230] UHL, M., SANDRATSKII, L. M., AND KÜBLER, J. Electronic and magnetic states of  $\gamma$ -Fe. *J. Magn. Magn. Mater.* 103 (1992), 314.
- [231] UHL, M., SANDRATSKII, L. M., AND KÜBLER, J. Spin fluctuations in  $\gamma$ -Fe and in Fe<sub>3</sub>Pt Invar from local-density-functional calculations. *Phys. Rev. B* 50 (1994), 291.
- [232] UPPEBRINK, J., JOHNSTON, R. L., AND MURRELL, J. N. Modelling transition metal surfaces with empirical potentials. *Surf. Science* 304 (1994), 223.
- [233] VALVIDARES, S. M., SCHROEDER, T., ROBACH, O., QUIRÓS, C., LEE, T.-L., AND FERRER, S. Structural and magnetic properties of bcc Co films on Pt(001) studied by magnetic resonant surface x-ray diffraction, STM, and magneto-optical Kerr effect. *Phys. Rev. B* 70 (2004), 224413.
- [234] VAN DE WALLE, A., AND CEDER, G. The effect of lattice vibrations on substitutional alloy thermodynamics. *Rev. Mod. Phys.* 74 (2002), 11.
- [235] VANHOOF, V., ROTS, M., AND COTTENIER, S. Spin-density wave in Cr: nesting versus low-lying thermal excitations. *Phys. Rev. B* 80 (2009), 184420.
- [236] ČERNÝ, M., ŠOB, M., POKLUDA, J., AND ŠANDERA, P. Ab initio calculations of ideal tensile strength and mechanical stability in copper. *J. Phys.: Condens. Matter* 16 (2004), 1045.
- [237] VILLARS, P., AND CALVERT, L. D. *Pearson's handbook of crystallographic data for intermetallic phases*, 2nd ed., vol. 4. ASM international, Materials Park, Ohio, 1991.
- [238] VON BARTH, U., AND HEDIN, L. A local exchange-correlation potential for the spin polarized case: I. *J. Phys. C: Solid State Phys.* 5 (1972), 1629.
- [239] VOSKO, S. H., WILK, L., AND NUSAIR, M. Accurate spin-dependent electron liquid correlation energies for local spin density calculations: a critical analysis. *Can. J. Phys.* 58 (1980), 1200.
- [240] ŠOB, M., FRIÁK, M., LEGUT, D., FIALA, J., AND VITEK, V. The role of ab initio electronic structure calculations in studies of the strength of materials. *Mat. Sci. Eng. A* 387-389 (2004), 148.
- [241] ŠOB, M., WANG, L. G., AND VITEK, V. Local stability of higher-energy phases in metallic materials and its relation to the structure of extended defects. *Comput. Mater. Sci.* 8 (1997), 100.
- [242] WANG, J.-T., WANG, D.-S., AND KAWAZOE, Y. Finite-temperature magnetism of tetragonal iron. *Appl. Phys. Lett.* 88 (2006), 132513.
- [243] WANG, L. G., AND ŠOB, M. Structural stability of higher-energy phases and its relation to the atomic configurations of extended defects: the example of Cu. *Phys. Rev. B* 60 (1999), 844.
- [244] WANG, L. G., ŠOB, M., AND ZHANG, Z. Instability of higher-energy phases in simple and transition metals. *J. Phys. Chem. Solids* 64 (2003), 863.
- [245] WANG, Z. Q., LU, S. H., LI, Y. S., JONA, F., AND MARCUS, P. M. Epitaxial growth of a metastable modification of copper with body-centered-cubic structure. *Phys. Rev. B* 35 (1987), 9322.
- [246] WARD, R. C. C., COWLEY, R. A., LING, N., GOETZE, W., LANDER, G. H., AND STIRLING, W. G. The structure of epitaxial layers of uranium. *J. Phys.: Condens. Matter* 20 (2008), 135003.
- [247] WATANABE, S., KOMINE, T., KAI, T., AND SHIIKI, K. First-principle band calculation of ruthenium for various phases. *J. Magn. Magn. Mater.* 220 (2000), 277.

## BIBLIOGRAPHY

---

- [248] WEDIG, U., JANSEN, M., PAULUS, B., ROSCISZEWSKI, K., AND SONY, P. Structural and electronic properties of Mg, Zn, and Cd from Hartree-Fock and density functional calculations including hybrid functionals. *Phys. Rev. B* 75 (2007), 205123.
- [249] WEI, S.-H., AND KRAKAUER, H. Local-density-functional calculation of the pressure-induced metallization of BaSe and BaTe. *Phys. Rev. Lett.* 55 (1985), 1200.
- [250] WILLIAMS, A. R., MORUZZI, V. L., KÜBLER, J., AND SCHWARZ, K. *title not available*. *Bull. Am. Phys. Soc.* 29 (1984), 278.
- [251] WILLS, J. M., ERIKSSON, O., SÖDERLIND, P., AND BORING, A. M. Trends in the elastic constants of cubic transition metals. *Phys. Rev. Lett.* 68 (1992), 2802.
- [252] WULFF, M., LANDER, G. H., LEBECH, B., AND DELAPALME, A. Cancellation of orbital and spin magnetism in UFe<sub>2</sub>. *Phys. Rev. B* 39 (1989), 4719.
- [253] WUTTIG, M., AND LIU, X. *Ultrathin metal films: magnetic and structural properties*. Springer, Berlin, 2004.
- [254] WUTTIG, M., AND THOMASSEN, J. Structure determination for Fe films on Cu(100). *Surf. Sci.* 282 (1993), 237.
- [255] YAMADA, T., KUNITOMI, N., NAKAI, Y., COX, D. E., AND SHIRANE, G. Magnetic structure of  $\alpha$ -Mn. *J. Phys. Soc. Jpn.* 28 (1970), 615.
- [256] YOUNG, D. A. *Phase diagrams of the elements*. University of California Press, Berkeley, 1991.
- [257] ZACHARIASEN, W. H. Crystal chemical study of the 5f-series of elements. XVI. identification and crystal structure of protactinium metal and of protactinium monoxide. *Acta Cryst.* 5 (1952), 19.
- [258] ZELENÝ, M., LEGUT, D., AND ŠOB, M. Ab initio study of Co and Ni under uniaxial and biaxial loading and in epitaxial overlayers. *Phys. Rev. B* 78 (2008), 224105.
- [259] ZHENG-JOHANSSON, J. X., ERIKSSON, O., JOHANSSON, B., FAST, L., AND AHUJA, R. Comment on "Stability and the equation of state of  $\alpha$ -manganese under ultrahigh pressure". *Phys. Rev. B* 57 (1995), 10989.

# Acknowledgement

Foremost, I would like to express my sincere gratitude to my advisor Prof. Dr. Helmut Eschrig for his continuous support during my Ph.D. study and research, his enthusiasm, and for guiding me with his comprehensive understanding of physics.

I am indebted to PD Dr. Manuel Richter for his ongoing encouragement, his ideas and suggestions, and the patience in discussions. His guidance and critical reading helped me in research and writing of this doctoral thesis, respectively.

Special thanks go to Prof. Dr. Jeroen van den Brink and Prof. Dr. Niels Egede Christensen for reviewing this thesis.

I am much obliged to Dr. Klaus Koepf for his insightful comments, our whiteboard discussions, and his assistance in calculations. Further, I thank PD Dr. Sibylle Gemming for her useful suggestions in the beginning of this project.

Also, I want to acknowledge Dipl.-Phys. Ulrike Nitzsche for providing a stable computing platform and numerous help in computational issues.

I thank my fellow workers Dipl.-Phys. Mathias Bayer, Dr. Daniel Fritsch, Dr. Steven Johnston, Dipl.-Phys. Carsten Neise, Dr. Carmine Ortix, Dipl.-Phys. Friedrich Roth, M.Sc. Jörn Venderbos, Dr. Hongbin Zhang, and Dr. Wenxu Zhang for stimulating discussions regardless of physical or non-physical origin. I am grateful to all my colleagues at the Institute for Theoretical Physics at the IFW Dresden for providing a pleasant working environment, in particular our secretaries Mrs. Angela Heinrich and Mrs. Grit Rötzer for their support in administrative matters.

Last but not the least, I would like to thank my family and my friends.



# Eidesstattliche Erklärung

Hiermit versichere ich, daß ich die vorliegende Arbeit ohne unzulässige Hilfe Dritter und ohne Benutzung anderer als der angegebenen Hilfsmittel angefertigt habe; die aus fremden Quellen direkt oder indirekt übernommenen Gedanken sind als solche kenntlich gemacht. Die Arbeit wurde bisher weder im Inland noch im Ausland in gleicher oder ähnlicher Form einer anderen Prüfungsbehörde vorgelegt.

Die vorliegende Dissertation wurde unter der wissenschaftlichen Betreuung von Herrn Prof. Dr. Helmut Eschrig im Institut für Theoretische Festkörperphysik am Leibniz-Institut für Festkörper- und Werkstoffforschung in Dresden angefertigt.

Bis zum jetzigen Zeitpunkt habe ich keinerlei erfolglose Promotionsverfahren absolviert.

Ich erkenne die Promotionsordnung der Fakultät für Mathematik und Naturwissenschaften der Technischen Universität Dresden an.

Ort, Datum

Stephan Schönecker